Stabilization-Free Virtual Element Methods for Solid Continua

By

ALVIN CHEN
DISSERTATION

Submitted in partial satisfaction of the requirements for the degree of

DOCTOR OF PHILOSOPHY

in

Applied Mathematics

in the

OFFICE OF GRADUATE STUDIES

of the

UNIVERSITY OF CALIFORNIA

DAVIS

Approved:

N. Sukumar, Chair

Elbridge Gerry Puckett

Joseph Teran

Committee in Charge

2024

To my late grandpa, Huan Long Chen

Contents

Abstract

The Virtual Element Method (VEM) is a recently introduced extension of the Finite Element Method (FEM) to general polygonal and polyhedral (polytopal) meshes. By using a set of virtual canonical basis functions, the method provides flexibility for meshing complex geometries with convex and nonconvex polygonal elements, as well as providing a simple approach to handling non-matching meshes and fracturing. Polynomial projection operators are introduced to provide approximation accuracy and to preserve polynomial consistency. However, one limitation of the VEM, is the need to devise a problem dependent stabilization term to retain coercivity. The choice of stabilization adds complexity in formulating new problems and an incorrect choice can adversely affect the solution accuracy. In this dissertation, we develop virtual element methods that do not rely on a stabilization term for problems in planar linear elasticity.

We first present strain-based approaches, which use higher order polynomials to enhance the strain polynomial approximation. In these methods, the polynomials are only chosen to preserve the stability of the system. We give theoretical arguments for the stability, well-posedness and prove convergence estimates for the first-order case. These approaches are numerically tested on benchmark elasticity problems, and the results show that the methods attain optimal convergence rates and provide a viable alternative to the standard VEM for compressible materials. However, for thin structures or nearly-incompressible materials, we find that the strain-based approaches and the standard VEM are overly stiff and suffer from locking phenomena.

To alleviate locking, we appeal to stress-based approaches that rely on the Hellinger–Reissner variational formulation. These methods use selectively chosen higher order divergence-free polynomials that preserve the stability as well as alleviate locking. Starting with quadrilateral elements, we use a five-parameter expansion of the stress field to construct a method that is free of volumetric and shear locking. For six-noded triangular elements, we find that a fifteen-term divergence-free stress expansion resulted in a method that does not require stabilization and shows immunity to locking. An alternative to using divergence-free polynomials is also explored. This approach uses a penalty term to weakly enforce the equilibrium equations. Numerical results reveal that the stress-based approaches provide optimal convergence, and robustness for compressible and nearly-incompressible problems.

Acknowledgments

I am very grateful to my advisor, Professor N. Sukumar, for his support, advice and inspiration throughout my time in graduate school.

I would like to thank Professors Elbridge Gerry Puckett and Joseph Teran for serving on my thesis committee; and to Professors Robert Guy and Adam Jacob for serving on my qualifying exam committee. I am also thankful to Dr. Joseph Bishop for his collaboration in research and for giving me the opportunity to spend a summer at Sandia National Lab.

Thank you to my friends and colleagues in Davis, in particular, Ben Godkin, Alex Lee and Girish Kumar for making graduate school life more enjoyable.

Finally, I would like to express my gratitude to my father Rong Jian Chen, my mother Xiu Qiu Chen, my grandma Xing Qi Zhang and my late grandpa Huan Long Chen for their support and care throughout my life. I am also thankful to my brother Ivan, and my extended family for their encouragement.

CHAPTER 1

Introduction

For many applications in science and engineering, there is a need to solve elliptic boundary-value problems (BVPs) that describe physical phenomena. Classically, the Finite Element Method (FEM) is used to solve these problems. Although the FEM has been successfully applied to many problems in computational mechanics, a long standing issue is to develop a finite element formulation that is robust (does not suffer from volumetric and shear locking) [3], accurate on coarse meshes, and can be easily meshed. Low-order, fully integrated displacement-based finite elements are prone to volumetric locking as the Poisson's ratio $\nu \to 0.5$, and for bending-dominated problems, spurious shear strains (element tends to be overly stiff) lead to shear locking phenomenon. Many techniques such as the B-bar and selective integration formulations [77, 94], method of incompatible modes [113], assumed enhanced strain [102, 103], stabilized elements [17, 18], mixed elements [121], and hybrid-stress methods [63, 64, 67, 89, 90, 91] have been developed to alleviate locking in the nearly-incompressible limit and for bending-dominated problems. However, many of these methods are only applicable to quadrilateral and hexahedral elements. For many complex geometries, meshes of quadrilateral and hexahedral elements must be manually constructed. This process is time consuming since there are currently no available high-quality automatic mesh generators for quadrilateral or hexahedral elements. Triangular and tetrahedral meshes can be automatically generated with well-established robust mesh generation tools; however, specialized methods are needed to treat locking. Progress has been made to construct modified triangular elements that are robust and accurate: the variational multiscale approach [99], hybrid-stress elements using Airy stress functions [69, 73, 75, 96, 111], Bézier elements [68], F-bar and reduced integration [50, 81] to name a few. Another promising approach is the use of composite elements [29, 57, 60, 72, 83, 108]. In this approach, an element is split into sub-triangles (sub-tetrahedra), and then on each sub-triangle the strain is approximated and combined to recover the strain field over the entire element. Similar constructions are also used in [23] to construct a three-dimensional brick element for nearly incompressible nonlinear elasticity problems and in [44, 45, 46, 55] for triangular bending elements.

The Virtual Element Method (VEM) [9,11,14] is a recently developed numerical method used to solve boundary-value problems. From [30], the method can be view as a generalization of the hourglass stabilized finite element method to polygonal (polyhedral) meshes. In the VEM, the polygonal basis functions are not explicitly computed and are unknown (virtual) in each element. However, the virtual functions are assigned values, called the degrees of freedom (DOF), that are sufficient to construct polynomial projection operators. These polynomial projections are needed to approximate the virtual functions inside an element. The polynomial functions are given in global coordinates and do not rely on the use of an isoparametric mapping. Therefore, the projections are well-defined for convex, nonconvex, and even degenerate polygonal shapes, which gives the method more flexibility when meshing complicated geometries. The flexibility of VEM has attracted many researchers to develop methods for applications in solid continua; examples include linear elasticity [6,11], applications in three-dimensional elasticity [58], linear elastodynamics [86,87], finite deformations [39,53,114], linear fracture mechanics [82], contact problems [115], mixed and hybrid formulations [7,8,24,48,51].

The advent of the virtual element method has also provided new routes to potentially alleviate locking for nearly-incompressible materials. Initially, mixed variational principles, hybrid formulations, node based methods, B-bar and selective reduced integration strategies that are prominent in finite element formulations for constrained problems have been adopted in the virtual element method [7,8,48,51,84,85]. In [24], a comparison of different virtual element methods to classical finite element techniques for incompressible problems is presented. Although the virtual element formulation have resolved many of the difficulties of the finite element method, one unsettled complication of the VEM is the need to construct a stabilization term. Many studies have focused on determining and testing the robustness of stabilization terms [30,52,78,97,110]. However, having a stabilization term adds complexity in formulating nonlinear problems and an incorrect choice can affect accuracy and conditioning.

In the past few years, there has been a growing interest in developing stabilization-free virtual element methods. For the Poisson equation, the pioneering development is introduced in [20], a stabilization-free mixed method is described in [25], and another approach using divergence-free basis functions is given in [21]. The application of the stabilization-free approach to the Laplacian eigenvalue problem is presented in [79]. There has also been progress in stabilization-free methods for computational mechanics. Early extensions to linear elasticity are given in [36,37] and an earlier approach explored in [54]. In [119,120] the SF-VEM is introduced for two-dimensional finite strain and three dimensional elasticity problems. In [70,71], a Hu–Washizu variational formulation is used to construct a stabilization-free method for static and dynamic problems on quadrilateral meshes, and in [47] the method is analyzed for stability and convergence. In [35,38] an alternative approach using a stress-based Hellinger–Reissner variational formulation is developed for quadrilateral and six-noded triangular meshes.

In this thesis, we investigate the recently introduced Stabilization-Free Virtual Element Method (SF-VEM) [20] and its applications to problems in linear elasticity. Then connecting the idea to hybrid-stress methods found in FEM, we explore the use of a hybrid variational approach to develop virtual element methods that have robust performance and are immune to locking.

Parts of this thesis have been published in peer-reviewed journals. Chapter 3 is based on [37], Chapter 4 describes work established in [36], Chapter 5 appears in [38], and Chapter 6 is found in [35].

In Chapter 2, we present the basic ideas and development of the virtual element method. We first introduce the necessary background spaces and the weak problem. Then, we discuss the construction of the standard virtual element element for the scalar Poisson equation, describe a suitable discrete bilinear form with stabilization, and show convergence results. Finally, we briefly discuss the standard virtual element method for linear elasticity problems.

In Chapter 3, we describe the extension of the first-order stabilization-free virtual element method to compressible linear elasticity problems. We detail the construction of an enhanced virtual element space, polynomial projection operators and the discrete weak problem. We show theoretical well-posedness and optimal convergence results. We also detail the numerical implementation and then present representative benchmark problems, which numerically affirm the convergence rates and applicability of the method.

Chapter 4 continues with the development of the stabilization-free virtual element method to arbitrary order. We apply the idea of serendipity elements to reduce the total number of degrees of freedom. A serendipity projection operator is presented and is used to construct a high-order strain projection. An eigenvalue analysis is then performed to determine a criterion to avoid needing a stabilization term. The method is tested on several benchmark problems and the convergence is compared to theoretical results.

In Chapter 5, to alleviate locking of thin structures and nearly incompressible materials, we revisit the hybrid-stress finite element method [89, 90] to develop a stress-hybrid virtual element method for quadrilateral elements. The Hellinger–Reissner variational principle, with initially independent stress and displacement fields, is used to derive the weak equilibrium equations and a new projection operator for the stress. An eigenvalue analysis is then used to examine the stability and rotational invariance of the method. A variety of nearly incompressible problems with convex and nonconvex meshes is solved and the performance of the stress-hybrid VEM is compared to the B-bar VEM [85].

In Chapter 6, we extend the quadrilateral SH-VEM to develop a stress-hybrid virtual element method for six-noded triangular meshes. We investigate the performance and stability for different choices of stress basis functions. For flexibility in the choice of stress basis functions, we also reintroduce a penalization term that weakly enforces the equilibrium conditions on the stress basis functions. Both of these methods are utilized to solve many benchmark problems in the nearly incompressible regime, and their performance is compared to the B-bar VEM and composite triangle FEM [60].

In Chapter 7, we summarize the main results obtained in this work and close with some final remarks on the promise of stabilization-free virtual element methods in computational solid mechanics.

CHAPTER 2

Virtual Element Method

In this chapter, we introduce some of the main features of the standard virtual element method for elliptic boundary-value problems. We start off by reviewing some preliminary definitions and notation of function spaces and functional analysis. Then we discuss the Poisson problem and derive its associated weak form. For the sake of comparison, we examine the basics of triangular finite element methods applied to the Poisson problem and outline some convergence results. We then investigate the same problem using the virtual element method, and review some of the stability and convergence results of the VEM. Finally, we briefly describe the extension of the VEM for linear elasticity problems.

2.1. Mathematical preliminaries

In this section, we introduce basic linear functional analysis concepts and variational calculus that will be used to study the weak form of an elliptic boundary-value problem. More details of the mathematical theory used for elliptic problems and in the finite element method can be found in [27, 28, 42].

2.1.1. Hilbert spaces. Let Ω be a bounded set with piecewise smooth boundary $\partial\Omega$. For this work, we use functions that are either square integrable or its derivatives are square integrable in Ω. We denote the space of functions that are square-integrable on Ω by:

$$L^2(\Omega) = \left\{ w : \int_\Omega w^2 \, d\boldsymbol{x} < \infty \right\}. \tag{2.1}$$

For every u, $v \in L^2(\Omega)$, define the inner product

$$(u, v)_{L^2} = \int_\Omega uv \, d\boldsymbol{x}, \tag{2.2}$$

and the induced norm

$$\|u\|_{L^2} = \sqrt{(u,u)_{L^2(\Omega)}} = \left(\int_\Omega u^2 \, d\boldsymbol{x}\right)^{\frac{1}{2}}. \tag{2.3}$$

The space $L^2(\Omega)$ equipped with the inner product is a Hilbert space (complete inner product space).

For the study of partial differential equations, we are also interested in the derivative (weak sense) of functions and the associated spaces. Let $\boldsymbol{\alpha} \in \mathbb{Z}^n_{\geq 0}$ be an element in the set of n-tuple non-negative integers and denote the magnitude of $\boldsymbol{\alpha}$ by $|\boldsymbol{\alpha}| = \alpha_1 + \alpha_2 + \cdots + \alpha_n$, where α_i is the i-th component of $\boldsymbol{\alpha}$. For a sufficiently smooth function g, the $\boldsymbol{\alpha}$-th partial derivative is given by

$$D^{\boldsymbol{\alpha}} g = \frac{\partial^{|\boldsymbol{\alpha}|} g}{\partial x_1^{\alpha_1} \partial x_2^{\alpha_2} \ldots \partial x_n^{\alpha_n}}. \tag{2.4}$$

However, the classical definition of the derivative is not well-defined for functions in L^2 or other similar function spaces. Therefore, we introduce the concept of the weak derivative. Let $g \in C_c^\infty(\Omega)$ be any infinitely differentiable function with compact support, then $u \in L^2(\Omega)$ is said to have an $\boldsymbol{\alpha}$-th weak derivative if there exists a function $v \in L^2(\Omega)$ such that

$$\int_\Omega v g \, d\boldsymbol{x} = (-1)^{|\boldsymbol{\alpha}|} \int_\Omega u D^{\boldsymbol{\alpha}} g \, d\boldsymbol{x}. \tag{2.5}$$

If such a function v exists, then it is called the $\boldsymbol{\alpha}$-th weak derivative of u (it is unique) and is denoted $v = D^{\boldsymbol{\alpha}} u$. Then define the space $H^k(\Omega)$ as the collection of L^2 functions with all of its weak derivatives up to order k that are square-integrable by

$$H^k(\Omega) = \left\{ u \in L^2(\Omega) : D^{\boldsymbol{\alpha}} u \in L^2(\Omega) \;\; \forall \, |\boldsymbol{\alpha}| \leq k \right\}, \tag{2.6}$$

For any u, $v \in H^k(\Omega)$, define the inner product

$$(u,v)_{H^k(\Omega)} = \sum_{|\boldsymbol{\alpha}| \leq k} \int_\Omega (D^{\boldsymbol{\alpha}} u)(D^{\boldsymbol{\alpha}} v) \, d\boldsymbol{x}, \tag{2.7}$$

and the induced norm

$$\|u\|_{H^k(\Omega)} = \sqrt{(u,u)_{H^k(\Omega)}} = \left(\sum_{|\boldsymbol{\alpha}| \leq k} \int_\Omega (D^{\boldsymbol{\alpha}} u)^2 \, d\boldsymbol{x} \right)^{\frac{1}{2}}. \tag{2.8}$$

For convenience, we also define the seminorm $|\cdot|_{H^K(\Omega)}$ by

$$|u|_{H^k(\Omega)} = \left(\sum_{|\boldsymbol{\alpha}|=k} \int_\Omega (D^{\boldsymbol{\alpha}} u)^2 \, d\boldsymbol{x} \right)^{\frac{1}{2}}. \tag{2.9}$$

In this work, we are mainly concerned with $H^1(\Omega)$; in this space, the weak derivative notation can be simplified by writing it in terms of the gradient function:

$$H^1(\Omega) = \left\{ u \in L^2(\Omega) : \nabla u \in L^2(\Omega) \right\}, \tag{2.10}$$

For any u, $v \in H^1(\Omega)$, define the inner product

$$(u, v)_{H^1(\Omega)} = \int_\Omega uv \, d\boldsymbol{x} + \int_\Omega \nabla u \cdot \nabla v \, d\boldsymbol{x}, \tag{2.11}$$

with the induced norm

$$\|u\|_{H^1(\Omega)} = \sqrt{(u,u)_{H^1(\Omega)}} = \left(\int_\Omega u^2 \, d\boldsymbol{x} + \int_\Omega |\nabla u|^2 \, d\boldsymbol{x} \right)^{\frac{1}{2}}, \tag{2.12}$$

and the seminorm $|\cdot|_{H^1(\Omega)}$:

$$|u|_{H^1(\Omega)} = \left(\int_\Omega |\nabla u|^2 \, d\boldsymbol{x} \right)^{\frac{1}{2}}. \tag{2.13}$$

For boundary-value problems, an important space is $H_0^1(\Omega) \subset H^1(\Omega)$ which contains functions that vanish along the boundary

$$H_0^1(\Omega) = \left\{ v \in H^1(\Omega) : v = 0 \text{ on } \partial\Omega \right\}. \tag{2.14}$$

We note that in the space $H^1(\Omega)$, the statement $v = 0$ is defined in terms of the trace operator and is not well-defined pointwise (see [27, 42]). The seminorm $|\cdot|_{H^1(\Omega)}$ on the space $H^1(\Omega)$ is a norm on $H_0^1(\Omega)$, and is equivalent to the norm $\|\cdot\|_{H^1(\Omega)}$. That is, for any $v \in H_0^1(\Omega)$,

$$\|v\|_{H_0^1(\Omega)} = |v|_{H^1(\Omega)}, \tag{2.15}$$

and there exists constants C_1, C_2 such that

$$C_1 \|v\|_{H^1(\Omega)} \leq \|v\|_{H_0^1(\Omega)} \leq C_2 \|v\|_{H^1\Omega)}, \tag{2.16}$$

where the equivalence (2.16) is shown using the Poincare–Friedrichs inequality [42].

In general, for a function space $V(\Omega)$, the notation $[V(\Omega)]^d$ represents a space of d-dimensional vector-valued functions such that each component is in $V(\Omega)$. If the dimension d of the space is clear, then for convenience, we may use the notation $\boldsymbol{V}(\Omega) := [V(\Omega)]^d$.

2.1.2. Bilinear forms and functionals.

Let V be a normed linear space and let $a : V \times V \to \mathbb{R}$ be a mapping that takes two elements from V and returns a scalar value. If the map $a(\cdot,\cdot)$ is linear in each argument, then it is called a bilinear form. A bilinear form is continuous (bounded) if there exists a constant $C_1 > 0$ such that

$$|a(u,v)| \leq C_1 \|u\|_V \|v\|_V \quad \forall u, v \in V, \tag{2.17}$$

and is coercive if there exists a $C_2 > 0$ such that

$$a(u,u) \geq C_2 \|u\|_V^2 \quad \forall u \in V. \tag{2.18}$$

A bilinear form $a(\cdot,\cdot)$ is called symmetric if it satisfies

$$a(u,v) = a(v,u) \quad \forall u, v \in V. \tag{2.19}$$

Combining (2.17) and (2.18), we have that a bounded and coercive bilinear form satisfies the relation:

$$C_2 \|u\|_V^2 \leq a(u,u) \leq C_1 \|u\|_V^2. \tag{2.20}$$

If $a(\cdot,\cdot)$ is also symmetric, then it defines an inner product and induces a norm $\|u\|_a = \sqrt{a(u,u)}$. By (2.20) this norm is equivalent to the norm on V. That is

$$C_2 \|u\|_V^2 \leq \|u\|_a^2 \leq C_1 \|u\|_V^2. \tag{2.21}$$

Let $F : V \to \mathbb{R}$ be a map that takes an element from V and returns a real number. If F is linear with respect to its argument then it is called a linear functional and if it satisfies for all $v \in V$ the condition

$$|F(v)| \leq C \|v\|_V, \tag{2.22}$$

then F is bounded (continuous).

Remark 2.1.1. *We note if V is an inner product space with inner product $(\cdot,\cdot)_V$, then for a fixed element $f \in V$, the map $(f,\cdot) : V \to \mathbb{R}$ defines a linear functional on V. Therefore, we will often use the notation $(f,\cdot)$ to refer to a linear functional.*

2.1.3. Weak form and variational principles.

Suppose we have a symmetric bounded bilinear form $a(\cdot,\cdot)$ and a bounded functional $F(\cdot)$ generated from a boundary-value problem. Then a general weak problem is of the form: find $u \in V$, such that

$$a(u,v) = F(v) \quad \forall v \in V. \tag{2.23}$$

For a symmetric bilinear form, this is equivalent to finding a solution to the variational problem:

$$\min_{v\in V} \Pi[v] := \min_{v\in V} \frac{1}{2} a(v,v) - F(v). \tag{2.24}$$

For the weak and variational problem, the Lax–Milgram theorem guarantees the existence and uniqueness of a solution:

Theorem 2.1.1. *Let V be a Hilbert space, $a(\cdot,\cdot) : V \times V \to \mathbb{R}$ a bounded (2.17), coercive (2.18) bilinear form, and $F : V \to \mathbb{R}$ a bounded linear functional. Then the weak problem given in (2.23) has a unique solution.*

Both (2.23) and (2.24) are used in this work to formulate virtual element methods.

2.2. Governing equation and weak form of Poisson's equation

For simplicity, we start with the scalar Poisson boundary-value problem with homogeneous boundary conditions given by

$$-\Delta u = f \ \text{ in } \Omega, \tag{2.25a}$$

$$u = 0 \ \text{ in } \partial\Omega, \tag{2.25b}$$

where $\Omega \subset \mathbb{R}^2$ is a bounded region and $f \in L^2(\Omega)$. This gives the strong form of the Poisson problem. Solutions to the strong form are twice continuously differentiable and satisfy the Poisson equation pointwise. However, for the finite element method, the virtual element method and other similar methods, this requirement is restrictive. Instead, we introduce the weak form of the

Poisson problem, which requires only weak differentiability and satisfaction of Poisson's equation in an integral sense.

Let v be a test function, multiply both sides of (2.25a) by v and integrate over the domain Ω:

$$-\int_\Omega v\Delta u\, d\boldsymbol{x} = \int_\Omega fv\, d\boldsymbol{x}. \tag{2.26}$$

Now we recall the vector identity

$$\nabla\cdot(v\nabla u) = \nabla v\cdot\nabla u + v\Delta u. \tag{2.27}$$

Then using (2.27), we rewrite the integral expression in (2.26) as

$$\int_\Omega \nabla v\cdot\nabla u\, d\boldsymbol{x} - \int_\Omega \nabla\cdot(v\nabla u)\ d\boldsymbol{x} = \int_\Omega fv\, d\boldsymbol{x}.$$

After applying the divergence theorem, we obtain

$$\int_\Omega \nabla v\cdot\nabla u\, d\boldsymbol{x} - \int_{\partial\Omega} (v\nabla u)\cdot n\, ds = \int_\Omega fv\, d\boldsymbol{x}.$$

By taking $v \in H_0^1(\Omega)$, we have that v vanishes along the boundary $\partial\Omega$, so the integral over the boundary also vanishes. Therefore, the original differential equation becomes

$$\int_\Omega \nabla v\cdot\nabla u\, d\boldsymbol{x} = \int_\Omega fv\, d\boldsymbol{x}. \tag{2.28}$$

Then we can define the weak problem as: find the function $u \in H_0^1(\Omega)$ such that

$$a(u,v) = (f,v) \quad \forall v \in H_0^1(\Omega), \tag{2.29a}$$

where the bilinear form $a(u,v)$ and linear functional (f,v) are given by

$$a(u,v) = \int_\Omega \nabla u\cdot\nabla v\, d\boldsymbol{x}, \tag{2.29b}$$

$$(f,v) = \int_\Omega fv\, d\boldsymbol{x}. \tag{2.29c}$$

We note, the bilinear form (2.29b) associated with the Poisson problem is the square of the H^1 seminorm (2.13). Since we are looking for solutions in $H_0^1(\Omega)$, the bilinear form induces the H_0^1 norm: $\sqrt{a(v_h,v_h)} = \|v_h\|_{H_0^1(\Omega)}$. It can be shown that this problem satisfies the Lax–Milgram theorem, and thus has a unique solution. This solution is called the weak solution to the Poisson boundary-value problem.

The weak problem seeks a solution in an infinite dimensional space of functions, which is still very difficult for general problems. In order to get useful results, we will need to approximate the problem on finite dimensional subspaces. The main technique of both the finite element method and virtual element method is to first break the domain Ω into finitely many pieces, next find a finite dimensional solution space and discrete versions of $a(\cdot,\cdot)$ that approximates the solution on each piece, finally combine the approximations into a single system of equations and solve.

2.3. Finite element method for Poisson's equation

As a point of reference, we first introduce the basics of classic finite element method applied to the Poisson equation. In the finite element method, the domain Ω is discretized into finitely many triangular or quadrilateral elements. For simplicity, we use meshes of triangular elements. Denote $\mathcal{T}^h$ as the decomposition of Ω into triangular elements E with vertices $\boldsymbol{x}_i = (x_i, y_i)$ (i=1,2,3). For each element E, denote the diameter of the element by h_E and the maximum diameter of the all the elements in the mesh by h. The goal is to construct a method that converges to the weak solution as the maximum diameter of the elements tend toward zero ($h \to 0$).

2.3.1. Finite element space. For the finite element method, we seek solutions over a finite dimensional subspace $V_h \subset H_0^1(\Omega)$. We start by building a local subspace over each element $E \in \mathcal{T}^h$. In particular, one key property of the local space is that it contains all the polynomials up to degree k (for a k-th order method). This property ensures that the finite element space will have the desired approximation accuracy. For triangular elements, it is sufficient to define the local space $V_h(E) = \mathbb{P}_k(E)$ as the set of all polynomial functions with degree less than or equal to k. In two dimensions, to uniquely define a polynomial in $\mathbb{P}_k(E)$ requires information at $N = \frac{(k+1)(k+2)}{2}$ suitably chosen points. These are called the elements degrees of freedom (DOF), and are usually chosen to be:

$$\begin{aligned}
&3 \text{ values of } v_h \text{ on the vertices,} \\
&(k-1) \text{ values of } v_h \text{ at points along each of the 3 edges,} \\
&\frac{(k-2)(k-1)}{2} \text{ values of } v_h \text{ at interior points.}
\end{aligned} \tag{2.30}$$

Denote the set of points corresponding to the degrees of freedom by $\{\boldsymbol{a}_j\}$ $(j = 1, 2, \ldots, N)$. We let $\{\phi_i\}$ denote the set of Lagrangian basis functions that span the space $\mathbb{P}_k(E)$ and satisfy the Lagrangian interpolation property

$$\phi_i(\boldsymbol{a}_j) = \delta_{ij}, \tag{2.31}$$

where δ_{ij} is the Kronecker delta. Then for any function $v_h \in V_h(E)$, we expand it in terms of the basis functions as

$$v_h(\boldsymbol{x}) = \sum_{i=1}^{N} v_h(\boldsymbol{a}_i)\phi_i(\boldsymbol{x}). \tag{2.32}$$

From the local spaces $V_h(E)$, the global space V_h of piecewise continuous polynomial functions is constructed:

$$V_h = \left\{ v_h \in H_0^1(\Omega) : v_h|_E \in V_h(E) = \mathbb{P}_k(E) \;\; \forall E \in \mathcal{T}^h \right\}. \tag{2.33}$$

Remark 2.3.1. *For general FEM applications, it is usually more convenient to prescribe the basis functions on a reference element. Then computations can be performed by mapping (isoparametric mapping) each element onto a reference element and using the same set of basis functions instead of having to find a basis for each element separately. However, one downside of using a mapping is the problem with badly-shaped elements. It is known that for nonconvex elements, the mapping becomes singular and the method will fail.*

2.3.2. Discrete weak problem. Now with the finite element space in hand, we construct the discrete problem. In the FEM, the exact bilinear form and forcing functional is applied over each element. That is, for each E let

$$a^E(u_h, v_h) = \int_E \nabla u_h \cdot \nabla v_h \, d\boldsymbol{x}, \quad (f, v_h)_E = \int_E f v_h \, d\boldsymbol{x}. \tag{2.34}$$

Then define the global discrete problem over V_h: find $u_h \in V_h$ such that

$$a(u_h, v_h) = (f, v_h) \quad \forall v_h \in V_h, \tag{2.35a}$$

where

$$a(u_h, v_h) = \sum_E a^E(u_h, v_h), \quad (f, v_h) = \sum_E (f, v_h)_E. \tag{2.35b}$$

Since the same bilinear form and forcing function from the weak problem (2.29) is used, the discrete problem satisfies the conditions of the Lax–Milgram theorem, and therefore has a unique solution.

2.3.3. Convergence results. With the discrete problem formed, we show that the discrete solution converges to the exact weak solution as the maximum mesh diameter $h \to 0$.

Let $u \in H_0^1(\Omega)$ be a solution to the weak problem, $u_h \in V_h$ the unique k-th order solution to the discrete problem (2.35). Then we have

$$a(u, v) = (f, v) \quad \forall v \in H_0^1(\Omega),$$

$$a(u_h, v_h) = (f, v_h) \quad \forall v_h \in V_h.$$

For any $v_h \in V_h$, we subtract the two expressions to get

$$a(u, v_h) - a(u_h, v_h) = (f, v_h) - (f, v_h) = 0,$$

that is,

$$a(u - u_h, v_h) = 0 \quad \forall v_h \in V_h. \tag{2.36}$$

The property (2.36) is called the Galerkin orthogonality condition and it implies that the finite element solution u_h is an orthogonal projection of the exact solution onto the discrete subspace V_h with respect to the bilinear form $a(\cdot, \cdot)$. Now, we use this orthogonality property to roughly estimate the error in H_0^1 norm. We recall for Poisson equation, the H_0^1 norm is induced by the bilinear form, that is $\|u - u_h\|_{H_0^1(\Omega)}^2 = a(u - u_h, u - u_h)$. Then by Galerkin orthoginality, we can write

$$\|u - u_h\|_{H_0^1(\Omega)}^2 = a(u - u_h, u - u_h) = a(u - u_h, u) - a(u - u_h, u_h) = a(u - u_h, u). \tag{2.37}$$

Let $v_h \in V_h$, then by adding and subtracting v_h from the second component and applying Galerkin orthogonality, we have

$$a(u - u_h, u) = a(u - u_h, u - v_h) + a(u - u_h, v_h) = a(u - u_h, u - v_h). \tag{2.38}$$

Since $a(\cdot,\cdot)$ is bounded, we estimate

$$a(u-u_h,u-v_h) \le C\|u-u_h\|_{H_0^1(\Omega)}\|u-v_h\|_{H_0^1(\Omega)}. \tag{2.39}$$

Now combining and simplifying, we find:

$$\|u-u_h\|_{H_0^1(\Omega)} \le C\|u-v_h\|_{H_0^1(\Omega)} \le C\min_{w_h\in V_h}\|u-w_h\|_{H_0^1(\Omega)}. \tag{2.40}$$

The inequality (2.40) is a special case of Cea's lemma, which shows that the finite element solution u_h is proportional to the best possible solution in the subspace V_h. However, Cea's lemma does not immediately give the convergence of the solution u_h to u. To remedy this, we must find an approximation to the value $\min_{w_h\in V_h}\|u-w_h\|_{H_0^1(\Omega)}$ which depends on the mesh parameter h. From [27, 42], it is known that there exists a unique interpolation function $u_I \in V_h$ which match the value of u at every vertex and satisfy the bound (for $u \in H^{k+1}(\Omega)$):

$$\|u-u_I\|_{H_0^1(\Omega)} \le Ch^k|u|_{H^{k+1}(\Omega)}. \tag{2.41}$$

Since $u_I \in V_h$, the error $\|u-u_I\|_{H_0^1(\Omega)}$ must be larger than the minimum; therefore, we immediately obtain the bound

$$\|u-u_h\|_{H_0^1(\Omega)} \le C\min_{w_h\in V_h}\|u-w_h\|_{H_0^1(\Omega)} \le C\|u-u_I\|_{H_0^1(\Omega)} \le Ch^k|u|_{H^{k+1}(\Omega)}. \tag{2.42}$$

The inequality (2.42), shows that a k-th order finite element solution will converge to the exact solution u in the H_0^1 norm as the mesh size $h \to 0$; and the order of convergence is of order k.

In many cases, we are also interested in the convergence in the L^2 norm. Since both $\|\cdot\|_{H_0^1(\Omega)}$ and $\|\cdot\|_{L^2(\Omega)}$ are norms on the space $H_0^1(\Omega)$, they are equivalent by Poincare–Friedrichs inequality:

$$\|u-u_h\|_{L^2(\Omega)} \le C\|u-u_h\|_{H_0^1(\Omega)} \le Ch^k|u|_{H^{k+1}(\Omega)}. \tag{2.43}$$

However, the L^2 norm measures the error of a function, while the H_0^1 norm measures the error in its derivative; therefore, it is expected that the L^2 error should be more accurate. We use a method called the Aubin–Nitsche technique (trick) [42] to improve the estimate. The idea of the Aubin–Nitsche trick is to relate the L^2 inner product to an associated adjoint problem. In particular, since we know the weak problem (2.29) has a unique solution for $f \in L^2$, we can choose the function

$u - u_h$. Let $\psi \in H_0^1 \cap H^2$ be the solution to the following adjoint problem:

$$a(v, \psi) = a(\psi, v) = (u - u_h, v) \quad \forall v \in H_0^1(\Omega), \tag{2.44}$$

where for the Poisson equation, the bilinear form is symmetric so the adjoint problem is equivalent to the original weak problem. It can be shown that for a convex polygonal domain, the elliptic regularity property holds for ψ [42]. That is, there exists constants C_1 and C_2 such that

$$|\psi|_{H^2(\Omega)} \leq C_1 \|u - u_h\|_{L^2(\Omega)}, \tag{2.45a}$$

$$|\psi|_{H^1(\Omega)} \leq C_2 \|u - u_h\|_{L^2(\Omega)}. \tag{2.45b}$$

Then, we write the L^2 norm as:

$$\|u - u_h\|^2_{L^2(\Omega)} = (u - u_h, u - u_h) = a(u - u_h, \psi). \tag{2.46}$$

By adding and subtracting an interpolation function ψ_I satisfying (2.41) (k=1) from the second component, applying linearity and Galerkin orthogonality, we get

$$a(u - u_h, \psi) = a(u - u_h, \psi - \psi_I) + a(u - u_h, \psi_I) = a(u - u_h, \psi - \psi_I).$$

Now, applying the boundedness property of the bilinear form:

$$\begin{aligned} a(u - u_h, \psi - \psi_I) &\leq C\|u - u_h\|_{H_0^1(\Omega)} \|\psi - \psi_I\|_{H_0^1(\Omega)} \\ &\leq Ch\|u - u_h\|_{H_0^1(\Omega)} |\psi|_{H^2(\Omega)} \\ &\leq Ch\|u - u_h\|_{H_0^1(\Omega)} \|u - u_h\|_{L^2(\Omega)}. \end{aligned} \tag{2.47}$$

Applying the bound (2.47) to (2.46) and using the estimate (2.42), we simplify to

$$\|u - u_h\|_{L^2(\Omega)} \leq Ch\|u - u_h\|_{H_0^1(\Omega)} \leq Ch^{k+1}|u|_{H^{k+1}(\Omega)}. \tag{2.48}$$

For a problem with sufficiently regular solutions, the bound in (2.48) implies that the L^2 of the finite element solution converges at a rate that is one order higher than in the H_0^1 norm.

Remark 2.3.2. *In the proof of convergence, the maximum element diameter h is used; however, when comparing different methods, it is often more useful to compare the total number of degrees* *of freedom needed. In two dimensions, the diameter is inversely proportional to the square root of the total number of degrees of freedom N_{DOF}. That is:*

$$h \sim \frac{1}{\sqrt{N_{DOF}}}. \tag{2.49}$$

In many of our numerical tests, we report the results with respect to the square root of the total number of degrees of freedom $\sqrt{N_{DOF}}$.

2.4. Virtual element method for Poisson's equation

Here, we examine the same Poisson boundary-value problem using the virtual element method. To construct a virtual element method, we first need to discretize the domain Ω into finitely many elements. In the finite element method, these elements are usually triangles or quadrilaterals; however, in the virtual element method, the elements are polygons that can have arbitrarily many vertices and can be convex, nonconvex or degenerate (see Figure 2.1). Let $\mathcal{T}^h$ be the decomposition of the region Ω into nonoverlapping polygons with a maximum diameter of h. For each polygon $E \in \mathcal{T}^h$, we denote its diameter by h_E and its centroid by $\boldsymbol{x}_E$. Each polygon E consists of N_E vertices (nodes) with N_E edges. Let $\mathcal{E}_E$ be the set of all edges of E. We denote the coordinates of each vertex by $\boldsymbol{x}_i := (x_i, y_i)$. In the VEM, standard mesh assumptions are placed on $\mathcal{T}^h$ (e.g., star-convexity of E) [9].

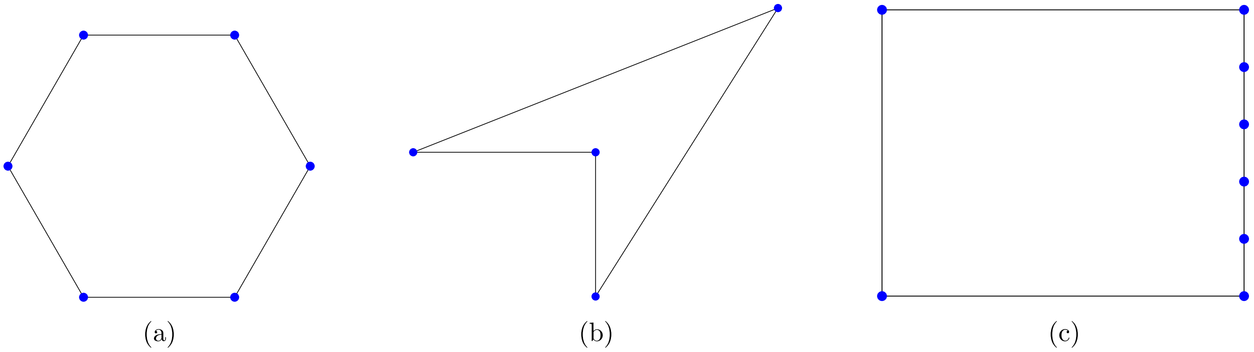
(a) (b) (c)

FIGURE 2.1. Examples of admissible elements in the virtual element method (a) convex element, (b) nonconvex element and (c) degenerate element.

2.4.1. Virtual element space. On each element E, we first construct a local finite dimensional subspace $V_h(E) \subset H^1(E)$, then by combining these spaces for every element E, we construct a global subspace $V_h \subset V := H^1_0(\Omega)$. In the k-th order finite element method for triangular elements, the local space contains all the polynomials up to degree k; therefore we require that the local virtual element space $V_h(E)$ also contain all the polynomials up to degree k. In addition, we also want the space to contain additional non-polynomial functions. We start with the boundary space $\mathbb{B}_k(\partial E)$. For the space $V_h(E)$ to contain polynomials, the functions restricted to the boundary must be continuous and also be polynomial along each edge. That is, we define the boundary space as

$$\mathbb{B}_k(\partial E) = \{v_h \in C^0(\partial E) : v_h|_e \in \mathbb{P}_k(e) \quad \forall \text{ edges } e \text{ on } \partial E\}. \tag{2.50}$$

For the interior of the element, we note that the boundary space can be viewed as prescribing boundary conditions to a boundary-value problem. The simplest partial differential equation we can impose is using the Laplacian operator Δ. Since the space contains all the polynomials $p \in \mathbb{P}_k(E)$ of degree less than or equal to k, we have $\Delta p \in \mathbb{P}_{k-2}(E)$. Therefore a natural requirement is that any function $v_h \in V_h(E)$ satisfies a Poisson condition $\Delta v_h \in \mathbb{P}_{k-2}(E)$. The Poisson condition and the prescribed polynomial boundary uniquely defines a function v_h. We define the local virtual element space $V_h(E)$ as

$$V_h(E) = \left\{v_h \in H^1(E) : \Delta v_h \in \mathbb{P}_{k-2}(E),\, v_h|_{\partial E} \in \mathbb{B}_k(\partial E)\right\}. \tag{2.51}$$

For a polygonal element E with N_E vertices, the space $V_h(E)$ is a finite dimensional space that can be described by $N = kN_E + \frac{k(k-1)}{2}$ conditions (degrees of freedom). In particular, the boundary space requires kN_E degrees of freedom to fully define a k-th order polynomial on each edge, while $\frac{k(k-1)}{2}$ conditions are needed to define an order $k-2$ polynomial in the element interior. For each of the $kN_E + \frac{k(k-1)}{2}$ degrees of freedom (DOF), we prescribe conditions that the function satisfy. The most common choice is given as [9]:

$$\begin{aligned} &N_E \text{ values of } v_h \text{ on the vertices,} \\ &(k-1) \text{ values of } v_h \text{ at quadrature points along each of the } N_E \text{ edges,} \\ &\frac{k(k-1)}{2} \text{ internal moments } : \frac{1}{|E|}\int_E v_h p \, d\boldsymbol{x} \quad \forall p \in \mathbb{P}_{k-2}(E). \end{aligned} \tag{2.52}$$

We note that for $k = 1$, the space is fully defined by the N_E values at the vertices and does not require values on the edges or internal moments. We use the notation $\texttt{dof}_i(v_h)$ as the evaluation of the i-th degree of freedom of a function v_h, in particular

$$\mathtt{dof}_i(v_h) = \begin{cases} v_h(x_i) \quad \text{for } i = 1, 2, \dots N_E, \\ v_h(x_i^e) \quad \text{for } i = N_E + 1, N_E + 2, \dots kN_E, \\ \frac{1}{|E|}\int_E v_h p \, d\boldsymbol{x} \quad \text{for } i = kN_E + 1, kN_E + 2, \dots N. \end{cases} \tag{2.53}$$

Following [9], we define the basis functions $\{\phi_i\}$ which correspond to the degrees of freedom by the Lagrangian property: $\mathtt{dof}_j(\phi_i) = \delta_{ij}$, where δ_{ij} is the Kronecker-delta operator.

With the definition of the virtual element space for each element E, we assemble the global virtual element space:

$$V_h = \{v_h \in H_0^1(\Omega) : v_h|_E \in V_h(E) \;\; \forall E \in \mathcal{T}^h\}. \tag{2.54}$$

In general, functions $v_h \in V_h(E)$ are solutions of a partial differential equation and are not computed (virtual). The only information is from their degrees of freedom. The main technique in the virtual element method, is to use the degrees of freedom to construct suitable polynomial projection operators that represent functions of interest. With these projection operators, we are able to determine a computable discrete bilinear form and define the discrete weak problem.

Remark 2.4.1. *Comparing* (2.52) *and* (2.30)*, we find that for* $k > 1$*, the virtual element method requires more degrees of freedom than the corresponding finite element for a triangular element. However, for* $k = 1$*, the two methods are identical.*

2.4.2. Discrete bilinear form. Now with the construction of the virtual element space, we also need to construct a suitable form for the discrete bilinear form $a_h(\cdot, \cdot)$. To motivate the bilinear form found in [9, 11, 13], we first let $\Pi_k : H^1(E) \to \mathbb{P}_k(E)$ be any projection onto the space of polynomials of degree k. Then we can expand the bilinear form as

$$\begin{aligned} a^E(u_h, v_h) &= a^E(u_h - \Pi_k u_h + \Pi_k u_h, v_h - \Pi_k v_h + \Pi_k v_h) \\ &= a^E(\Pi_k u_h, \Pi_k v_h) + a^E(u_h - \Pi_k u_h, v_h - \Pi_k v_h) + a^E(u_h - \Pi_k u_h, \Pi_k v_h) \\ &\quad + a^E(\Pi_k u_h, v_h - \Pi_k v_h), \end{aligned}$$

where $a^E(u_h, v_h)$ is the bilinear form restricted to the element E. A natural choice for the projection Π_k for the Poisson problem is the elliptic projection Π_k^∇, which satisfies the orthogonality condition:

$$a^E(u_h - \Pi_k^\nabla u_h, p) = 0 \quad \forall p \in \mathbb{P}_k(E). \tag{2.55}$$

This allows us to simplify

$$a^E(u_h, v_h) = a^E(\Pi_k^\nabla u_h, \Pi_k^\nabla v_h) + a^E(u_h - \Pi_k^\nabla u_h, v_h - \Pi_k^\nabla v_h). \tag{2.56}$$

The first term in (2.56) is the bilinear form acting on polynomials, which provide the polynomial consistency property (reproduces polynomial solutions) and can be handled in the same way as in standard finite elements. The second term is a stabilization term that relies on knowing information about u_h and v_h. Since in VEM we do not want to explicitly construct these functions, we will need to approximate this term as well. This leads us to the definition of the standard VEM bilinear form

$$a_h^E(u_h, v_h) := a^E(\Pi_k^\nabla u_h, \Pi_k^\nabla v_h) + S^E(u_h - \Pi_k^\nabla u_h, v_h - \Pi_k^\nabla v_h), \tag{2.57}$$

where $S^E(u_h - \Pi_k^\nabla u_h, v_h - \Pi_k^\nabla v_h)$ is an approximation of the term $a^E(u_h - \Pi_k^\nabla u_h, v_h - \Pi_k^\nabla v_h)$. This term controls the stability (coercivity) of the problem and is thus important for convergence in the standard VEM. A necessary condition for the stabilization term is that there exists constants C_1 and C_2 such that [9]

$$C_1 a^E(v_h, v_h) \leq S^E(v_h, v_h) \leq C_2 a^E(v_h, v_h) \quad \forall v_h \in V_h(E) \text{ with } \Pi_k^\nabla v_h = 0. \tag{2.58}$$

However, the choice of the function $S^E(\cdot, \cdot)$ is not unique and in many cases is problem dependent. This is undesirable so we are interested in developing a virtual element method without the stabilization term $S^E(\cdot, \cdot)$ (see Chapter 3).

REMARK 2.4.2. *The projections described throughout this work are defined on the element level and should be denoted with element dependence (such as $\Pi_{k,E}$). However, for simplicity, we omit the dependence on E unless when needed to avoid confusion.*

Now that we have the discrete bilinear form, we also need to construct a weak loading term to define the discrete weak problem. We define the approximate load term given by the inner product

$$(f_h, v_h)_E = \int_E f_h v_h \, d\boldsymbol{x},$$

where f_h is an approximation of the function f. We note that for general $v_h \in V_h(E)$, this integral is not computable; however, from the degrees of freedoms in $V_h(E)$, we can find $\int_E p v_h d\boldsymbol{x}$ for any $p \in \mathbb{P}_{k-2}$. Therefore, a natural approximation is to take $f_h = \Pi^*_{k-2} f$ as a projection of f onto the space of polynomials degree $k - 2$. Then we have:

$$(f_h, v_h)_E = \int_E (\Pi^*_{k-2} f) v_h \, d\boldsymbol{x}. \tag{2.59}$$

The standard projection operator originally described in [9, 11] is the L^2 projection Π^0_{k-2}, which satisfies the L^2 orthogonality condition:

$$\int_E (\Pi^0_{k-2} v_h - v_h) p \, d\boldsymbol{x} = 0 \quad \forall p \in \mathbb{P}_{k-2}(E). \tag{2.60}$$

By using the L^2 projection in (2.59), the forcing term is now written as

$$(f_h, v_h)_E := \int_E (\Pi^0_{k-2} f) v_h \, d\boldsymbol{x} = \int_E f \Pi^0_{k-2} v_h \, d\boldsymbol{x}, \tag{2.61}$$

where the last expression is obtained on applying L^2 orthogonality.

REMARK 2.4.3. *For the case $k = 1$, we can use $\Pi^0_0 f$ as the constant projection or equivalently approximate v_h using $\Pi^0_0 v_h$. A more detailed implementation for $k = 1$ can be found in Section 3.3.3. In Section 2.4.6, we construct an enhanced space that allows us to compute Π^0_k using only the degrees of freedom.*

The local discrete weak problem is to find the function $u_h \in V_h(E)$ such that

$$a^E_h(u_h, v_h) = (f_h, v_h)_E \quad \forall v_h \in V_h(E), \tag{2.62a}$$

where

$$a_h^E(u_h, v_h) = a^E(\Pi_k u_h, \Pi_k v_h) + S^E(u_h - \Pi_k u_h, v_h - \Pi_k v_h), \tag{2.62b}$$

$$(f_h, v_h)_E = \int_E (\Pi^0_{k-2} f) v_h \, d\boldsymbol{x}. \tag{2.62c}$$

The associated global discrete problem is to find $u_h \in V_h$ such that

$$a_h(u_h, v_h) = (f_h, v_h) \quad \forall v_h \in V_h, \tag{2.63a}$$

where

$$a_h(u_h, v_h) = \sum_E a_h^E(u_h, v_h), \quad (f_h, v_h) = \sum_E (f_h, v_h)_E. \tag{2.63b}$$

A solution to (2.63) is called a discrete solution.

2.4.3. Choice of stabilization term. The choice of a stabilization term is not unique; however, it must satisfy certain inequality estimates (2.58) in order to preserve the coercivity of the bilinear form. We examine the structure of the bilinear form to motivate a choice of the stability term. Let $u_h \in V_h(E)$, then we have:

$$a^E(u_h - \Pi_k^\nabla u_h, v_h - \Pi_k^\nabla v_h) = \int_E \nabla(u_h - \Pi_k^\nabla u_h) \cdot \nabla(u_h - \Pi_k^\nabla u_h) \, d\boldsymbol{x}.$$

Since u_h and $\Pi_k^\nabla u_h \in V_h(E)$, we can expand $u_h - \Pi_k^\nabla u_h$ in terms of the basis functions of $V_h(E)$. That is, $u_h - \Pi_k^\nabla u_h = \sum_{i=1}^N \mathtt{dof}_i(u_h - \Pi_k^\nabla u_h)\phi_i$. Then we have

$$\begin{aligned} a^E(u_h - \Pi_k^\nabla u_h, v_h - \Pi_k^\nabla v_h) &= \sum_{i=1}^N \sum_{j=1}^N \mathtt{dof}_i(u_h - \Pi_k^\nabla u_h) \left(\int_E \nabla\phi_i \cdot \nabla\phi_j \, d\boldsymbol{x} \right) \mathtt{dof}_j(u_h - \Pi_k^\nabla u_h) \\ &= \sum_{i=1}^N \sum_{j=1}^N \mathtt{dof}_i(u_h - \Pi_k^\nabla u_h) a^E(\phi_i, \phi_j) \mathtt{dof}_j(u_h - \Pi_k^\nabla u_h), \end{aligned} \tag{2.64}$$

where $\mathtt{dof}_i(u)$ is the i-th degree of freedom of a function u. The expression (2.64) suggests that the approximate stability term $S^E(\cdot,\cdot)$ should take the form:

$$S^E(u_h, v_h) = \sum_{i=1}^N \sum_{j=1}^N \mathtt{dof}_i(u_h) \boldsymbol{S}^E_{ij} \mathtt{dof}_j(v_h), \tag{2.65}$$

where $\boldsymbol{S}^E$ is any symmetric positive-definite matrix with components that scales like $a^E(\phi_i, \phi_j)$. In [9], the suggested matrix is the identity matrix $\boldsymbol{S}^E_{ij} = \delta_{ij}$, there δ_{ij} is the Kronecker delta. The resulting simplified stabilization term (so-called dofi-dofi stabilization) is given by

$$S^E(u_h, v_h) = \sum_{i=1}^{N} \mathtt{dof}_i(u_h)\mathtt{dof}_i(v_h). \tag{2.66}$$

This term is sufficient to preserve the stabilization criterion (2.58). In particular, we first note for $v_h \in V_h(E)$

$$S^E(v_h, v_h) = \sum_{i=1}^{N} \mathtt{dof}_i(v_h)^2, \tag{2.67}$$

defines a ℓ^2 norm over the space $\mathbb{R}^N$. Now consider

$$\begin{aligned} a^E(v_h, v_h) = \int_E \nabla v_h \cdot \nabla v_h \, d\boldsymbol{x} &= \sum_{i=1}^{N}\sum_{j=1}^{N} \mathtt{dof}_i(v_h) \left(\int_E \nabla \phi_i \cdot \nabla \phi_j \, d\boldsymbol{x} \right) \mathtt{dof}_j(v_h) \\ &\le \max_{i,j} \left\{ a^E(\phi_i, \phi_j) \right\} \sum_{i=1}^{N}\sum_{j=1}^{N} \mathtt{dof}_i(v_h)\mathtt{dof}_j(v_h) \\ &\le C_1 \sum_{i=1}^{N} \mathtt{dof}_i(v_h)^2, \end{aligned}$$

where the last inequality is from the equivalence of norms in $\mathbb{R}^N$. Similarily, we can bound

$$\begin{aligned} a^E(v_h, v_h) &\ge \min_{i,j} \left\{ a^E(\phi_i, \phi_j) \right\} \sum_{i=1}^{N}\sum_{j=1}^{N} \mathtt{dof}_i(v_h)\mathtt{dof}_j(v_h) \\ &\ge C_2 \sum_{i=1}^{N} \mathtt{dof}_i(v_h)^2. \end{aligned}$$

By rearranging the two inequalities, we obtain the desired stability inequality.

There are many other types of stabilization that are not of the form (2.65). Some examples include boundary stabilization [15], projection based stabilization [49], energy based stabilization [114] and the DOF based stabilization in [6].

2.4.4. Convergence of the discrete problem. In the virtual element method, there are two important conditions that the discrete bilinear form needs to satisfy in order for the discrete weak problem (2.63) to attain a unique solution and to converge to the exact weak solution at the correct rate. The first condition is polynomial consistency:

$$a_h^E(p, v_h) = a^E(p, v_h) \quad \forall p \in \mathbb{P}_k(E) \text{ and } \forall v_h \in V_h(E). \tag{2.68}$$

The condition (2.68) ensures that the discrete problem will reproduce any polynomial solution of order k of the weak problem (2.29). It also controls the solution accuracy and convergence rates of the method. The second condition is for $a_h^E(\cdot, \cdot)$ to satisfy a stability bound:

$$C_1 a^E(v_h, v_h) \leq a_h^E(v_h, v_h) \leq C_2 a^E(v_h, v_h) \quad \forall v_h \in V_h(E). \tag{2.69}$$

The stability bound assures that the discrete problem is bounded and coercive and thus attains a unique solution. In particular, we have by the stability of $a_h^E(\cdot, \cdot)$, coercivity of $a(\cdot, \cdot)$ and Cauchy–Schwarz inequality:

$$a_h^E(u_h, v_h) \leq \sqrt{a_h^E(u_h, u_h)}\sqrt{a_h^E(v_h, v_h)} \leq C_2\sqrt{a^E(u_h, u_h)}\sqrt{a^E(v_h, v_h)} \leq C|u_h|_{H^1(E)}|v_h|_{H^1(E)}, \tag{2.70}$$

so $a_h^E(\cdot, \cdot)$ is bounded on each element E. Similarly, we have

$$a_h^E(v_h, v_h) \geq C_1 a^E(v_h, v_h) \geq C|v_h|^2_{H^1(E)}, \tag{2.71}$$

so $a_h^E(\cdot, \cdot)$ is coercive on E. By summing the inequalities (2.70) and (2.71) for each element, it is realized that the global discrete form $a_h(\cdot, \cdot)$ is bounded and coercive on Ω with respect to the H_0^1 norm.

Now we examine the global forcing term (f_h, v_h). In our construction of a computable forcing term, we chose a discrete forcing function $f_h = \Pi^0_{k-2} f$ on each element E. We first show that $\|\Pi^0_{k-2} f\|_{L^2(E)}$ is bounded by $\|f\|_{L^2(E)}$. By applying the definition of the L^2 projection and the Cauchy-Schwarz inequality, we have that

$$\|\Pi^0_{k-2} f\|^2_{L^2(E)} = \int_E (\Pi^0_{k-2} f)^2 \, d\boldsymbol{x} = \int_E f \Pi^0_{k-2} f \, d\boldsymbol{x} \leq \|\Pi^0_{k-2} f\|_{L^2(E)} \|f\|_{L^2(E)}, \tag{2.72}$$

which implies that

$$\|\Pi^0_{k-2} f\|_{L^2(E)} \leq \|f\|_{L^2(E)}. \tag{2.73}$$

Next, we show that the functional (f_h, v_h) remains bounded:

$$
\begin{aligned}
|(f_h, v_h)| = \left| \sum_E \int_E (\Pi^0_{k-2} f) v_h \, d\boldsymbol{x} \right| &\leq \sum_E \|\Pi^0_{k-2} f\|_{L^2(E)} \|v_h\|_{L^2(E)} \\
&\leq \sum_E \|f\|_{L^2(E)} \|v_h\|_{L^2(E)} \\
&\leq C \|f\|_{L^2(\Omega)} \|v_h\|_{H^1_0(\Omega)}, \qquad (2.74)
\end{aligned}
$$

where the final inequality is from applying the Cauchy–Schwarz and Poincare–Friedrich inequalities. Then by the Lax–Milgram theorem, since $a_h(\cdot, \cdot)$ is bounded and coercive, and (f_h, v_h) is bounded, the discrete problem (2.63) has a unique solution.

We know that the discrete problem attains a unique solution; however, it still needs to be shown that this solution converges to the weak solution of (2.29) as the mesh is refined ($h \to 0$). To show convergence, we introduce some classical interpolation and projection estimates from finite elements. More information on the mathematical theory and proofs of these estimates can be found in [**14**, **26**, **27**, **42**].

Lemma 2.4.0.1. *Let $w \in H^{k+1}(\Omega)$ be a sufficiently smooth function, then there exists an interpolation function $w_I \in V_h(E)$ that satisfies*

$$
\mathrm{dof}_i(w - w_I) = 0, \quad i = 1, 2, \ldots N, \qquad (2.75)
$$

and a piecewise polynomial function $w_\pi \in \mathbb{P}_k(E)$ that satisfies

$$
\|w - w_I\|_{L^2(E)} + h_E |w - w_I|_{H^1(E)} \leq C_1 h_E^{k+1} |w|_{H^{k+1}(E)}, \qquad (2.76a)
$$

$$
\|w - w_\pi\|_{L^2(E)} + h_E |w - w_\pi|_{H^1(E)} \leq C_2 h_E^{k+1} |w|_{H^{k+1}(E)}. \qquad (2.76b)
$$

for some constants C_1 and C_2 that are independent of h.

Lemma 2.4.0.2. *Let $w \in H^{k+1}(E)$ be a sufficiently smooth function. Then the k-th order L^2 projection operator satisfies*

$$
|w - \Pi^0_k w|_{H^1(E)} \leq C_1 h_E^k |w|_{H^{k+1}(E)}, \qquad (2.77a)
$$

$$
\|w - \Pi^0_k w\|_{L^2(E)} \leq C_2 h_E^{k+1} |w|_{H^{k+1}(E)}. \qquad (2.77b)
$$

for some constants C_1 and C_2 that are independent of h.

With the introduction of an approximate forcing term, we also need to know how much error is introduced to the global problem. In particular, we estimate the difference

$$\begin{aligned}(f - f_h, v_h) &= \sum_E (f - \Pi^0_{k-2} f, v_h)_E \\ &= \sum_E (f - \Pi^0_{k-2} f, v_h - \Pi^0_0 v_h + \Pi^0_0 v_h)_E \\ &= \sum_E (f - \Pi^0_{k-2} f, v_h - \Pi^0_0 v_h)_E \\ &\leq \sum_E \|f - \Pi^0_{k-2} f\|_{L^2(E)} \|v_h - \Pi^0_0 v_h\|_{L^2(E)}. \end{aligned} \tag{2.78}$$

By applying (2.77b), we get the estimate

$$(f - f_h, v_h) \leq Ch^k |f|_{H^{k-1}(\Omega)} |v_h|_{H^1(\Omega)}. \tag{2.79}$$

The inequality (2.79) implies that as the mesh is refined, the $k-2$-th order approximate forcing term will weakly converge to the exact forcing and will not hinder the convergence of the VEM.

In [2, 9], it is shown that for a k-th order VEM on sufficiently nice meshes and sufficiently regular functions, the rates of convergence in the H^1_0 norm and the L^2 norm are given by:

$$\|u - u_h\|_{H^1_0(\Omega)} \leq C_1 h^k (|u|_{H^{k+1}(\Omega)} + |f|_{H^{k-1}(\Omega)}), \tag{2.80a}$$

$$\|u - u_h\|_{L^2(\Omega)} \leq C_2 h^{k+1} (|u|_{H^{k+1}(\Omega)} + |f|_{H^{k}(\Omega)}), \tag{2.80b}$$

where C_1, C_2 are constants that depend on the geometry but independent of the maximum element diameter h.

We first show the H^1_0 estimate (2.80a). Let u be the unique weak solution, u_h the discrete solution, u_I denote the interpolation function which satisfies the bound in (2.76a) and u_π the polynomial approximation function satisfying (2.76b). Then by the triangle inequality:

$$\|u - u_h\|_{H^1_0(\Omega)} \leq \|u - u_I\|_{H^1_0(\Omega)} + \|u_I - u_h\|_{H^1_0(\Omega)}. \tag{2.81}$$

For the first term of (2.81), we estimate

$$\|u-u_I\|^2_{H^1_0(\Omega)} = \sum_E |u-u_I|^2_{H^1(E)} \le \sum_E C(h_E^k)^2|u|^2_{H^{k+1}(\Omega)} \le C(h^k)^2|u|^2_{H^{k+1}(\Omega)}. \tag{2.82}$$

Therefore,

$$\|u-u_I\|_{H^1_0(\Omega)} \le Ch^k|u|_{H^{k+1}(\Omega)}. \tag{2.83}$$

For the second term in (2.81), by applying the stability property and definition of the discrete solution we get

$$\begin{aligned}
C\|u_I-u_h\|^2_{H^1_0(\Omega)} &\le a_h(u_I-u_h,u_I-u_h)\\
&= \sum_E \left(a_h^E(u_I-u_h,u_I) - a_h^E(u_I-u_h,u_h)\right)\\
&= \sum_E a_h^E(u_I-u_h,u_I) - (f_h,u_I-u_h).
\end{aligned}$$

Now, add and subtract u_π in the first term, apply linearity and consistency of $a_h(\cdot,\cdot)$

$$\begin{aligned}
&= \sum_E \left(a_h^E(u_I-u_h,u_I-u_\pi) + a_h^E(u_I-u_h,u_\pi)\right) - (f_h,u_I-u_h)\\
&= \sum_E \left(a_h^E(u_I-u_h,u_I-u_\pi) + a^E(u_I-u_h,u_\pi)\right) - (f_h,u_I-u_h).
\end{aligned} \tag{2.84}$$

Add and subtract u in the second term, then we get the bound

$$\begin{aligned}
C\|u_I-u_h\|^2_{H^1_0(\Omega)} &\le \sum_E \left(a_h^E(u_I-u_h,u_I-u_\pi) + a^E(u_I-u_h,u_\pi-u)\right)\\
&\quad + a(u_I-u_h,u) - (f_h,u_I-u_h)\\
&= \sum_E a_h^E(u_I-u_h,u_I-u_\pi) + \sum_E a^E(u_I-u_h,u_\pi-u)\\
&\quad + (f,u_I-u_h) - (f_h,u_I-u_h)\\
&= \underbrace{\sum_E a_h^E(u_I-u_h,u_I-u_\pi)}_{A} + \underbrace{\sum_E a^E(u_I-u_h,u_\pi-u)}_{B} + \underbrace{(f-f_h,u_I-u_h)}_{C}.
\end{aligned} \tag{2.85}$$

We estimate each term of (2.85) individually. For term A, we apply the boundedness of $a_h(\cdot,\cdot)$, the triangle inequality, and the estimates (2.76a) and (2.76b) to each element E to write

$$\begin{aligned}\sum_E a_h^E(u_I - u_h, u_I - u_\pi) &\leq C \sum_E |u_I - u_h|_{H^1(E)} |u_I - u_\pi|_{H^1(E)} \\ &\leq C \sum_E \big(|u_I - u|_{H^1(E)} + |u - u_\pi|_{H^1(E)}\big) \|u_I - u_h\|_{H_0^1(\Omega)} \\ &\leq C_1 h^k |u|_{H^{k+1}(\Omega)} \|u_I - u_h\|_{H_0^1(\Omega)}. \qquad (2.86)\end{aligned}$$

For term B, following a similar strategy, we get

$$\sum_E a^E(u_I - u_h, u_\pi - u) \leq C_2 h^k |u|_{H^{k+1}(\Omega)} \|u_I - u_h\|_{H_0^1(\Omega)}. \qquad (2.87)$$

For term C, apply the inequality (2.79) to get

$$(f - f_h, u_I - u_h) \leq C_3 h^k |f|_{H^{k-1}(\Omega)} \|u_I - u_h\|_{H_0^1(\Omega)}. \qquad (2.88)$$

Combining terms, we find that

$$C\|u_I - u_h\|^2_{H_0^1(\Omega)} \leq h^k \big(C_1 |u|_{H^{k+1}(\Omega)} + C_2 |u|_{H^{k+1}(\Omega)} + C_3 |f|_{H^{k-1}(\Omega)}\big) \|u_I - u_h\|_{H_0^1(\Omega)},$$

which results in the estimate

$$\|u_I - u_h\|_{H_0^1(\Omega)} \leq C h^k \big(|u|_{H^{k+1}(\Omega)} + |f|_{H^{k-1}(\Omega)}\big). \qquad (2.89)$$

Finally, from (2.83) and (2.89) we have

$$\|u - u_h\|_{H_0^1(\Omega)} \leq C h^k \big(|u|_{H^{k+1}(\Omega)} + |f|_{H^{k-1}(\Omega)}\big). \qquad (2.90)$$

We now show the L^2 estimate (2.80b). By Poincare–Friedrichs inequality, it is known that the L^2 error has an immediate bound of order k. However, for a sufficiently regular solution and geometry, the bound can be increased to order $k+1$ using the Aubin–Nitsche trick [42]. In addition, for the estimate to be of correct order, we also require the use of the L^2 projection operator of order $k-1$ to approximate the forcing function f_h. In the original virtual element space, this projection is not computable from the degrees of freedom; however, in Section 2.4.6 an enhanced space is introduced that allows for the computation of $f_h = \Pi^0_{k-1} f$. By using this f_h in the proof of the H^1

error, we get a modified bound for sufficiently small h:

$$\|u-u_h\|_{H_0^1(\Omega)} \le Ch^k\big(|u|_{H^{k+1}(\Omega)} + h|f|_{H^k(\Omega)}\big) \le Ch^k|u|_{H^{k+1}(\Omega)}. \tag{2.91}$$

We consider

$$\|u-u_h\|^2_{L^2(\Omega)} = (u-u_h, u-u_h). \tag{2.92}$$

Following the idea of the Aubin–Nitsche trick used in Section 2.3.3, let $\psi \in H_0^1(\Omega)\cap H^2(\Omega)$ be the solution to the following adjoint problem

$$a(\psi, v) = (u-u_h, v) \quad \forall v \in V, \tag{2.93}$$

and assume the elliptic regularity estimates hold for some constant C_1 and C_2:

$$|\psi|_{H^2(\Omega)} \le C_1\|u-u_h\|_{L^2(\Omega)}, \tag{2.94a}$$

$$|\psi|_{H^1(\Omega)} \le C_2\|u-u_h\|_{L^2(\Omega)}. \tag{2.94b}$$

Then we can rewrite the L^2 error as

$$\|u-u_h\|^2_{L^2(\Omega)} = a(\psi, u-u_h). \tag{2.95}$$

Let ψ_I be the interpolation function of ψ that satisfies the global estimate (2.76a)

$$\|\psi-\psi_I\|_{H_0^1(\Omega)} = |\psi-\psi_I|_{H^1(\Omega)} \le Ch|\psi|_{H^2(\Omega)}, \tag{2.96a}$$

$$\|\psi-\psi_I\|_{L^2(\Omega)} \le Ch^2|\psi|_{H^2(\Omega)}. \tag{2.96b}$$

Then, by adding and subtracting ψ_I, and applying linearity of $a(\cdot,\cdot)$, we write

$$a(\psi, u-u_h) = a(\psi-\psi_I, u-u_h) + a(\psi_I, u-u_h). \tag{2.97}$$

For the first term, we estimate

$$\begin{aligned} a(\psi-\psi_I,u-u_h) &\le C\|\psi-\psi_I\|_{H_0^1(\Omega)}\|u-u_h\|_{H_0^1(\Omega)} \\ &\le Ch|\psi|_{H^2(\Omega)}\|u-u_h\|_{H_0^1(\Omega)} \\ &\le Ch\|u-u_h\|_{L^2(\Omega)}\|u-u_h\|_{H_0^1(\Omega)} \\ &\le Ch^{k+1}|u|_{H^{k+1}(\Omega)}\|u-u_h\|_{L^2(\Omega)} \qquad (2.98) \end{aligned}$$

Note that, for simplicity of the proof, we skip the step of applying estimates over each element and instead directly applied the global estimates. The resulting error bounds are the same in either case. For the second term, we have

$$\begin{aligned} a(\psi_I,u-u_h) &= a(\psi_I,u)-a(\psi_I,u_h) \\ &= a(\psi_I,u)-a_h(\psi_I,u_h)+a_h(\psi_I,u_h)-a(\psi_I,u_h) \\ &= (f,\psi_I)-(f_h,\psi_I)+a_h(\psi_I,u_h)-a(\psi_I,u_h) \\ &= \underbrace{(f-f_h,\psi_I)}_{A}+\underbrace{a_h(\psi_I,u_h)-a(\psi_I,u_h)}_{B}. \qquad (2.99) \end{aligned}$$

For term A, we write for sufficiently small h:

$$\begin{aligned} (f-f_h,\psi_I) &= (f-\Pi_{k-1}^0 f,\psi_I) \\ &= (f-\Pi_{k-1}^0 f,\psi_I-\psi)+(f-\Pi_{k-1}^0 f,\psi) \\ &= (f-\Pi_{k-1}^0 f,\psi_I-\psi)+(f-\Pi_{k-1}^0 f,\psi-\Pi_0^0\psi) \\ &\le \|f-\Pi_{k-1}^0 f\|_{L^2(\Omega)}\|\psi-\psi_I\|_{L^2(\Omega)}+\|f-\Pi_{k-1}^0 f\|_{L^2(\Omega)}\|\psi-\Pi_0^0\psi\|_{L^2(\Omega)} \\ &\le C_1h^{k+2}|f|_{H^k(\Omega)}|\psi|_{H^2(\Omega)}+C_2h^{k+1}|f|_{H^k(\Omega)}|\psi|_{H^1(\Omega)} \\ &\le Ch^{k+1}\big(|f|_{H^k(\Omega)}+h|f|_{H^k(\Omega)}\big)\|u-u_h\|_{L^2(\Omega)} \\ &\le Ch^{k+1}|f|_{H^k(\Omega)}\|u-u_h\|_{L^2(\Omega)}. \qquad (2.100) \end{aligned}$$

Remark 2.4.4. *To simplify the expressions using global estimates, we have abused the notation* $\|\Pi_{k-2}^0 w\|_{L^2(\Omega)}$ *to indicate the norm of a projection of* w *over the entire domain* Ω*; however, the projection operators* $\Pi_{k-2}^0 := \Pi_{k-2,E}^0$ *are only defined locally on each element* E*. Therefore, the full* *expression is actually given by the contributions of the norms over each element:*

$$\|\Pi^0_{k-2}w\|_{L^2(\Omega)} = \left(\sum_E \|\Pi^0_{k-2,E}w\|^2_{L^2(E)}\right)^{\frac{1}{2}}. \tag{2.101}$$

We use this same notation for proofs in Section 3.4.2.

For term B, we add an subtract $\Pi^0_1\psi$ and $\Pi^0_k u$ to both $a_h(\cdot,\cdot)$ and $a(\cdot,\cdot)$. Then by applying the consistency property, we have

$$\begin{aligned}
a_h(\psi_I, u_h) - a(\psi_I, u_h) &= a_h(\psi_I - \Pi^0_1\psi + \Pi^0_1\psi, u_h - \Pi^0_k u + \Pi^0_k u) \\
&\qquad - a(\psi_I - \Pi^0_1\psi + \Pi^0_1\psi, u_h - \Pi^0_k u + \Pi^0_k u) \\
&= a_h(\psi_I - \Pi^0_1\psi, u_h - \Pi^0_k u) - a(\psi_I - \Pi^0_1\psi, u_h - \Pi^0_k u).
\end{aligned} \tag{2.102}$$

Now, applying the boundedness of $a_h(\cdot,\cdot)$ and $a(\cdot,\cdot)$, the triangle inequality, (2.77a) and (2.94a)

$$\begin{aligned}
a_h(\psi_I, u_h) - a(\psi_I, u_h) &\leq |\psi_I - \Pi^0_1\psi|_{H^1(\Omega)}|u_h - \Pi^0_k u|_{H^1(\Omega)} + |\psi_I - \Pi^0_1\psi|_{H^1(\Omega)}|u_h - \Pi^0_k u|_{H^1} \\
&\leq C\left(|\psi_I - \psi|_{H^1(\Omega)} + |\psi - \Pi^0_1\psi|_{H^1(\Omega)}\right)\left(|u_h - u|_{H^1(\Omega)} + |u - \Pi^0_k u|_{H^1(\Omega)}\right) \\
&\leq Ch^{k+1}|u|_{H^{k+1}(\Omega)}|\psi|_{H^2(\Omega)} \\
&\leq Ch^{k+1}|u|_{H^{k+1}(\Omega)}\|u - u_h\|_{L^2(\Omega)}.
\end{aligned} \tag{2.103}$$

Combining (2.100) and (2.103), we have the estimate

$$a(\psi_I, u - u_h) \leq Ch^{k+1}\big(|u|_{H^{k+1}(\Omega)} + |f|_{H^k(\Omega)}\big)\|u - u_h\|_{L^2(\Omega)}. \tag{2.104}$$

Finally, combining (2.98) and (2.104), we get

$$\|u - u_h\|^2_{L^2(\Omega)} \leq Ch^{k+1}\big(|u|_{H^{k+1}(\Omega)} + |f|_{H^k(\Omega)}\big)\|u - u_h\|_{L^2(\Omega)}, \tag{2.105}$$

which can be simplified to the desired bound.

We note that compared to the finite element method (see Section 2.3.3), the analysis of the virtual element method is more delicate and requires more estimates. This is because the virtual element method uses both a discrete approximation of the bilinear form and an approximation to the forcing term. However, the VEM converges at the same (optimal) rate as the finite element method in both L^2 and H^1_0 norms.

Remark 2.4.5. *For general problems, it is usually the case (if sufficiently regular solutions and geometry) that the optimal convergence rate in the* L^2 *norm of* u_h *will be one order higher than a norm involving the derivative of* u_h *(such as the energy seminorm or taking the* L^2 *norm of the stress and strain).*

Remark 2.4.6. *Although the theoretical estimates in* (2.80) *are established using the discrete solution* u_h*, in numerical applications this solution is unknown except at the degrees of freedom. Therefore, suitable discrete error measures that depend on the projection operator or degrees of freedom are used to compute the convergence rates in numerical tests. Some examples of discrete norms are shown later in Sections 3.5 and 5.4.*

2.4.5. Element stiffness matrix and element force vector.

In order to solve the resulting discrete equations in (2.63), we convert the equations into a linear system of equations $\boldsymbol{K}\boldsymbol{d} = \boldsymbol{f}$, where $\boldsymbol{K}$ is the global stiffness matrix and $\boldsymbol{f}$ is the global force vector. We construct the local stiffness matrix and local forcing vectors on each element E, then the global system is assembled with the standard finite element operations.

To build the element stiffness matrix $\boldsymbol{K}_E$, we consider the bilinear form in (2.57) using the dofi-dofi stabilization (2.66):

$$\begin{aligned} a_h^E(u_h, v_h) &= a^E(\Pi_k^\nabla u_h, \Pi_k^\nabla v_h) + S^E(u_h - \Pi_k^\nabla u_h, v_h - \Pi_k^\nabla v_h) \\ &= \int_E \nabla \Pi_k^\nabla u_h \cdot \nabla \Pi_k^\nabla v_h \, d\boldsymbol{x} + \sum_{r=1}^{N} \mathtt{dof}_r(u_h - \Pi_k^\nabla u_h)\mathtt{dof}_r(v_h - \Pi_k^\nabla v_h). \end{aligned}$$

Since we can use any function u_h, $v_h \in V_h(E)$, a natural choice is to use the basis functions $\{\phi_i\}$. Letting $u_h = \phi_i$ and $v_h = \phi_j$, we define the ij-th component of the element stiffness matrix by:

$$(\boldsymbol{K}_E)_{ij} := (\boldsymbol{K}_E^c)_{ij} + (\boldsymbol{K}_E^s)_{ij}, \tag{2.106a}$$

where $\boldsymbol{K}_E^c$ is the consistency matrix and $\boldsymbol{K}_E^s$ is the stability matrix with components given by

$$(\boldsymbol{K}_E^c)_{ij} = \int_E \nabla \Pi_k^\nabla \phi_i \cdot \nabla \Pi_k^\nabla \phi_j \, d\boldsymbol{x}, \tag{2.106b}$$

$$(\boldsymbol{K}_E^s)_{ij} = \sum_{r=1}^{N} \mathtt{dof}_r(\phi_i - \Pi_k^\nabla \phi_i)\mathtt{dof}_r(\phi_j - \Pi_k^\nabla \phi_j). \tag{2.106c}$$

Now for the local forcing vector $\boldsymbol{f}_E$, we set $v_h = \phi_i$ into (2.61). Then the i-th component of the forcing vector is

$$(\boldsymbol{f}_E)_i = (f_h, \phi_i)_E = \int_E f \Pi^0_{k-2} \phi_i \, d\boldsymbol{x}. \tag{2.107}$$

2.4.6. Enhanced virtual element space. The approach shown in the previous sections have been widely studied and applied; however, in the development of the methods in the remaining chapters, we need the concept of an enhanced virtual element space as introduced in [2] and extended in [20]. To motivate the necessity of this space, we recall that in the forcing term (2.61) we used the L^2 projection Π^0_{k-2} into the space $\mathbb{P}_{k-2}(E)$. However, in the proof of the optimal convergence of the L^2 norm (see Section 2.4.4), we found that the projection of at least Π^0_{k-1} was needed. Since the space $V_h(E)$ contains k-th order polynomials, it is useful to also have the L^2 projection Π^0_k. Following (2.60), we define Π^0_k by the condition

$$\int_E \Pi^0_k v_h p \, d\boldsymbol{x} = \int_E v_h p \, d\boldsymbol{x} \quad \forall p \in \mathbb{P}_k(E). \tag{2.108}$$

For $p \in \mathbb{P}_{k-2}(E)$, the integral on the right hand side of (2.108) can be computed using the moment degrees of freedom (2.52); however the remaining integrals for polynomials of degree $k-1$ and k are unknown. In [2], it is suggested that the elliptic projection $\Pi^\nabla_k v_h$ can be used as a rough approximation to compute the missing moments. That is,

$$\int_E v_h p \, d\boldsymbol{x} \approx \int_E \Pi^\nabla_k v_h p \, d\boldsymbol{x} \quad \forall p \in [\mathbb{P}_k/\mathbb{P}_{k-2}(E)], \tag{2.109}$$

where $[\mathbb{P}_k/\mathbb{P}_{k-2}(E)]$ is the space of polynomials in $\mathbb{P}_k(E)$ that is orthogonal to $\mathbb{P}_{k-2}(E)$ with respect to the L^2 inner product (or equivalently can take the quotient of the spaces). In the space $V_h(E)$ the condition (2.109) will only be an approximation; however, by modifying the definition of the virtual element space, equality of the integrals can be enforced. We first define a space of functions that satisfy (2.109) exactly:

$$\mathcal{EN}^E_k = \left\{ v_h \in H^1(E) : \int_E v_h p \, d\boldsymbol{x} = \int_E \Pi^\nabla_k v_h p \, d\boldsymbol{x} \ \ \forall p \in [\mathbb{P}_k/\mathbb{P}_{k-2}(E)] \right\}. \tag{2.110}$$

Then define the enhanced virtual element space by

$$W_h(E) = \left\{ v_h \in \mathcal{EN}^E_k : \Delta v_h \in \mathbb{P}_k(E), \, v_h|_{\partial E} \in \mathbb{B}_k(\partial E) \right\}, \tag{2.111}$$

where $\mathbb{B}_k(\partial E)$ is the boundary space given in (2.50). We note that this space requires functions $\Delta v_h \in \mathbb{P}_k(E)$, which makes the space richer than $V_h(E)$; however, it is shown in [2] that the enhancing condition in (2.110) reduces the dimension of the space to the same size as $V_h(E)$. Since the enhanced space has the same dimension as the standard virtual element space, we use the degrees of freedom and basis functions given in (2.53). On this space, the L^2 projection Π_k^0 is now computable. In Section 3.2 we use a similar procedure to develop spaces to compute the L^2 projection of the strain and in Section 5.2.2 we use this procedure to develop the space for the stress projection.

Remark 2.4.7. *We followed the approach in [14] to define the enhanced virtual element space without making a choice of a basis for $\mathbb{P}_k$. An alternative approach is to use the construction of [2], where an explicit basis for $\mathbb{P}_k$ is chosen and the condition* (2.110) *is only enforced for the basis functions that have exactly degree $k-1$ and k.*

2.5. Strong form and weak form for linear elasticity

For the remainder of this dissertation, we will focus on the solution of the boundary-value problem for two-dimensional linear elasticity. In this section, we first introduce the governing equations for a linear elastic material and then develop the weak form, which is used in the numerical computations.

We consider an elastic body that occupies the region $\Omega \subset \mathbb{R}^2$ with boundary $\partial\Omega$. Assume that the boundary $\partial\Omega$ can be written as the disjoint union of two parts Γ_u and Γ_t with prescribed Dirichlet and Neumann conditions on Γ_u and Γ_t, respectively (see Figure 2.2).

The strong form for the elastostatic problem is:

$$\nabla \cdot \boldsymbol{\sigma} + \boldsymbol{b} = \boldsymbol{0} \quad \text{in } \Omega, \qquad \boldsymbol{\sigma} = \boldsymbol{\sigma}^T \quad \text{in } \Omega, \tag{2.112a}$$

$$\boldsymbol{\varepsilon}(\boldsymbol{u}) = \nabla_s \boldsymbol{u} = \frac{1}{2}(\nabla \boldsymbol{u} + \nabla \boldsymbol{u}^T), \tag{2.112b}$$

$$\boldsymbol{\sigma}(\boldsymbol{u}) = \mathbb{C} : \boldsymbol{\varepsilon}(\boldsymbol{u}), \tag{2.112c}$$

$$\boldsymbol{u} = \boldsymbol{u}_0 \quad \text{on } \Gamma_u, \tag{2.112d}$$

$$\boldsymbol{\sigma} \cdot \mathbf{n} = \bar{\boldsymbol{t}} \quad \text{on } \Gamma_t, \tag{2.112e}$$

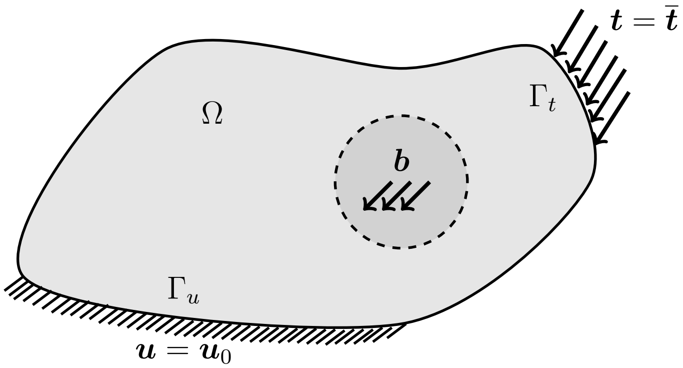

FIGURE 2.2. Two-dimensional solid that occupies the region Ω with body force $\boldsymbol{b}$, and is subjected to displacement and traction boundary conditions.

where $\boldsymbol{b} \in [L^2(\Omega)]^2$ is the body force per unit volume, $\boldsymbol{\sigma}$ is the Cauchy stress tensor, $\boldsymbol{\varepsilon}$ is the small-strain tensor with $\nabla_s(\cdot)$ being the symmetric gradient operator, $\boldsymbol{u}$ is the displacement field, $\boldsymbol{u}_0$ and $\bar{\boldsymbol{t}}$ are the imposed essential boundary and traction boundary data, and $\boldsymbol{n}$ is the unit outward normal on the boundary. Linear elastic constitutive material relation ($\mathbb{C}$ is the material moduli tensor) and small-strain kinematics are assumed.

Now to convert to the weak form, we take the inner (dot) product of (2.112a) with a test function $\boldsymbol{v} \in [H^1(\Omega)]^2$ that vanishes along the Dirichlet boundary Γ_u and integrate over the domain Ω:

$$\int_\Omega \nabla \cdot \boldsymbol{\sigma}(\boldsymbol{u}) \cdot \boldsymbol{v} \, d\boldsymbol{x} + \int_\Omega \boldsymbol{b} \cdot \boldsymbol{v} \, d\boldsymbol{x} = 0.$$

Then by applying the divergence theorem and simplifying, we rewrite the expression as:

$$\int_\Omega \boldsymbol{\sigma}(\boldsymbol{u}) : \boldsymbol{\varepsilon}(\boldsymbol{v}) \, d\boldsymbol{x} = \int_\Omega \boldsymbol{b} \cdot \boldsymbol{v} \, d\boldsymbol{x} + \int_{\partial\Omega} (\boldsymbol{\sigma}(\boldsymbol{u}) \cdot \boldsymbol{n}) \cdot \boldsymbol{v} \, ds,$$

where $\boldsymbol{\sigma}(\boldsymbol{u}) : \boldsymbol{\varepsilon}(\boldsymbol{v})$ is the tensor contraction operator. By assumption, the boundary is written as the disjoint union $\partial\Omega = \Gamma_u \cup \Gamma_t$; therefore, we write the expression as

$$\int_\Omega \boldsymbol{\sigma}(\boldsymbol{u}) : \boldsymbol{\varepsilon}(\boldsymbol{v}) \, d\boldsymbol{x} = \int_\Omega \boldsymbol{b} \cdot \boldsymbol{v} \, d\boldsymbol{x} + \int_{\Gamma_u} (\boldsymbol{\sigma}(\boldsymbol{u}) \cdot \boldsymbol{n}) \cdot \boldsymbol{v} \, ds + \int_{\Gamma_t} (\boldsymbol{\sigma}(\boldsymbol{u}) \cdot \boldsymbol{n}) \cdot \boldsymbol{v} \, ds.$$

After using the conditions that $\boldsymbol{\sigma}(\boldsymbol{u}) \cdot \boldsymbol{n} = \bar{\boldsymbol{t}}$ along Γ_t and $\boldsymbol{v} = \boldsymbol{0}$ along Γ_u, the resulting equation is given by

$$\int_\Omega \boldsymbol{\sigma}(\boldsymbol{u}) : \boldsymbol{\varepsilon}(\boldsymbol{v}) \, d\boldsymbol{x} = \int_\Omega \boldsymbol{b} \cdot \boldsymbol{v} \, d\boldsymbol{x} + \int_{\Gamma_t} \bar{\boldsymbol{t}} \cdot \boldsymbol{v} \, ds.$$

Then, the associated weak problem for the linear elastic boundary-value problem is to find the displacement field $\boldsymbol{u} \in \boldsymbol{V}$, where $\boldsymbol{V} := \{\boldsymbol{u} : \boldsymbol{u} \in [H^1(\Omega)]^2,\ \boldsymbol{u} = \boldsymbol{u}_0 \text{ on } \Gamma_u\}$, such that

$$a(\boldsymbol{u}, \boldsymbol{v}) = \ell(\boldsymbol{v}) \quad \forall \boldsymbol{v} \in \boldsymbol{V}_0, \tag{2.113a}$$

where $\boldsymbol{V}_0 := \{\boldsymbol{v} : \boldsymbol{v} \in [H^1(\Omega)]^2,\ \boldsymbol{v} = \boldsymbol{0} \text{ on } \Gamma_u\}$ and

$$a(\boldsymbol{u}, \boldsymbol{v}) = \int_\Omega \boldsymbol{\sigma}(\boldsymbol{u}) : \boldsymbol{\varepsilon}(\boldsymbol{v}) \, d\boldsymbol{x}, \tag{2.113b}$$

$$\ell(\boldsymbol{v}) = \int_\Omega \boldsymbol{b} \cdot \boldsymbol{v} \, d\boldsymbol{x} + \int_{\Gamma_t} \bar{\boldsymbol{t}} \cdot \boldsymbol{v} \, ds. \tag{2.113c}$$

2.6. Virtual element method for linear elasticity

Following the construction of the VEM for Poisson's equation, let $\mathcal{T}^h$ be the decomposition of the region Ω into nonoverlapping polygons. For each polygon $E \in \mathcal{T}^h$, denote its diameter by h_E and its centroid by $\boldsymbol{x}_E$. Each polygon E consists of N_E vertices (nodes) with N_E edges. Let $\mathcal{E}_E$ be the set of all edges of E and denote the coordinates of each vertex by $\boldsymbol{x}_i := (x_i, y_i)$.

2.6.1. Energy projection. In this section, we introduce the k-th order energy projection operator for linear elasticity. Since many of the following chapters utilize this projection, we provide a more detailed outline for its construction. To construct the necessary polynomial projection operators, we will need a basis for the space of polynomials $[\mathbb{P}_k(E)]^2$. Define the k-th order scaled monomial vectorial basis set as:

$$\widehat{\boldsymbol{M}}_k(E) = \left[\begin{Bmatrix} 1 \\ 0 \end{Bmatrix}, \begin{Bmatrix} 0 \\ 1 \end{Bmatrix}, \begin{Bmatrix} -\eta \\ \xi \end{Bmatrix}, \begin{Bmatrix} \eta \\ \xi \end{Bmatrix}, \begin{Bmatrix} \xi \\ 0 \end{Bmatrix}, \begin{Bmatrix} 0 \\ \eta \end{Bmatrix}, \dots, \begin{Bmatrix} \eta^k \\ 0 \end{Bmatrix}, \begin{Bmatrix} 0 \\ \eta^k \end{Bmatrix} \right], \tag{2.114a}$$

where

$$\xi = \frac{x - x_E}{h_E}, \quad \eta = \frac{y - y_E}{h_E}. \tag{2.114b}$$

The α-th element of the set $\widehat{\boldsymbol{M}}_k(E)$ is denoted by $\boldsymbol{m}_\alpha$ and we define the matrix $\tilde{\boldsymbol{N}}^p$ that contains the basis elements as

$$\tilde{\boldsymbol{N}}^p := \begin{bmatrix} 1 & 0 & -\eta & \eta & \xi & 0 & \dots & \eta^k & 0 \\ 0 & 1 & \xi & -\xi & 0 & \eta & \dots & 0 & \eta^k \end{bmatrix}. \tag{2.114c}$$

Based on the argument for the Poisson equation, the projection we use for the standard virtual element method with linear elasticity is the energy projection satisfying $a^E(p, \boldsymbol{u}_h - \Pi_k^\varepsilon \boldsymbol{u}_h) = 0 \quad \forall \boldsymbol{p} \in [\mathbb{P}_k(E)]^2$. Rewriting as an equivalent expression in terms of the basis functions $\boldsymbol{m}_\alpha$, we have that $\Pi_k^\varepsilon \boldsymbol{u}_h$ is defined by the orthogonality condition:

$$\int_E \boldsymbol{\sigma}(\boldsymbol{m}_\alpha) : \boldsymbol{\varepsilon}(\Pi_k^\varepsilon \boldsymbol{u}_h)\, d\boldsymbol{x} = \int_E \boldsymbol{\sigma}(\boldsymbol{m}_\alpha) : \boldsymbol{\varepsilon}(\boldsymbol{u}_h)\, d\boldsymbol{x} \quad \forall \boldsymbol{m}_\alpha \in \widehat{\boldsymbol{M}}_k(E). \tag{2.115}$$

We notice that for $\alpha = 1, 2, 3$, the vector functions $\boldsymbol{m}_\alpha$ represent rigid-body modes. That is, they satisfy $\boldsymbol{\sigma}(\boldsymbol{m}_\alpha) = \boldsymbol{0} \quad (\alpha = 1, 2, 3)$. So there will be three trivial equations, $0 = 0$, and the projection is only uniquely defined up to a rigid-body mode. To fully define the projection, we introduce the additional conditions that the nodal averages of $\boldsymbol{u}_h$ and its projection $\Pi_k^\varepsilon \boldsymbol{u}_h$ for a rigid-body mode must be equal:

$$\frac{1}{N_E} \sum_{j=1}^{N_E} (\boldsymbol{u}_h - \Pi_k^\varepsilon \boldsymbol{u}_h)(\boldsymbol{x}_j) \cdot \boldsymbol{m}_\alpha(\boldsymbol{x}_j) = 0 \quad (\alpha = 1, 2, 3). \tag{2.116}$$

Combining the conditions, we have the system that defines the energy projection as

$$\int_E \boldsymbol{\sigma}(\boldsymbol{m}_\alpha) : \boldsymbol{\varepsilon}(\Pi_k^\varepsilon \boldsymbol{u}_h)\, d\boldsymbol{x} = \int_E \boldsymbol{\sigma}(\boldsymbol{m}_\alpha) : \boldsymbol{\varepsilon}(\boldsymbol{v})\, d\boldsymbol{x} \quad (\alpha = 4, 5, \dots), \tag{2.117a}$$

$$\frac{1}{N_E} \sum_{j=1}^{N_E} \Pi_k^\varepsilon \boldsymbol{u}_h(\boldsymbol{x}_j) \cdot \boldsymbol{m}_\alpha(\boldsymbol{x}_j) = \frac{1}{N_E} \sum_{j=1}^{N_E} \boldsymbol{u}_h(\boldsymbol{x}_j) \cdot \boldsymbol{m}_\alpha(\boldsymbol{x}_j) \quad (\alpha = 1, 2, 3). \tag{2.117b}$$

Further details for the case $k = 1$ can be found in Sections 3.1.2 and 3.3.1.

Remark 2.6.1. *In general, the condition* (2.116) *can be replaced by any computable operator* $P_0(\cdot, \cdot)$ *and the condition*

$$P_0(\boldsymbol{u}_h - \Pi^\varepsilon \boldsymbol{u}_h, \boldsymbol{m}_\alpha) = 0 \quad (\alpha = 1, 2, 3).$$

The choice in (2.116) *is to define* $P_0(\cdot, \cdot)$ *as*

$$P_0(\boldsymbol{u}, \boldsymbol{v}) := \frac{1}{N_E} \sum_{j=1}^{N_E} \boldsymbol{u}(\boldsymbol{x}_j) \cdot \boldsymbol{v}(\boldsymbol{x}_j).$$

Another common choice (see [15]), valid for any $k \geq 1$, *is to use an integral average over the boundary*

$$P_0(\boldsymbol{u}, \boldsymbol{v}) := \frac{1}{|\partial E|} \int_{\partial E} \boldsymbol{u} \cdot \boldsymbol{v}\, d\boldsymbol{x},$$

or for $k \geq 3$*, we can use the element average*

$$P_0(\boldsymbol{u}, \boldsymbol{v}) := \frac{1}{|E|} \int_E \boldsymbol{u} \cdot \boldsymbol{v} \, d\boldsymbol{x}.$$

2.6.2. Virtual element space. We now extend the enhanced virtual element space for scalar fields given in (2.111) to vector fields. For each element E, define the enhanced space as

$$[\mathcal{EN}_k^E]^2 = \left\{ \boldsymbol{v}_h \in [H^1(E)]^2 : \int_E \boldsymbol{v}_h \cdot \boldsymbol{p} \, d\boldsymbol{x} = \int_E \Pi_k^\varepsilon \boldsymbol{v}_h \cdot \boldsymbol{p} \, d\boldsymbol{x} \;\; \forall \boldsymbol{p} \in [\mathbb{P}_k / \mathbb{P}_{k-2}(E)]^2 \right\}, \tag{2.119}$$

and the virtual element space by

$$\boldsymbol{V}_h(E) = [V_h(E)]^2 = \left\{ \boldsymbol{v}_h \in [\mathcal{EN}_k^E]^2 : \Delta \boldsymbol{v}_h \in [\mathbb{P}_k(E)]^2, \, \boldsymbol{v}_h|_{\partial E} \in [\mathbb{B}_k(\partial E)]^2 \right\}, \tag{2.120}$$

where the notation $[U]^2$ denotes a space containing vector functions where each component lies in the space U. In particular, each component of the vector-valued functions in $\boldsymbol{V}_h(E)$ will be functions in a scalar virtual element space. Therefore, the dimension of this space is twice the dimension of the scalar space and for an element E with N_E vertices is given by $2N = 2kN_E + k(k-1)$, where N is the number of DOF of the scalar space. Any function $\boldsymbol{v}_h \in \boldsymbol{V}_h(E)$ can be described by the degrees of freedoms and basis functions from the scalar space. That is, let $\{\phi_i\}$ be the scalar basis associated with the degrees of freedom (2.53), then we can write any $\boldsymbol{v}_h$ as:

$$\begin{aligned}
\boldsymbol{v}_h = \begin{Bmatrix} v_h^1 \\ v_h^2 \end{Bmatrix} &= \begin{bmatrix} \phi_1 & \phi_2 & \dots & \phi_N & 0 & 0 & \dots & 0 \\ 0 & 0 & \dots & 0 & \phi_1 & \phi_2 & \dots & \phi_N \end{bmatrix} \begin{Bmatrix} v_1^1 \\ v_2^1 \\ \vdots \\ v_N^2 \end{Bmatrix} && (2.121) \\
&= \sum_{i=1}^{N} \boldsymbol{\varphi}_i \texttt{dof}_i(v_h^1) + \sum_{i=1}^{N} \boldsymbol{\varphi}_{N+i} \texttt{dof}_i(v_h^2) && (2.122) \\
&:= \sum_{i=1}^{2N} \boldsymbol{\varphi}_i \texttt{dof}_i(\boldsymbol{v}_h), && (2.123)
\end{aligned}$$

where $\boldsymbol{\varphi}_i = (\phi_i, 0)^T$ and $\boldsymbol{\varphi}_{N+i} = (0, \phi_i)^T$ are the vector basis functions, and $\texttt{dof}_i(\boldsymbol{v}_h) = \texttt{dof}_i(v_h^1)$ and $\texttt{dof}_{N+i}(\boldsymbol{v}_h) = \texttt{dof}_i(v_h^2)$ are the scalar degrees of freedom of a vector-valued function $\boldsymbol{v}_h$ (for $i = 1, 2, \dots N$).

2.6.3. Discrete problem. Following the discussion for the Poisson problem, if we use the energy projection, then the discrete bilinear form is written as

$$a_h^E(\boldsymbol{u}_h, \boldsymbol{v}_h) := a^E(\Pi_k^\varepsilon \boldsymbol{u}_h, \Pi_k^\varepsilon \boldsymbol{v}_h) + S^E(\boldsymbol{u}_h - \Pi_k^\varepsilon \boldsymbol{u}_h, \boldsymbol{v}_h - \Pi_k^\varepsilon \boldsymbol{v}_h), \tag{2.124}$$

for some stabilization term $S^E(\cdot,\cdot)$. For the Poisson problem, the simplified stabilization term (2.66) is usually sufficient (see [30]); however, in elasicity, the bilinear form scales with the material modulii tensor, so the corresponding stabilization matrix $\boldsymbol{S}^E$ in (2.65) should contain suitable scaling parameters. There are a few common choices for the stabilization matrix $\boldsymbol{S}^E$ as given in [86], the simplest choice is to include a constant parameter that is proportional to the trace of the material modulii tensor $\mathbb{C}$ (scaled dofi-dofi stabilization). That is, we let

$$(\boldsymbol{S}^E)_{ij} = \frac{\texttt{tr}(\mathbb{C})}{3}\delta_{ij}. \tag{2.125a}$$

Alternatively, we can scale each of the diagonal terms separately (so-called D-recipe stabilization)

$$(\boldsymbol{S}^E)_{ij} = \max\left(\frac{\texttt{tr}(\mathbb{C})}{3}, a^E(\Pi_k^\varepsilon \boldsymbol{\varphi}_i, \Pi_k^\varepsilon \boldsymbol{\varphi}_j)\right)\delta_{ij}. \tag{2.125b}$$

The local forcing functional is given by

$$\begin{aligned} \ell_h^E(\boldsymbol{v}_h) &= \int_E \Pi_k^0 \boldsymbol{b} \cdot \boldsymbol{v_h}\, d\boldsymbol{x} + \int_{\Gamma_t \cap \partial E} \bar{\boldsymbol{t}} \cdot \boldsymbol{v_h}\, ds \\ &= \int_E \boldsymbol{b} \cdot \Pi_k^0 \boldsymbol{v_h}\, d\boldsymbol{x} + \int_{\Gamma_t \cap \partial E} \bar{\boldsymbol{t}} \cdot \boldsymbol{v_h}\, ds, \end{aligned} \tag{2.126}$$

where the final expression is obtained by applying the orthogonality property of the L^2 projection operator.

2.6.4. Matrix-vector representation. For later computations, it is more convenient to reduce the tensor expressions into equivalent matrix and vector representations. We first note that for plane elasticity we can express the components of the stress and strain tensors as symmetric 2×2 matrices. However, instead of using symmetric matrices, we adopt Voigt notation to represent the matrices as 3×1 arrays. In particular, for any symmetric 2×2 matrix $\boldsymbol{A}$, denote its Voigt representation $\overline{\boldsymbol{A}}$ by:

$$\boldsymbol{A} = \begin{bmatrix} a_{11} & a_{12} \\ a_{12} & a_{22} \end{bmatrix}, \quad \overline{\boldsymbol{A}} = \begin{Bmatrix} a_{11} \\ a_{22} \\ a_{12} \end{Bmatrix}. \tag{2.127}$$

On using Voigt (engineering) notation, we can write the stress and strain in terms of 3 × 1 arrays:

$$\overline{\boldsymbol{\sigma}} = \begin{Bmatrix} \sigma_{11} \\ \sigma_{22} \\ \sigma_{12} \end{Bmatrix}, \quad \overline{\boldsymbol{\varepsilon}} = \begin{Bmatrix} \varepsilon_{11} \\ \varepsilon_{22} \\ 2\varepsilon_{12} \end{Bmatrix}. \tag{2.128}$$

Furthermore, on using these conventions we can also express the strain-displacement relation and the constitutive law in matrix form as:

$$\overline{\boldsymbol{\sigma}} = \boldsymbol{C}\overline{\boldsymbol{\varepsilon}}, \quad \overline{\boldsymbol{\varepsilon}} = \boldsymbol{S}\boldsymbol{u}, \tag{2.129a}$$

where $\boldsymbol{S}$ is a matrix differential operator that is given by

$$\boldsymbol{S} = \begin{bmatrix} \frac{\partial}{\partial x} & 0 \\ 0 & \frac{\partial}{\partial y} \\ \frac{\partial}{\partial y} & \frac{\partial}{\partial x} \end{bmatrix}, \tag{2.129b}$$

and $\boldsymbol{C}$ is the associated matrix representation of the material tensor that is given by

$$\boldsymbol{C} = \frac{E_Y}{(1-\nu^2)} \begin{bmatrix} 1 & \nu & 0 \\ \nu & 1 & 0 \\ 0 & 0 & \frac{1-\nu}{2} \end{bmatrix} \qquad \text{(plane stress)}, \tag{2.130a}$$

$$\boldsymbol{C} = \frac{E_Y}{(1+\nu)(1-2\nu)} \begin{bmatrix} 1-\nu & \nu & 0 \\ \nu & 1-\nu & 0 \\ 0 & 0 & \frac{1-2\nu}{2} \end{bmatrix} \qquad \text{(plane strain)}, \tag{2.130b}$$

where E_Y is the Young's modulus and ν is the Poisson's ratio of the material.

2.6.5. Element stiffness matrix and element force vector for elasticity. Following (2.106a), the element stiffness matrix for linear elasticity has the following form:

$$\boldsymbol{K_E} = \boldsymbol{K}_E^c + \boldsymbol{K}_E^s, \tag{2.131a}$$

where $\boldsymbol{K}_E^c$ and $\boldsymbol{K}_E^s$ have components given by

$$(\boldsymbol{K}_E^c)_{ij} = \int_E \boldsymbol{\sigma}(\Pi_k^\varepsilon \boldsymbol{\varphi}_i) : \boldsymbol{\varepsilon}(\Pi_k^\varepsilon \boldsymbol{\varphi_j})\, d\boldsymbol{x} \tag{2.131b}$$

$$(\boldsymbol{K}_E^s)_{ij} = \sum_{r=1}^{2N} \sum_{s=1}^{2N} \mathtt{dof}_r(\boldsymbol{\varphi}_i - \Pi_k^\varepsilon \boldsymbol{\varphi}_i) \boldsymbol{S}_{rs}^E \mathtt{dof}_s(\boldsymbol{\varphi}_j - \Pi_k^\varepsilon \boldsymbol{\varphi}_j), \tag{2.131c}$$

where we have not specified a stabilization matrix $\boldsymbol{S}^E$.

For each element E, the element force vector is given by

$$(\boldsymbol{f}_E)_i = \int_E \boldsymbol{b} \cdot \Pi_k^0 \boldsymbol{\varphi}_i \, d\boldsymbol{x} + \int_{\Gamma_t \cap \partial E} \bar{\boldsymbol{t}} \cdot \boldsymbol{\varphi}_i \, ds, \tag{2.132}$$

where Π_k^0 is the L^2 projection operator into the space of vector-valued polynomials of degree less than or equal to k. For the standard virtual element method, we only outline the construction of the element stiffness and forcing terms. A more detailed implementation can be found in [13, 80].

CHAPTER 3

Stabilization-Free Virtual Element Method

In this chapter, we first construct a low order virtual element method that does not require a stabilization term. In the standard virtual element method, a stability term is usually required to preserve the coercivity of the discrete bilinear operator; however the choice of the stabilization term in the VEM is non-unique and is problem dependent. An incorrect choice of stabilization can result in overly stiff and inaccurate results. Therefore it is of interest to construct a method that is independent of a stabilization term. The main idea of the stabilization-free approach, as described for the Poisson problem in [**20**], is to modify the virtual element space to allow for the construction of a higher order L^2 projection of the strain (gradient). This process requires additional internal degrees of freedom; however, these can be removed by utilizing a secondary projection operator of the displacement field as originally shown in [**2**]. A similar approach is given in [**54**]; however, they used static condensation instead of a secondary projection to remove the excess degrees of freedom.

We start by defining the necessary polynomial spaces, and projection operators for the displacement and the strain fields. With the projection operators on hand, we construct an enhanced virtual element space and define an alternate weak bilinear form that does not require a stabilization term. Next, we detail the numerical implementation of the method, show that the problem is well defined, and give convergence error estimates. We conclude the chapter by presenting numerical results of the SF-VEM on a series of benchmark problems in linear elasticity: the patch test, bending of a cantilever beam, infinite plate with a circular hole under uniaxial tension, and hollow cylinder under internal pressure. The numerical convergence rates are found to be in agreement with the theoretical results.

This chapter is based on the work published in [**37**].

3.1. Polynomial space and projection operators

We present the derivation of the two projections that are used in the stabilization-free VEM: energy projection of the displacement field and L^2 projection of the strain field.

3.1.1. Polynomial basis. For the initial stabilization-free virtual element method, we only consider a first-order method; therefore, we use a first-order polynomial projection to approximate the displacement field inside an element. Over each element E, we define $[\mathbb{P}_1(E)]^2$ as the space of of two-dimensional vector-valued polynomials of degree less than or equal to 1. On each E, we will also need to choose a basis. In particular, we choose the basis as:

$$\widehat{\boldsymbol{M}}(E) = \left[\begin{Bmatrix} 1 \\ 0 \end{Bmatrix}, \begin{Bmatrix} 0 \\ 1 \end{Bmatrix}, \begin{Bmatrix} -\eta \\ \xi \end{Bmatrix}, \begin{Bmatrix} \eta \\ \xi \end{Bmatrix}, \begin{Bmatrix} \xi \\ 0 \end{Bmatrix}, \begin{Bmatrix} 0 \\ \eta \end{Bmatrix} \right], \tag{3.1}$$

where ξ and η given in (2.114b). The α-th element of the set $\widehat{\boldsymbol{M}}(E)$ is denoted by $\boldsymbol{m}_\alpha$. We note that this basis is equivalent to the first six basis functions given in (2.114a).

In the stabilization-free approach, we directly approximate the strain tensor (matrix) inside an element with a high-order matrix polynomial. Therefore, we also define the space $\mathbb{P}_\ell(E)^{2\times 2}_{\text{sym}}$ that represents 2×2 symmetric matrix polynomials of degree less than or equal to ℓ. Since the matrices are symmetric we can represent them in terms of 3×1 vectors using Voigt notation in (2.127). On each element E, we choose the basis

$$\widehat{\boldsymbol{M}}^{2\times 2}(E) = \left[\begin{Bmatrix} 1 \\ 0 \\ 0 \end{Bmatrix}, \begin{Bmatrix} 0 \\ 1 \\ 0 \end{Bmatrix}, \begin{Bmatrix} 0 \\ 0 \\ 1 \end{Bmatrix}, \begin{Bmatrix} \xi \\ 0 \\ 0 \end{Bmatrix}, \begin{Bmatrix} 0 \\ \xi \\ 0 \end{Bmatrix}, \begin{Bmatrix} 0 \\ 0 \\ \xi \end{Bmatrix}, \dots \begin{Bmatrix} \eta^\ell \\ 0 \\ 0 \end{Bmatrix}, \begin{Bmatrix} 0 \\ \eta^\ell \\ 0 \end{Bmatrix}, \begin{Bmatrix} 0 \\ 0 \\ \eta^\ell \end{Bmatrix} \right]. \tag{3.2a}$$

We denote the α-th vector in this set as $\widehat{\boldsymbol{m}}_\alpha$ and define the matrix $\boldsymbol{N}^p$ that contains these basis elements as

$$\boldsymbol{N}^p := \begin{bmatrix} 1 & 0 & 0 & \xi & 0 & 0 & \dots & \eta^\ell & 0 & 0 \\ 0 & 1 & 0 & 0 & \xi & 0 & \dots & 0 & \eta^\ell & 0 \\ 0 & 0 & 1 & 0 & 0 & \xi & \dots & 0 & 0 & \eta^\ell \end{bmatrix}. \tag{3.2b}$$

3.1.2. Energy projection of the displacement field. For completeness and since we rely on the first-order energy projection in the remainder of this work, we detail the construction of the first-order projection denoted by Π^ε. Let E be any generic element with $\boldsymbol{H}^1(E) := [H^1(E)]^2$. We now define the energy projection operator $\Pi^\varepsilon : \boldsymbol{H}^1(E) \to [\mathbb{P}_1(E)]^2$ by the unique function that satisfies the orthogonality relation:

$$a^E(\boldsymbol{m}_\alpha, \boldsymbol{v} - \Pi^\varepsilon \boldsymbol{v}) = 0 \quad \forall \boldsymbol{m}_\alpha \in \widehat{\boldsymbol{M}}(E), \tag{3.3}$$

where $\widehat{\boldsymbol{M}}(E)$ given in (3.1). Note that for $\alpha = 1, 2, 3$, which corresponds to the rigid-body modes, we obtain $\boldsymbol{\sigma}(\boldsymbol{m}_\alpha) = \boldsymbol{0}$. So we obtain three trivial equations, $0 = 0$. To fully define the projection, we need to choose a suitable projection operator $P_0 : \boldsymbol{H}^1(E) \times \boldsymbol{H}^1(E) \to \mathbb{R}$. In particular, we select it as a discrete L^2 inner product on E:

$$P_0(\boldsymbol{u}, \boldsymbol{v}) := \frac{1}{N_E} \sum_{j=1}^{N_E} \boldsymbol{u}(\boldsymbol{x}_j) \cdot \boldsymbol{v}(\boldsymbol{x}_j), \tag{3.4}$$

and require the condition

$$P_0(\boldsymbol{m}_\alpha, \boldsymbol{v} - \Pi^\varepsilon \boldsymbol{v}) = \frac{1}{N_E} \sum_{j=1}^{N_E} (\boldsymbol{v} - \Pi^\varepsilon \boldsymbol{v})(\boldsymbol{x}_j) \cdot \boldsymbol{m}_\alpha(\boldsymbol{x}_j) = 0 \quad (\alpha = 1, 2, 3). \tag{3.5}$$

On writing out the expressions, we have the equivalent system

$$\int_E \boldsymbol{\sigma}(\boldsymbol{m}_\alpha) : \boldsymbol{\varepsilon}(\Pi^\varepsilon \boldsymbol{v}) \, d\boldsymbol{x} = \int_E \boldsymbol{\sigma}(\boldsymbol{m}_\alpha) : \boldsymbol{\varepsilon}(\boldsymbol{v}) \, d\boldsymbol{x} \quad (\alpha = 4, 5, 6), \tag{3.6a}$$

$$\frac{1}{N_E} \sum_{j=1}^{N_E} \Pi^\varepsilon \boldsymbol{v}(\boldsymbol{x}_j) \cdot \boldsymbol{m}_\alpha(\boldsymbol{x}_j) = \frac{1}{N_E} \sum_{j=1}^{N_E} \boldsymbol{v}(\boldsymbol{x}_j) \cdot \boldsymbol{m}_\alpha(\boldsymbol{x}_j) \quad (\alpha = 1, 2, 3). \tag{3.6b}$$

We can also rewrite this using the matrix-vector representation. For the right-hand side of (3.6a), we use (2.128) to write

$$\begin{aligned} \boldsymbol{\sigma}(\boldsymbol{m}_\alpha) : \boldsymbol{\varepsilon}(\boldsymbol{v}) = \overline{\boldsymbol{\varepsilon}(\boldsymbol{v})} \cdot \overline{\boldsymbol{\sigma}(\boldsymbol{m}_\alpha)} &= \left(\overline{\boldsymbol{\varepsilon}(\boldsymbol{v})}\right)^T \overline{\boldsymbol{\sigma}(\boldsymbol{m}_\alpha)} \\ &= (\boldsymbol{S}\boldsymbol{v})^T (\boldsymbol{C}\boldsymbol{S}\boldsymbol{m}_\alpha) . \end{aligned}$$

Similarly, the left-hand side can be written as

$$\boldsymbol{\sigma}(\boldsymbol{m}_\alpha) : \boldsymbol{\varepsilon}(\Pi^\varepsilon \boldsymbol{v}) := \left(\overline{\boldsymbol{\varepsilon}(\Pi^\varepsilon \boldsymbol{v})}\right)^T (\boldsymbol{C}\boldsymbol{S}\boldsymbol{m}_\alpha) = (\boldsymbol{S}\Pi^\varepsilon \boldsymbol{v})^T (\boldsymbol{C}\boldsymbol{S}\boldsymbol{m}_{\boldsymbol{\alpha}}) .$$

Therefore, we can express (3.6a) in matrix-vector form as:

$$\int_E (\boldsymbol{S}\Pi^\varepsilon \boldsymbol{v})^T (\boldsymbol{C}\boldsymbol{S}\boldsymbol{m}_\alpha) \, d\boldsymbol{x} = \int_E (\boldsymbol{S}\boldsymbol{v})^T (\boldsymbol{C}\boldsymbol{S}\boldsymbol{m}_\alpha) \, d\boldsymbol{x}. \tag{3.7}$$

3.1.3. $\mathbf{L^2}$ projection of the strain field. We define the associated L^2 projection operator $\Pi^0_\ell \boldsymbol{\varepsilon}(.) : \boldsymbol{H}^1(E) \to \mathbb{P}_\ell(E)^{2\times 2}_{\text{sym}}$ of the strain tensor by the unique operator that satisfies

$$(\boldsymbol{\varepsilon}^p, \boldsymbol{\varepsilon}(\boldsymbol{v}) - \Pi^0_\ell \boldsymbol{\varepsilon}(\boldsymbol{v}))_E = 0 \quad \forall \boldsymbol{\varepsilon}^p \in \mathbb{P}_\ell(E)^{2\times 2}_{\text{sym}}, \tag{3.8a}$$

where we use the standard L^2 inner product:

$$(\boldsymbol{\varepsilon}^p, \boldsymbol{\varepsilon})_E = \int_E \boldsymbol{\varepsilon}^p : \boldsymbol{\varepsilon}\, d\boldsymbol{x}. \tag{3.8b}$$

Writing out the expression in (3.8a), we have

$$\int_E \boldsymbol{\varepsilon}^p : \Pi^0_\ell \boldsymbol{\varepsilon}(\boldsymbol{v})\, d\boldsymbol{x} = \int_E \boldsymbol{\varepsilon}^p : \boldsymbol{\varepsilon}(\boldsymbol{v})\, d\boldsymbol{x}. \tag{3.9}$$

On expanding the right-hand side of (3.9), and on applying integration by parts and the divergence theorem, we obtain

$$\begin{aligned}\int_E \boldsymbol{\varepsilon}^p : \boldsymbol{\varepsilon}(\boldsymbol{v}) d\boldsymbol{x} &= \int_E \nabla \cdot (\boldsymbol{v} \cdot \boldsymbol{\varepsilon}^p)\, d\boldsymbol{x} - \int_E \boldsymbol{v} \cdot (\nabla \cdot \boldsymbol{\varepsilon}^p)\, d\boldsymbol{x} \\ &= \int_{\partial E} \boldsymbol{n} \cdot (\boldsymbol{v} \cdot \boldsymbol{\varepsilon}^p)\, ds - \int_E \boldsymbol{v} \cdot (\nabla \cdot \boldsymbol{\varepsilon}^p)\, d\boldsymbol{x}.\end{aligned}$$

Then, (3.9) becomes

$$\int_E \boldsymbol{\varepsilon}^p : \Pi^0_\ell \boldsymbol{\varepsilon}(\boldsymbol{v})\, d\boldsymbol{x} = \int_{\partial E} \boldsymbol{v} \cdot (\boldsymbol{\varepsilon}^p \cdot \boldsymbol{n})\, ds - \int_E \boldsymbol{v} \cdot (\nabla \cdot \boldsymbol{\varepsilon}^p)\, d\boldsymbol{x}. \tag{3.10}$$

On using the matrix-vector representation in (2.128), the first term on the right-hand side of (3.10) becomes

$$\boldsymbol{v} \cdot (\boldsymbol{\varepsilon}^p \cdot \boldsymbol{n}) = \boldsymbol{v}^T \begin{bmatrix} \varepsilon^p_{11} & \varepsilon^p_{12} \\ \varepsilon^p_{12} & \varepsilon^p_{22} \end{bmatrix} \begin{Bmatrix} n_1 \\ n_2 \end{Bmatrix} = \boldsymbol{v}^T \begin{bmatrix} n_1 & 0 & n_2 \\ 0 & n_2 & n_1 \end{bmatrix} \begin{Bmatrix} \varepsilon^p_{11} \\ \varepsilon^p_{22} \\ \varepsilon^p_{12} \end{Bmatrix} := \boldsymbol{v}^T \boldsymbol{N}^{\partial E}_* \overline{\boldsymbol{\varepsilon}^p}, \tag{3.11a}$$

where $\boldsymbol{N}^{\partial E}_*$ is the matrix of element normal components, which is defined as

$$\boldsymbol{N}^{\partial E}_* := \begin{bmatrix} n_1 & 0 & n_2 \\ 0 & n_2 & n_1 \end{bmatrix}. \tag{3.11b}$$

For the second term on the right-hand side of (3.10), we have

$$\boldsymbol{v}\cdot(\nabla\cdot\boldsymbol{\varepsilon}^p) = \boldsymbol{v}^T \begin{Bmatrix} \frac{\partial \varepsilon^p_{11}}{\partial x} + \frac{\partial \varepsilon^p_{12}}{\partial y} \\ \frac{\partial \varepsilon^p_{12}}{\partial x} + \frac{\partial \varepsilon^p_{22}}{\partial y} \end{Bmatrix} = \boldsymbol{v}^T \begin{bmatrix} \frac{\partial}{\partial x} & 0 & \frac{\partial}{\partial y} \\ 0 & \frac{\partial}{\partial y} & \frac{\partial}{\partial x} \end{bmatrix} \begin{Bmatrix} \varepsilon^p_{11} \\ \varepsilon^p_{22} \\ \varepsilon^p_{12} \end{Bmatrix} := \boldsymbol{v}^T \boldsymbol{\partial}\overline{\boldsymbol{\varepsilon}^p}, \tag{3.12a}$$

where $\boldsymbol{\partial}$ is a matrix operator that is defined as

$$\boldsymbol{\partial} := \begin{bmatrix} \frac{\partial}{\partial x} & 0 & \frac{\partial}{\partial y} \\ 0 & \frac{\partial}{\partial y} & \frac{\partial}{\partial x} \end{bmatrix}. \tag{3.12b}$$

Now we can express (3.10) as

$$\int_E \boldsymbol{\varepsilon}^p : \Pi^0_\ell \boldsymbol{\varepsilon}(\boldsymbol{v})\,d\boldsymbol{x} = \int_{\partial E} \boldsymbol{v}^T \boldsymbol{N}^{\partial E}_* \overline{\boldsymbol{\varepsilon}^p}\,ds + \int_E \boldsymbol{v}^T \boldsymbol{\partial}\overline{\boldsymbol{\varepsilon}^p}\,d\boldsymbol{x}. \tag{3.13}$$

Since $\Pi^0_\ell \boldsymbol{\varepsilon}(\boldsymbol{v})$ is the projection of the strain tensor onto symmetric matrix polynomials, we use (2.128) to represent it in terms of a vector. In particular, we set

$$\overline{\Pi^0_\ell \boldsymbol{\varepsilon}(\boldsymbol{v})} = \begin{Bmatrix} (\Pi^0_\ell \boldsymbol{\varepsilon}(\boldsymbol{v}))_{11} \\ (\Pi^0_\ell \boldsymbol{\varepsilon}(\boldsymbol{v}))_{22} \\ 2(\Pi^0_\ell \boldsymbol{\varepsilon}(\boldsymbol{v}))_{12} \end{Bmatrix}.$$

Now, we can also write

$$\boldsymbol{\varepsilon}^p : \Pi^0_\ell \boldsymbol{\varepsilon}(\boldsymbol{v}) = \overline{\Pi^0_\ell \boldsymbol{\varepsilon}(\boldsymbol{v})} \cdot \overline{\boldsymbol{\varepsilon}^p} = \left(\overline{\Pi^0_\ell \boldsymbol{\varepsilon}(\boldsymbol{v})}\right)^T \overline{\boldsymbol{\varepsilon}^p}.$$

On using the above relations in (3.13), we seek the L^2 projection that satisfies

$$\int_E \left(\overline{\Pi^0_\ell \boldsymbol{\varepsilon}(\boldsymbol{v})}\right)^T \overline{\boldsymbol{\varepsilon}^p}\,d\boldsymbol{x} = \int_{\partial E} \boldsymbol{v}^T \boldsymbol{N}^{\partial E}_* \overline{\boldsymbol{\varepsilon}^p}\,ds + \int_E \boldsymbol{v}^T \boldsymbol{\partial}\overline{\boldsymbol{\varepsilon}^p}\,d\boldsymbol{x} \quad \forall \boldsymbol{\varepsilon}^p \in \mathbb{P}_\ell(E)^{2\times 2}_{\text{sym}}. \tag{3.14}$$

3.2. Enlarged enhanced virtual element space

With the preliminary results in place, we now construct the discrete space for the stabilization-free virtual element method. Let E be any polygonal element from $\mathcal{T}^h$, then following [20], we select the smallest value $\ell = \ell(E)$ that satisfies[1]

$$\frac{3}{2}(\ell+1)(\ell+2) - \dim(\mathbb{P}_\ell^{\text{ker}}(E)) \geq 2N_E - 3, \tag{3.15}$$

where N_E is the number of vertices (nodes) of element E and $\mathbb{P}_\ell^{\text{ker}}(E)$ is the space defined by

$$\mathbb{P}_\ell^{\text{ker}}(E) := \left\{ \boldsymbol{\varepsilon}^p \in \mathbb{P}_\ell(E)^{2\times 2}_{\text{sym}} : \int_{\partial E} (\boldsymbol{v} - P_r(\boldsymbol{v}))|_{\partial E} \cdot (\boldsymbol{\varepsilon}^p \cdot \boldsymbol{n}) \; ds = 0 \;\; \forall \boldsymbol{v} \right\},$$

where $P_r(\boldsymbol{v})$ is a projection of $\boldsymbol{v}$ onto rigid-body modes with $\boldsymbol{\varepsilon}(P_r(\boldsymbol{v})) = \boldsymbol{0}$. It can be shown that the dimension of the space $\mathbb{P}_\ell^{\text{ker}}(E)$ is bounded from above, and we include this result as a lemma.

Lemma 3.2.0.1. *Let E be any polygonal element and $\ell \in \mathbb{N}$. Then*

$$dim(\mathbb{P}_\ell^{ker}(E)) \leq \frac{\ell}{2}(3\ell + 1). \tag{3.16}$$

Proof. Following [20], we define for each element E, the subspace of polynomials

$$\tilde{\mathbb{H}}_{\ell+1}(E) = \{\boldsymbol{p} \in [\mathbb{P}_{\ell+1}(E)]^2 : \nabla \cdot \boldsymbol{\sigma}(\boldsymbol{p}) = \boldsymbol{0}\}.$$

For a given ℓ, this space is shown to have dimension $4\ell + 6$ in [31]. We then consider the space $\boldsymbol{\sigma}(\tilde{\mathbb{H}}_{\ell+1}(E))$, and it can be shown that this space has dimension $4\ell+3$. Both $\mathbb{P}_\ell^{\text{ker}}(E)$ and $\boldsymbol{\sigma}(\tilde{\mathbb{H}}_{\ell+1}(E))$ are subspaces of $\mathbb{P}_\ell(E)^{2\times 2}_{\text{sym}}$, so the sum $\mathbb{P}_\ell^{\text{ker}}(E) + \boldsymbol{\sigma}(\tilde{\mathbb{H}}_{\ell+1}(E))$ is also a subspace and the dimension is bounded by:

$$\begin{aligned} \dim(\mathbb{P}_\ell(E)^{2\times 2}_{\text{sym}}) &\geq \dim(\mathbb{P}_\ell^{\text{ker}}(E) + \boldsymbol{\sigma}(\tilde{\mathbb{H}}_{\ell+1}(E))) \\ &= \dim(\mathbb{P}_\ell^{\text{ker}}(E)) + \dim(\boldsymbol{\sigma}(\tilde{\mathbb{H}}_{\ell+1}(E)) - \dim(\mathbb{P}_\ell^{\text{ker}}(E) \cap \boldsymbol{\sigma}(\tilde{\mathbb{H}}_{\ell+1}(E))). \end{aligned}$$

Now we show that $\mathbb{P}_\ell^{\text{ker}}(E) \cap \boldsymbol{\sigma}(\tilde{\mathbb{H}}_{\ell+1}(E)) = \{\boldsymbol{0}\}$. To this end, let $\boldsymbol{p} \in \tilde{\mathbb{H}}_{\ell+1}(E)$, and assume that $\boldsymbol{\sigma}(\boldsymbol{p}) \in \mathbb{P}_\ell^{\text{ker}}(E)$. Then we have for any $\boldsymbol{v} \in \boldsymbol{H}^1(E)$,

$$\int_E \nabla \cdot \boldsymbol{\sigma}(\boldsymbol{p}) \cdot (\boldsymbol{v} - P_r(\boldsymbol{v})) \; d\boldsymbol{x} = 0.$$

---

[1] In [54], the following inequality for $\ell = \ell(E)$ is proposed: $\frac{3}{2}(\ell+1)(\ell+2) \geq m - 3$, where m is the total number of degrees of freedom, which includes an additional $\ell(\ell+1)$ degrees of freedom due to extending the vector polynomial approximation space. However, a counterexample on regular polygons (A. Russo, personal communication, April 2022) shows that this condition is not sufficient.

On applying the divergence theorem and using the definition of $\mathbb{P}_\ell^{\ker}(E)$, we can write

$$\int_{\partial E} (\boldsymbol{v} - P_r(\boldsymbol{v}))|_{\partial E} \cdot (\boldsymbol{\sigma}(\boldsymbol{p}) \cdot \boldsymbol{n}) \; ds - \int_E \boldsymbol{\varepsilon}(\boldsymbol{v} - P_r(\boldsymbol{v})) : \boldsymbol{\sigma}(\boldsymbol{p}) \, d\boldsymbol{x} = -\int_E \boldsymbol{\varepsilon}(\boldsymbol{v}) : \boldsymbol{\sigma}(\boldsymbol{p}) = 0.$$

This is true for all $\boldsymbol{v}$, which implies that $\boldsymbol{\sigma}(\boldsymbol{p}) = \boldsymbol{0}$. Otherwise, suppose this is not true, then following a similar argument from [20], there exists an open set $\omega \subset E$ such that $\boldsymbol{\sigma}(\boldsymbol{p}) \neq \boldsymbol{0}$ and in particular $\boldsymbol{p} \neq \boldsymbol{0}$ over ω . Now define a (smooth) bump function by:

$$\begin{cases} -\nabla \cdot \boldsymbol{\sigma}(\boldsymbol{b}_\omega) = \boldsymbol{p} & \text{in } \omega, \\ \boldsymbol{b}_\omega = \boldsymbol{0} & \text{on } E \setminus \omega. \end{cases}$$

Then, we consider

$$0 = (\boldsymbol{\sigma}(\boldsymbol{p}), \boldsymbol{\varepsilon}(\boldsymbol{b}_\omega))_E = (\boldsymbol{\sigma}(\boldsymbol{p}), \boldsymbol{\varepsilon}(\boldsymbol{b}_\omega))_\omega = (\boldsymbol{\varepsilon}(\boldsymbol{p}), \boldsymbol{\sigma}(\boldsymbol{b}_\omega))_\omega$$

On applying the divergence theorem, we obtain

$$\begin{aligned} 0 = (\boldsymbol{\varepsilon}(\boldsymbol{p}), \boldsymbol{\sigma}(\boldsymbol{b}_\omega))_\omega = \int_\omega \boldsymbol{\varepsilon}(\boldsymbol{p}) : \boldsymbol{\sigma}(\boldsymbol{b}_\omega) \; d\boldsymbol{x} &= \int_{\partial\omega} (\boldsymbol{\sigma}(\boldsymbol{b}_\omega) \cdot \boldsymbol{n}) \cdot \boldsymbol{p} \; ds - \int_\omega \boldsymbol{p} \cdot (\nabla \cdot \boldsymbol{\sigma}(\boldsymbol{b}_\omega)) \; d\boldsymbol{x} \\ &= \int_\omega \boldsymbol{p} \cdot \boldsymbol{p} \; d\boldsymbol{x} > 0, \end{aligned}$$

which leads to a contradiction, and therefore $\boldsymbol{\sigma}(\boldsymbol{p}) = \boldsymbol{0}$ holds on E. This implies that $\mathbb{P}_\ell^{\ker}(E) \cap \boldsymbol{\sigma}(\tilde{\mathbb{H}}_{\ell+1}(E)) = \{\boldsymbol{0}\}$. Now it follows that

$$\begin{aligned} \dim(\mathbb{P}_\ell^{\ker}(E)) &\leq \dim(\mathbb{P}_\ell(E)^{2\times 2}_{\text{sym}}) - \dim(\boldsymbol{\sigma}(\tilde{\mathbb{H}}_{\ell+1}(E))) + \dim(\mathbb{P}_\ell^{\ker}(E) \cap \boldsymbol{\sigma}(\tilde{\mathbb{H}}_{\ell+1}(E))) \\ &= \frac{3}{2}(\ell+1)(\ell+2) - (4\ell+3) \\ &= \frac{\ell}{2}(3\ell+1). \end{aligned}$$

□

Combining (3.16) and (3.15), we get a sufficient bound on the number of vertices required for any ℓ. In particular, we have a more restrictive bound:

$$N_E \leq 2\ell + 3. \tag{3.17}$$

On using this value of ℓ, we define the set of all functions $\boldsymbol{v} \in \boldsymbol{H}^1(E)$ that satisfy the property that the inner product of the function and any vector polynomial in $[\mathbb{P}_{\ell-1}(E)]^2$ is equal to that of the inner product with the energy projection. That is, we define the set $\mathcal{EN}^E_{1,\ell}$ as

$$\mathcal{EN}^E_{1,\ell} = \left\{ \boldsymbol{v} : \int_E \boldsymbol{v} \cdot \boldsymbol{p} \, d\boldsymbol{x} = \int_E \Pi^\varepsilon \boldsymbol{v} \cdot \boldsymbol{p} \, d\boldsymbol{x} \quad \forall \boldsymbol{p} \in [\mathbb{P}_{\ell-1}(E)]^2 \right\}. \tag{3.18}$$

We define the local enlarged virtual element space as:

$$\boldsymbol{V}^E_{1,\ell} := \left\{ \boldsymbol{v}_h \in \mathcal{EN}^E_{1,\ell} : \Delta \boldsymbol{v}_h \in [\mathbb{P}_{\ell-1}(E)]^2, \ \gamma^e(\boldsymbol{v}_h) \in [\mathbb{P}_1(e)]^2 \ \forall e \in \mathcal{E}_E, \ \boldsymbol{v}_h \in [C^0(\partial E)]^2 \right\}, \tag{3.19}$$

where $\gamma^{e_i}(\cdot)$ is the trace of a function (its argument) on an edge e_i. In the above space we require functions to be linear on the edges, in which case we can take the degrees of freedom to be the values of the function at the vertices of the polygon E. There will be a total of $2N_E$ degrees of freedom on each element E.

With the local space so defined, we define the global enlarged virtual element space as

$$\boldsymbol{V}_{1,\boldsymbol{\ell}} := \{ \boldsymbol{v}_h \in [H^1(\Omega)]^2 : \boldsymbol{v}_h|_E \in \boldsymbol{V}^E_{1,\ell} \ \text{ for } \ell = \ell(E) \}. \tag{3.20}$$

For each E, we assign a suitable basis to the local virtual element space $\boldsymbol{V}^E_{1,\ell}$. Let $\{\phi_i\}$ be the set of generalized barycentric coordinates (canonical basis functions) [61] that satisfy $\phi_i(\boldsymbol{x}_j) = \delta_{ij}$. We express the components of any $\boldsymbol{v}_h \in \boldsymbol{V}^E_{1,\ell}$ as the sum of these basis functions:

$$\boldsymbol{v}_h = \begin{Bmatrix} v_h^1 \\ v_h^2 \end{Bmatrix} = \begin{bmatrix} \phi_1 & \phi_2 & \dots & \phi_{N_E} & 0 & 0 & \dots & 0 \\ 0 & 0 & \dots & 0 & \phi_1 & \phi_2 & \dots & \phi_{N_E} \end{bmatrix} \begin{Bmatrix} v_1^1 \\ v_2^1 \\ \vdots \\ v_{N_E}^2 \end{Bmatrix} := \boldsymbol{N}^v \tilde{\boldsymbol{v}}_h, \tag{3.21a}$$

where we define $\boldsymbol{N}^v$ as the matrix of vectorial basis functions:

$$\boldsymbol{N}^v = \begin{bmatrix} \phi_1 & \phi_2 & \dots & \phi_{N_E} & 0 & 0 & \dots & 0 \\ 0 & 0 & \dots & 0 & \phi_1 & \phi_2 & \dots & \phi_{N_E} \end{bmatrix} := \begin{bmatrix} \boldsymbol{\varphi}_1 & \dots & \boldsymbol{\varphi}_{N_E} & \dots & \boldsymbol{\varphi}_{2N_E} \end{bmatrix}. \tag{3.21b}$$

We now define the weak form of the virtual element method on this space. On defining a discrete bilinear operator $a_h^E : \boldsymbol{V}^E_{1,\ell} \times \boldsymbol{V}^E_{1,\ell} \to \mathbb{R}$ and a discrete linear functional $\ell_h^E : \boldsymbol{V}^E_{1,\ell} \to \mathbb{R}$, we seek the solution to the problem: find $\boldsymbol{u}_h \in \boldsymbol{V}^E_{1,\ell}$ such that

$$a_h^E(\boldsymbol{u}_h, \boldsymbol{v}_h) = \ell_h^E(\boldsymbol{v}_h) \quad \forall \boldsymbol{v}_h \in \boldsymbol{V}^E_{1,\ell}. \tag{3.22}$$

Following [20], we introduce the local discrete bilinear form in matrix-vector form:

$$a_h^E(\boldsymbol{u}_h, \boldsymbol{v}_h) := \int_E \left(\overline{\Pi_\ell^0 \boldsymbol{\varepsilon}(\boldsymbol{v_h})}\right)^T \boldsymbol{C}\, \overline{\Pi_\ell^0 \boldsymbol{\varepsilon}(\boldsymbol{u}_h)}\, d\boldsymbol{x}, \tag{3.23}$$

with the associated global operator defined as

$$a_h(\boldsymbol{u}_h, \boldsymbol{v}_h) := \sum_E a_h^E(\boldsymbol{u}_h, \boldsymbol{v}_h). \tag{3.24}$$

We also define a local linear functional by

$$\ell_h^E(\boldsymbol{v}_h) = \int_E \boldsymbol{v}_h^T \boldsymbol{b}_h\, d\boldsymbol{x} + \int_{\Gamma_t \cap \partial E} \boldsymbol{v}_h^T \bar{\boldsymbol{t}}\, ds, \tag{3.25}$$

with the associated global functional

$$\ell_h(\boldsymbol{v}_h) = \sum_E \ell_h^E(\boldsymbol{v}_h), \tag{3.26}$$

where $\boldsymbol{b}_h$ is some approximation to $\boldsymbol{b}$. For first-order methods it is sufficient to consider the L^2 projection onto constants, namely $\boldsymbol{b}_h = \Pi_0^0 \boldsymbol{b}$.

Remark 3.2.1. *We note that the discrete bilinear form $a_h^E(\cdot,\cdot)$ given in this section differs from the standard VEM* (2.124)*. The first difference is that* (3.23) *contains only the polynomial approximation term and does not have a stabilization term $S^E(\cdot,\cdot)$. Another major difference is that the strain operator is directly approximated by a projection operator $\Pi_\ell^0 \boldsymbol{\varepsilon}(\cdot)$ instead of as the strain operator acting on a polynomial $\boldsymbol{\varepsilon}(\Pi^\varepsilon(\cdot))$. For linear polynomials, these two approaches are equivalent; however, it is shown in [14] that for high order methods, the standard VEM bilinear form can lead to suboptimal results in certain problems.*

3.3. Numerical implementation

With the definitions of the discrete spaces and projections on hand, we now detail the implementation of the method. We present the derivation of the equations to compute the energy projection, the L^2 projection, and the element stiffness matrix.

3.3.1. Implementation of energy projector. We start with the energy projection. From (3.7), we have for $\alpha = 4, 5, 6$, the equation

$$\int_E \left(\boldsymbol{S}\Pi^\varepsilon \boldsymbol{v}_h\right)^T \left(\boldsymbol{C}\boldsymbol{S}\boldsymbol{m}_\alpha\right)\, d\boldsymbol{x} = \int_E \left(\boldsymbol{S}\boldsymbol{v}_h\right)^T \left(\boldsymbol{C}\boldsymbol{S}\boldsymbol{m}_\alpha\right)\, d\boldsymbol{x}.$$

In particular, we are interested in the case when $\boldsymbol{v}_h = \boldsymbol{\varphi}_i$, the basis functions in $\boldsymbol{V}_{1,\ell}^E$. By definition of the energy projection, $\Pi^\varepsilon \boldsymbol{\varphi}_i$ is a vector polynomial of degree one. Therefore, we can expand it in terms of its basis functions:

$$\Pi^\varepsilon \boldsymbol{\varphi}_i = \sum_{\beta=1}^{6} s_\beta^i \boldsymbol{m}_\beta. \tag{3.27}$$

We can express the left-hand side as

$$\int_E \left(\boldsymbol{S}\Pi^\varepsilon \boldsymbol{\varphi}_i\right)^T \left(\boldsymbol{C}\boldsymbol{S}\boldsymbol{m}_\alpha\right) d\boldsymbol{x} = \sum_{\beta=1}^{6} s_\beta^i \int_E \left(\boldsymbol{S}\boldsymbol{m}_\beta\right)^T \left(\boldsymbol{C}\boldsymbol{S}\boldsymbol{m}_\alpha\right) d\boldsymbol{x}. \tag{3.28}$$

Define the matrix $\tilde{\boldsymbol{G}}$ for $\beta = 1, 2, \ldots, 6$, and $\alpha = 4, 5, 6$ by

$$\tilde{\boldsymbol{G}}_{\alpha\beta} = \int_E \left(\boldsymbol{S}\boldsymbol{m}_\beta\right)^T \left(\boldsymbol{C}\boldsymbol{S}\boldsymbol{m}_\alpha\right) d\boldsymbol{x}. \tag{3.29}$$

Similarly, the matrix $\tilde{\boldsymbol{B}}$ representing the right-hand side of (3.7) becomes

$$\tilde{\boldsymbol{B}}_{\alpha i} = \int_E \left(\boldsymbol{S}\boldsymbol{\varphi}_i\right)^T \left(\boldsymbol{C}\boldsymbol{S}\boldsymbol{m}_\alpha\right)\, d\boldsymbol{x}. \tag{3.30}$$

To fully define these matrices for all α, we consider the additional projection equation (3.6b). When $\boldsymbol{v} = \boldsymbol{\varphi}_i$, we obtain

$$\frac{1}{N_E} \sum_{j=1}^{N_E} \Pi^\varepsilon \boldsymbol{\varphi}_i(\boldsymbol{x}_j) \cdot \boldsymbol{m}_\alpha(\boldsymbol{x}_j) = \frac{1}{N_E} \sum_{j=1}^{N_E} \boldsymbol{\varphi}_i(\boldsymbol{x}_j) \cdot \boldsymbol{m}_\alpha(\boldsymbol{x}_j).$$

As we have done previously, on expanding $\Pi^\varepsilon \boldsymbol{\varphi}_i$ with (3.27) leads to

$$\sum_{\beta=1}^{6} s_\beta^i \frac{1}{N_E} \sum_{j=1}^{N_E} \boldsymbol{m}_\beta(\boldsymbol{x}_j) \cdot \boldsymbol{m}_\alpha(\boldsymbol{x}_j) = \frac{1}{N_E} \sum_{j=1}^{N_E} \boldsymbol{\varphi}_i(\boldsymbol{x}_j) \cdot \boldsymbol{m}_\alpha(\boldsymbol{x}_j). \tag{3.31}$$

Now we can define the remaining $\alpha = 1, 2, 3$ terms of the matrices $\tilde{\boldsymbol{G}}$ and $\tilde{\boldsymbol{B}}$ as

$$\tilde{\boldsymbol{G}}_{\alpha\beta} = \frac{1}{N_E}\sum_{j=1}^{N_E} \boldsymbol{m}_\beta(\boldsymbol{x}_j) \cdot \boldsymbol{m}_\alpha(\boldsymbol{x}_j), \quad \tilde{\boldsymbol{B}}_{\alpha i} = \frac{1}{N_E}\sum_{j=1}^{N_E} \boldsymbol{\varphi}_i(\boldsymbol{x}_j) \cdot \boldsymbol{m}_\alpha(\boldsymbol{x}_j). \tag{3.32}$$

Combining the results, we obtain $\tilde{\boldsymbol{G}}$ for all $\beta = 1, 2, \dots, 6$:

$$\tilde{\boldsymbol{G}}_{\alpha\beta} = \begin{cases} \frac{1}{N_E}\sum_{j=1}^{N_E} \boldsymbol{m}_\beta(\boldsymbol{x}_j) \cdot \boldsymbol{m}_\alpha(\boldsymbol{x}_j) & (\alpha = 1, 2, 3) \\ \int_E (\boldsymbol{S}\boldsymbol{m}_\beta)^T (\boldsymbol{C}\boldsymbol{S}\boldsymbol{m}_\alpha) d\boldsymbol{x} & (\alpha = 4, 5, 6), \end{cases} \tag{3.33a}$$

and for all $i = 1, 2 \dots, 2N_E$, we have

$$\tilde{\boldsymbol{B}}_{\alpha i} = \begin{cases} \frac{1}{N_E}\sum_{j=1}^{N_E} \boldsymbol{\varphi}_i(\boldsymbol{x}_j) \cdot \boldsymbol{m}_\alpha(\boldsymbol{x}_j) & (\alpha = 1, 2, 3) \\ \int_E (\boldsymbol{S}\boldsymbol{\varphi}_i)^T (\boldsymbol{C}\boldsymbol{S}\boldsymbol{m}_\alpha) \, d\boldsymbol{x} & (\alpha = 4, 5, 6). \end{cases} \tag{3.33b}$$

After combining these equations, we can determine the coefficients for the projection as the solution of the system:

$$\tilde{\boldsymbol{G}}\boldsymbol{\Pi}_*^{\boldsymbol{\varepsilon}} = \tilde{\boldsymbol{B}}, \tag{3.34}$$

where $(\boldsymbol{\Pi}_*^{\boldsymbol{\varepsilon}})_{\beta i} = s_\beta^i$. We start by considering the matrix $\tilde{\boldsymbol{G}}$. For $\alpha = 1, 2, 3$, $\tilde{\boldsymbol{G}}$ is the sum of polynomials evaluated at the vertex points, which can be directly computed. For $\alpha = 4, 5, 6$, since the basis functions $\boldsymbol{m}_\alpha$ are linear, the matrix differential operator acting on $\boldsymbol{m}_\alpha$ will result in a constant vector. For a constant material matrix $\boldsymbol{C}$, the expression $(\boldsymbol{S}\boldsymbol{m}_\beta)^T (\boldsymbol{C}\boldsymbol{S}\boldsymbol{m}_\alpha)$ is a constant matrix. Therefore, we can write:

$$\tilde{\boldsymbol{G}}_{\alpha\beta} = (\boldsymbol{S}\boldsymbol{m}_\beta)^T (\boldsymbol{C}\boldsymbol{S}\boldsymbol{m}_\alpha)|E| \quad (\alpha = 4, 5, 6).$$

On using (3.33b) and simplifying, we can write $\tilde{\boldsymbol{B}}$ for $\alpha = 1, 2, 3$ as

$$\tilde{\boldsymbol{B}}_{\alpha i} = \begin{cases} \frac{1}{N_E}\sum_{j=1}^{N_E} \begin{pmatrix} \phi_i(\boldsymbol{x}_j) \\ 0 \end{pmatrix} \cdot \boldsymbol{m}_\alpha(\boldsymbol{x}_j) = \frac{1}{N_E} m_\alpha^1(\boldsymbol{x}_i) & (i = 1, 2, \dots, N_E) \\ \frac{1}{N_E}\sum_{j=1}^{N_E} \begin{pmatrix} 0 \\ \phi_i(\boldsymbol{x}_j) \end{pmatrix} \cdot \boldsymbol{m}_\alpha(\boldsymbol{x}_j) = \frac{1}{N_E} m_\alpha^2(\boldsymbol{x}_i) & (i = N_E + 1, N_E + 2, \dots, 2N_E), \end{cases}$$

where m_α^k is the k-th component of $\boldsymbol{m}_\alpha$. For $\alpha = 4, 5, 6$, we can apply the definition of the matrix differential operator and use the divergence theorem to write

$$\tilde{\boldsymbol{B}}_{\alpha i} = \int_E \left(\boldsymbol{S}\boldsymbol{\varphi}_i\right)^T \left(\boldsymbol{C}\boldsymbol{S}\boldsymbol{m}_\alpha\right) d\boldsymbol{x} = \left(\int_E \left(\boldsymbol{S}\boldsymbol{\varphi}_i\right)^T \, d\boldsymbol{x}\right) \boldsymbol{C}\boldsymbol{S}\boldsymbol{m}_\alpha = \sum_{j=1}^{N_E} \left(\int_{e_j} {\boldsymbol{\varphi}_i}^T \boldsymbol{N}_*^{\partial E} \, ds\right) \boldsymbol{C}\boldsymbol{S}\boldsymbol{m}_\alpha,$$

where e_j is the j-th edge of the element E and $\boldsymbol{N}_*^{\partial E}$ is the matrix of normal components given in (3.11b). On simplification, we obtain for $\alpha = 4, 5, 6$,

$$\tilde{\boldsymbol{B}}_{\alpha i} = \begin{cases} \Big(\int_{e_{i-1}} \begin{pmatrix} \phi_i n_1^{(i-1)} & 0 & \phi_i n_2^{(i-1)} \end{pmatrix} ds \\ \qquad + \int_{e_i} \begin{pmatrix} \phi_i n_1^{(i)} & 0 & \phi_i n_2^{(i)} \end{pmatrix} ds \Big) \boldsymbol{C}\boldsymbol{S}\boldsymbol{m}_\alpha & (i = 1, 2, \ldots, N_E) \\ \Big(\int_{e_{i-1}} \begin{pmatrix} 0 & \phi_i n_2^{(i-1)} & \phi_i n_1^{(i-1)} \end{pmatrix} ds \\ \qquad + \int_{e_i} \begin{pmatrix} 0 & \phi_i n_2^{(i)} & \phi_i n_1^{(i)} \end{pmatrix} ds \Big) \boldsymbol{C}\boldsymbol{S}\boldsymbol{m}_\alpha & (i = N_E + 1, N_E + 2, \ldots, 2N_E). \end{cases}$$

These are integrals of a linear function over a line segment, which are exactly computed using a two-point Gauss-Lobatto quadrature scheme.

3.3.2. Implementation of $\mathbf{L^2}$ projector.

Now that we have a computable form of the energy projection, we can construct the L^2 projection. From (3.14), we have

$$\int_E \left(\overline{\Pi_\ell^0 \boldsymbol{\varepsilon}(\boldsymbol{v}_h)}\right)^T \overline{\boldsymbol{\varepsilon}^p} \, d\boldsymbol{x} = \int_{\partial E} \boldsymbol{v}_h^T \boldsymbol{N}_*^{\partial E} \overline{\boldsymbol{\varepsilon}^p} \, ds + \int_E \boldsymbol{v}_h^T \boldsymbol{\partial} \overline{\boldsymbol{\varepsilon}^p} \, d\boldsymbol{x}. \tag{3.35}$$

On expanding $\boldsymbol{v}_h$ in terms of its basis in $\boldsymbol{V}_{1,\ell}^E$, we obtain $\boldsymbol{v}_h = \boldsymbol{N}^v \tilde{\boldsymbol{v}}_h$. We can also expand the symmetric function $\overline{\boldsymbol{\varepsilon}^p}$ in terms of the polynomial basis in $\mathbb{P}_\ell(E)^{2\times 2}_{\text{sym}}$ with $\overline{\boldsymbol{\varepsilon}^p} = \boldsymbol{N}^p \tilde{\boldsymbol{\varepsilon}}^p$. Following [6], we also define a matrix $\boldsymbol{\Pi}^m$ such that we can write the projected strain in terms of the polynomial basis in $\mathbb{P}_\ell(E)^{2\times 2}_{\text{sym}}$. In particular, we write

$$\overline{\Pi_\ell^0 \boldsymbol{\varepsilon}(\boldsymbol{v}_h)} = \boldsymbol{N}^p \boldsymbol{\Pi}^m \tilde{\boldsymbol{v}}_h,$$

Substituting these into (3.35), we obtain

$$\int_E \left(\boldsymbol{N}^p \boldsymbol{\Pi}^m \tilde{\boldsymbol{v}}_h\right)^T \boldsymbol{N}^p \tilde{\boldsymbol{\varepsilon}}^p \, d\boldsymbol{x} = \int_{\partial E} \left(\boldsymbol{N}^v \tilde{\boldsymbol{v}}_h\right)^T \boldsymbol{N}_*^{\partial E} \boldsymbol{N}^p \tilde{\boldsymbol{\varepsilon}}^p \, ds + \int_E \left(\boldsymbol{N}^v \tilde{\boldsymbol{v}}_h\right)^T \boldsymbol{\partial} \boldsymbol{N}^p \tilde{\boldsymbol{\varepsilon}}^p \, d\boldsymbol{x},$$

which on simplifying becomes

$$\int_E \tilde{\boldsymbol{v}}_h^T \left(\boldsymbol{\Pi}^m \boldsymbol{N}^p\right)^T \boldsymbol{N}^p \tilde{\boldsymbol{\varepsilon}}^p \, d\boldsymbol{x} = \int_{\partial E} \tilde{\boldsymbol{v}}_h^T (\boldsymbol{N}^v)^T \boldsymbol{N}_*^{\partial E} \boldsymbol{N}^p \tilde{\boldsymbol{\varepsilon}}^p \, ds + \int_E \tilde{\boldsymbol{v}}_h^T (\boldsymbol{N}^v)^T \boldsymbol{\partial} \boldsymbol{N}^p \tilde{\boldsymbol{\varepsilon}}^p \, d\boldsymbol{x}.$$

Since this is true for all $\tilde{\boldsymbol{v}}_h$ and $\tilde{\boldsymbol{\varepsilon}}^p$, we can rewrite the equation as:

$$(\tilde{\boldsymbol{\varepsilon}}^p)^T \left(\int_E (\boldsymbol{N}^p)^T \boldsymbol{N}^p d\boldsymbol{x}\right) \boldsymbol{\Pi}^m \tilde{\boldsymbol{v}}_h = (\tilde{\boldsymbol{\varepsilon}}^p)^T \left(\int_{\boldsymbol{\partial} E} \left(\boldsymbol{N}_*^{\partial E} \boldsymbol{N}^p\right)^T \boldsymbol{N}^v ds - \int_E (\boldsymbol{\partial} \boldsymbol{N}^p)^T \boldsymbol{N}^v d\boldsymbol{x}\right) \tilde{\boldsymbol{v}}_h.$$

So now we can solve for the projection matrix $\boldsymbol{\Pi}^m$ via

$$\boldsymbol{\Pi}^m = \boldsymbol{G}^{-\mathbf{1}} \boldsymbol{B}, \tag{3.36a}$$

where $\boldsymbol{G}$ and $\boldsymbol{B}$ are defined as

$$\boldsymbol{G} := \int_E (\boldsymbol{N}^p)^T \boldsymbol{N}^p \, d\boldsymbol{x}, \tag{3.36b}$$

$$\boldsymbol{B} := \int_{\partial E} \left(\boldsymbol{N}_*^{\partial E} \boldsymbol{N}^p\right)^T \boldsymbol{N}^v \, ds - \int_E (\boldsymbol{\partial} \boldsymbol{N}^p)^T \boldsymbol{N}^v \, d\boldsymbol{x}. \tag{3.36c}$$

We can explicitly construct the forms for $\boldsymbol{G}$ and $\boldsymbol{B}$. From (3.36b), we expand the integrand $(\boldsymbol{N}^p)^T \boldsymbol{N}^p$, where $\boldsymbol{N}^p$ is given by (3.2b). If we let $\boldsymbol{I}$ be the 3×3 identity matrix, we can write $\boldsymbol{N}^p$ as

$$\boldsymbol{N}^p := \begin{bmatrix} \boldsymbol{I} & \xi \boldsymbol{I} & \eta \boldsymbol{I} \dots \eta^\ell \boldsymbol{I} \end{bmatrix}$$

and the product $(\boldsymbol{N}^p)^T \boldsymbol{N}^p$ can be written in compact form as:

$$(\boldsymbol{N}^p)^T \boldsymbol{N}^p = \begin{bmatrix} \boldsymbol{I} & \xi \boldsymbol{I} & \eta \boldsymbol{I} & \dots & \eta^l \boldsymbol{I} \\ \xi \boldsymbol{I} & \xi^2 \boldsymbol{I} & \xi\eta \boldsymbol{I} & \dots & \xi\eta^\ell \boldsymbol{I} \\ \eta \boldsymbol{I} & \xi\eta \boldsymbol{I} & \ddots & \vdots & \\ \vdots & \vdots & \dots & & \\ \eta^\ell \boldsymbol{I} & \xi\eta^\ell \boldsymbol{I} & \eta^{\ell+1} \boldsymbol{I} & \dots & \eta^{2\ell} \boldsymbol{I} \end{bmatrix}.$$

Integrating each term of the matrix, we find that we only need to determine integrals of the form

$$\int_E \xi^r \eta^k \, d\boldsymbol{x} \quad \text{for } 0 \le r + k \le 2\ell,$$

which can be computed either by partitioning E into triangles and then adopting a Gauss quadrature rule on triangles or by using the schemes developed in [40, 41].

The construction of the $\boldsymbol{B}$ matrix reveals the major difference between the stabilization-free method and a standard VEM for plane elasticity. For the first term in (3.36c), we expand the integral over ∂E as the sum of integrals over edge e_i:

$$\int_{\partial E} \left(\boldsymbol{N}_*^{\partial E}\boldsymbol{N}^p\right)^T \boldsymbol{N}^v \, ds = \sum_{i=1} \int_{e_i} \left(\boldsymbol{N}_*^{\partial E}\boldsymbol{N}^p\right)^T \boldsymbol{N}^v|_{e_i} \, ds.$$

Now we examine $\boldsymbol{N}^v|_{e_i}$,

$$\boldsymbol{N}^v|_{e_i} = \begin{bmatrix} \phi_1 & \phi_2 & \dots & \phi_{N_E} & 0 & \dots & 0 & \\ 0 & 0 & \dots & 0 & \phi_1 & \phi_2 & \dots & \phi_{N_E} \end{bmatrix}\Bigg|_{e_i}.$$

By definition of the Lagrange property, each ϕ_i is only nonzero when evaluated at the i-th degree of freedom, therefore the only contributions along the edge e_i are from $\phi_i|_{e_i}$ and $\phi_{i+1}|_{e_i}$. As a consequence, $\boldsymbol{N}^v|_{e_i}$ has only four nonzero elements, namely

$$\boldsymbol{N}^v|_{e_i} = \begin{bmatrix} 0 & 0 & \dots & \phi_i|_{e_i} & \phi_{i+1}|_{e_i} & \dots & 0 & 0 & \dots & 0 \\ 0 & 0 & \dots & 0 & 0 & \dots & \phi_i|_{e_i} & \phi_{i+1}|_{e_i} & \dots & 0 \end{bmatrix}. \tag{3.37}$$

We note from (3.19) that ϕ_i and ϕ_{i+1} are linear functions along the edges so they can be represented exactly via a parametrization of e_i. We also note that the product $\boldsymbol{N}_*^{\partial E}\boldsymbol{N}^p$ is at most polynomials of degree ℓ, so that the terms of the form $(\boldsymbol{N}_*^{\partial E}\boldsymbol{N}^p)^T\boldsymbol{N}^v|_{e_i}$ are at most a polynomial of degree $\ell+1$. This suggests that if we parametrize e_i by $t \in [-1,1]$, we can use a one-dimensional Gauss quadrature rule to compute these integrals. In particular, let $r_i(t) : [-1,1] \to e_i$ be a parametrization of the i-th edge and let $\{\omega_1, \cdots, \omega_r\}$, $\{t_1, \cdots, t_r\}$ be the associated Gauss quadrature weights and nodes. Then, after simplifications we have

$$\int_{e_i} \left(\boldsymbol{N}_*^{\partial E}\boldsymbol{N}^p\right)^T \boldsymbol{N}^v|_{e_i} \, ds = \frac{|e_i|}{2}\int_{-1}^{1} \left(\boldsymbol{N}_*^{\partial E}\boldsymbol{N}^p\right)^T \boldsymbol{N}^v(r_i(t)) \, dt = \frac{|e_i|}{2}\sum_{j=1}^{r} \omega_j \left(\boldsymbol{N}_*^{\partial E}\boldsymbol{N}^p\right)^T \boldsymbol{N}^v(r_i(t_j)).$$

On examining the second term in (3.36c), we note that $\boldsymbol{\partial}$ is a matrix operator of first-order derivatives, and $\boldsymbol{N}^p$ is a matrix of polynomials of degree less than or equal to ℓ. This implies that the product $\boldsymbol{\partial N^p}$ is a matrix polynomial of degree at most $\ell - 1$. Then the product $(\boldsymbol{\partial N^p})^T\boldsymbol{N}^v$ contains terms of the form $\int_E \boldsymbol{p}_{\ell-1} \cdot \boldsymbol{\varphi}_j$. On applying the enhancing property of the space (3.19), we can replace these integrals with the integrals of the elliptic projection, that is

$$\int_E \boldsymbol{p}_{\ell-1} \cdot \boldsymbol{\varphi}_j \, d\boldsymbol{x} = \int_E \boldsymbol{p}_{\ell-1} \cdot \Pi^{\varepsilon} \boldsymbol{\varphi}_j \, d\boldsymbol{x},$$

which in matrix form can be written as

$$\int_E (\boldsymbol{\partial} \boldsymbol{N}^p)^T \boldsymbol{N}^v \, d\boldsymbol{x} = \int_E (\boldsymbol{\partial} \boldsymbol{N}^p)^T \Pi^{\varepsilon} \boldsymbol{N}^v \, d\boldsymbol{x}, \tag{3.38a}$$

where we have the natural definition

$$\Pi^{\varepsilon} \boldsymbol{N}^v := \begin{bmatrix} \Pi^{\varepsilon} \boldsymbol{\varphi}_1 & \Pi^{\varepsilon} \boldsymbol{\varphi}_2 & \ldots & \Pi^{\varepsilon} \boldsymbol{\varphi}_{2N_E} \end{bmatrix}. \tag{3.38b}$$

The integral in (3.38a) is computed using a cubature scheme. With these matrices, we can compute the L^2 projection $\overline{\Pi_\ell^0 \boldsymbol{\varepsilon}(\boldsymbol{v}_h)}$ using (3.36).

3.3.3. Element stiffness matrix and force vector. To construct the element stiffness, we first rewrite the bilinear form a_h^E in terms of the matrices that we have constructed:

$$\begin{aligned} a_h^E(\boldsymbol{u}_h, \boldsymbol{v}_h) &:= \int_E \left(\overline{\Pi_\ell^0 \boldsymbol{\varepsilon}(\boldsymbol{v}_h)} \right)^T \boldsymbol{C} \, \overline{\Pi_\ell^0 \boldsymbol{\varepsilon}(\boldsymbol{u}_h)} \, d\boldsymbol{x} \\ &= \int_E \left(\boldsymbol{N}^p \boldsymbol{\Pi}^m \tilde{\boldsymbol{v}}_h \right)^T \boldsymbol{C} \left(\boldsymbol{N}^p \boldsymbol{\Pi}^m \tilde{\boldsymbol{u}}_h \right) \, d\boldsymbol{x} \\ &= \tilde{\boldsymbol{v}}_h^T \left(\boldsymbol{\Pi}^m \right)^T \left(\int_E (\boldsymbol{N}^p)^T \boldsymbol{C} \boldsymbol{N}^p \, d\boldsymbol{x} \right) \boldsymbol{\Pi}^m \tilde{\boldsymbol{u}}_h. \end{aligned}$$

Then, define the element stiffness matrix $\boldsymbol{K}_E$ by

$$\boldsymbol{K}_E := (\boldsymbol{\Pi}^m)^T \left(\int_E (\boldsymbol{N}^p)^T \boldsymbol{C} \boldsymbol{N}^p \, d\boldsymbol{x} \right) \boldsymbol{\Pi}^m, \tag{3.39}$$

where $\boldsymbol{\Pi}^m$ is given in (3.36).

We construct the forcing term given in (3.25) as

$$\ell_h^E(\boldsymbol{v}_h) = \int_E \boldsymbol{v}_h^T \boldsymbol{b}_h \, d\boldsymbol{x} + \int_{\Gamma_t \cap \partial E} \boldsymbol{v}_h^T \bar{\boldsymbol{t}} \, ds,$$

which is rewritten in the form

$$\ell_h^E(\boldsymbol{v}_h) = (\tilde{\boldsymbol{v}}_h)^T \left(\int_E (\boldsymbol{N}^v)^T \boldsymbol{b}_h \, d\boldsymbol{x} + \int_{\Gamma_t \cap \partial E} (\boldsymbol{N}^v)^T \bar{\boldsymbol{t}} \, ds \right).$$

The element force vector is then defined as

$$\boldsymbol{f}_E := \int_E (\boldsymbol{N}^v)^T \boldsymbol{b}_h \, d\boldsymbol{x} + \int_{\Gamma_t \cap \partial E} (\boldsymbol{N}^v)^T \bar{\boldsymbol{t}} \, ds. \tag{3.40}$$

Since we are using a low-order scheme, we use the approximation

$$\int_E (\boldsymbol{N}^v)^T \boldsymbol{b}_h \, d\boldsymbol{x} \approx \overline{(\boldsymbol{N}^v)^T} \int_E \boldsymbol{b}_h \, d\boldsymbol{x} \approx |E| \overline{(\boldsymbol{N}^v)^T} \boldsymbol{b}(\boldsymbol{x}_E),$$

where $\overline{(\boldsymbol{N}^v)^T}$ is the matrix of average values of ϕ. Specifically, denoting the j-th vertex by $\boldsymbol{x}_j$, we define the average value as

$$\overline{\phi} = \frac{1}{N_E} \sum_{j=1}^{N_E} \phi(\boldsymbol{x}_j),$$

and let

$$\overline{\boldsymbol{N}^v} = \begin{bmatrix} \overline{\phi_1} & \overline{\phi_2} & \dots & \overline{\phi_{N_E}} & 0 & 0 & \dots & 0 \\ 0 & 0 & \dots & 0 & \overline{\phi_1} & \overline{\phi_2} & \dots & \overline{\phi_{N_E}} \end{bmatrix} = \begin{bmatrix} \frac{1}{N_E} & \frac{1}{N_E} & \dots & \frac{1}{N_E} & 0 & 0 & \dots & 0 \\ 0 & 0 & \dots & 0 & \frac{1}{N_E} & \frac{1}{N_E} & \dots & \frac{1}{N_E} \end{bmatrix}.$$

For constant tractions, we obtain a closed-form solution for the traction integral:

$$\left(\int_{\Gamma_t \cap \partial E} (\boldsymbol{N}^v)^T \, ds \right) \bar{\boldsymbol{t}} = \left(\sum_{e_j \in \partial E} \int_{e_j} (\boldsymbol{N}^v)^T |_{e_j} \, ds \right) \bar{\boldsymbol{t}}.$$

Now applying a similar argument as in (3.37), we can simplify this integral as

$$\int_{e_j} (\boldsymbol{N}^v)^T |_{e_j} \, ds = |e_j| \begin{bmatrix} 0 & 0 & \dots & \frac{1}{2} & \frac{1}{2} & \dots & 0 & 0 & \dots & 0 \\ 0 & 0 & \dots & 0 & 0 & \dots & \frac{1}{2} & \frac{1}{2} & \dots & 0 \end{bmatrix}.$$

3.4. Theoretical results

We examine the well-posedness of the discrete problem (3.22) and derive error estimates in the L^2 norm and energy seminorm. To simplify the analysis we resort to the study of the boundary-value problem with homogeneous Dirichlet boundary data. We expect the results can be extended to the inhomogeneous case.

3.4.1. Well-posedness of discrete problem.

The approach follows ideas from [19], and we start by showing that the energy seminorm is equivalent with the chosen norm for the space $\boldsymbol{V}_{1,\boldsymbol{\ell}}$, and use this norm to show that the bilinear form in (3.24) satisfies the properties of the Lax–Milgram theorem. We begin by first defining a candidate discrete norm operator:

Definition 3.4.1. *Let a_h be the bilinear form defined in (3.24), then define an operator $\|.\|_{\boldsymbol{\ell}}$: $\boldsymbol{V}_{1,\boldsymbol{\ell}} \to \mathbb{R}$ by*

$$\|\boldsymbol{u}\|_{\boldsymbol{\ell}} := (a_h(\boldsymbol{u},\boldsymbol{u}))^{\frac{1}{2}} = \left(\sum_E a_h^E(\boldsymbol{u},\boldsymbol{u})\right)^{\frac{1}{2}}. \tag{3.41}$$

For specific $\boldsymbol{\ell}$ values, this operator is a norm and is equivalent to the natural norm in the space $[H_0^1(\Omega)]^2$. The main difficulty is showing that the operator is positive definite, i.e., $\|\boldsymbol{u}\|_{\boldsymbol{\ell}} = 0 \implies \boldsymbol{u} = \boldsymbol{0}$. To this end, we introduce a theorem given in [19]:

Theorem 3.4.2. *Let E be any element in the space, and $\boldsymbol{u} \in \boldsymbol{V}_{1,\ell}^E$. Choose $\ell \in \mathbb{N}$ satisfying*

$$\frac{3}{2}(\ell+1)(\ell+2) - dim(\mathbb{P}_\ell^{ker}(E)) \geq 2N_E - 3,$$

or in general choose $\ell \in \mathbb{N}$ satisfying

$$N_E \leq 2\ell + 3,$$

then we have

$$\Pi_\ell^0 \boldsymbol{\varepsilon}(\boldsymbol{u}) = \boldsymbol{0} \implies \boldsymbol{\varepsilon}(\boldsymbol{u}) = \boldsymbol{0}. \tag{3.42}$$

To prove this theorem, we introduce the following lemma:

Lemma 3.4.2.1. *Let $\boldsymbol{u} \in \boldsymbol{V}_{1,\ell}^E$, with $\ell \geq 1$, then the following implication holds*

$$\Pi_\ell^0 \boldsymbol{\varepsilon}(\boldsymbol{u}) = \boldsymbol{0} \implies \boldsymbol{\varepsilon}(\Pi^\varepsilon \boldsymbol{u}) = \boldsymbol{0}. \tag{3.43}$$

Proof. Assume that $\Pi_\ell^0 \boldsymbol{\varepsilon}(\boldsymbol{u}) = \boldsymbol{0}$, then by definition of the L^2 projection, we have

$$(\boldsymbol{\varepsilon}(\boldsymbol{u}), \boldsymbol{\varepsilon}^p)_E = 0 \quad \forall \boldsymbol{\varepsilon}^p \in \mathbb{P}_\ell(E)^{2\times 2}_{\text{sym}}.$$

In particular, if we let $\boldsymbol{p} \in [\mathbb{P}_1(E)]^2$, then $\boldsymbol{\sigma}(\boldsymbol{p}) \in \mathbb{P}_0(E)^{2\times 2}_{\text{sym}} \subseteq \mathbb{P}_\ell(E)^{2\times 2}_{\text{sym}}$. So we have

$$(\boldsymbol{\varepsilon}(\boldsymbol{u}), \boldsymbol{\sigma}(\boldsymbol{p}))_E = 0 \quad \forall \boldsymbol{p} \in [\mathbb{P}_1(E)]^2.$$

Applying the definition of the energy projection $\Pi^{\varepsilon}\boldsymbol{u}$, we get

$$(\boldsymbol{\varepsilon}(\Pi^{\varepsilon}\boldsymbol{u}), \boldsymbol{\sigma}(\boldsymbol{p}))_E = 0.$$

Since this is true for any $\boldsymbol{p} \in [\mathbb{P}_1(E)]^2$, this results in

$$\boldsymbol{\varepsilon}(\Pi^{\varepsilon}\boldsymbol{u}) = \boldsymbol{0}. \qquad \square$$

In order to show that the defined operator is a norm we use an inf-sup type argument. To establish the results, we construct some additional spaces and operators. To motivate the constructions, we assume that the condition $\Pi^0_{\ell}\boldsymbol{\varepsilon}(\boldsymbol{u}) = \boldsymbol{0}$ holds. This implies that the following equality holds:

$$\int_E \Pi^0_{\ell}\boldsymbol{\varepsilon}(\boldsymbol{u}) : \boldsymbol{\varepsilon}^p \, d\boldsymbol{x} = 0 \quad \forall \boldsymbol{\varepsilon}^p \in \mathbb{P}_{\ell}(E)^{2\times 2}_{\text{sym}}.$$

Applying the definition of the L^2 projection in (3.8), we also obtain

$$\int_E \boldsymbol{\varepsilon}(\boldsymbol{u}) : \boldsymbol{\varepsilon}^p \, d\boldsymbol{x} = 0.$$

Using the divergence theorem, we can rewrite this equality as

$$\int_E \boldsymbol{\varepsilon}(\boldsymbol{u}) : \boldsymbol{\varepsilon}^p \, d\boldsymbol{x} = \int_{\partial E} \boldsymbol{u} \cdot (\boldsymbol{\varepsilon}^p \cdot \boldsymbol{n}) \, ds - \int_E \boldsymbol{u} \cdot (\nabla \cdot \boldsymbol{\varepsilon}^p) \, d\boldsymbol{x} = 0.$$

We note that $\nabla \cdot \boldsymbol{\varepsilon}^p \in [\mathbb{P}_{l-1}]^2 \subseteq [\mathbb{P}_{l+1}]^2$, and using the definition of the space $\boldsymbol{V}^E_{1,\ell}$, Lemma 3.4.2.1 and applying the divergence theorem, the second term becomes

$$\int_E \boldsymbol{u} \cdot (\nabla \cdot \boldsymbol{\varepsilon}^p) \, d\boldsymbol{x} = \int_E \Pi^{\varepsilon}\boldsymbol{u} \cdot \ (\nabla \cdot \boldsymbol{\varepsilon}^p) \, d\boldsymbol{x} = \int_{\partial E} \Pi^{\varepsilon}\boldsymbol{u} \cdot (\boldsymbol{\varepsilon}^p \cdot \boldsymbol{n}) \, ds.$$

This gives us the equality

$$\begin{aligned} 0 = \int_E \boldsymbol{\varepsilon}(\boldsymbol{u}) : \boldsymbol{\varepsilon}^p \, d\boldsymbol{x} &= \int_{\partial E} \boldsymbol{u} \cdot (\boldsymbol{\varepsilon^p \cdot n}) \, ds - \int_{\partial E} \Pi^{\varepsilon}\boldsymbol{u} \cdot (\boldsymbol{\varepsilon}^p \cdot \boldsymbol{n}) \, ds \\ &= \int_{\partial E} (\boldsymbol{u} - \Pi^{\varepsilon}\boldsymbol{u})|_{\partial E} \cdot (\boldsymbol{\varepsilon}^p \cdot \boldsymbol{n}) \, ds, \end{aligned} \tag{3.44}$$

where we use the notation $(\boldsymbol{u} - \Pi^{\varepsilon}\boldsymbol{u})|_{\partial E}$ to explicitly indicate that the function is evaluated on the boundary. This suggests that we study the operator of the form $\int_{\partial E} \boldsymbol{v} \cdot (\boldsymbol{Q} \cdot \boldsymbol{n}) \, ds$.

DEFINITION 3.4.3. *Define the bilinear operator* $b : R_Q(E) \times [\boldsymbol{V}]^2 \to \mathbb{R}$ *by [19]*

$$b(\boldsymbol{v}, \boldsymbol{Q}) = \int_{\partial E} \boldsymbol{v} \cdot (\boldsymbol{Q} \cdot \boldsymbol{n})\, ds, \tag{3.45}$$

where $\boldsymbol{v}$ *is defined over the boundary* ∂E*. The spaces* $R_Q(E)$ *and* $[\boldsymbol{V}]^2$ *are chosen later.*

In particular, we study the special case when $\boldsymbol{v} = (\boldsymbol{u} - \Pi^\varepsilon \boldsymbol{u})|_{\partial E}$. Since we are interested in all such functions $\boldsymbol{u} \in \boldsymbol{V}_{1,\ell}^E$, we study the space of all linear combination of the basis functions $(\boldsymbol{\varphi}_i - \Pi^\varepsilon \boldsymbol{\varphi}_i)|_{\partial E}$. This motivates the next definition:

DEFINITION 3.4.4. *Define the space* $Q(\partial E)$ *by*

$$Q(\partial E) := span\{(\boldsymbol{\varphi}_i - \Pi^\varepsilon \boldsymbol{\varphi}_i)|_{\partial E} : i = 1, 2 \ldots, 2N_E\}. \tag{3.46}$$

Now given a function on $Q(\partial E)$, we need to extend it to a function defined on the entire element E. One way to achieve this is to first triangulate the polygon E. Let $\tau \subseteq E$ be any triangular subelement. Denote τ_i as the triangle with vertices $\boldsymbol{x}_i, \boldsymbol{x}_{i+1}, \boldsymbol{x_c}$, for each $i = 1, 2, \ldots, N_E$, where $\boldsymbol{x}_c$ is the centroid of E. We denote the edge connecting the vertices $\boldsymbol{x}_i$ and $\boldsymbol{x}_c$ by e_i, and the unit outward normal as $\boldsymbol{n}^{e_i}$. With this triangulation, we extend $\boldsymbol{v}$ to be a function $\overline{\overline{\boldsymbol{v}}}$ on E by requiring that $\overline{\overline{\boldsymbol{v}}}$ agrees with $\boldsymbol{v}|_e$ over each edge e and $\overline{\overline{\boldsymbol{v}}}|_\tau \in [\mathbb{P}_1(\tau)]^2$ over every triangular element τ. To obtain a unique vector-valued function, we require that $\overline{\overline{\boldsymbol{v}}}(\boldsymbol{x}_c) = \boldsymbol{0}$. We use this to define the space $R_Q(E)$ of extended functions over the entire element E.

DEFINITION 3.4.5. *Define the space* $R_Q(E)$ *by*

$$R_Q(E) := \{\overline{\overline{\boldsymbol{v}}} : \overline{\overline{\boldsymbol{v}}}|_\tau \in [\mathbb{P}_1(\tau)]^2 \quad \forall \tau \subseteq E,\ \overline{\overline{\boldsymbol{v}}}|_{\partial E} \in Q(\partial E),\ \overline{\overline{\boldsymbol{v}}}(\boldsymbol{x_c}) = \boldsymbol{0}\}. \tag{3.47}$$

Using (3.45), we express (3.44) as

$$b(\boldsymbol{u} - \Pi^\varepsilon \boldsymbol{u}, \boldsymbol{\varepsilon}^p) = 0. \tag{3.48}$$

But the extended function $\overline{\overline{\boldsymbol{u} - \Pi^\varepsilon \boldsymbol{u}}}$ is equal to $\boldsymbol{u} - \Pi^\varepsilon \boldsymbol{u}$ over the boundary, so applying the expression to the extended function, we get

$$b(\overline{\overline{\boldsymbol{u} - \Pi^\varepsilon \boldsymbol{u}}}, \boldsymbol{\varepsilon}^p) = 0 \quad \forall \boldsymbol{\varepsilon}^p \in \mathbb{P}_\ell(E)^{2\times 2}_{\text{sym}}.$$

To show that $\boldsymbol{\varepsilon}(\boldsymbol{u}) = \boldsymbol{0}$, it is sufficient to establish that $\boldsymbol{u} = \Pi^{\varepsilon}\boldsymbol{u}$ is a rigid-body mode. This is equivalent to showing that

$$\|\boldsymbol{u} - \Pi^{\varepsilon}\boldsymbol{u}\| = 0$$

in some norm. From [19], it is sufficient to show an inf-sup condition:

$$\sup_{\boldsymbol{\varepsilon}^p \in \mathbb{P}_\ell(E)^{2\times 2}_{\text{sym}}} \frac{b(\boldsymbol{u} - \Pi^{\varepsilon}\boldsymbol{u}, \boldsymbol{\varepsilon}^p)}{\|\boldsymbol{\varepsilon}^p\|} \geq \beta \|\boldsymbol{u} - \Pi^{\varepsilon}\boldsymbol{u}\|. \tag{3.49}$$

To formalize this, we first construct a suitable space with a suitable norm.

Definition 3.4.6. *For every element E, let $\boldsymbol{H}^1_\tau(E)$ be the broken Sobolev space that is defined by*

$$\boldsymbol{H}^1_\tau(E) := \bigcup_\tau \boldsymbol{H}^1(\tau), \tag{3.50}$$

where $\boldsymbol{H}^1(\tau) = [H^1(\tau)]^2$ is the standard Sobolev space defined on a triangular subelement. On this space, equip the seminorm and norm:

$$|\boldsymbol{u}|^2_{\boldsymbol{H}^1_\tau(E)} := \sum_\tau \|\nabla \boldsymbol{u}\|^2_{\boldsymbol{L}^2(\tau)} + \sum_{i=1}^{N_E} \|[\![\boldsymbol{u}]\!]_{e_i}\|^2_{\boldsymbol{L}^2(e_i)}, \tag{3.51a}$$

$$\|\boldsymbol{u}\|^2_{\boldsymbol{H}^1_\tau(E)} := |\boldsymbol{u}|^2_{\boldsymbol{H}^1_\tau(E)} + \sum_\tau \|\boldsymbol{u}\|^2_{\boldsymbol{L}^2(\tau)}. \tag{3.51b}$$

Again, let $\gamma^{e_i}(.)$ be the trace of its argument on edge e_i. We then define $[\![.]\!]_{e_i} : \boldsymbol{H}^1_\tau \to \boldsymbol{L}^2(e_i)$ as the jump across the i-th edge of the triangulation, which is given by

$$[\![\boldsymbol{u}]\!]_{e_i} := \gamma^{e_i}(\boldsymbol{u}|_{\tau_i}) - \gamma^{e_i}(\boldsymbol{u}|_{\tau_{i-1}}).$$

We now define a space of functions with finite jumps across edges in the triangulation.

Definition 3.4.7. *Define the space $\boldsymbol{V} = \boldsymbol{V}(E) \subseteq \bigcup_\tau \boldsymbol{H}(div, \tau)$ by*

$$\boldsymbol{V}(E) := \left\{ \boldsymbol{v} \in \bigcup_\tau \boldsymbol{H}(div, \tau) : \|[\![\boldsymbol{v}]\!]_{e_i}\|_{\boldsymbol{L}^\infty(e_i)} < \infty \quad \forall e_i \right\}, \tag{3.52}$$

where $\boldsymbol{H}(div, \tau)$ is the space of functions that have finite divergence in the L^2 norm over a triangular subelement. On this space, define the seminorm and norm as

$$|\boldsymbol{v}|^2_{\boldsymbol{V}} := \sum_{\tau} \|\nabla \cdot \boldsymbol{v}\|^2_{\boldsymbol{L}^2(\tau)} + h_E^2 \|[\![\boldsymbol{v}]\!]_{I_E}\|^2_{\boldsymbol{L}^\infty(I_E)}, \tag{3.53a}$$

$$\|\boldsymbol{v}\|^2_{\boldsymbol{V}} := |\boldsymbol{v}|^2_{\boldsymbol{V}} + \sum_{\tau} \|\boldsymbol{v}\|^2_{\boldsymbol{L}^2(\tau)}, \tag{3.53b}$$

where

$$\|[\![\boldsymbol{v}]\!]_{I_E}\|^2_{\boldsymbol{L}^\infty(I_E)} = \max_i \|[\![\boldsymbol{v}]\!]_{e_i}\|^2_{\boldsymbol{L}^\infty(e_i)} \tag{3.53c}$$

is the maximum of the jumps over all edges in the triangulation.

Now we show that the bilinear operator defined in (3.45) is continuous on the newly defined spaces $R_Q(E) \times [\boldsymbol{V}]^2$.

Lemma 3.4.7.1. *Let b be the bilinear form defined in (3.45), then there exists a constant $C > 0$, such that*

$$|b(\boldsymbol{v}, \boldsymbol{Q})| \leq C \|\boldsymbol{v}\|_{\boldsymbol{H}^1_\tau(E)} \|\boldsymbol{Q}\|_{[\boldsymbol{V}]^2} \ \forall \boldsymbol{v} \in R_Q(E) \text{ and } \forall \boldsymbol{Q} \in [\boldsymbol{V}]^2. \tag{3.54}$$

Proof. By definition, we have

$$b(\boldsymbol{v}, \boldsymbol{Q}) = \int_{\partial E} \boldsymbol{v} \cdot (\boldsymbol{Q} \cdot \boldsymbol{n}) \, ds.$$

We partition each element E into a union of triangles $\{\tau_i\}$, and again letting $\{e_i\}$ denote the edge connecting the i-th vertex to the center, we rewrite the integral as

$$b(\boldsymbol{v}, \boldsymbol{Q}) = \sum_i \left[\int_{\partial \tau_i} \boldsymbol{v} \cdot (\boldsymbol{Q} \cdot \boldsymbol{n}) \, ds - \int_{e_i} \gamma^{e_i}(\boldsymbol{v}|_{\tau_i}) \cdot (\boldsymbol{Q}^{e_i}_{\tau_i} \cdot \boldsymbol{n}^{\tau_i}_{e_i}) \, ds \right.$$
$$\left. - \int_{e_i} \gamma^{e_i}(\boldsymbol{v}|_{\tau_{i-1}}) \cdot (\boldsymbol{Q}^{e_i}_{\tau_{i-1}} \cdot \boldsymbol{n}^{\tau_{i-1}}_{e_i}) \, ds \right].$$

We first note that by assumption $\boldsymbol{v} \in R_Q(E)$, which implies that $\boldsymbol{v}$ along the i-th edge is the same from either triangle. So we now have

$$\gamma^{e_i}(\boldsymbol{v}|_{\tau_i}) = \gamma^{e_i}(\boldsymbol{v}|_{\tau_{i-1}}).$$

In addition, since $\boldsymbol{n}_{e_i}^{\tau_i} = -\boldsymbol{n}_{e_i}^{\tau_{i-1}}$, we can rewrite $b(\boldsymbol{v}, \boldsymbol{Q})$ as

$$\begin{aligned} b(\boldsymbol{v}, \boldsymbol{Q}) &= \sum_i \int_{\partial\tau_i} \boldsymbol{v} \cdot (\boldsymbol{Q} \cdot \boldsymbol{n})\, ds - \int_{e_i} \gamma^{e_i}(\boldsymbol{v}|_{\tau_i}) \cdot (\boldsymbol{Q}_{\tau_i}^{e_i} - \boldsymbol{Q}_{\tau_{i-1}}^{e_i}) \cdot \boldsymbol{n}_{e_i}^{\tau_i}\, ds \\ &= \sum_i \int_{\partial\tau_i} \boldsymbol{v} \cdot (\boldsymbol{Q} \cdot \boldsymbol{n})\, ds - \int_{e_i} \gamma^{e_i}(\boldsymbol{v}|_{\tau_i}) \cdot ([\![\boldsymbol{Q}]\!]_{e_i} \cdot \boldsymbol{n}_{e_i}^{\tau_i})\, ds. \end{aligned} \tag{3.55}$$

For the first term in (3.55), we apply the divergence theorem to obtain

$$\int_{\partial\tau_i} \boldsymbol{v} \cdot (\boldsymbol{Q} \cdot \boldsymbol{n})\, ds = \int_{\tau_i} \nabla \cdot (\boldsymbol{v} \cdot \boldsymbol{Q})\, d\boldsymbol{x} = \int_{\tau_i} [\nabla \boldsymbol{v} : \boldsymbol{Q} + \boldsymbol{v} \cdot (\nabla \cdot \boldsymbol{Q})]\, d\boldsymbol{x}.$$

We now have

$$b(\boldsymbol{v}, \boldsymbol{Q}) = \sum_i \int_{\tau_i} [\nabla \boldsymbol{v} : \boldsymbol{Q} + \boldsymbol{v} \cdot (\nabla \cdot \boldsymbol{Q})]\, d\boldsymbol{x} - \int_{e_i} \gamma^{e_i}(\boldsymbol{v}|_{\tau_i}) \cdot ([\![\boldsymbol{Q}]\!]_{e_i} \cdot \boldsymbol{n}_{e_i}^{\tau_i})\, ds,$$

and can bound $|b(\boldsymbol{v}, \boldsymbol{Q}|$ in (3.55) as

$$|b(\boldsymbol{v}, \boldsymbol{Q})| \leq \underbrace{|\sum_i \int_{\tau_i} [\nabla \boldsymbol{v} : \boldsymbol{Q} + \boldsymbol{v} \cdot (\nabla \cdot \boldsymbol{Q})]\, d\boldsymbol{x}\,|}_{A} + \underbrace{|\sum_i \int_{e_i} \gamma^{e_i}(\boldsymbol{v}|_{\tau_i}) \cdot ([\![\boldsymbol{Q}]\!]_{e_i} \cdot \boldsymbol{n}_{e_i}^{\tau_i})\, ds|}_{B}. \tag{3.56}$$

We estimate each term in (3.56) separately. For term A in (3.56), we have

$$\begin{aligned} &|\sum_i \int_{\tau_i} [\nabla \boldsymbol{v} : \boldsymbol{Q} + \boldsymbol{v} \cdot (\nabla \cdot \boldsymbol{Q})]\, d\boldsymbol{x}| \leq \sum_i \Big[\|\nabla \boldsymbol{v}\|_{\boldsymbol{L}^2(\tau_i)} \|\boldsymbol{Q}\|_{\boldsymbol{L}^2(\tau_i)} + \|\boldsymbol{v}\|_{\boldsymbol{L}^2(\tau_i)} \|\nabla \cdot \boldsymbol{Q}\|_{\boldsymbol{L}^2(\tau_i)}\Big] \\ &\leq \sum_i \Big[\|\nabla \boldsymbol{v}\|_{\boldsymbol{L}^2(\tau_i)} \Big(\|\boldsymbol{Q}\|_{\boldsymbol{L}^2(\tau_i)} + \|\nabla \cdot \boldsymbol{Q}\|_{\boldsymbol{L}^2(\tau_i)}\Big) + \|\boldsymbol{v}\|_{\boldsymbol{L}^2(\tau_i)} \Big(\|\boldsymbol{Q}\|_{\boldsymbol{L}^2(\tau_i)} + \|\nabla \cdot \boldsymbol{Q}\|_{\boldsymbol{L}^2(\tau_i)}\Big)\Big] \\ &\leq C \sum_i \Big(\|\boldsymbol{v}\|_{\boldsymbol{L}^2(\tau_i)} + \|\nabla \boldsymbol{v}\|_{\boldsymbol{L}^2(\tau_i)}\Big)\Big(\|\boldsymbol{Q}\|_{\boldsymbol{L}^2(\tau_i)} + \|\nabla \cdot \boldsymbol{Q}\|_{\boldsymbol{L}^2(\tau_i)}\Big) \\ &\leq C \|\boldsymbol{v}\|_{\boldsymbol{H}^1_\tau} \sum_i \Big(\|\boldsymbol{Q}\|_{\boldsymbol{L}^2(\tau_i)} + \|\nabla \cdot \boldsymbol{Q}\|_{\boldsymbol{L}^2(\tau_i)}\Big). \end{aligned} \tag{3.57}$$

Now for term B in (3.56), we estimate

$$\sum_i |\int_{e_i} \gamma^{e_i}(\boldsymbol{v}|_{\tau_i}) \cdot ([\![\boldsymbol{Q}]\!]_{e_i} \cdot \boldsymbol{n}_{e_i}^{\tau_i})\, ds| \leq \sum_i \|\gamma^{e_i}(\boldsymbol{v}|_{\tau_i})\|_{\boldsymbol{L}^2(e_i)} \|[\![\boldsymbol{Q}]\!]_{e_i}\|_{\boldsymbol{L}^2(e_i)}.$$

Since $\boldsymbol{v} \in R_Q(E)$, it is linear on each of the edges e_i. It can be shown using a three-point Gauss-Lobatto quadrature scheme and equivalent norms, that

$$\|\gamma^{e_i}(\boldsymbol{v}|_{\tau_i})\|_{\boldsymbol{L}^2(e_i)} = \sqrt{\frac{|e_i|}{3}} |\boldsymbol{v}(\boldsymbol{x}_i)|.$$

We can also estimate that

$$\begin{aligned}\|[\![\boldsymbol{Q}]\!]_{e_i}\|_{\boldsymbol{L}^2(e_i)} &\leq \sqrt{|e_i|}\|[\![\boldsymbol{Q}]\!]_{e_i}\|_{\boldsymbol{L}^\infty(e_i)}\\ &\leq \sqrt{|e_i|}\|[\![\boldsymbol{Q}]\!]_{I_E}\|_{\boldsymbol{L}^\infty(I_E)}.\end{aligned}$$

Combining the two terms and using equivalent norms, we get

$$\begin{aligned}\sum_i \Big|\int_{e_i}\gamma^{e_i}(\boldsymbol{v}|_{\tau_i})\cdot([\![\boldsymbol{Q}]\!]_{e_i}\cdot\boldsymbol{n}_{e_i}^{\tau_i})\,ds\Big| &\leq \sum_i \frac{|e_i|}{\sqrt{3}}|\boldsymbol{v}(\boldsymbol{x}_i)|\|[\![\boldsymbol{Q}]\!]_{I_E}\|_{\boldsymbol{L}^\infty(I_E)}\\ &\leq Ch_E\|[\![\boldsymbol{Q}]\!]_{I_E}\|_{\boldsymbol{L}^\infty(I_E)}\|\boldsymbol{v}\|_{\boldsymbol{H}^1_\tau(E)}.\end{aligned} \tag{3.58}$$

Combining these two terms in (3.57) and (3.58), we find that

$$\begin{aligned}|b(\boldsymbol{v},\boldsymbol{Q})| &\leq C_1\|\boldsymbol{v}\|_{\boldsymbol{H}^1_\tau}\sum_i(\|\boldsymbol{Q}\|_{\boldsymbol{L}^2(\tau_i)}+\|\nabla\cdot\boldsymbol{Q}\|_{\boldsymbol{L}^2(\tau_i)})+C_2h_E\|\boldsymbol{v}\|_{\boldsymbol{H}^1_\tau(E)}\|[\![\boldsymbol{Q}]\!]_{I_E}\|_{\boldsymbol{L}^\infty(I_E)}\\ &\leq C\|\boldsymbol{v}\|_{\boldsymbol{H}^1_\tau(E)}\|\boldsymbol{Q}\|_{[\boldsymbol{V}]^2}.\end{aligned}$$

□

Using this bilinear form b and the specific norms, we formalize the inf-sup condition that is stated in (3.49).

PROPOSITION 3.4.1. *Let* $\boldsymbol{u}\in\boldsymbol{V}^E_{1,\ell}$ *and* b *as defined in* (3.45)*. If there exists a constant* $\beta>0$*, independent of* h_E*, such that*

$$\forall\boldsymbol{v}\in R_Q(E),\qquad \sup_{\boldsymbol{Q}\in\mathbb{P}_\ell(E)^{2\times 2}_{sym}}\frac{b(\boldsymbol{v},\boldsymbol{Q})}{\|\boldsymbol{Q}\|_{[\boldsymbol{V}]^2}}\geq\beta\|\boldsymbol{v}\|_{\boldsymbol{H}^1_\tau(E)}, \tag{3.59}$$

then

$$\Pi^0_\ell\boldsymbol{\varepsilon}(\boldsymbol{u})=\boldsymbol{0}\implies\boldsymbol{\varepsilon}(\boldsymbol{u})=\boldsymbol{0}.$$

PROOF. Assume that $\Pi^0_\ell\boldsymbol{\varepsilon}(\boldsymbol{u})=0$, then by (3.48), we have

$$b(\overline{\overline{\boldsymbol{u}-\Pi^\varepsilon\boldsymbol{u}}},\boldsymbol{\varepsilon}^p)=0.$$

Then by assumption

$$\beta\|\overline{\overline{\boldsymbol{u}-\Pi^\varepsilon\boldsymbol{u}}}\|_{\boldsymbol{H}^1_\tau(E)}=0,$$

which implies that

$$\overline{\overline{\boldsymbol{u} - \Pi^{\varepsilon}\boldsymbol{u}}} = \mathbf{0}.$$

Then we also have on the boundary,

$$\boldsymbol{u} - \Pi^{\varepsilon}\boldsymbol{u}|_{\partial E} = \mathbf{0}.$$

But for $\boldsymbol{u} \in \boldsymbol{V}_{1,\ell}^{E}$, this implies that $\boldsymbol{u} = \Pi^{\varepsilon}\boldsymbol{u}$. Then by Lemma (3.4.2.1), we get $\boldsymbol{\varepsilon}(\boldsymbol{u}) = \mathbf{0}$. $\square$

In order for the previous proposition to hold for any constant, we include a stronger result as proven in [19] for scalar equations. The proof of these results relies on the construction of a Fortin operator $\boldsymbol{\Pi}_E$, as shown for general cases in [28].

PROPOSITION 3.4.2. *Assume there exists an operator* $\boldsymbol{\Pi}_E : [\boldsymbol{V}]^2 \to [\mathbb{P}_l(E)]^{2\times 2}$ *satisfying [28]*

$$b(\boldsymbol{v}, \boldsymbol{\Pi}_E\boldsymbol{Q} - \boldsymbol{Q}) = 0 \quad \forall \boldsymbol{v} \in R_Q(E) \tag{3.60}$$

and assume there is some constant $C_\Pi > 0$*, independent of* h_E*, such that*

$$\|\boldsymbol{\Pi}_E\boldsymbol{Q}\|_{[\boldsymbol{V}]^2} \leq C_\Pi \|\boldsymbol{Q}\|_{[V]^2} \quad \forall \boldsymbol{Q} \in [\boldsymbol{V}]^2. \tag{3.61}$$

Assume further that there exists a $\eta > 0$*, independent of* h_E*, such that*

$$\inf_{\boldsymbol{v}\in R_Q(E)} \sup_{\boldsymbol{Q}\in[\boldsymbol{V}]^2} \frac{b(\boldsymbol{v}, \boldsymbol{Q})}{\|\boldsymbol{v}\|_{\boldsymbol{H}_\tau^1(E)} \|\boldsymbol{Q}\|_{[\boldsymbol{V}]^2}} \geq \eta. \tag{3.62}$$

Then the discrete inf-sup condition given in (3.59) *is satisfied.*

PROPOSITION 3.4.3. *Let* b *be defined by* (3.45)*, then the inf-sup condition given in* (3.62) *holds.*

For the proof of these propositions we refer the reader to Propositions 2 and 3 in [19], and for the explicit construction of the operator $\boldsymbol{\Pi}_E$, we also point to Proposition 4 in [19]. The construction methods appear to generalize directly to the vectorial case. We now show that the operator given in (3.41) satisfies the positive-definite property and is thus a norm.

PROPOSITION 3.4.4. *For any* $\boldsymbol{u} \in \boldsymbol{V}_{1,\boldsymbol{\ell}}$*, with* $\ell(E) \in \mathbb{N}$ *satisfying* (3.15) *for all elements* E*,*

$$\|\boldsymbol{u}\|_{\boldsymbol{\ell}} = 0 \implies \boldsymbol{u} = \mathbf{0}, \tag{3.63}$$

where the norm $\|.\|_{\boldsymbol{\ell}}$ *is defined in* (3.41)*.*

PROOF. Let $\boldsymbol{u} \in \boldsymbol{V}_{1,\boldsymbol{\ell}}$ and assume $\|\boldsymbol{u}\|_{\boldsymbol{\ell}}^2 = 0$. This implies that

$$\sum_E \int_E \Pi_\ell^0 \boldsymbol{\varepsilon}(\boldsymbol{u}) : \mathbb{C} : \Pi_\ell^0 \boldsymbol{\varepsilon}(\boldsymbol{u})\, d\boldsymbol{x} = 0.$$

Assuming $\mathbb{C}$ is a positive-definite material tensor, we must have

$$\Pi_\ell^0 \boldsymbol{\varepsilon}(\boldsymbol{u}) = \boldsymbol{0}.$$

Since ℓ satisfies (3.15), we know by Theorem 3.4.2 that $\boldsymbol{\varepsilon}(\boldsymbol{u}) = \boldsymbol{0}$ for each E. This implies that $\boldsymbol{u}$ is a rigid-body mode. But due to homogeneous boundary conditions, no nonzero rigid-body modes are present, and therefore $\boldsymbol{u} = \boldsymbol{0}$. ☐

We also have that under the condition (3.15), that the norm (3.41) is equivalent to the standard norm in $\boldsymbol{H}_0^1$.

LEMMA 3.4.7.2. *For all* $\boldsymbol{u} \in \boldsymbol{V}_{1,\boldsymbol{\ell}}$*, there exists a* $C_1 > 0$ *such that*

$$\|\boldsymbol{u}\|_{\boldsymbol{\ell}} \leq C_1 \|\boldsymbol{u}\|_{\boldsymbol{H}_0^1(\Omega)}, \tag{3.64a}$$

and if for every element E*,* $\ell(E)$ *satisfies* (3.15)*, there also exists a constant* $C_2 > 0$ *such that*

$$\|\boldsymbol{u}\|_{\boldsymbol{\ell}} \geq C_2 \|\boldsymbol{u}\|_{\boldsymbol{H}_0^1(\Omega)}. \tag{3.64b}$$

PROOF. We first estimate

$$\begin{aligned}
\|\boldsymbol{u}\|_{\boldsymbol{\ell}}^2 &= \sum_E \int_E \Pi_\ell^0 \boldsymbol{\varepsilon}(\boldsymbol{u}) : \mathbb{C} : \Pi_\ell^0 \boldsymbol{\varepsilon}(\boldsymbol{u})\, d\boldsymbol{x} \\
&= \sum_E \int_E \boldsymbol{\varepsilon}(\boldsymbol{u}) : \mathbb{C} : \Pi_\ell^0 \boldsymbol{\varepsilon}(\boldsymbol{u})\, d\boldsymbol{x} \\
&\leq \sum_E \|\boldsymbol{\varepsilon}(\boldsymbol{u})\|_{\boldsymbol{L}^2(E)} \|\mathbb{C} : \Pi_\ell^0 \boldsymbol{\varepsilon}(\boldsymbol{u})\|_{\boldsymbol{L}^2(E)} \\
&\leq C \|\boldsymbol{\varepsilon}(\boldsymbol{u})\|_{\boldsymbol{L}^2(\Omega)} \|\boldsymbol{\varepsilon}(\boldsymbol{u})\|_{\boldsymbol{L}^2(\Omega)} \\
&\leq C_1 \|\boldsymbol{u}\|_{\boldsymbol{H}_0^1(\Omega)} \|\boldsymbol{u}\|_{\boldsymbol{H}_0^1(\Omega)} \\
&\leq C_1 \|\boldsymbol{u}\|_{\boldsymbol{H}_0^1(\Omega)}^2.
\end{aligned}$$

Now if we have ℓ that satisfies (3.15) for all E , then $\|.\|_{\boldsymbol{\ell}}$ is also a norm. Since both $\|.\|_{\boldsymbol{\ell}}$ and $\|.\|_{\boldsymbol{H}_0^1}$ are norms in the finite-dimensional subspace $\boldsymbol{V}_{1,\boldsymbol{\ell}}$, they are equivalent. In particular, there exists a constant $C_2 > 0$ such that

$$\|\boldsymbol{u}\|_{\boldsymbol{\ell}} \geq C_2 \|\boldsymbol{u}\|_{\boldsymbol{H}_0^1(\Omega)}. \qquad \square$$

We now show that the discrete bilinear form a_h is continuous and coercive, which by the Lax–Milgram theorem implies that a unique solution exists.

THEOREM 3.4.8. *If $\ell(E)$ satisfies (3.15) for each E, then there exist constants $C_1, C_2 > 0$ such that the bilinear form defined in (3.24) satisfies the inequalities*

$$|a_h(\boldsymbol{u}, \boldsymbol{v})| \leq C_1 \|\boldsymbol{u}\|_{\boldsymbol{H}_0^1(\Omega)} \|\boldsymbol{v}\|_{\boldsymbol{H}_0^1(\Omega)} \tag{3.65a}$$

and

$$a_h(\boldsymbol{v}, \boldsymbol{v}) \geq C_2 \|\boldsymbol{v}\|^2_{\boldsymbol{H}_0^1(\Omega)}. \tag{3.65b}$$

PROOF. We estimate the first inequality:

$$\begin{aligned} |a_h(\boldsymbol{u}, \boldsymbol{v})| &= \sum_E \int_E \Pi^0_\ell \boldsymbol{\varepsilon}(\boldsymbol{u}) : \mathbb{C} : \Pi^0_\ell \boldsymbol{\varepsilon}(\boldsymbol{v}) \, d\boldsymbol{x} \\ &\leq C \sum_E \|\Pi^0_\ell \boldsymbol{\varepsilon}(\boldsymbol{u})\|_{\boldsymbol{L}^2(E)} \|\Pi^0_\ell \boldsymbol{\varepsilon}(\boldsymbol{v})\|_{\boldsymbol{L}^2(E)} \\ &\leq C \|\boldsymbol{u}\|_{\boldsymbol{H}_0^1(\Omega)} \|\boldsymbol{v}\|_{\boldsymbol{H}_0^1(\Omega)}. \end{aligned}$$

For the second inequality, on using the definition of the bilinear form a_h and Lemma 3.4.7.2, we have

$$a_h(\boldsymbol{v}, \boldsymbol{v}) = \|\boldsymbol{v}\|^2_{\boldsymbol{\ell}} \geq C \|\boldsymbol{v}\|^2_{\boldsymbol{H}_0^1(\Omega)}. \qquad \square$$

3.4.2. Error estimates. Now that we have well-posedness of the discrete problem, we study the errors of the approximation. In particular, we consider the errors in the $\boldsymbol{L}^2$ and $\boldsymbol{H}_0^1$ norms. Many of the techniques and estimates are detailed in [26,27,28,42]. We introduce lemmas adapted from [19] that we expect can be extended to our specific case. We first define an interpolation function $\boldsymbol{u}_I : \boldsymbol{H}^2(\Omega) \to \boldsymbol{V}_{1,\boldsymbol{\ell}}$ by

$$\boldsymbol{u}_I = \sum_i \mathtt{dof}_i(\boldsymbol{u})\boldsymbol{\xi}_i, \tag{3.66}$$

where $\mathtt{dof}_i(\boldsymbol{u})$ is the i-th degree of freedom of $\boldsymbol{u}$ and $\boldsymbol{\xi}_i$ is a global basis function satisfying $\mathtt{dof}_j(\boldsymbol{\xi}_i) = \delta_{ij}$.

Lemma 3.4.8.1. *Let $\boldsymbol{w}$ be any sufficiently smooth function, and let $\boldsymbol{w}_I \in \boldsymbol{V}_{1,\boldsymbol{\ell}}$ be the associated interpolation function (3.66). Then the following inequality holds for some constant $C > 0$ and all $h > 0$:*

$$\|\boldsymbol{w} - \boldsymbol{w}_I\|_{\boldsymbol{L}^2(\Omega)} + h\|\boldsymbol{w} - \boldsymbol{w}_I\|_{\boldsymbol{H}_0^1(\Omega)} \leq Ch^2|\boldsymbol{w}|_{\boldsymbol{H}^2(\Omega)}. \tag{3.67}$$

Lemma 3.4.8.2. *For any sufficiently smooth function $\boldsymbol{w}$, there exist constants C_1, $C_2 > 0$ such that*

$$\|\Pi_\ell^0\boldsymbol{\varepsilon}(\boldsymbol{w}) - \boldsymbol{\varepsilon}(\boldsymbol{w})\|_{\boldsymbol{L}^2(\Omega)} \leq C_1h|\boldsymbol{w}|_{\boldsymbol{H}^2(\Omega)}, \tag{3.68a}$$

$$\|\Pi_0^0\boldsymbol{w} - \boldsymbol{w}\|_{\boldsymbol{L}^2(\Omega)} \leq C_2h\|\boldsymbol{w}\|_{\boldsymbol{H}_0^1(\Omega)}, \tag{3.68b}$$

where we denote $\Pi_0^0\boldsymbol{w}$ as the L^2 projection of $\boldsymbol{w}$ onto the space of constants.

Now we consider the error in $\boldsymbol{H}_0^1$.

Proposition 3.4.5. *Let $\boldsymbol{u}$ be the exact solution to the strong problem in (2.112), and $\boldsymbol{b}$ the associated body force. For h sufficiently small, there exists a constant $C > 0$ such that the error of the solution $\boldsymbol{u}_h$ to the discrete weak problem is bounded in the $\boldsymbol{H}_0^1$ norm by*

$$\|\boldsymbol{u} - \boldsymbol{u}_h\|_{\boldsymbol{H}_0^1(\Omega)} \leq Ch\left(|\boldsymbol{u}|_{\boldsymbol{H}^2(\Omega)} + \|\boldsymbol{b}\|_{\boldsymbol{L}^2(\Omega)}\right). \tag{3.69}$$

Proof. Let $\boldsymbol{u}_h$ be the unique solution to the discrete problem (3.22), $\boldsymbol{u}$ the exact solution to (2.112) and $\boldsymbol{u}_I$ the associated interpolation function (3.66). We can then estimate the error as:

$$\|\boldsymbol{u} - \boldsymbol{u}_h\|_{\boldsymbol{H}_0^1(\Omega)} \leq \|\boldsymbol{u} - \boldsymbol{u}_I\|_{\boldsymbol{H}_0^1(\Omega)} + \|\boldsymbol{u}_I - \boldsymbol{u}_h\|_{\boldsymbol{H}_0^1(\Omega)}. \tag{3.70}$$

For the first term, we apply (3.67) to get the bound

$$\|\boldsymbol{u}-\boldsymbol{u}_I\|_{\boldsymbol{H}_0^1(\Omega)} \leq Ch|\boldsymbol{u}|_{\boldsymbol{H}^2(\Omega)}. \tag{3.71}$$

For the second term, we have the estimate

$$\begin{aligned}
C\|\boldsymbol{u}_I-\boldsymbol{u}_h\|^2_{\boldsymbol{H}_0^1(\Omega)} &\leq \|\boldsymbol{u}_I-\boldsymbol{u}_h\|^2_\ell = a_h(\boldsymbol{u}_I-\boldsymbol{u}_h,\boldsymbol{u}_I-\boldsymbol{u}_h)\\
&\leq -a_h(\boldsymbol{u}_h,\boldsymbol{u}_I-\boldsymbol{u}_h)+a_h(\boldsymbol{u}_I,\boldsymbol{u}_I-\boldsymbol{u}_h)\\
&\leq -(\boldsymbol{b}_h,\boldsymbol{u}_I-\boldsymbol{u}_h)+a_h(\boldsymbol{u}_I,\boldsymbol{u}_I-\boldsymbol{u}_h)\\
&\leq -(\boldsymbol{b}_h,\boldsymbol{u}_I-\boldsymbol{u}_h)+a_h(\boldsymbol{u}_I-\boldsymbol{u}+\boldsymbol{u},\boldsymbol{u}_I-\boldsymbol{u}_h)\\
&\leq \underbrace{(-\boldsymbol{b}_h,\boldsymbol{u}_I-\boldsymbol{u}_h)}_{A}+\underbrace{a_h(\boldsymbol{u}_I-\boldsymbol{u},\boldsymbol{u}_I-\boldsymbol{u}_h)}_{B}+\underbrace{a_h(\boldsymbol{u},\boldsymbol{u}_I-\boldsymbol{u}_h)}_{C}.
\end{aligned} \tag{3.72}$$

We estimate each of the three terms. For term B in (3.72), we use Cauchy–Schwarz and (3.67) to estimate

$$\begin{aligned}
a_h(\boldsymbol{u}_I-\boldsymbol{u},\boldsymbol{u}_I-\boldsymbol{u}_h) &= \sum_E \int_E \Pi_\ell^0\boldsymbol{\varepsilon}(\boldsymbol{u}_I-\boldsymbol{u}) : \mathbb{C} : \Pi_\ell^0\boldsymbol{\varepsilon}(\boldsymbol{u}_I-\boldsymbol{u}_h)\,d\boldsymbol{x}\\
&\leq C\sum_E \|\Pi_\ell^0\boldsymbol{\varepsilon}(\boldsymbol{u}_I-\boldsymbol{u})\|_{\boldsymbol{L}^2(E)}\|\Pi_\ell^0\boldsymbol{\varepsilon}(\boldsymbol{u}_I-\boldsymbol{u}_h)\|_{\boldsymbol{L}^2(E)}\\
&\leq C\|\Pi_\ell^0\boldsymbol{\varepsilon}(\boldsymbol{u}_I-\boldsymbol{u})\|_{\boldsymbol{L}^2(\Omega)}\|\Pi_\ell^0\boldsymbol{\varepsilon}(\boldsymbol{u}_I-\boldsymbol{u}_h)\|_{\boldsymbol{L}^2(\Omega)}\\
&\leq C\|\boldsymbol{u}_I-\boldsymbol{u}\|_{\boldsymbol{H}_0^1(\Omega)}\|\boldsymbol{u}_I-\boldsymbol{u}_h\|_{\boldsymbol{H}_0^1(\Omega)}\\
&\leq Ch|\boldsymbol{u}|_{\boldsymbol{H}^2(\Omega)}\|\boldsymbol{u}_I-\boldsymbol{u}_h\|_{\boldsymbol{H}_0^1(\Omega)}
\end{aligned}$$

For term C in (3.72), we write

$$\begin{aligned}
a_h(\boldsymbol{u}, \boldsymbol{u}_I - \boldsymbol{u}_h) &= \sum_E \int_E \Pi_\ell^0 \boldsymbol{\varepsilon}(\boldsymbol{u}) : \mathbb{C} : \Pi_\ell^0 \boldsymbol{\varepsilon}(\boldsymbol{u}_I - \boldsymbol{u}_h)\, d\boldsymbol{x} \\
&= \sum_E \int_E \Pi_\ell^0 \boldsymbol{\varepsilon}(\boldsymbol{u}) : \mathbb{C} : \boldsymbol{\varepsilon}(\boldsymbol{u}_I - \boldsymbol{u}_h)\, d\boldsymbol{x} \\
&= \sum_E \int_E [(\Pi_\ell^0 \boldsymbol{\varepsilon}(\boldsymbol{u}) - \boldsymbol{\varepsilon}(\boldsymbol{u}) + \boldsymbol{\varepsilon}(\boldsymbol{u})) : \mathbb{C} : \boldsymbol{\varepsilon}(\boldsymbol{u}_I - \boldsymbol{u}_h)]\, d\boldsymbol{x} \\
&= \sum_E \int_E (\Pi_\ell^0 \boldsymbol{\varepsilon}(\boldsymbol{u}) - \boldsymbol{\varepsilon}(\boldsymbol{u})) : \mathbb{C} : \boldsymbol{\varepsilon}(\boldsymbol{u}_I - \boldsymbol{u}_h)\, d\boldsymbol{x} \\
&\quad + \sum_E \int_E \boldsymbol{\varepsilon}(\boldsymbol{u}) : \mathbb{C} : \boldsymbol{\varepsilon}(\boldsymbol{u}_I - \boldsymbol{u}_h)\, d\boldsymbol{x}.
\end{aligned}$$

Then applying the definition of the bilinear form (2.113) and using Cauchy–Schwarz inequality, we write

$$\begin{aligned}
a_h(\boldsymbol{u}, \boldsymbol{u}_I - \boldsymbol{u}_h) &= \sum_E \Big[\int_E (\Pi_\ell^0 \boldsymbol{\varepsilon}(\boldsymbol{u}) - \boldsymbol{\varepsilon}(\boldsymbol{u})) : \mathbb{C} : \boldsymbol{\varepsilon}(\boldsymbol{u}_I - \boldsymbol{u}_h)\, d\boldsymbol{x} \Big] + a(\boldsymbol{u}, \boldsymbol{u}_I - \boldsymbol{u}_h) \\
&= \sum_E \Big[\int_E (\Pi_\ell^0 \boldsymbol{\varepsilon}(\boldsymbol{u}) - \boldsymbol{\varepsilon}(\boldsymbol{u})) : \mathbb{C} : \boldsymbol{\varepsilon}(\boldsymbol{u}_I - \boldsymbol{u}_h)\, d\boldsymbol{x} \Big] + (\boldsymbol{b}, \boldsymbol{u}_I - \boldsymbol{u}_h) \\
&\leq Ch |\boldsymbol{u}|_{\boldsymbol{H}^2(\Omega)} \|\boldsymbol{u}_I - \boldsymbol{u}_h\|_{\boldsymbol{H}_0^1(\Omega)} + (\boldsymbol{b}, \boldsymbol{u}_I - \boldsymbol{u}_h).
\end{aligned}$$

Combining the three terms, we have

$$C\|\boldsymbol{u}_I - \boldsymbol{u}_h\|^2_{\boldsymbol{H}_0^1(\Omega)} \leq (\boldsymbol{b} - \boldsymbol{b}_h, \boldsymbol{u}_I - \boldsymbol{u}_h) + C_1 h |\boldsymbol{u}|_{\boldsymbol{H}^2(\Omega)} \|\boldsymbol{u}_I - \boldsymbol{u}_h\|_{\boldsymbol{H}_0^1(\Omega)}.$$

To estimate the term $(\boldsymbol{b}-\boldsymbol{b}_h, \boldsymbol{u}_I-\boldsymbol{u}_h)$, it is sufficient to take $\boldsymbol{b}_h = \Pi_0^0\boldsymbol{b}$ as the L^2 projection onto constants.

$$\begin{aligned}
(\boldsymbol{b}-\boldsymbol{b}_h, \boldsymbol{u}_I-\boldsymbol{u}_h) &= (\boldsymbol{b}-\Pi_0^0\boldsymbol{b}, \boldsymbol{u}_I-\boldsymbol{u}_h)\\
&= \sum_E \int_E (\boldsymbol{b}-\Pi_0^0\boldsymbol{b})\cdot(\boldsymbol{u}_I-\boldsymbol{u}_h)\,d\boldsymbol{x}\\
&= \sum_E \Big[\int_E \boldsymbol{b}\cdot(\boldsymbol{u}_I-\boldsymbol{u}_h)\,d\boldsymbol{x} - \int_E \Pi_0^0\boldsymbol{b}\cdot(\boldsymbol{u}_I-\boldsymbol{u}_h)\,d\boldsymbol{x}\Big]\\
&= \sum_E \Big[\int_E \boldsymbol{b}\cdot(\boldsymbol{u}_I-\boldsymbol{u}_h)\,d\boldsymbol{x} - \int_E \boldsymbol{b}\cdot\Pi_0^0(\boldsymbol{u}_I-\boldsymbol{u}_h)\,d\boldsymbol{x}\Big]\\
&= \sum_E \int_E \boldsymbol{b}\cdot\big[(\boldsymbol{u}_I-\boldsymbol{u}_h)-\Pi_0^0(\boldsymbol{u}_I-\boldsymbol{u}_h)\big]\,d\boldsymbol{x}\\
&\le \sum_E \|\boldsymbol{b}\|_{\boldsymbol{L}^2(E)}\|(\boldsymbol{u}_I-\boldsymbol{u}_h)-\Pi_0^0(\boldsymbol{u}_I-\boldsymbol{u}_h))\|_{\boldsymbol{L}^2(E)}\\
&\le C_1 h\|\boldsymbol{b}\|_{\boldsymbol{L}^2(\Omega)}\|\boldsymbol{u}_I-\boldsymbol{u}_h\|_{\boldsymbol{H}_0^1(\Omega)}.
\end{aligned}$$

On combining the terms, we obtain

$$C\|\boldsymbol{u}_I-\boldsymbol{u}_h\|^2_{\boldsymbol{H}_0^1(\Omega)} \le C_1 h(\|\boldsymbol{b}\|_{\boldsymbol{L}^2(\Omega)} + |\boldsymbol{u}|_{\boldsymbol{H}^2(\Omega)})\|\boldsymbol{u}_I-\boldsymbol{u}_h\|_{\boldsymbol{H}_0^1(\Omega)}.$$

Now we have the estimate of the $\boldsymbol{H}_0^1$ error as

$$\begin{aligned}
\|\boldsymbol{u}-\boldsymbol{u}_h\|_{\boldsymbol{H}_0^1(\Omega)} &\le C_1 h|\boldsymbol{u}|_{\boldsymbol{H}^2(\Omega)} + C_2 h(\|\boldsymbol{b}\|_{\boldsymbol{L}^2(\Omega)} + |\boldsymbol{u}|_{\boldsymbol{H}^2(\Omega)})\\
&\le Ch(\|\boldsymbol{b}\|_{\boldsymbol{L}^2(\Omega)} + |\boldsymbol{u}|_{\boldsymbol{H}^2(\Omega)}).
\end{aligned}$$

□

With the error in $\boldsymbol{H}_0^1$, we can also find an error estimate for the $\boldsymbol{L}^2$ norm.

PROPOSITION 3.4.6. *Let $\boldsymbol{u}$ be the exact solution to the strong problem (2.112), and $\boldsymbol{b}$ the associated body force. For h sufficiently small, there exists a constant $C > 0$ such that the error of the solution $\boldsymbol{u}_h$ to the discrete weak problem is bounded in the $\boldsymbol{L}^2$ norm by*

$$\|\boldsymbol{u}-\boldsymbol{u}_h\|_{\boldsymbol{L}^2(\Omega)} \le Ch^2\left(|\boldsymbol{u}|_{\boldsymbol{H}^2(\Omega)} + \|\boldsymbol{b}\|_{\boldsymbol{H}^1(\Omega)}\right). \tag{3.73}$$

Proof. First, let $\boldsymbol{\psi}$ be a solution to the auxiliary problem: find $\boldsymbol{\psi} \in \boldsymbol{H}^2 \cap \boldsymbol{H}_0^1$ such that

$$a(\boldsymbol{\psi}, \boldsymbol{v}) = (\boldsymbol{u} - \boldsymbol{u}_h, \boldsymbol{v}) \quad \forall \boldsymbol{v} \in \boldsymbol{H}_0^1. \tag{3.74}$$

Then $\boldsymbol{\psi}$ can be shown to satisfy the following inequalities [11]:

$$|\boldsymbol{\psi}|_{\boldsymbol{H}^2(\Omega)} \leq C_1 \|\boldsymbol{u} - \boldsymbol{u}_h\|_{\boldsymbol{L}^2(\Omega)}, \tag{3.75a}$$

$$\|\boldsymbol{\psi}\|_{\boldsymbol{H}_0^1(\Omega)} \leq C_2 \|\boldsymbol{u} - \boldsymbol{u}_h\|_{\boldsymbol{L}^2(\Omega)}. \tag{3.75b}$$

We estimate

$$\begin{aligned}
\|\boldsymbol{u} - \boldsymbol{u}_h\|_{\boldsymbol{L}^2}^2 &= (\boldsymbol{u} - \boldsymbol{u}_h, \boldsymbol{u} - \boldsymbol{u}_h) \\
&= a(\boldsymbol{\psi}, \boldsymbol{u} - \boldsymbol{u}_h) \\
&= a(\boldsymbol{\psi} - \boldsymbol{\psi}_I + \boldsymbol{\psi}_I, \boldsymbol{u} - \boldsymbol{u}_h) \\
&= a(\boldsymbol{\psi} - \boldsymbol{\psi}_I, \boldsymbol{u} - \boldsymbol{u}_h) + a(\boldsymbol{\psi}_I, \boldsymbol{u} - \boldsymbol{u}_h),
\end{aligned}$$

where $\boldsymbol{\psi}_I$ is the interpolation of $\boldsymbol{\psi}$. We now estimate each of the terms separately. For the second term, we write

$$\begin{aligned}
a(\boldsymbol{\psi}_I, \boldsymbol{u} - \boldsymbol{u}_h) &= a(\boldsymbol{\psi}_I, \boldsymbol{u}) - a(\boldsymbol{\psi}_I, \boldsymbol{u}_h) \\
&= a(\boldsymbol{\psi}_I, \boldsymbol{u}) - a_h(\boldsymbol{\psi}_I, \boldsymbol{u}_h) + a_h(\boldsymbol{\psi}_I, \boldsymbol{u}_h) - a(\boldsymbol{\psi}_I, \boldsymbol{u}_h) \\
&= (\boldsymbol{b}, \boldsymbol{\psi}_I) - (\boldsymbol{b}_h, \boldsymbol{\psi}_I) + a_h(\boldsymbol{\psi}_I, \boldsymbol{u}_h) - a(\boldsymbol{\psi}_I, \boldsymbol{u}_h) \\
&= (\boldsymbol{b} - \boldsymbol{b}_h, \boldsymbol{\psi}_I) + \big(a_h(\boldsymbol{\psi}_I, \boldsymbol{u}_h) - a(\boldsymbol{\psi}_I, \boldsymbol{u}_h)\big).
\end{aligned}$$

Then we have

$$\|\boldsymbol{u} - \boldsymbol{u}_h\|_{\boldsymbol{L}^2}^2 = \underbrace{a(\boldsymbol{\psi} - \boldsymbol{\psi}_I, \boldsymbol{u} - \boldsymbol{u}_h)}_{A} + \underbrace{(\boldsymbol{b} - \boldsymbol{b}_h, \boldsymbol{\psi}_I)}_{B} + \underbrace{\big(a_h(\boldsymbol{\psi}_I, \boldsymbol{u}_h) - a(\boldsymbol{\psi}_I, \boldsymbol{u}_h)\big)}_{C}. \tag{3.76}$$

We estimate each of the terms separately using Cauchy–Schwarz, (3.67), (3.68b), and (3.69). For term A in (3.76), we estimate

$$\begin{aligned} a(\boldsymbol{\psi} - \boldsymbol{\psi}_I, \boldsymbol{u} - \boldsymbol{u}_h) &\leq \|\boldsymbol{\psi} - \boldsymbol{\psi}_I\|_{\boldsymbol{H}_0^1(\Omega)} \|\boldsymbol{u} - \boldsymbol{u}_h\|_{\boldsymbol{H}_0^1(\Omega)} \\ &\leq Ch\|\boldsymbol{u} - \boldsymbol{u}_h\|_{\boldsymbol{H}_0^1(\Omega)} |\psi|_{\boldsymbol{H}^2(\Omega)} \\ &\leq Ch\|\boldsymbol{u} - \boldsymbol{u}_h\|_{\boldsymbol{H}_0^1(\Omega)} \|\boldsymbol{u} - \boldsymbol{u}_h\|_{\boldsymbol{L}^2(\Omega)} \\ &\leq Ch^2\|\boldsymbol{u} - \boldsymbol{u}_h\|_{\boldsymbol{L}^2(\Omega)} (|\boldsymbol{u}|_{\boldsymbol{H}^2(\Omega)} + \|\boldsymbol{b}\|_{\boldsymbol{L}^2(\Omega)}). \end{aligned} \tag{3.77}$$

For term B in (3.76), we compute

$$\begin{aligned} (\boldsymbol{b} - \boldsymbol{b}_h, \boldsymbol{\psi}_I) &= (\boldsymbol{b} - \Pi_0^0 \boldsymbol{b}, \boldsymbol{\psi}_I) \\ &= (\boldsymbol{b} - \Pi_0^0 \boldsymbol{b}, \boldsymbol{\psi}_I - \boldsymbol{\psi} + \boldsymbol{\psi}) \\ &= (\boldsymbol{b} - \Pi_0^0 \boldsymbol{b}, \boldsymbol{\psi}_I - \boldsymbol{\psi}) + (\boldsymbol{b} - \Pi_0^0 \boldsymbol{b}, \boldsymbol{\psi}) \\ &= (\boldsymbol{b} - \Pi_0^0 \boldsymbol{b}, \boldsymbol{\psi}_I - \boldsymbol{\psi}) + (\boldsymbol{b} - \Pi_0^0 \boldsymbol{b}, \boldsymbol{\psi} - \Pi_0^0 \boldsymbol{\psi}) + (\boldsymbol{b} - \Pi_0^0 \boldsymbol{b}, \Pi_0^0 \boldsymbol{\psi}). \end{aligned}$$

But by definition of $\Pi_0^0 \boldsymbol{b}$, we have $(\boldsymbol{b} - \Pi_0^0 \boldsymbol{b}, \Pi_0^0 \boldsymbol{\psi}) = 0$, and hence

$$\begin{aligned} (\boldsymbol{b} - \boldsymbol{b}_h, \boldsymbol{\psi}_I) &= (\boldsymbol{b} - \Pi_0^0 \boldsymbol{b}, \boldsymbol{\psi}_I - \boldsymbol{\psi}) + (\boldsymbol{b} - \Pi_0^0 \boldsymbol{b}, \boldsymbol{\psi} - \Pi_0^0 \boldsymbol{\psi}) \\ &\leq \|\boldsymbol{b} - \Pi_0^0 \boldsymbol{b}\|_{\boldsymbol{L}^2(\Omega)} \|\boldsymbol{\psi}_I - \boldsymbol{\psi}\|_{\boldsymbol{L}^2(\Omega)} + \|\boldsymbol{b} - \Pi_0^0 \boldsymbol{b}\|_{\boldsymbol{L}^2(\Omega)} \|\boldsymbol{\psi} - \Pi_0^0 \boldsymbol{\psi}\|_{\boldsymbol{L}^2(\Omega)} \\ &\leq \|\boldsymbol{b} - \Pi_0^0 \boldsymbol{b}\|_{\boldsymbol{L}^2(\Omega)} (\|\boldsymbol{\psi}_I - \boldsymbol{\psi}\|_{\boldsymbol{L}^2(\Omega)} + \|\boldsymbol{\psi} - \Pi_0^0 \boldsymbol{\psi}\|_{\boldsymbol{L}^2(\Omega)}) \\ &\leq C_1 h \|\boldsymbol{b}\|_{\boldsymbol{H}_0^1(\Omega)} (C_2 h^2 |\boldsymbol{\psi}|_{\boldsymbol{H}^2(\Omega)} + C_3 h \|\boldsymbol{\psi}\|_{\boldsymbol{H}_0^1(\Omega)}) \\ &\leq Ch^2 \|\boldsymbol{b}\|_{\boldsymbol{H}_0^1(\Omega)} \|\boldsymbol{u} - \boldsymbol{u}_h\|_{\boldsymbol{L}^2(\Omega)}. \end{aligned} \tag{3.78}$$

For term C in (3.76), we first apply the definition of the L^2 projection to rewrite it as:

$$\begin{aligned} a_h(\boldsymbol{\psi}_I, \boldsymbol{u}_h) - a(\boldsymbol{\psi}_I, \boldsymbol{u}_h) &= \sum_E \int_E \left[\Pi_\ell^0 \boldsymbol{\varepsilon}(\boldsymbol{\psi}_I) : \mathbb{C} : \Pi_\ell^0 \boldsymbol{\varepsilon}(\boldsymbol{u}_h) - \boldsymbol{\varepsilon}(\boldsymbol{\psi}_I) : \mathbb{C} : \boldsymbol{\varepsilon}(\boldsymbol{u}_h)\right] d\boldsymbol{x} \\ &= \sum_E \int_E \left[\boldsymbol{\varepsilon}(\boldsymbol{\psi}_I) : \mathbb{C} : \Pi_\ell^0 \boldsymbol{\varepsilon}(\boldsymbol{u}_h) - \boldsymbol{\varepsilon}(\boldsymbol{\psi}_I) : \mathbb{C} : \boldsymbol{\varepsilon}(\boldsymbol{u}_h)\right] d\boldsymbol{x} \\ &= \sum_E \int_E \boldsymbol{\varepsilon}(\boldsymbol{\psi}_I) : \mathbb{C} : (\Pi_\ell^0 \boldsymbol{\varepsilon}(\boldsymbol{u}_h) - \boldsymbol{\varepsilon}(\boldsymbol{u}_h))\, d\boldsymbol{x}. \end{aligned}$$

Now, add and subtract $\Pi_\ell^0\boldsymbol{\varepsilon}(\boldsymbol{\psi}_I)$ and apply the definition of $\Pi_\ell^0\boldsymbol{\varepsilon}(\boldsymbol{u}_h)$ to simplify:

$$\begin{aligned} a_h(\boldsymbol{\psi}_I, \boldsymbol{u}_h) - a(\boldsymbol{\psi}_I, \boldsymbol{u}_h) &= \sum_E \bigg[\int_E (\boldsymbol{\varepsilon}(\boldsymbol{\psi}_I) - \Pi_\ell^0\boldsymbol{\varepsilon}(\boldsymbol{\psi}_I)) : \mathbb{C} : (\Pi_\ell^0\boldsymbol{\varepsilon}(\boldsymbol{u}_h) - \boldsymbol{\varepsilon}(\boldsymbol{u}_h))\, d\boldsymbol{x} \\ &\qquad + \int_E \Pi_\ell^0\boldsymbol{\varepsilon}(\boldsymbol{\psi}_I) : \mathbb{C} : (\Pi_\ell^0\boldsymbol{\varepsilon}(\boldsymbol{u}_h) - \boldsymbol{\varepsilon}(\boldsymbol{u}_h))\, d\boldsymbol{x} \bigg] \\ &= \sum_E \int_E (\boldsymbol{\varepsilon}(\boldsymbol{\psi}_I) - \Pi_\ell^0\boldsymbol{\varepsilon}(\boldsymbol{\psi}_I)) : \mathbb{C} : (\Pi_\ell^0\boldsymbol{\varepsilon}(\boldsymbol{u}_h) - \boldsymbol{\varepsilon}(\boldsymbol{u}_h))\, d\boldsymbol{x}. \end{aligned}$$

Adding and subtracting terms $\Pi_\ell^0\boldsymbol{\varepsilon}(\boldsymbol{u})$ and $\boldsymbol{\varepsilon}(\boldsymbol{u})$, we obtain

$$\begin{aligned} &\sum_E \int_E (\boldsymbol{\varepsilon}(\boldsymbol{\psi}_I) - \Pi_\ell^0\boldsymbol{\varepsilon}(\boldsymbol{\psi}_I)) : \mathbb{C} : (\Pi_\ell^0\boldsymbol{\varepsilon}(\boldsymbol{u}_h) - \boldsymbol{\varepsilon}(\boldsymbol{u}_h))\, d\boldsymbol{x} \\ &= \sum_E \bigg[\underbrace{\int_E (\boldsymbol{\varepsilon}(\boldsymbol{\psi}_I) - \Pi_\ell^0\boldsymbol{\varepsilon}(\boldsymbol{\psi}_I)) : \mathbb{C} : (\Pi_\ell^0\boldsymbol{\varepsilon}(\boldsymbol{u}_h) - \Pi_\ell^0\boldsymbol{\varepsilon}(\boldsymbol{u}))\, d\boldsymbol{x}}_{D} \\ &\qquad + \underbrace{\int_E (\boldsymbol{\varepsilon}(\boldsymbol{\psi}_I) - \Pi_\ell^0\boldsymbol{\varepsilon}(\boldsymbol{\psi}_I)) : \mathbb{C} : (\Pi_\ell^0\boldsymbol{\varepsilon}(\boldsymbol{u}) - \boldsymbol{\varepsilon}(\boldsymbol{u}))\, d\boldsymbol{x}}_{E} \\ &\qquad + \underbrace{\int_E (\boldsymbol{\varepsilon}(\boldsymbol{\psi}_I) - \Pi_\ell^0\boldsymbol{\varepsilon}(\boldsymbol{\psi}_I)) : \mathbb{C} : (\boldsymbol{\varepsilon}(\boldsymbol{u}) - \boldsymbol{\varepsilon}(\boldsymbol{u}_h))\, d\boldsymbol{x}}_{F} \bigg]. \end{aligned}$$

We estimate the three terms separately. For term D, we apply the Cauchy–Schwarz inequality and a standard estimate of the L^2 projection to write

$$\begin{aligned} &\sum_E \int_E (\boldsymbol{\varepsilon}(\boldsymbol{\psi}_I) - \Pi_\ell^0\boldsymbol{\varepsilon}(\boldsymbol{\psi}_I)) : \mathbb{C} : (\Pi_\ell^0\boldsymbol{\varepsilon}(\boldsymbol{u}_h) - \Pi_\ell^0\boldsymbol{\varepsilon}(\boldsymbol{u}))\, d\boldsymbol{x} \\ &\qquad \leq C_1 \|\boldsymbol{\varepsilon}(\boldsymbol{\psi}_I) - \Pi_\ell^0\boldsymbol{\varepsilon}(\boldsymbol{\psi}_I)\|_{\boldsymbol{L}^2(\Omega)} \|\boldsymbol{u} - \boldsymbol{u}_h\|_{\boldsymbol{H}_0^1(\Omega)}. \end{aligned} \tag{3.79}$$

For term E, we again apply Cauchy–Schwarz and (3.68a) to write

$$\begin{aligned} &\sum_E \int_E (\boldsymbol{\varepsilon}(\boldsymbol{\psi}_I) - \Pi_\ell^0\boldsymbol{\varepsilon}(\boldsymbol{\psi}_I)) : \mathbb{C} : (\Pi_\ell^0\boldsymbol{\varepsilon}(\boldsymbol{u}) - \boldsymbol{\varepsilon}(\boldsymbol{u}))\, d\boldsymbol{x} \\ &\qquad \leq C_2 h \|\boldsymbol{\varepsilon}(\boldsymbol{\psi}_I) - \Pi_\ell^0\boldsymbol{\varepsilon}(\boldsymbol{\psi}_I)\|_{\boldsymbol{L}^2(\Omega)} |\boldsymbol{u}|_{\boldsymbol{H}^2(\Omega)}. \end{aligned} \tag{3.80}$$

Similarly for term F, we estimate

$$\begin{aligned}&\sum_E \int_E (\boldsymbol{\varepsilon}(\boldsymbol{\psi}_I) - \Pi_\ell^0 \boldsymbol{\varepsilon}(\boldsymbol{\psi}_I)) : \mathbb{C} : (\boldsymbol{\varepsilon}(\boldsymbol{u}) - \boldsymbol{\varepsilon}(\boldsymbol{u}_h))\, d\boldsymbol{x} \\ &\qquad \leq C_3 \|\boldsymbol{\varepsilon}(\boldsymbol{\psi}_I) - \Pi_\ell^0 \boldsymbol{\varepsilon}(\boldsymbol{\psi}_I)\|_{\boldsymbol{L}^2(\Omega)} \|\boldsymbol{u} - \boldsymbol{u}_h\|_{\boldsymbol{H}_0^1(\Omega)}.\end{aligned} \tag{3.81}$$

Now combining (3.79), (3.80), (3.81) and using (3.68a) and (3.75a), we obtain the estimate

$$a_h(\boldsymbol{\psi}_I, \boldsymbol{u}_h) - a(\boldsymbol{\psi}_I, \boldsymbol{u}_h) \leq Ch^2 \|\boldsymbol{u} - \boldsymbol{u}_h\|_{\boldsymbol{L}^2(\Omega)} (|\boldsymbol{u}|_{\boldsymbol{H}^2(\Omega)} + \|\boldsymbol{b}\|_{\boldsymbol{L}^2(\Omega)}). \tag{3.82}$$

Combining all the necessary terms from (3.77), (3.78), (3.82), the estimate becomes

$$\begin{aligned}\|\boldsymbol{u} - \boldsymbol{u}_h\|_{\boldsymbol{L}^2(\Omega)} &\leq Ch^2 (|\boldsymbol{u}|_{\boldsymbol{H}^2(\Omega)} + \|\boldsymbol{b}\|_{\boldsymbol{L}^2(\Omega)} + \|\boldsymbol{b}\|_{\boldsymbol{H}_0^1(\Omega)}) \\ &\leq Ch^2 (|\boldsymbol{u}|_{\boldsymbol{H}^2(\Omega)} + \|\boldsymbol{b}\|_{\boldsymbol{H}^1(\Omega)}).\end{aligned} \qquad \square$$

3.5. Numerical results for SF-VEM

We present a series of numerical examples showing the application of the method to well-known benchmark problems in plane elasticity. We examine the errors using the L^∞ and L^2 norms, as well as the energy seminorm, and compare the convergence rates of the method with the theoretical estimates. In particular, we use the following discrete measures:

$$\|\boldsymbol{u} - \boldsymbol{u}_h\|_{\boldsymbol{L}^\infty(\Omega)} = \max_{\boldsymbol{x}_i \in \Omega} |\boldsymbol{u}(\boldsymbol{x}_i) - \boldsymbol{u}_h(\boldsymbol{x}_i)|, \tag{3.83a}$$

$$\|\boldsymbol{u} - \boldsymbol{u}_h\|_{\boldsymbol{L}^2(\Omega)} = \sqrt{\sum_E \int_E |\boldsymbol{u} - \Pi^\varepsilon \boldsymbol{u}_h|^2 \, d\boldsymbol{x}}, \tag{3.83b}$$

$$\|\boldsymbol{u} - \boldsymbol{u}_h\|_a = \sqrt{\sum_E \int_E (\overline{\boldsymbol{\varepsilon}} - \overline{\Pi_\ell^0 \boldsymbol{\varepsilon}(\boldsymbol{u}_h)})^T \boldsymbol{C} (\overline{\boldsymbol{\varepsilon}} - \overline{\Pi_\ell^0 \boldsymbol{\varepsilon}(\boldsymbol{u}_h)}) \, d\boldsymbol{x}}. \tag{3.83c}$$

In order to compute the integrals in (3.83), we adopt the scaled boundary cubature scheme [41]. In the SBC method, an integral over a general polygonal element E is written as the sum of integrals over triangles that are mapped onto the unit square. Let f be any scalar function and $\boldsymbol{c}_i(t)$ be the parametric representation of the edge e_i. Define ℓ_i to be the signed distance from a fixed point $\boldsymbol{x}_0$ to the line containing e_i and $|e_i|$ denote the length of the i-th edge. On using the scaled-boundary parametrization, $\boldsymbol{x} = \boldsymbol{\varphi}_i(\xi, t) = \boldsymbol{x}_0 + \xi(\boldsymbol{c}_i(t) - \boldsymbol{x}_0)$, the integral of f over E can be expressed as [41]:

$$\int_E f \, d\boldsymbol{x} = \sum_{i=1}^{N_E} \ell_i |e_i| \int_0^1 \int_0^1 \xi f\big(\boldsymbol{\varphi}_i(\xi, t)\big) \, d\xi dt, \tag{3.84}$$

where in the computations we set $\boldsymbol{x}_0$ to be a vertex of the polygon. To compute the integral over the unit square in (3.84), we use a tensor-product Gauss quadrature rule.

3.5.1. Patch test. The displacement patch test is widely used to test the polynomial consistency of a finite element method. In this test, an exact polynomial displacement field is imposed along the boundary of the domain Ω. If a method is consistent, it will exactly reproduce the exact solution up to machine precision (and small numerical rounding). For the first-order stabilization-free VEM, the displacement field is approximated by the energy projection onto linear (affine) polynomials; therefore, it should reproduce any affine displacement field.

Let $\Omega = (0, 1)^2$, and we impose an affine displacement field on the boundary:

$$u(\boldsymbol{x}) = x \quad \text{and} \quad v(\boldsymbol{x}) = x + y \quad \text{on } \partial\Omega.$$

The exact solution is the extension of the boundary conditions onto the entire domain Ω. We assess the accuracy of the numerical solution for three different types of meshes with 16 elements in each case. The first is a uniform square mesh, the second is a random Voronoi mesh, and the third is a Voronoi mesh that is obtained after applying three Lloyd iterations (see Figure 3.1). The results are listed in Table 3.1, which show that near machine-precision accuracy is realized. This indicates that the method passes the linear displacement patch test.

Mesh type	L^∞ error	L^2 error	Energy error
Uniform	3×10^{-16}	2×10^{-16}	1×10^{-15}
Random	2×10^{-13}	5×10^{-14}	9×10^{-13}
Lloyd iterated	3×10^{-14}	8×10^{-15}	2×10^{-13}

TABLE 3.1. Errors in the patch test on different types of meshes.

3.5.2. Eigenvalue analysis. Consider the closed domain (unit square), $\overline{\Omega} = [0, 1]^2$, which is discretized using nine quadrilateral elements. We are interested in the validity of the bounds in (3.15). To this end, we solve the element-eigenvalue problem, $\boldsymbol{K}_E \boldsymbol{d}_E = \lambda \boldsymbol{d}_E$, to assess the physical and nonphysical (spurious) modes of the element. Each element has three rigid-body

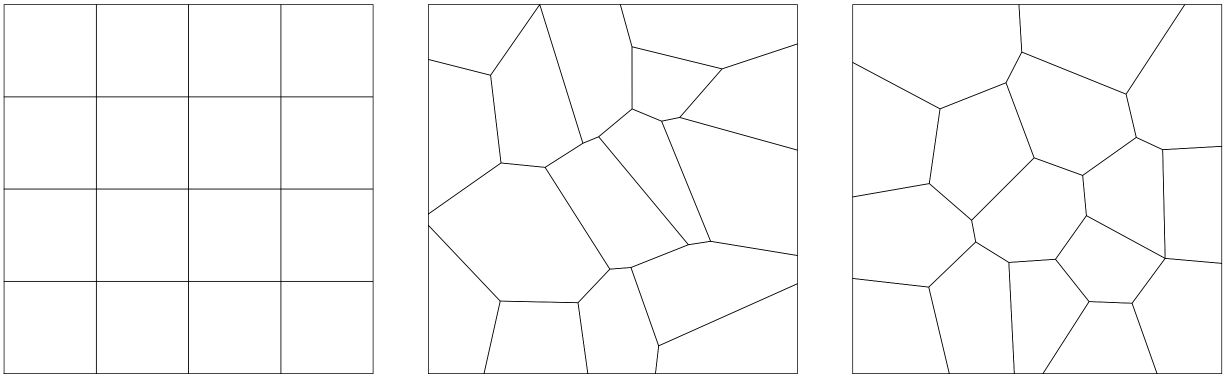
(a) Uniform mesh (b) Random mesh (c) Lloyd iterated

FIGURE 3.1. Sample meshes used for the patch test.

(zero-energy) modes that each correspond to a vanishing eigenvalue ($\lambda = 0$). For a stable element, all other eigenvalues must be positive and bounded away from zero. We choose $\ell = 0, 1, 2, 3$ and measure the maximum number of spurious eigenvalues of the element stiffness matrix as we artificially increase the number of nodes of the central element. For a well-posed discrete problem, the number of spurious eigenvalues should remain at zero. We show a few sample meshes in Figure 3.2. In Figure 3.3, the resulting number of spurious eigenvalues as a function of the number of nodes of an element are plotted for $\ell = 0, 1, 2, 3$.

We find that for $\ell = 0$, any polygon that is not a triangle ($N_E \geq 4$) has spurious modes, whereas for $\ell = 1$, an element with $N_E \geq 6$ has spurious modes. For $\ell = 2$ and $\ell = 3$, spurious eigenvalues appear for $N_E \geq 9$ and $N_E \geq 11$ in the central quadrilateral element, respectively. This shows that (3.17) is sufficient but not strictly required to ensure that the element stiffness matrix has the correct rank and is devoid of nonphysical zero-energy modes.

To further test the bound in (3.17), we examine the eigenvalues of the element stiffness matrix over a series of regular polygons (A. Russo, personal communication, April 2022). A few sample regular polygons are shown in Figure 3.4. In Figure 3.5, we plot the number of spurious eigenvalues as a function of the number of nodes of a regular polygon. We again find that $\ell = 0$ has spurious modes for all regular polygons $N_E \geq 4$, and for $\ell = 1$, regular polygons with $N_E \geq 5$ have spurious modes. For $\ell = 2$ and $\ell = 3$, there are additional eigenvalues that appear for $N_E \geq 7$ and $N_E \geq 9$, respectively. This shows that the inequality in (3.17) is strict for regular polygons.

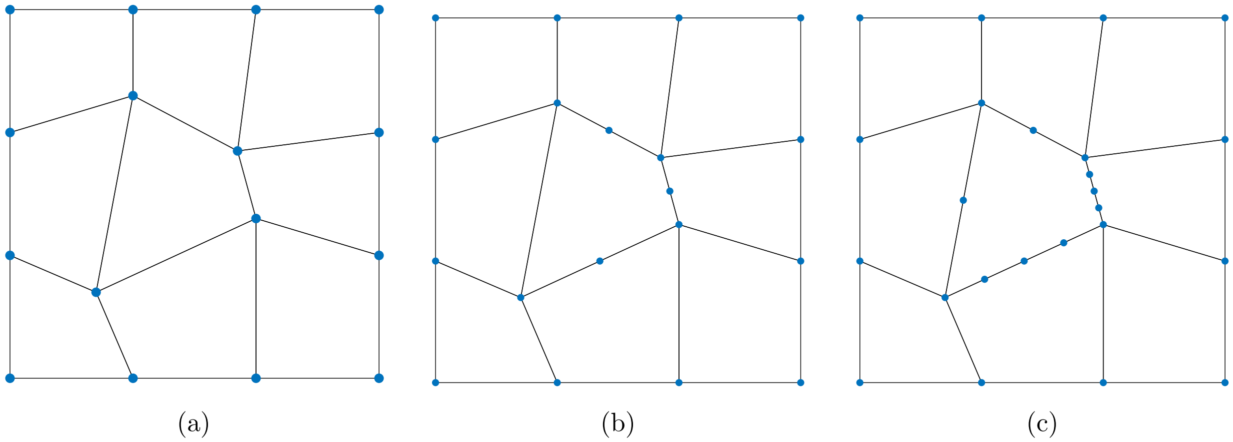

(a) (b) (c)

FIGURE 3.2. Sample meshes used in the element-eigenvalue analysis for $\ell = 0, 1, 2, 3$. The central quadrilateral element has (a) 4 nodes, (b) 7 nodes, and (c) 12 nodes.

3.5.3. Cantilever beam. We now consider the problem of a cantilever beam, subjected to a shear end load [109]. In particular we consider the problem with material properties $E_Y = 2 \times 10^5$ psi and $\nu = 0.3$, with plane stress assumptions. The beam has length $L = 8$ inch, height $D = 1$ inch and unit thickness. We apply a constant load $P = -1000$ psi on the right boundary. We test this problem on Lloyd iterated Voronoi meshes [107]. In Figure 3.6, we show a few representative meshes. For this problem, we compare the results of the stabilization-free VEM to a standard VEM method with a stabilization term [9]. In Figure 3.7, we plot the L^2 and energy errors of both the stabilization-free VEM and the standard VEM. We find that for the L^2 norm and energy seminorm, both methods produce second-order and first-order convergence rates, respectively. This agrees with the theoretical error estimates and demonstrates that the stabilization-free method compares favorably with the standard stabilized virtual element method.

This problem is also tested on nonconvex meshes. We start with a uniform quadrilateral mesh and split each element into two nonconvex heptagonal elements. In the convergence study, a sequence of successively refined meshes are used; three meshes from this sequence are presented in Figure 3.8. In Figure 3.9, we plot the L^2 and energy errors of both the stabilization-free VEM and the standard VEM. The errors are comparable to the results in Figure 3.7 and reveals that the stabilization-free method also performs equally well on nonconvex meshes.

3.5.4. Infinite plate with a circular hole. We next consider the problem of an infinite plate with a circular hole under uniaxial tension. The hole is subject to traction-free condition,

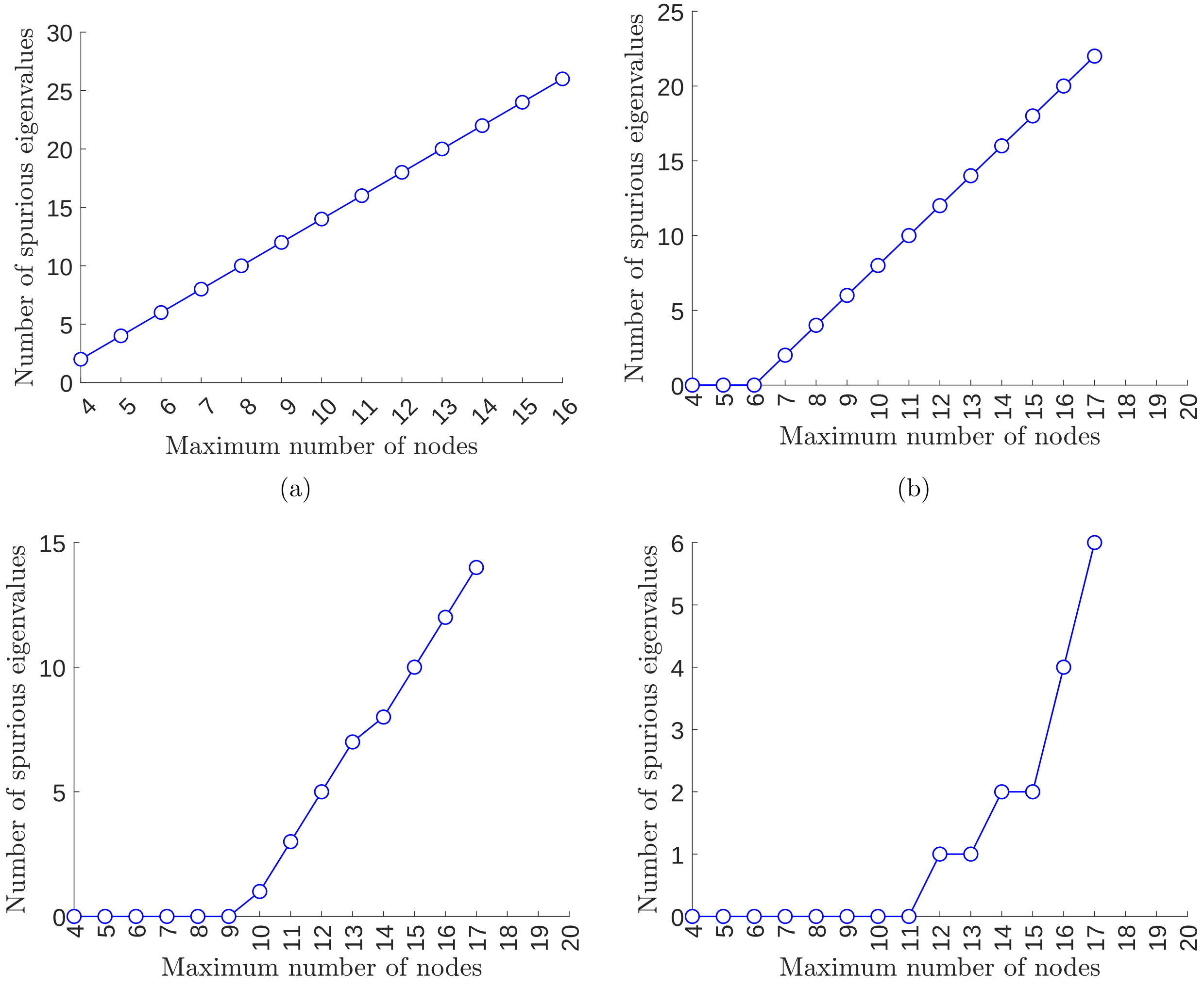

(a) (b) (c) (d)

FIGURE 3.3. Results of the element-eigenvalue analysis for (a) $\ell = 0$, (b) $\ell = 1$, (c) $\ell = 2$, and (d) $\ell = 3$.

while a far field uniaxial tension $\sigma_0 = 1$ psi, is applied to the plate in the x-direction. We use the material properties $E_Y = 2 \times 10^7$ psi and $\nu = 0.3$, with a hole radius $a = 1$ inch. Due to symmetry, we model a quarter of the finite plate ($L = 5$ inch), with exact boundary tractions prescribed as data. Plane strain conditions are assumed. A Lloyd iterated Voronoi meshing is used [107]. In Figure 3.10, we show a few illustrative meshes. We also plot the convergence curves for the three associated errors in Figure 3.11. From this plot, we observe that the L^2 norm converges with order 2, and the energy is decaying at order 1, which agree with the theoretical predictions.

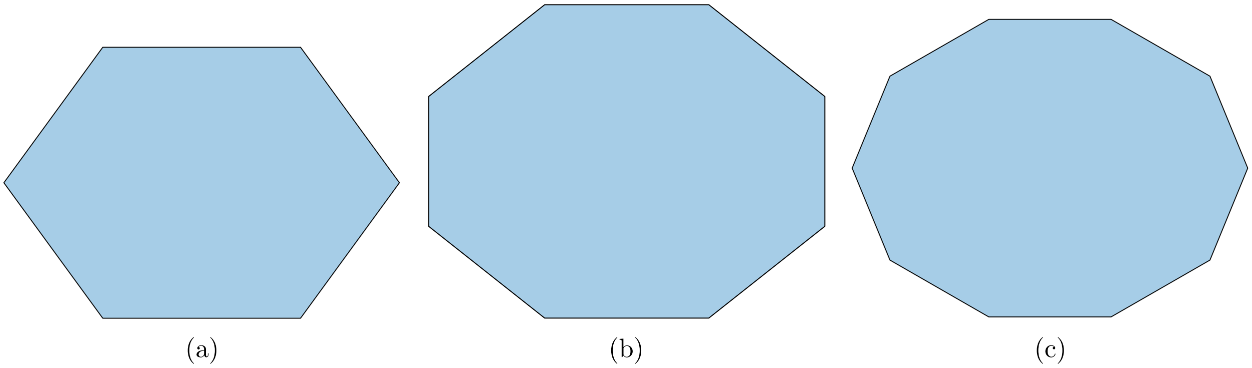
(a) (b) (c)

FIGURE 3.4. Sample regular polygons used in the element-eigenvalue analysis for $\ell = 0, 1, 2, 3$.

3.5.5. Hollow cylinder under internal pressure. Finally, we consider the problem of a hollow cylinder that is subject to internal pressure [109]. The inner and outer radii of the cylinder are chosen as $a = 1$ inch and $b = 5$ inch, respectively. We apply a uniform constant pressure of $p = 10^5$ psi on the inner radius, while the outer radius is traction-free. In Figure 3.12, we present a few sample meshes that are generated using [107]. In Figure 3.13, we plot the errors in the three norms and compare it with the maximum diameter on the mesh. We find that the convergence rates in both the L^2 norm and the energy seminorm are in agreement with the theoretical rates.

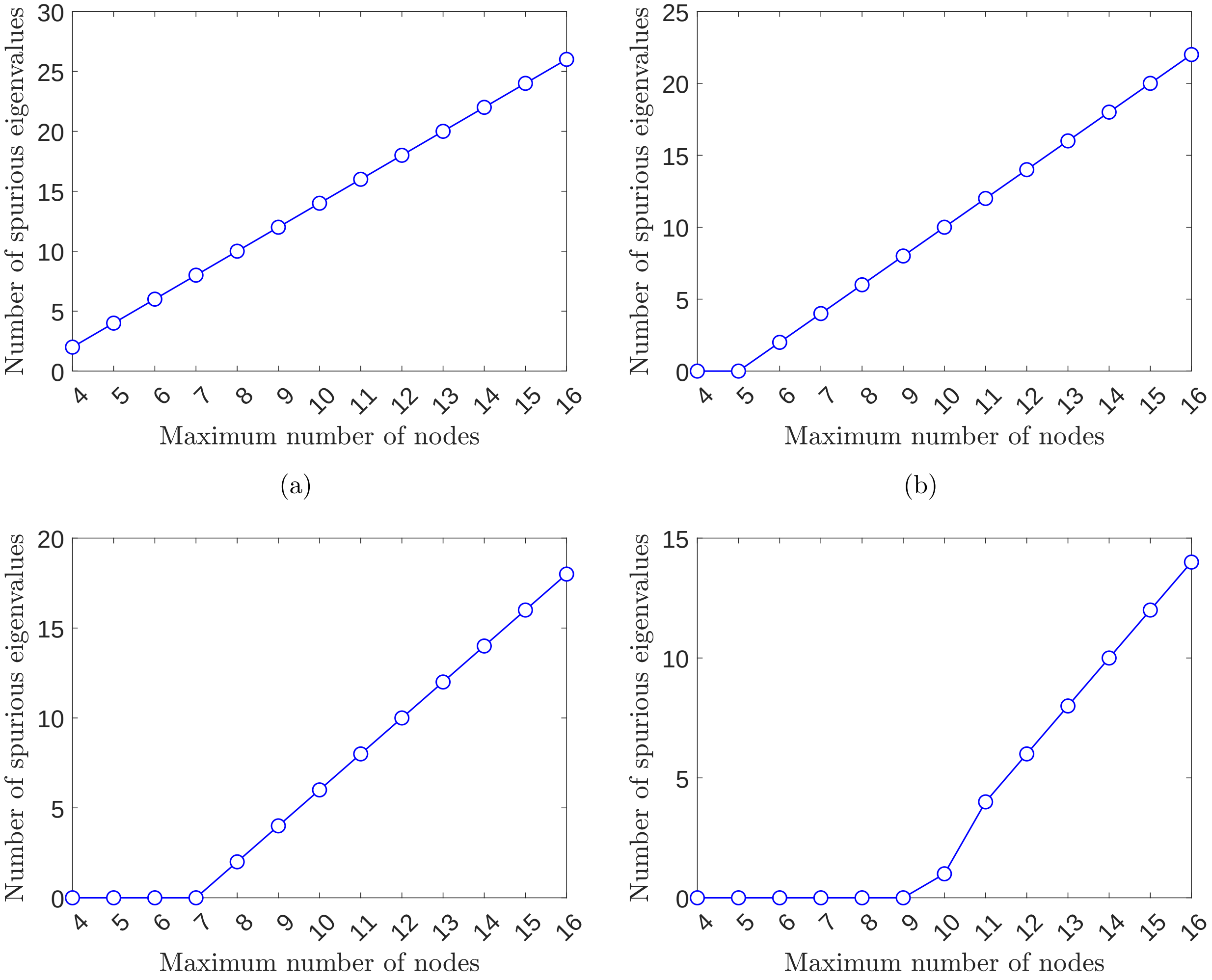

(a) (b) (c) (d)

Figure 3.5. Results of the regular polygon element-eigenvalue analysis for (a) $\ell = 0$, (b) $\ell = 1$, (c) $\ell = 2$, and (d) $\ell = 3$.

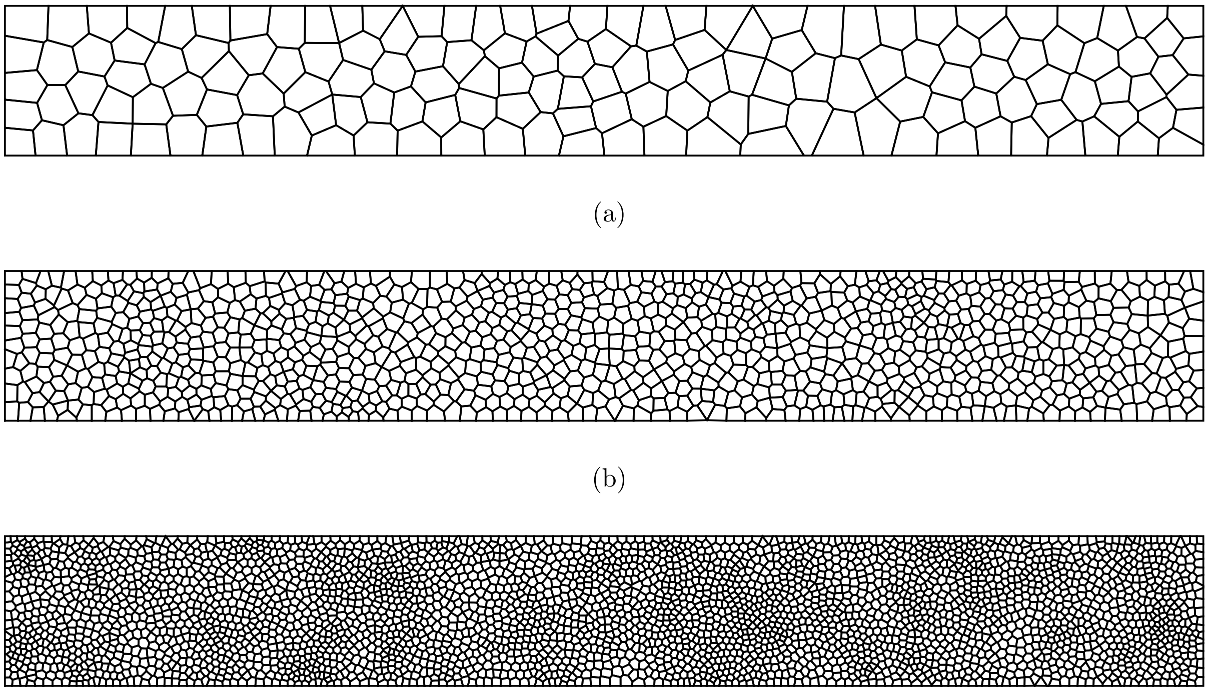

(a)

(b)

(c)

FIGURE 3.6. Polygonal meshes used for the cantilever beam problem. (a) 150 elements, (b) 1000 elements and (c) 3500 elements.

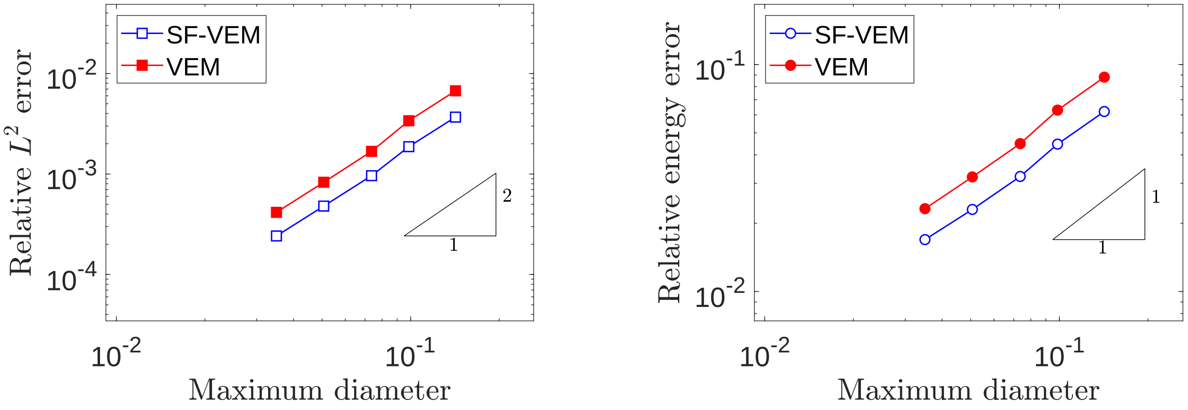

(a)

(b)

FIGURE 3.7. Comparison of the convergence of the stabilization-free VEM (SF) and a standard VEM with a stabilization term for the cantilever beam problem. (a) L^2 error and (b) energy error.

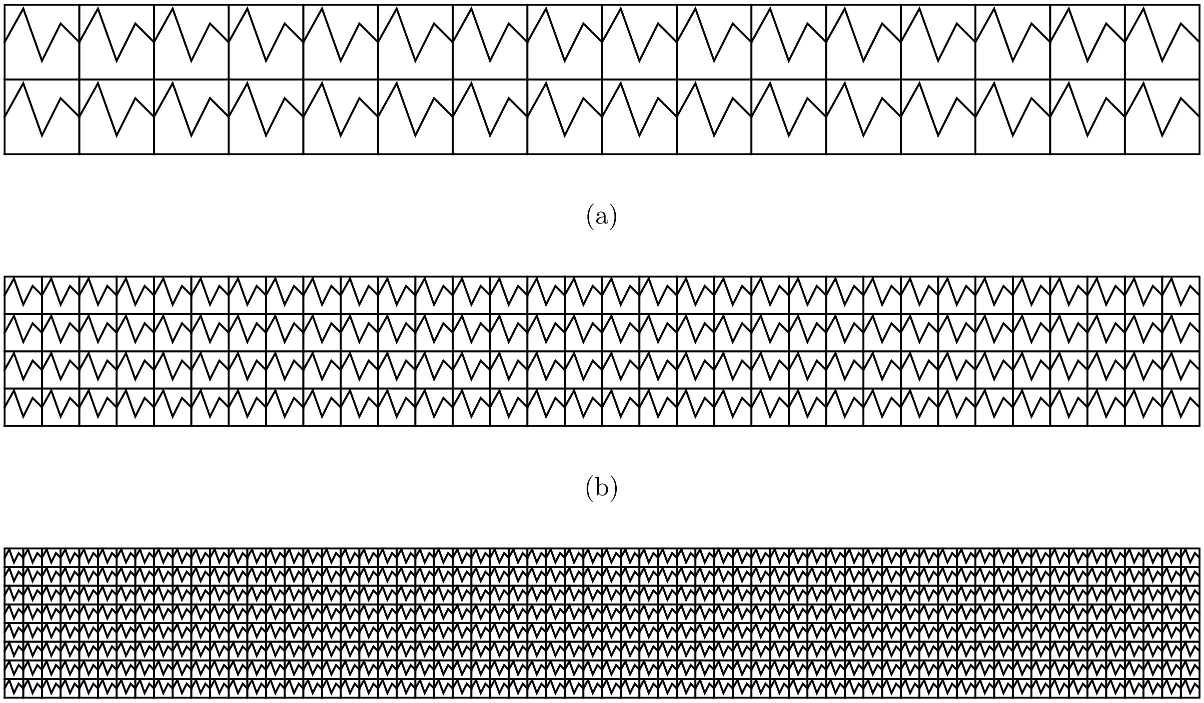

(a)

(b)

(c)

FIGURE 3.8. Nonconvex polygonal meshes for the cantilever beam problem. (a) 64 elements, (b) 256 elements and (c) 1024 elements.

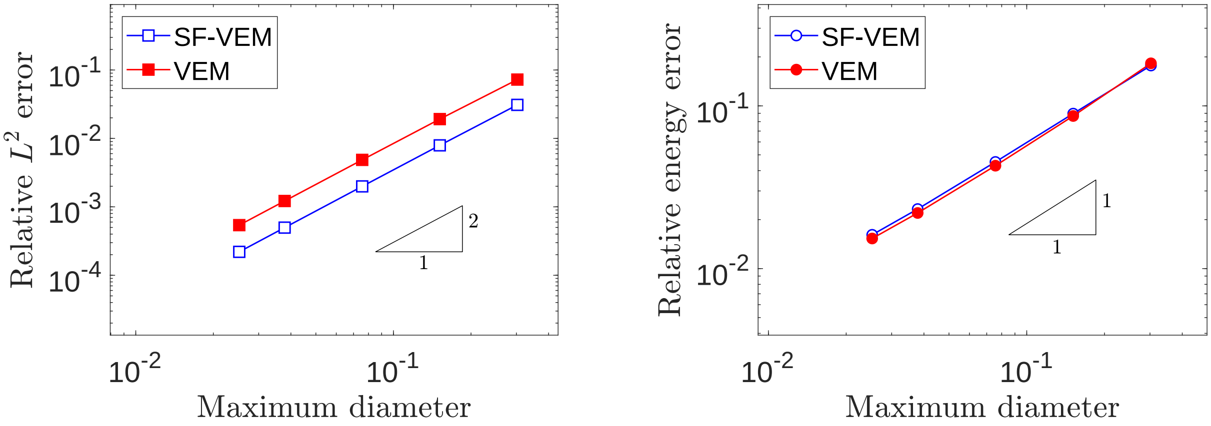

(a) (b)

FIGURE 3.9. Comparison of the convergence of the stabilization-free VEM (SF) and a standard VEM with a stabilization term for the cantilever beam problem on nonconvex meshes. (a) L^2 error and (b) energy error.

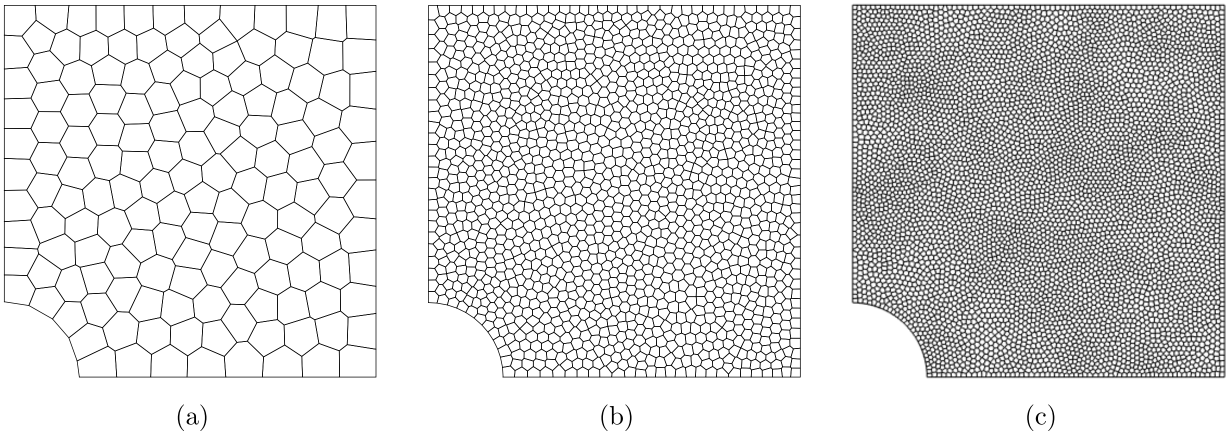
(a)
(b)
(c)

FIGURE 3.10. Polygonal meshes used for the plate with a circular hole problem. (a) 250 elements, (b) 1500 elements, and (c) 6000 elements.

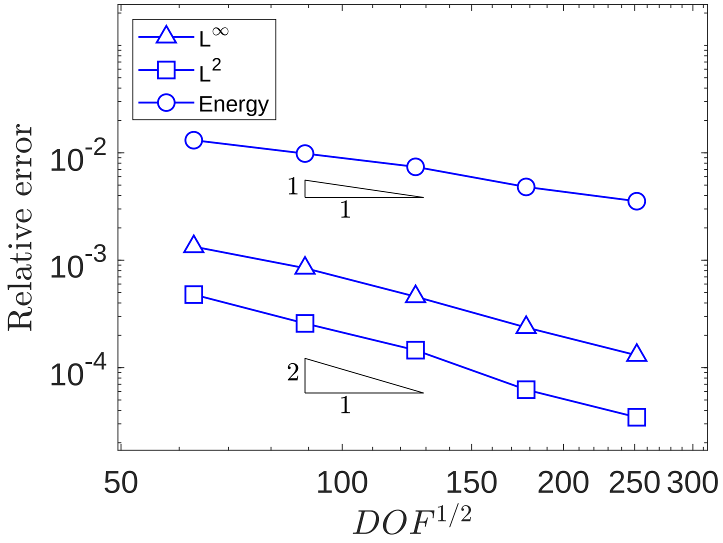

FIGURE 3.11. Convergence curves for the plate with a hole problem.

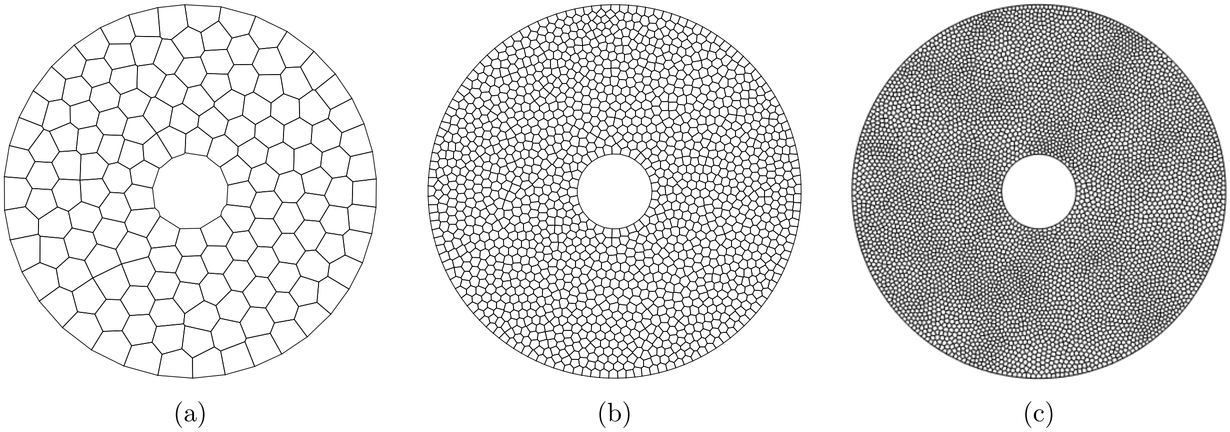
(a) (b) (c)

Figure 3.12. Polygonal meshes used for the pressurized cylinder problem. (a) 250 elements , (b) 1500 elements, and (c) 6000 elements.

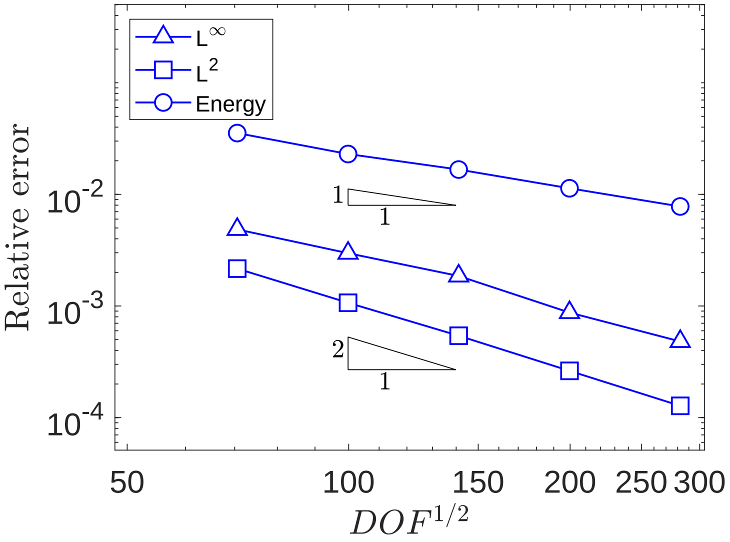

Figure 3.13. Convergence curves for the hollow cylinder under internal pressure problem.

CHAPTER 4

Stabilization-Free Serendipity Virtual Element Method

For some problems with nonlinear materials, acoustics and other wave propagation problems, highly accurate numerical methods are needed to fully resolve the underlying physical phenomena. For these problems, the stabilization term may not be easily constructed or may interfere with the accuracy of the solution. Therefore it is desirable to construct an arbitrary order virtual element method without a stabilization term. From Section 2.4, to construct a standard k-th order VEM would require the use of $\frac{k(k-1)}{2}$ additional internal moment degrees of freedom. This increases the cost to solve the system or requires applying static condensation. From serendipity FEM [4], it was shown that by modifying the basis functions, the number of degrees of freedom can be greatly reduced. A similar idea was pursued in [10, 12] to develop the serendipity virtual element method for scalar problems and in [53] for nonlinear elasticity problems. Serendipity VEM was found to be robust for general polygonal meshes; however, it still requires a suitable stabilization term.

In this chapter, we combine the serendipity VEM approach [12] with the stabilization-free VEM [37] in the previous chapter to construct arbitrary order stabilization-free virtual element methods, which in many cases will not have any internal degrees of freedom.

We first introduce the serendipity space and the corresponding serendipity projection operator. Then following the previous chapters use construct an virtual element space enhanced with the serendipity projection. We show the numerical implementation of the higher-order VEM and perform an eigenvalue analysis to determine a sufficient stability condition. We close the chapter by applying a second- and third-order method to the patch test, two manufactured problems with exact solutions, a beam subjected to sinusoidal load, and the infinite plate with a circular hole problem.

This chapter is based on the work published in [36].

4.1. Serendipity space and projection

We first introduce some properties of the serendipity space and define the serendipity projection of the displacement field as proposed in [12]. We then present the derivation of two L^2 projection operators, the L^2 projection of the displacement and the L^2 projection of the strain.

4.1.1. Properties of serendipity virtual elements. We recall some results on serendipity virtual element methods for scalar problems from [12]. Let E be a polygon with N_E edges and let η_E be the minimum number of unique lines to cover ∂E. For a k-th order method there are a total of kN_E boundary degrees of freedom and $\frac{k(k-1)}{2}$ internal degrees of freedom (see Section 2.4). The idea of serendipity VEM is that we are able to fully define a computable projection operator by only retaining a subset of all the degrees of freedom. In particular, it is desirable to keep all of the degrees of freedom on the boundary to preserve continuity of the solution and to reduce the number of internal moments for computational efficiency. To do this, we introduce two propositions as proven in [12].

Proposition 4.1.1. *For $k < \eta_E$, if the set of S degrees of freedom $\{\delta_1, \delta_2, \dots \delta_S\}$ contains all of the kN_E boundary degrees of freedom, then the following property holds true:*

$$\delta_1(p_k) = \delta_2(p_k) = \cdots = \delta_S(p_k) = 0 \implies p_k \equiv 0 \quad \forall p_k \in \mathbb{P}_k(E), \tag{4.1}$$

where $\delta_i(\cdot)$ is the i-th degree of freedom of its argument.

Proposition 4.1.2. *For $k \geq \eta_E$, if the set of S degrees of freedom $\{\delta_1, \delta_2, \dots, \delta_S\}$ contains all kN_E boundary degrees of freedom and contain all internal moments of order $\leq k - \eta_E$, then the set satisfies*

$$\delta_1(p_k) = \delta_2(p_k) = \cdots = \delta_S(p_k) = 0 \implies p_k \equiv 0 \quad \forall p_k \in \mathbb{P}_k(E). \tag{4.2}$$

Once these degrees of freedom are chosen, we can construct a serendipity projection operator Π_k^S such that it satisfies the properties:

$$\Pi_k^S \text{ can be fully computed using } \delta_1, \delta_2, \dots, \delta_S, \tag{4.3a}$$

and

$$\Pi_k^S p_k = p_k \quad \forall p_k \in \mathbb{P}_k(E). \tag{4.3b}$$

This operator is used to define a serendipity virtual element space for a vector field and to construct two L^2 operators.

Remark 4.1.1. *In [12], the notation $\delta_i(\cdot)$ is used to denote the i-th degree of freedom. For consistency, we use the same notation in this chapter instead of the one introduced in (2.53).*

Remark 4.1.2. *For $k = 2$, on any polygonal element E it is sufficient to take $\{\delta_1, \delta_2, \ldots, \delta_S\}$ to be the vertex and edge degrees of freedom. For $k = 3$, if E is at least a quadrilateral with four distinct sides then it is also sufficient to take $\{\delta_1, \delta_2, \ldots, \delta_S\}$ as the vertex and edge degrees of freedom.*

4.1.2. Serendipity projection. For any element E, denote $\boldsymbol{H}^1(E) := [H^1(E)]^2$ and $\boldsymbol{C}^0(\overline{E}) := [C^0(\overline{E})]^2$. Let S be the number of sufficient degrees of freedom for a scalar function as defined in Proposition 4.1.1 and 4.1.2, and then define the operator $D : \boldsymbol{H}^1(E) \cap \boldsymbol{C}^0(\overline{E}) \to \mathbb{R}^{2S}$ by

$$D(\boldsymbol{v}) = \big(\delta_1(\boldsymbol{v}), \delta_2(\boldsymbol{v}), \ldots, \delta_{2S}(\boldsymbol{v})\big), \tag{4.4}$$

where $\delta_i(\boldsymbol{v})$ is the i-th degree of freedom of the vector field $\boldsymbol{v}$. We define the serendipity projection operator $\Pi_k^S : \boldsymbol{H}^1(E) \cap \boldsymbol{C}^0(\overline{E}) \to [\mathbb{P}_k(E)]^2$ as the unique function that satisfies the orthogonality condition:

$$\big(D(\Pi_k^S \boldsymbol{v} - \boldsymbol{v}), D(\boldsymbol{m}_\alpha)\big)_{\mathbb{R}^{2S}} = 0 \quad \forall \boldsymbol{m}_\alpha \in [\mathbb{P}_k(E)]^2. \tag{4.5a}$$

On writing out the expressions, we get the equivalent system:

$$\sum_{j=1}^{2S} \delta_j(\Pi_k^S \boldsymbol{v}) \delta_j(\boldsymbol{m}_\alpha) = \sum_{j=1}^{2S} \delta_j(\boldsymbol{v}) \delta_j(\boldsymbol{m}_\alpha) \quad \forall \boldsymbol{m}_\alpha \in [\mathbb{P}_k(E)]^2. \tag{4.5b}$$

4.1.3. $\mathbf{L^2}$ projection of the displacement field. We define the L^2 projection operator $\Pi_k^0 : \boldsymbol{H}^1(E) \to [\mathbb{P}_k(E)]^2$ of the displacement field by the function that satisfies the L^2 orthogonality relation:

$$(\boldsymbol{p}, \boldsymbol{v} - \Pi_k^0 \boldsymbol{v})_E = 0 \quad \forall \boldsymbol{p} \in [\mathbb{P}_k(E)]^2, \tag{4.6a}$$

where we use the standard L^2 inner product for vector fields:

$$(\boldsymbol{p}, \boldsymbol{v})_E = \int_E \boldsymbol{p} \cdot \boldsymbol{v} \, d\boldsymbol{x}. \tag{4.6b}$$

Expanding (4.6a) and rewriting in matrix-vector operations, we have

$$\int_E \boldsymbol{p}^T \Pi_k^0 \boldsymbol{v} \, d\boldsymbol{x} = \int_E \boldsymbol{p}^T \boldsymbol{v} \, d\boldsymbol{x} \quad \forall \boldsymbol{p} \in [\mathbb{P}_k(E)]^2. \tag{4.6c}$$

4.1.4. $\mathbf{L^2}$ projection of the strain field. Similar to the L^2 projection of the strain given in Section 3.1.3 for the first-order method, we define the associated L^2 projection operator $\Pi_\ell^0 \boldsymbol{\varepsilon}(.) : \boldsymbol{H}^1(E) \to \mathbb{P}_\ell(E)^{2\times 2}_{\text{sym}}$ of the strain tensor by the unique operator that satisfies

$$(\boldsymbol{\varepsilon}^p, \boldsymbol{\varepsilon}(\boldsymbol{v}) - \Pi_\ell^0 \boldsymbol{\varepsilon}(\boldsymbol{v}))_E = 0 \quad \forall \boldsymbol{\varepsilon}^p \in \mathbb{P}_\ell(E)^{2\times 2}_{\text{sym}}, \tag{4.7a}$$

where we use the L^2 inner product (double contraction) for rank-2 tensor fields:

$$(\boldsymbol{\varepsilon}^p, \boldsymbol{\varepsilon})_E = \int_E \boldsymbol{\varepsilon}^p : \boldsymbol{\varepsilon} \, d\boldsymbol{x}. \tag{4.7b}$$

After using Voigt notation and simplifying, we obtain the system for the L^2 strain projection as

$$\int_E \left(\overline{\Pi_\ell^0 \boldsymbol{\varepsilon}(\boldsymbol{v})} \right)^T \overline{\boldsymbol{\varepsilon}^p} \, d\boldsymbol{x} = \int_{\partial E} \boldsymbol{v}^T \boldsymbol{N}_*^{\partial E} \overline{\boldsymbol{\varepsilon}^p} \, ds + \int_E \boldsymbol{v}^T \boldsymbol{\partial} \overline{\boldsymbol{\varepsilon}^p} \, d\boldsymbol{x} \quad \forall \boldsymbol{\varepsilon}^p \in \mathbb{P}_\ell(E)^{2\times 2}_{\text{sym}}, \tag{4.8a}$$

where

$$\boldsymbol{N}_*^{\partial E} := \begin{bmatrix} n_1 & 0 & n_2 \\ 0 & n_2 & n_1 \end{bmatrix}, \tag{4.8b}$$

$$\boldsymbol{\partial} := \begin{bmatrix} \frac{\partial}{\partial x} & 0 & \frac{\partial}{\partial y} \\ 0 & \frac{\partial}{\partial y} & \frac{\partial}{\partial x} \end{bmatrix}, \tag{4.8c}$$

and $\overline{\boldsymbol{\varepsilon}^p}$, $\overline{\Pi_\ell^0 \boldsymbol{\varepsilon}(\boldsymbol{v})}$ are the Voigt representations of $\boldsymbol{\varepsilon}^p$ and $\Pi_\ell^0 \boldsymbol{\varepsilon}(\boldsymbol{v})$, respectively.

REMARK 4.1.3. *For the implementation of the projection operators, we use the monomial basis given in* (2.114) *and* (3.2).

4.1.5. Enlarged Enhanced Serendipity Virtual Element Space.

The integral defined on the right-hand side of (4.6c) and the last integral on the right-hand side of (4.8a) are not computable from the degrees of freedom of a standard k-th order virtual element space. We follow a similar process from Section 3.2 to construct an enhanced virtual element space where it is possible to compute these integrals.

For any element E, fix a $\ell = \ell(E)$ and define the set $\mathcal{EN}^E_{k,\ell}$ as

$$\mathcal{EN}^E_{k,\ell} := \Big\{ \boldsymbol{v} \in \boldsymbol{H}^1(E) \cap \boldsymbol{C}^0(\overline{E}) : \int_E \boldsymbol{v} \cdot \boldsymbol{p}\, d\boldsymbol{x} = \int_E \Pi^S_k \boldsymbol{v} \cdot \boldsymbol{p}\, d\boldsymbol{x} \\ \forall \boldsymbol{p} \in [\mathbb{P}_{\ell-1}(E)]^2 / [\mathbb{P}_{k-\eta_E}(E)]^2 \Big\}, \tag{4.9}$$

where $[\mathbb{P}_{\ell-1}(E)]^2/[\mathbb{P}_{k-\eta_E}(E)]^2$ denotes the set of vector polynomials in $[\mathbb{P}_{\ell-1}(E)]^2$ that are orthogonal to $[\mathbb{P}_{k-\eta_E}(E)]^2$ with respect to the L^2 inner product on E. We then define the local enlarged virtual element space as:

$$\boldsymbol{V}^E_{k,\ell} := \big\{ \boldsymbol{v}_h \in \mathcal{EN}^E_{k,\ell} : \Delta \boldsymbol{v}_h \in [\mathbb{P}_{\ell-1}(E)]^2,\ \gamma^e(\boldsymbol{v}_h) \in [\mathbb{P}_k(e)]^2\ \forall e \in \mathcal{E}_E,\ \boldsymbol{v}_h \in [C^0(\partial E)]^2 \big\}, \tag{4.10}$$

where $\gamma^{e_i}(\cdot)$ is the trace of a function (its argument) on an edge e_i. In the above space we require functions to be k-th order vector polynomials on the edges, and by the serendipity condition we take the degrees of freedom to be the values of the function at the vertices and edges of the polygon E and possibly all the internal moments up to order $k - \eta_E$. In general, there are a total of

$$2S = \max\{2kN_E, 2kN_E + (k - \eta_E + 1)(k - \eta_E + 2)\}$$

degrees of freedom. With the local space defined, we define the global enhanced virtual element space as

$$\boldsymbol{V}_{k,\boldsymbol{\ell}} := \{ \boldsymbol{v}_h \in [H^1(\Omega)]^2 : \boldsymbol{v}_h|_E \in \boldsymbol{V}^E_{k,\ell} \ \text{ for } \ell = \ell(E) \}. \tag{4.11}$$

For each E, we assign a suitable basis to the local virtual element space $\boldsymbol{V}^E_{k,\ell}$. Let $\{\phi_i\}$ be the set of canonical basis functions [9, 13] that satisfy $\delta_j(\phi_i) = \delta_{ij}$, where δ_{ij} is the Kronecker-delta.

We express the components of any $\boldsymbol{v}_h \in \boldsymbol{V}_{k,\ell}^E$ as the sum of these basis functions:

$$\boldsymbol{v}_h = \begin{Bmatrix} v_h^1 \\ v_h^2 \end{Bmatrix} = \begin{bmatrix} \phi_1 & \phi_2 & \dots & \phi_S & 0 & 0 & \dots & 0 \\ 0 & 0 & \dots & 0 & \phi_1 & \phi_2 & \dots & \phi_S \end{bmatrix} \begin{Bmatrix} v_1^1 \\ v_2^1 \\ \vdots \\ v_S^2 \end{Bmatrix} := \boldsymbol{N}^v \tilde{\boldsymbol{v}}_h, \tag{4.12a}$$

where we define $\boldsymbol{N}^v$ as the matrix of vectorial basis functions:

$$\boldsymbol{N}^v = \begin{bmatrix} \phi_1 & \phi_2 & \dots & \phi_S & 0 & 0 & \dots & 0 \\ 0 & 0 & \dots & 0 & \phi_1 & \phi_2 & \dots & \phi_S \end{bmatrix} := \begin{bmatrix} \boldsymbol{\varphi}_1 & \dots & \boldsymbol{\varphi}_S & \dots & \boldsymbol{\varphi}_{2S} \end{bmatrix}. \tag{4.12b}$$

We now define the weak form of the virtual element method on this space. On defining a discrete bilinear operator $a_h^E : \boldsymbol{V}_{k,\ell}^E \times \boldsymbol{V}_{k,\ell}^E \to \mathbb{R}$ and a discrete linear functional $\ell_h^E : \boldsymbol{V}_{k,\ell}^E \to \mathbb{R}$, we seek the solution to the problem: find $\boldsymbol{u}_h \in \boldsymbol{V}_{k,\ell}^E$ such that

$$a_h^E(\boldsymbol{u}_h, \boldsymbol{v}_h) = \ell_h^E(\boldsymbol{v}_h) \quad \forall \boldsymbol{v}_h \in \boldsymbol{V}_{k,\ell}^E. \tag{4.13}$$

Following [19], we introduce the local discrete bilinear form in matrix-vector form:

$$a_h^E(\boldsymbol{u}_h, \boldsymbol{v}_h) := \int_E \left(\overline{\Pi_\ell^0 \boldsymbol{\varepsilon}(\boldsymbol{v_h})}\right)^T \boldsymbol{C}\, \overline{\Pi_\ell^0 \boldsymbol{\varepsilon}(\boldsymbol{u}_h)}\, d\boldsymbol{x}, \tag{4.14}$$

with the associated global operator defined as

$$a_h(\boldsymbol{u}_h, \boldsymbol{v}_h) := \sum_E a_h^E(\boldsymbol{u}_h, \boldsymbol{v}_h). \tag{4.15}$$

We also define a local linear functional by

$$\ell_h^E(\boldsymbol{v}_h) = \int_E \boldsymbol{v}_h^T \boldsymbol{b}_h \, d\boldsymbol{x} + \int_{\Gamma_t \cap \partial E} \boldsymbol{v}_h^T \bar{\boldsymbol{t}}\, ds, \tag{4.16}$$

with the associated global functional

$$\ell_h(\boldsymbol{v}_h) = \sum_E \ell_h^E(\boldsymbol{v}_h), \tag{4.17}$$

where $\boldsymbol{b}_h$ is some approximation to $\boldsymbol{b}$. For a k-th order method we use $\boldsymbol{b}_h = \Pi_k^0 \boldsymbol{b}$, but from [6], it is sufficient to take $\boldsymbol{b}_h = \Pi_{k-2}^0 \boldsymbol{b}$.

4.2. Numerical implementation of higher order methods

For simplicity of implementation, we only consider the case $k < \eta_E$ (meshes do not contain triangles for $k = 3$). This removes the need for internal moment degrees of freedom in the construction of the serendipity projection and simplifies the space $\mathcal{EN}^E_{k,\ell}$.

4.2.1. Implementation of serendipity projector.

We start with the implementation of the serendipity projector. From (4.5b), we have for $\alpha = 1, 2, \ldots, N_k$, where $N_k = \dim([\mathbb{P}_k(E)]^2) = (k+1)(k+2)$, the condition

$$\sum_{j=1}^{2S} \delta_j(\Pi^S_k \boldsymbol{v}_h)\delta_j(\boldsymbol{m}_\alpha) = \sum_{j=1}^{2S} \delta_j(\boldsymbol{v}_h)\delta_j(\boldsymbol{m}_\alpha).$$

We choose $\boldsymbol{v}_h = \boldsymbol{\varphi}_i$, the basis functions in $\boldsymbol{V}^E_{k,\ell}$, and expand $\Pi^S_k \boldsymbol{\varphi}_i$ in terms of the scaled monomial basis functions:

$$\Pi^S_k \boldsymbol{\varphi}_i = \sum_{\beta=1}^{N_k} s^i_\beta \boldsymbol{m}_\beta, \tag{4.18}$$

where $\boldsymbol{m}_\alpha$ is an element of $\widehat{\boldsymbol{M}_k}(E)$ in (2.114). Expanding the left-hand side of (4.5b), we have

$$\sum_{j=1}^{2S} \delta_j(\Pi^S_k \boldsymbol{v}_h)\delta_j(\boldsymbol{m}_\alpha) = \sum_{\beta=1}^{N_k} s^i_\beta \sum_{j=1}^{2S} \delta_j(\boldsymbol{m}_\beta)\delta_j(\boldsymbol{m}_\alpha). \tag{4.19}$$

Define the matrix $\widehat{\boldsymbol{G}}$ $(\alpha, \beta = 1, 2, \ldots, N_k)$ by

$$\widehat{\boldsymbol{G}}_{\alpha\beta} = \sum_{j=1}^{2S} \delta_j(\boldsymbol{m}_\beta)\delta_j(\boldsymbol{m}_\alpha). \tag{4.20a}$$

Similarly, we define the matrix $\widehat{\boldsymbol{B}}$ representing the right-hand side of (4.5b) by

$$\widehat{\boldsymbol{B}}_{\alpha i} = \sum_{j=1}^{2S} \delta_j(\boldsymbol{\varphi}_i)\delta_j(\boldsymbol{m}_\alpha). \tag{4.20b}$$

Now combining these linear equations we can determine the coefficients $\{s^i_\beta\}$ for the serendipity projection by solving the linear system:

$$\boldsymbol{\Pi}^S = \widehat{\boldsymbol{G}}^{-1}\widehat{\boldsymbol{B}}, \tag{4.20c}$$

where $(\boldsymbol{\Pi}^S)_{\beta i} = s^i_\beta$ is the matrix representation of the serendipity projection operator in the scaled monomial vectorial basis set.

Remark 4.2.1. *To compute the matrix* $\widehat{\boldsymbol{G}}$*, it is convenient to use*

$$\widehat{\boldsymbol{G}} = \boldsymbol{D}^T \boldsymbol{D},$$

where $\boldsymbol{D}$ *is the* $2S \times N_k$ *matrix that is defined by*

$$\boldsymbol{D}_{j\alpha} := \delta_j(\boldsymbol{m}_\alpha) \quad (j = 1, 2, \ldots 2S,\ \alpha = 1, 2, \ldots N_k).$$

.

4.2.2. Implementation of the $\mathbf{L^2}$ displacement projector. With the serendipity projection matrix on hand, we now construct the remaining projection matrices. We start with the construction of the L^2 projection operator of the displacement field. From (4.6c), we have the relation

$$\int_E \boldsymbol{p}^T \Pi^0_k \boldsymbol{v}_h \, d\boldsymbol{x} = \int_E \boldsymbol{p}^T \boldsymbol{v}_h \, d\boldsymbol{x}. \tag{4.21}$$

Expanding $\boldsymbol{v}_h$ in terms of the basis in $\boldsymbol{V}^E_{k,\ell}$, we have $\boldsymbol{v}_h = \boldsymbol{N}^v \tilde{\boldsymbol{v}}_h$. Similarly we expand $\boldsymbol{p}$ and $\Pi^0_k \boldsymbol{v}_h$ in terms of the polynomial basis in $[\mathbb{P}_k(E)]^2$. In particular we obtain $\boldsymbol{p} = \tilde{\boldsymbol{N}}^p \tilde{\boldsymbol{p}}$ and $\Pi^0_k \boldsymbol{v}_h = \tilde{\boldsymbol{N}}^p \tilde{\boldsymbol{\Pi}}^0 \tilde{\boldsymbol{v}}_h$, where $\tilde{\boldsymbol{N}}^p$ is given in (2.114) and $\tilde{\boldsymbol{\Pi}}^0$ is the matrix of coefficients of the L^2 projection . On substituting into (4.6c) and simplifying, we obtain

$$\tilde{\boldsymbol{p}}^T \left(\int_E (\tilde{\boldsymbol{N}}^p)^T \tilde{\boldsymbol{N}}^p \, d\boldsymbol{x} \right) \tilde{\boldsymbol{\Pi}}^0 \tilde{\boldsymbol{v}}_h = \tilde{\boldsymbol{p}}^T \left(\int_E (\tilde{\boldsymbol{N}}^p)^T \boldsymbol{N}^v \, d\boldsymbol{x} \right) \tilde{\boldsymbol{v}}_h. \tag{4.22}$$

Define the matrix

$$\tilde{\boldsymbol{G}} := \int_E (\tilde{\boldsymbol{N}}^p)^T \tilde{\boldsymbol{N}}^p \, d\boldsymbol{x}. \tag{4.23a}$$

The integral on the right-hand side of (4.22) is not computable directly; however by applying the enhancing property of the space (4.9), we can realize an equivalent computable matrix:

$$\tilde{\boldsymbol{B}} := \int_E (\tilde{\boldsymbol{N}}^p)^T \Pi^S_k \boldsymbol{N}^v \, d\boldsymbol{x}. \tag{4.23b}$$

Then, we solve for the projection matrix $\tilde{\mathbf{\Pi}}^0$ in terms of the matrices $\tilde{\boldsymbol{G}}$ and $\tilde{\boldsymbol{B}}$:

$$\tilde{\mathbf{\Pi}}^0 = \tilde{\boldsymbol{G}}^{-1}\tilde{\boldsymbol{B}}.$$

This projection matrix is used to compute the element force integral which appears in (4.26b).

4.2.3. Implementation of the $\mathbf{L^2}$ strain projector. To compute the L^2 projection of the strain we follow the construction in Section 3.3.2. Expand $\boldsymbol{v}_h = \boldsymbol{N}^v\tilde{\boldsymbol{v}}_h$, $\overline{\boldsymbol{\varepsilon}^p} = \boldsymbol{N}^p\tilde{\boldsymbol{\varepsilon}}^p$ and $\overline{\Pi_\ell^0\boldsymbol{\varepsilon}(\boldsymbol{v}_h)} = \boldsymbol{N}^p\mathbf{\Pi}\tilde{\boldsymbol{v}}_h$. Substituting into (4.8a) and simplifying, we get the expression:

$$(\tilde{\boldsymbol{\varepsilon}}^p)^T\left(\int_E (\boldsymbol{N}^p)^T\,\boldsymbol{N}^p d\boldsymbol{x}\right)\mathbf{\Pi}\tilde{\boldsymbol{v}}_h = (\tilde{\boldsymbol{\varepsilon}}^p)^T\left(\int_{\boldsymbol{\partial} E}\left(\boldsymbol{N}_*^{\partial E}\boldsymbol{N}^p\right)^T\boldsymbol{N}^v ds - \int_E (\boldsymbol{\partial}\boldsymbol{N}^p)^T\,\boldsymbol{N}^v d\boldsymbol{x}\right)\tilde{\boldsymbol{v}}_h.$$

Define the matrix

$$\boldsymbol{G} := \int_E (\boldsymbol{N}^p)^T\,\boldsymbol{N}^p\,d\boldsymbol{x}. \tag{4.24a}$$

Similar to (4.23b), the last integral in (4.8a) is not computable, so we again use the enhancing property in (4.9) to construct an equivalent computable matrix:

$$\boldsymbol{B} := \int_{\partial E}\left(\boldsymbol{N}_*^{\partial E}\boldsymbol{N}^p\right)^T\boldsymbol{N}^v\,ds - \int_E (\boldsymbol{\partial}\boldsymbol{N}^p)^T\,\Pi_k^S\boldsymbol{N}^v\,d\boldsymbol{x}. \tag{4.24b}$$

We now solve for the strain projection matrix $\mathbf{\Pi}$ in terms of $\boldsymbol{G}$ and $\boldsymbol{B}$ by

$$\mathbf{\Pi} = \boldsymbol{G}^{-1}\boldsymbol{B}. \tag{4.24c}$$

4.2.4. Implementation of element stiffness matrix and force vector. To construct the element stiffness, we first rewrite (4.14) in terms of the matrices that have been constructed:

$$\begin{aligned}
a_h^E(\boldsymbol{u}_h,\boldsymbol{v}_h) &:= \int_E\left(\overline{\Pi_\ell^0\boldsymbol{\varepsilon}(\boldsymbol{v}_h)}\right)^T\boldsymbol{C}\,\overline{\Pi_\ell^0\boldsymbol{\varepsilon}(\boldsymbol{u}_h)}\,d\boldsymbol{x}\\
&= \int_E (\boldsymbol{N}^p\mathbf{\Pi}\tilde{\boldsymbol{v}}_h)^T\,\boldsymbol{C}\,(\boldsymbol{N}^p\mathbf{\Pi}\tilde{\boldsymbol{u}}_h)\;d\boldsymbol{x}\\
&= \tilde{\boldsymbol{v}}_h^T\,(\mathbf{\Pi})^T\left(\int_E (\boldsymbol{N}^p)^T\boldsymbol{C}\boldsymbol{N}^p\,d\boldsymbol{x}\right)\mathbf{\Pi}\tilde{\boldsymbol{u}}_h.
\end{aligned}$$

Then, define the element stiffness matrix $\boldsymbol{K}_E$ by

$$\boldsymbol{K}_E := (\mathbf{\Pi})^T\left(\int_E (\boldsymbol{N}^p)^T\boldsymbol{C}\boldsymbol{N}^p\,d\boldsymbol{x}\right)\mathbf{\Pi}, \tag{4.25}$$

where $\mathbf{\Pi}$ is given in (4.24c).

We now construct the element forcing term given in (4.16) as

$$\ell_h^E(\boldsymbol{v}_h) = \int_E \boldsymbol{v}_h^T \boldsymbol{b}_h \, d\boldsymbol{x} + \int_{\Gamma_t \cap \partial E} \boldsymbol{v}_h^T \, \bar{\boldsymbol{t}} \, ds.$$

After making the approximations $\boldsymbol{b}_h = \Pi_k^0 \boldsymbol{b}$ and simplifying, we can rewrite the expression in the form

$$\begin{aligned} \ell_h^E(\boldsymbol{v}_h) &= \int_E \boldsymbol{v}_h^T \Pi_k^0 \boldsymbol{b} \, d\boldsymbol{x} + \int_{\Gamma_t \cap \partial E} \boldsymbol{v}_h^T \, \bar{\boldsymbol{t}} \, ds \\ &= \int_E \left(\Pi_k^0 \boldsymbol{v}_h \right)^T \boldsymbol{b} \, d\boldsymbol{x} + \int_{\Gamma_t \cap \partial E} \left(\boldsymbol{N}^v \tilde{\boldsymbol{v}}_h \right)^T \bar{\boldsymbol{t}} \, ds \\ &= \tilde{\boldsymbol{v}}_h^T \left[\int_E \left(\tilde{\boldsymbol{N}}^p \tilde{\mathbf{\Pi}}^0 \right)^T \boldsymbol{b} \, d\boldsymbol{x} + \int_{\Gamma_t \cap \partial E} \left(\boldsymbol{N}^v \right)^T \bar{\boldsymbol{t}} \, ds \right]. \end{aligned} \tag{4.26a}$$

Then, define the element force vector by

$$\boldsymbol{f}_E := \left[\int_E \left(\tilde{\boldsymbol{N}}^p \tilde{\mathbf{\Pi}}^0 \right)^T \boldsymbol{b} \, d\boldsymbol{x} + \int_{\Gamma_t \cap \partial E} \left(\boldsymbol{N}^v \right)^T \bar{\boldsymbol{t}} \, ds \right]. \tag{4.26b}$$

All integrals that are required to form the element stiffness matrix in (4.25) and the element force vector in (4.26b) are computed with the scaled boundary cubature (SBC) scheme [41].

4.3. Choice of ℓ

In the previous sections, we have left the choice of $\ell = \ell(E)$ open. However, for a choice of ℓ that is too small, the resulting system will be unstable and contain nonphysical zero-energy modes. For a choice of ℓ that is too large, the number of basis functions will be overly large and the system will be expensive to solve. We now numerically establish a choice of ℓ that results in a well-posed, stable discrete problem by performing an eigenvalue analysis. We examine specifically the case of second- and third-order methods.

4.3.1. Eigenanalysis for regular polygons. We first study the stability on regular polygons by considering the element eigenvalue problem $\boldsymbol{K}_E \boldsymbol{d}_E = \lambda \boldsymbol{d}_E$. For plane elasticity, the element stiffness should have three zero eigenvalues that correspond to the three rigid-body modes, with any additional zero eigenvalue being a non-physical (spurious) mode. We measure the number of spurious eigenvalues of the local stiffness matrix over the set of regular n-gons. We fix $\ell = 3, 4, 5$ and measure the number of spurious eigenvalues on a given regular polygon. In Figure 4.1 a few sample polygons are shown, and in Figures 4.2 and 4.3 we plot the number of spurious eigenvalues as a function of the vertices of the corresponding polygon. The analyses over regular polygons reveals that the element stiffness matrix is stable with the correct rank if the inequalities $N_E \leq 2\ell+1$ and $N_E \leq 2\ell-1$ hold for $k=2,3$ respectively. In [37], it was shown that for $k=1$ the inequality is given by $N_E \leq 2\ell+3$ for regular polygons. We conjecture that this pattern holds, and for a general k-th order method, a sufficient inequality is given by $N_E \leq 2\ell-2k+5$.

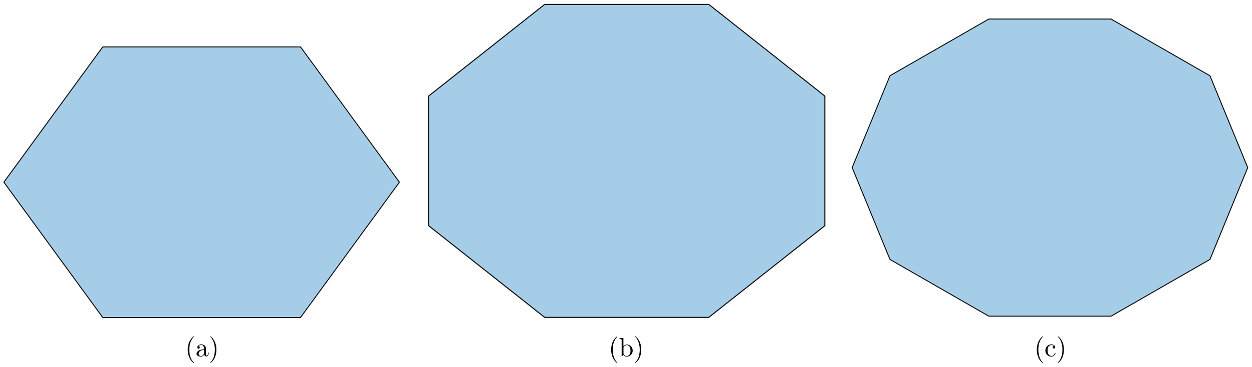
(a) (b) (c)

FIGURE 4.1. Regular polygons that are used in the eigenanalysis.

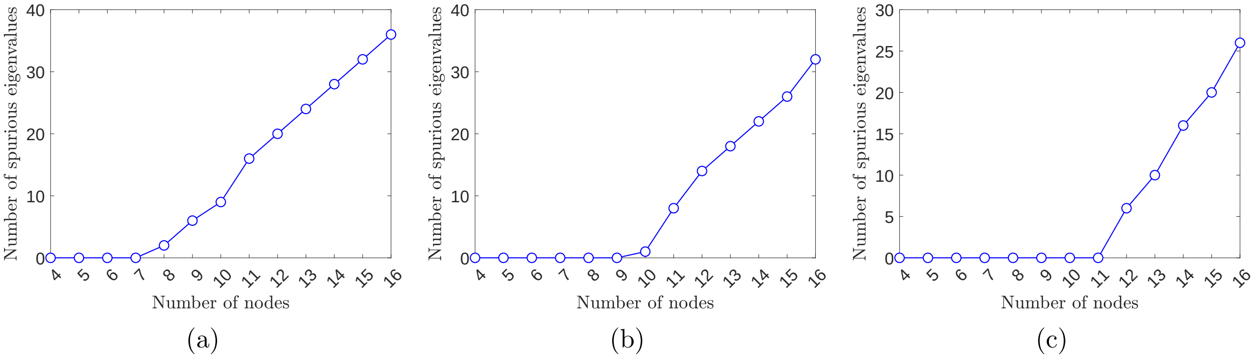

(a) (b) (c)

FIGURE 4.2. Eigenvalue analysis on regular polygons with the second-order method. (a) $\ell=3$, (b) $\ell=4$ and (c) $\ell=5$.

We are also interested in robustness of the inequality when the vertices of an element are perturbed. In particular, for $k=2,3$ we first fix $\ell=3,4,5$, then take the respective regular hexagon, octagon, decagon and perturb one component of a vertex by δ. We measure the number of spurious modes as a function of δ. For $k=2$ the three elements will satisfy the inequality $N_E \leq 2\ell+1$, so we expect no spurious eigenvalues to appear, but for $k=3$ the inequality $N_E \leq 2\ell-1$ is not satisfied so we expect to see some additional spurious eigenvalues. From Figure 4.4, we observe

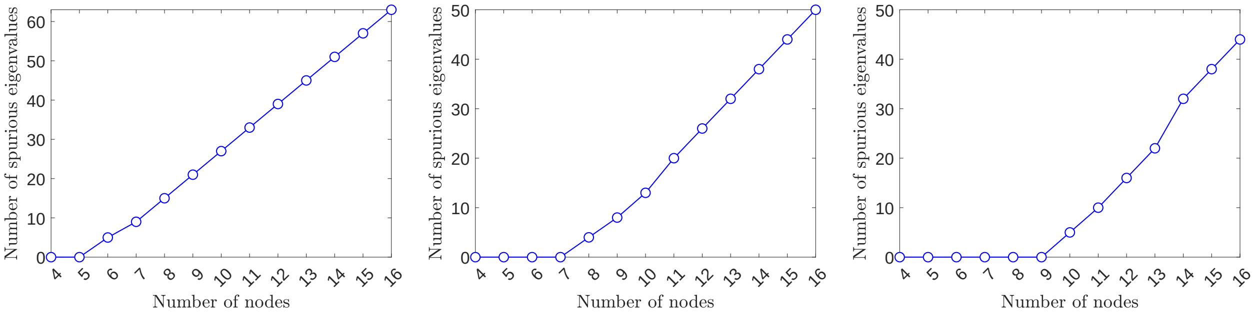

(a) (b) (c)

FIGURE 4.3. Eigenvalue analysis on regular polygons with the third-order method. (a) $\ell = 3$, (b) $\ell = 4$ and (c) $\ell = 5$.

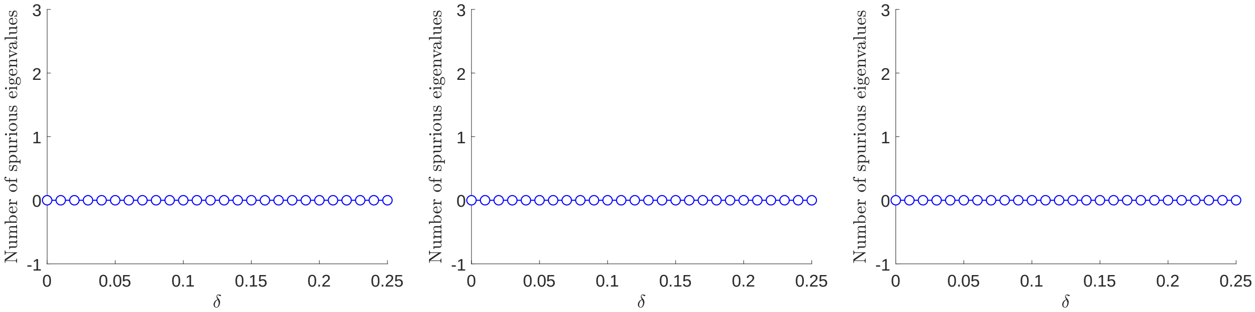

(a) (b) (c)

FIGURE 4.4. Eigenvalue analysis on the perturbed regular polygons with the second-order method. (a) $\ell = 3$ on hexagon, (b) $\ell = 4$ on octagon and (c) $\ell = 5$ on decagon.

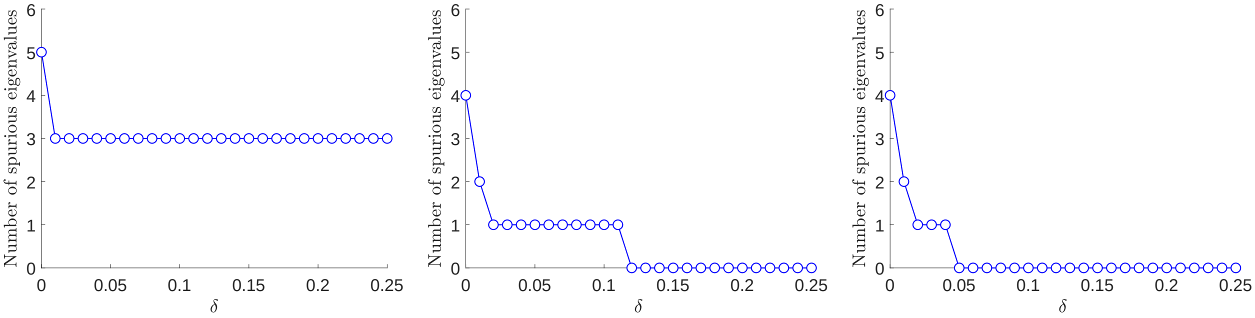

(a) (b) (c)

FIGURE 4.5. Eigenvalue analysis on the perturbed regular polygons with the third-order method. (a) $\ell = 3$ on hexagon, (b) $\ell = 4$ on octagon and (c) $\ell = 5$ on decagon.

that for small perturbations of the hexagon, octagon, and decagon that no spurious eigenvalues arise. In Figure 4.5, we see that by perturbing the octagon and decagon, we are able to reduce the number of spurious eigenvalues to zero when using $\ell = 4, 5$ respectively.

4.3.2. Eigenanalysis for general polygons. We now consider a more general polygonal mesh. Consider the unit square, $\Omega = (0,1)^2$, which is discretized using nine quadrilateral elements. We again solve the element-eigenvalue problem, $\boldsymbol{K}_E \boldsymbol{d}_E = \lambda \boldsymbol{d}_E$. We choose $\ell = 3, 4, 5$ and measure the maximum number of spurious eigenvalues of the element stiffness matrix as we artificially increase the number of nodes of the central element. We show a few sample meshes in Figure 4.6. In Figure 4.7, the resulting number of spurious eigenvalues as a function of the number of nodes of an element from the second-order method are plotted for $\ell = 3, 4, 5$ and similarly the results of the third-order method is plotted in Figure 4.8. We see that for $k = 2$, the spurious modes seem to appear later than in the regular polygons, while for $k = 3$ the results are closer to the regular polygonal case. This suggests that the inequalities $N_E \leq 2\ell + 1$ and $N_E \leq 2\ell - 1$ provide an upper bound for the choice of ℓ for $k = 2, 3$, respectively.

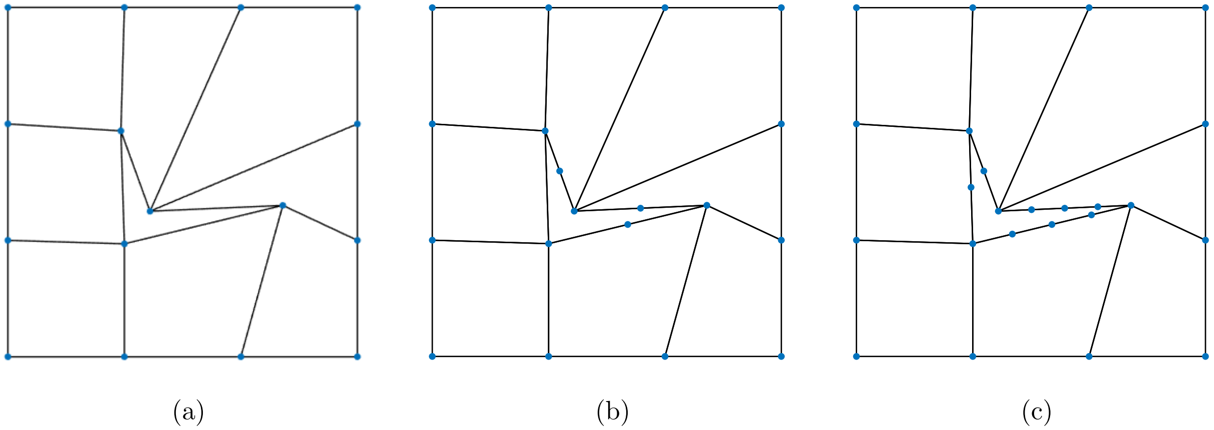
(a) (b) (c)

FIGURE 4.6. Sample meshes used in the element-eigenvalue analysis for $\ell = 3, 4, 5$. The central quadrilateral element has (a) 4 nodes, (b) 7 nodes, and (c) 12 nodes.

4.4. Numerical results for serendipity SF-VEM

We present a series of numerical examples in plane elasticity for second- and third-order serendipity methods. For these tests we use the inequalities $N_E \leq 2\ell + 1$ and $N_E \leq 2\ell - 1$ for $k = 2$ and $k = 3$, respectively. We examine the errors using the L^∞ and L^2 norms, as well as the energy seminorm, and compare the convergence rates of the method with the theoretical

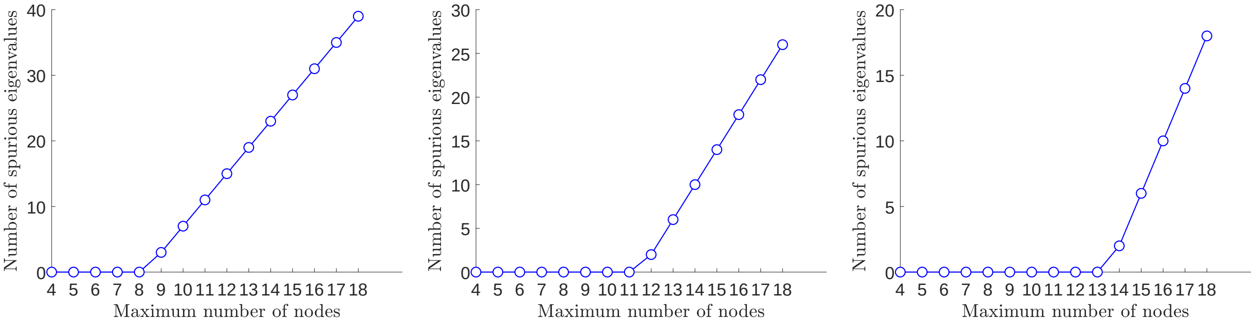

(a) (b) (c)

FIGURE 4.7. Eigenvalue analysis on the meshes shown in Figure 4.6 with the second-order method. (a) $\ell = 3$, (b) $\ell = 4$ and (c) $\ell = 5$.

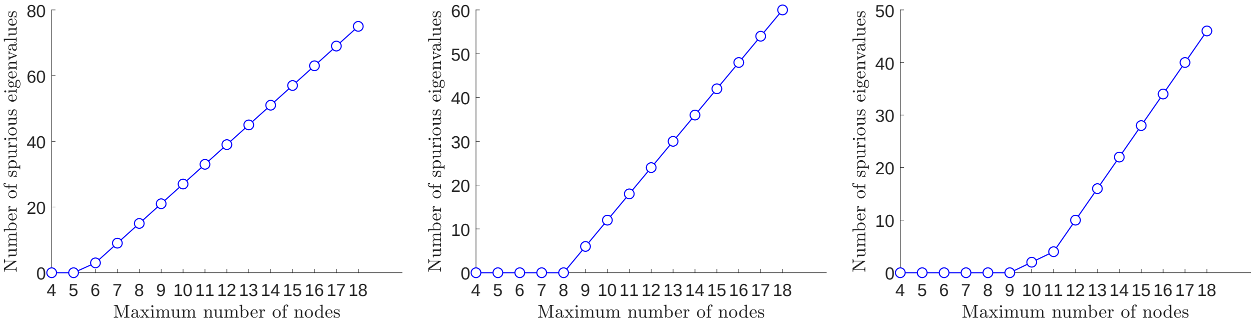

(a) (b) (c)

FIGURE 4.8. Eigenvalue analysis on the meshes shown in Figure 4.6 with the third-order method. (a) $\ell = 3$, (b) $\ell = 4$ and (c) $\ell = 5$.

estimates of standard VEM. We use the following discrete measures:

$$\|\boldsymbol{u} - \boldsymbol{u}_h\|_{\boldsymbol{L}^\infty(\Omega)} = \max_{\boldsymbol{x}_i \in \Omega} |\boldsymbol{u}(\boldsymbol{x}_i) - \boldsymbol{u}_h(\boldsymbol{x}_i)|, \tag{4.27a}$$

$$\|\boldsymbol{u} - \boldsymbol{u}_h\|_{\boldsymbol{L}^2(\Omega)} = \sqrt{\sum_E \int_E |\boldsymbol{u} - \Pi_k^S \boldsymbol{u}_h|^2 \, d\boldsymbol{x}}, \tag{4.27b}$$

$$\|\boldsymbol{u} - \boldsymbol{u}_h\|_a = \sqrt{\sum_E \int_E (\overline{\boldsymbol{\varepsilon}} - \overline{\Pi_\ell^0 \boldsymbol{\varepsilon}(\boldsymbol{u}_h)})^T \boldsymbol{C} (\overline{\boldsymbol{\varepsilon}} - \overline{\Pi_\ell^0 \boldsymbol{\varepsilon}(\boldsymbol{u}_h)}) \, d\boldsymbol{x}}. \tag{4.27c}$$

4.4.1. Patch test. To test the consistency of the second- and third-order methods, we first consider the quadratic and cubic displacement patch test. Let $\Omega = (0,1)^2$, $E_Y = 1$ psi and $\nu = 0.3$ be the material properties. For the quadratic patch test, we impose a quadratic displacement field on the boundary and an associated load vector:

$$u(\boldsymbol{x}) = x^2 + 3xy + 7y^2 + 5x + 2y + 8,$$

$$v(\boldsymbol{x}) = 6x^2 + 3xy + y^2 + 4x + 9y + 1 \quad \text{on } \partial\Omega,$$

$$\boldsymbol{b}(\boldsymbol{x}) = \left\{ \begin{matrix} \frac{-E}{1-\nu^2}\left(2 + 3\nu + \frac{17}{2}(1-\nu)\right) \\ \frac{-E}{1-\nu^2}\left(2 + 3\nu + \frac{15}{2}(1-\nu)\right) \end{matrix} \right\}.$$

For the cubic patch test we impose a cubic displacement field and load vector:

$$u(\boldsymbol{x}) = 3x^3 + 6x^2y + 7xy^2 + 8y^3 + x^2 + 3xy + y^2 + 5x + 2y + 4,$$

$$v(\boldsymbol{x}) = 4x^3 + 7x^2y + 8xy^2 + 11y^3 + 2x^2 + xy + 4y^2 + 8x + 9y + 11 \quad \text{on } \partial\Omega,$$

$$\boldsymbol{b}(\boldsymbol{x}) = \left\{ \begin{matrix} \frac{-E}{1-\nu^2}\left(18x + 12y + 2 + \nu(14x + 16y + 1) + \frac{1-\nu}{2}(36x + 28y + 7)\right) \\ \frac{-E}{1-\nu^2}\left(\frac{1-\nu}{2}(36x + 28y + 7) + \nu(14y + 3 + 12x) + 16x + 66y + 8\right) \end{matrix} \right\}.$$

The exact solutions is the extension of the boundary data onto the entire domain Ω. We test the numerical solution for the two methods for four different meshes with 16 elements in each case. First we have a uniform square mesh, second we use a random Voronoi mesh, next we use a Voronoi mesh after applying three Lloyd iterations and finally we use a non-convex mesh. The results for the quadratic test are listed in Table 4.1, and the cubic test in Table 4.2. They show that the errors are near machine precision, which indicate that the second- and third-order method passes the quadratic and cubic patch tests respectively.

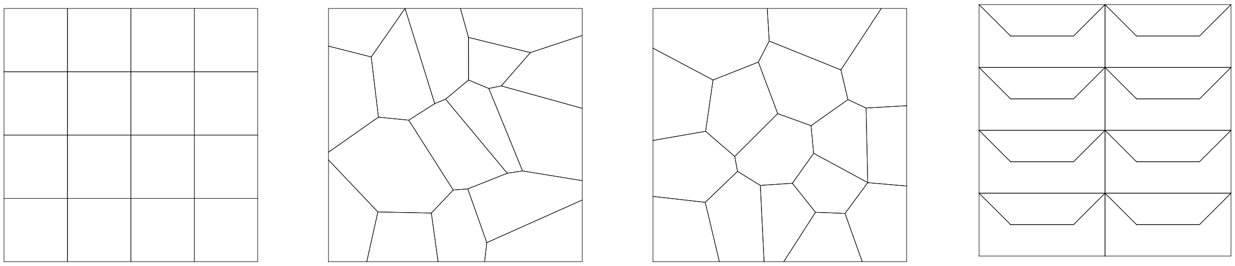

(a) Uniform (b) Random (c) Lloyd iterated (d) Nonconvex elements

FIGURE 4.9. Sample meshes used for the displacement patch test.

For most problems in mechanics, Neumann (traction) boundary conditions are applied on the boundary; therefore, we are also interested in the patch test when Neumann boundary conditions are imposed. Let $\Omega = (0, 8) \times (-0.5, 0.5)$ be a long slender bar with material properties $E_Y = 1$ psi

Mesh type	L^∞ error	L^2 error	Energy error
Uniform	1×10^{-15}	1×10^{-15}	8×10^{-14}
Random	6×10^{-15}	1×10^{-15}	1×10^{-14}
Lloyd iterated	7×10^{-15}	1×10^{-15}	2×10^{-14}
Nonconvex	4×10^{-15}	3×10^{-15}	3×10^{-14}

TABLE 4.1. Errors for the quadratic displacement patch test on different types of meshes.

Mesh type	L^∞ error	L^2 error	Energy error
Uniform	7×10^{-15}	2×10^{-15}	2×10^{-14}
Random	6×10^{-14}	4×10^{-14}	3×10^{-13}
Lloyd iterated	1×10^{-15}	6×10^{-15}	4×10^{-14}
Nonconvex	3×10^{-15}	2×10^{-15}	2×10^{-14}

TABLE 4.2. Errors for the cubic displacement patch test on different types of meshes.

and $\nu = 0.3$. For $k = 2$, we construct the following exact solution:

$$u(\boldsymbol{x}) = xy \quad \text{and} \quad v(\boldsymbol{x}) = x \quad \text{in } \Omega,$$

$$\boldsymbol{b}(\boldsymbol{x}) = \left\{ \begin{matrix} 0 \\ -\dfrac{E}{2(1-\nu)} \end{matrix} \right\},$$

where the Dirichlet boundary is imposed along $x = 0$, and the remaining boundary conditions on other edges are set to the exact tractions. For $k = 3$, we use the cantilever beam under shear end load [109]. We obtain the numerical solutions over a set of three meshes with 16 elements in each. The results for the quadratic and cubic cases are listed in Tables 4.3 and 4.4, respectively. The results show that both the second- and third-order method pass this patch test with errors at worst of $\mathcal{O}(10^{-11})$.

Mesh type	L^∞ error	L^2 error	Energy error
Uniform	2×10^{-11}	1×10^{-13}	1×10^{-13}
Random	3×10^{-13}	3×10^{-13}	4×10^{-14}
Lloyd iterated	2×10^{-12}	2×10^{-12}	4×10^{-14}

TABLE 4.3. Errors for the quadratic equilibrium patch test on different types of meshes.

4.4.2. Manufactured solution. We consider two manufactured problem as given in [54] with known exact polynomial and nonpolynomial solutions over the unit square under plane stress

Mesh type	L^∞ error	L^2 error	Energy error
Uniform	2×10^{-11}	2×10^{-11}	1×10^{-11}
Random	6×10^{-12}	6×10^{-12}	6×10^{-12}
Lloyd iterated	7×10^{-13}	8×10^{-13}	2×10^{-12}

Table 4.4. Errors for the cubic equilibrium patch test on different types of meshes.

conditions. The material properties are: $E_Y = 2.5$ psi and $\nu = 0.25$. The exact solution and the associated loading for the first problem are:

$$u(\boldsymbol{x}) = -\frac{x^6}{80} + \frac{x^4y^2}{2} - \frac{13}{16}x^2y^4 + \frac{3}{40}y^6 \quad \text{and} \quad v(\boldsymbol{x}) = \frac{xy^5}{2} - \frac{5}{12}x^3y^3,$$
$$\boldsymbol{b}(\boldsymbol{x}) = \begin{Bmatrix} 0 \\ 0 \end{Bmatrix},$$

and for the second problem are:

$$u(\boldsymbol{x}) = x\sin(\pi x)\sin(\pi y) \quad \text{and} \quad v(\boldsymbol{x}) = y\sin(\pi x)\sin(\pi y),$$
$$\boldsymbol{b}(\boldsymbol{x}) = \begin{Bmatrix} \frac{11}{3}\pi^2 x\sin(\pi x)\sin(\pi y) - \frac{5}{3}\pi^2 y\cos(\pi x)\cos(\pi y) - 7\pi\cos(\pi x)\sin(\pi y) \\ \frac{11}{3}\pi^2 y\sin(\pi x)\sin(\pi y) - \frac{5}{3}\pi^2 x\cos(\pi x)\cos(\pi y) - 7\pi\cos(\pi y)\sin(\pi x) \end{Bmatrix}.$$

We include the results for both these tests in Figures 4.10 and 4.11. In both figures, we plot the discrete errors as a function of the square root of the number of degrees of freedom. From the plots, we observe that the convergence rates for $k = 2, 3$ in the L^2 and energy seminorm are in agreement with the theoretical rates. This shows that the stabilization-free virtual element method can reproduce the results from [54].

4.4.3. Beam subjected to transverse sinusoidal loading.

Next, we consider the problem of a simply-supported beam subjected to a transversely sinusoidal load [98]. The material properties are chosen as: $E_Y = 2 \times 10^5$ psi and $\nu = 0.3$, and plane stress conditions are assumed. The beam has length $L = 8$ inch, height $D = 1$ inch and unit thickness. We apply a sinusoidal load $P = -100\sin(\frac{\pi x}{L})$ lb along the top edge, and along the two side edges we prescribe shear stresses to keep the beam in equilibrium. This problem does not have a closed-form solution; however, it can be shown that a generalized solution (one that satisfies some of the boundary conditions in an average sense) can be found with a Fourier series Airy stress function. In [98], the solution for this

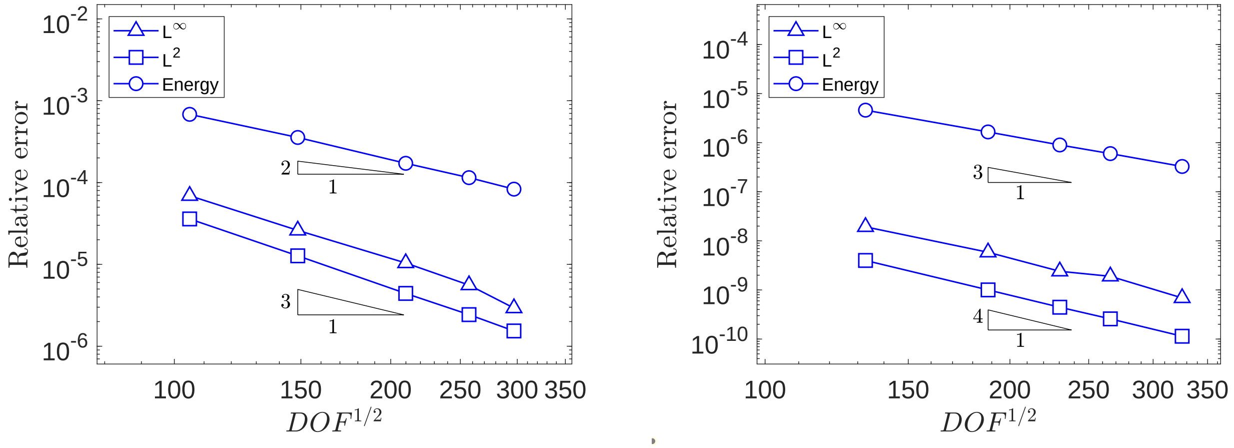

(a) (b)

FIGURE 4.10. Convergence curves for first manufactured solution on convex polygonal meshes with (a) $k = 2$ and (b) $k = 3$.

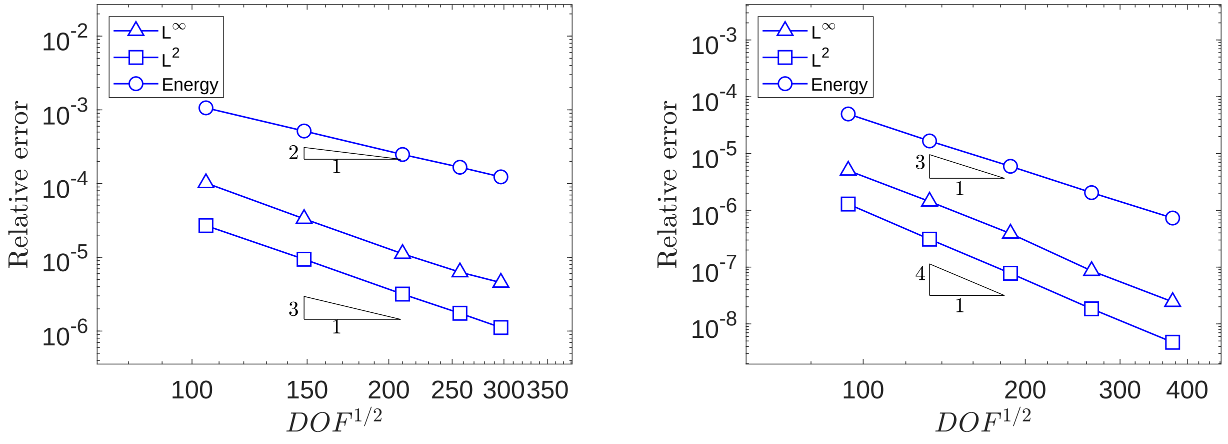

(a) (b)

FIGURE 4.11. Convergence curves for second manufactured solution on convex polygonal meshes with (a) $k = 2$ and (b) $k = 3$.

simply-supported beam is given as:

$$
\begin{aligned}
u(\boldsymbol{x}) = -\frac{\beta}{E}\cos(\beta x)\,\{&A(1+\nu)\sinh(\beta y) + B(1+\nu)\cosh(\beta y) \\
&+ C\left[(1+\nu)\beta y\sinh(\beta y) + 2\cosh(\beta y)\right] \\
&+ D\left[(1+\nu)\beta y\cosh(\beta y) + 2\sinh(\beta y)\right]\,\} + u_0, \\
v(\boldsymbol{x}) = -\frac{\beta}{E}\sin(\beta x)\,\{&A(1+\nu)\cosh(\beta y) + B(1+\nu)\sinh(\beta y)
\end{aligned}
$$

$$+ C\left[(1+\nu)\beta y\cosh(\beta y) - (1-\nu)\sinh(\beta y)\right]$$

$$+ D\left[(1+\nu)\beta y\sinh(\beta y) - (1-\nu)\cosh(\beta y)\right]\Big\},$$

where the constants A, B, C, D, β, u_0 are detailed in [98]. In Figure 4.12, we show a few sample meshes for the beam, and in Figure 4.13 we show the convergence results. From these figures, we observe that optimal convergence rates in Sobolev norms are achieved for both $k = 2$ and $k = 3$.

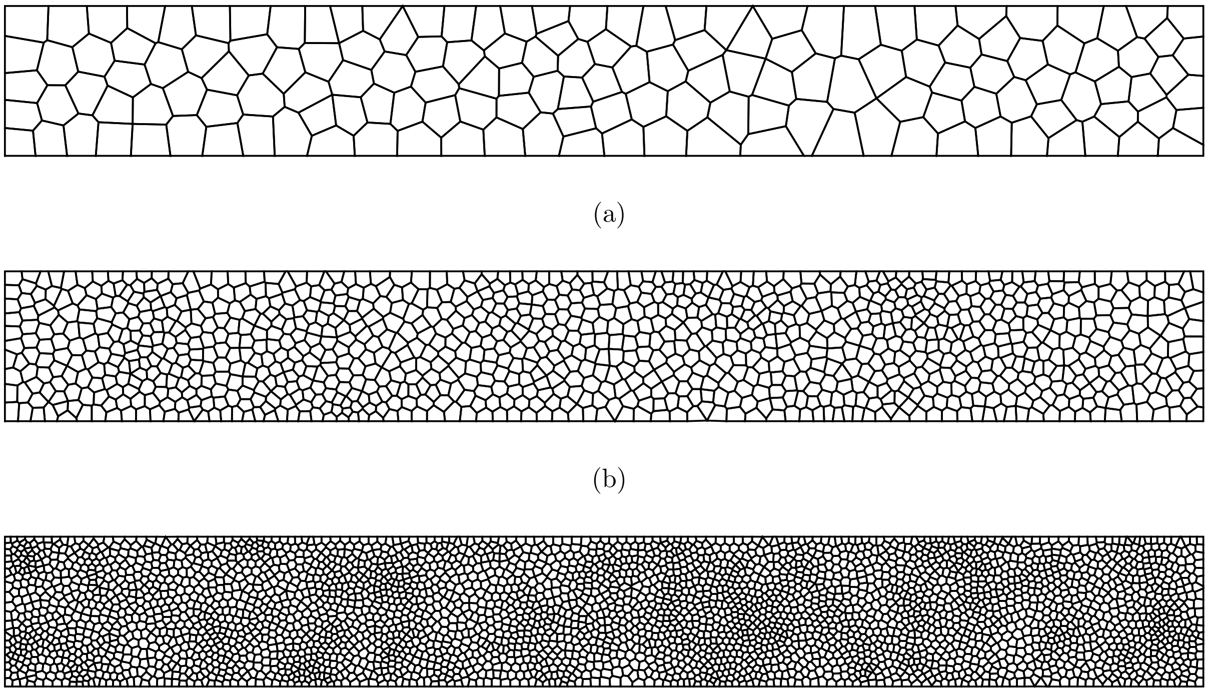
(a)

(b)

(c)

Figure 4.12. Polygonal meshes for the loaded beam problem. (a) 150 elements, (b) 1000 elements and (c) 3500 elements.

We also test this problem with nonconvex meshes. We start with a uniform rectangular mesh, then we split each element into a convex quadrilateral and a non-convex hexagonal element. We show a few sample meshes in Figure 4.14. In Figure 4.15, the results show that the errors on nonconvex meshes still retains the optimal convergence rate.

4.4.4. Infinite plate with a circular hole. Finally, we revist the infinite plate with a circular hole problem used earlier to test the first-order stabilization-free VEM in the previous chapter (see Section 3.5.4). For the first-order case, it was shown that the SF-VEM was able to produce

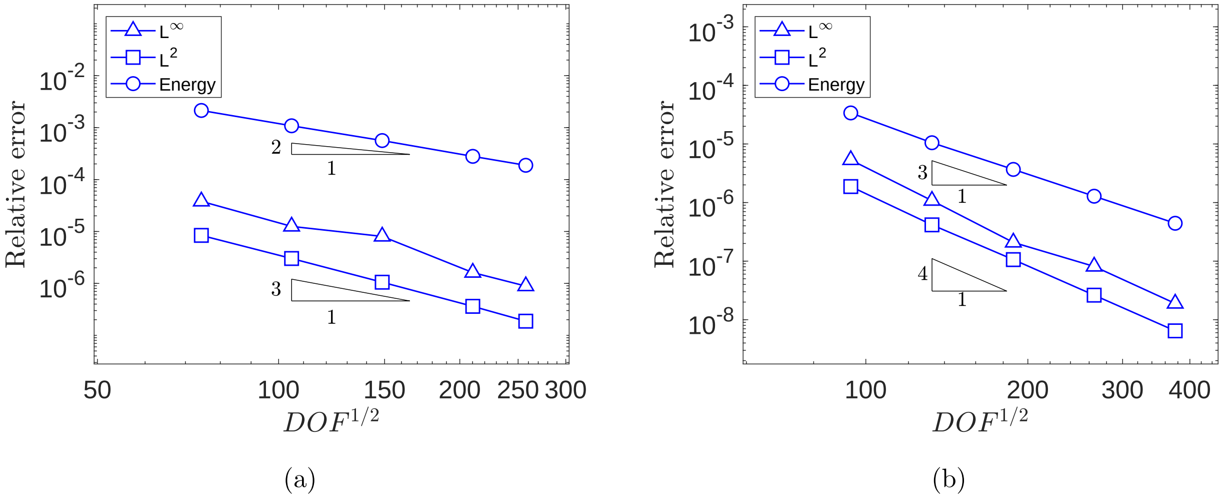

FIGURE 4.13. Convergence curves of serenedipity VEM on convex meshes for sinusoidal loaded beam problem. (a) $k = 2$ and (b) $k = 3$.

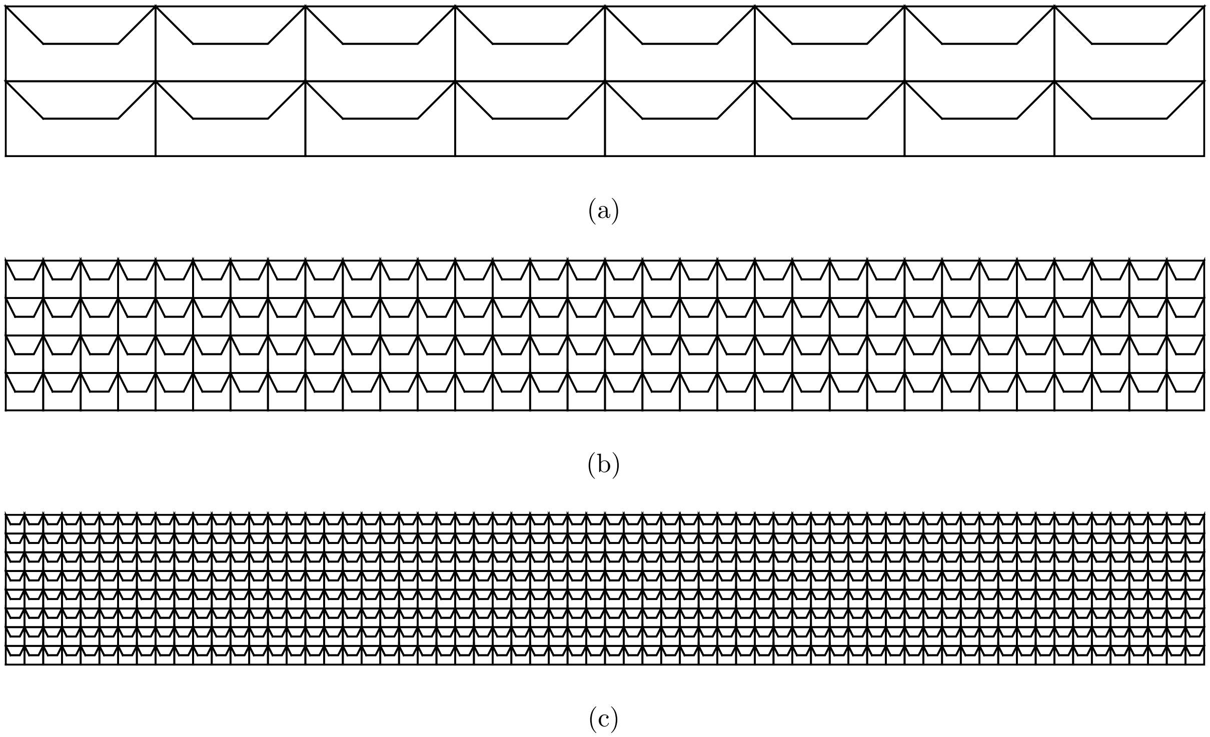

FIGURE 4.14. Nonconvex polygonal meshes for the loaded beam problem. (a) 32 elements, (b) 256 elements and (c) 1024 elements.

results that matched theoretical convergence results. However, it is known from [5,16], that standard VEM methods with order $k \geq 2$ will suffer from loss of convergence rates when approximating

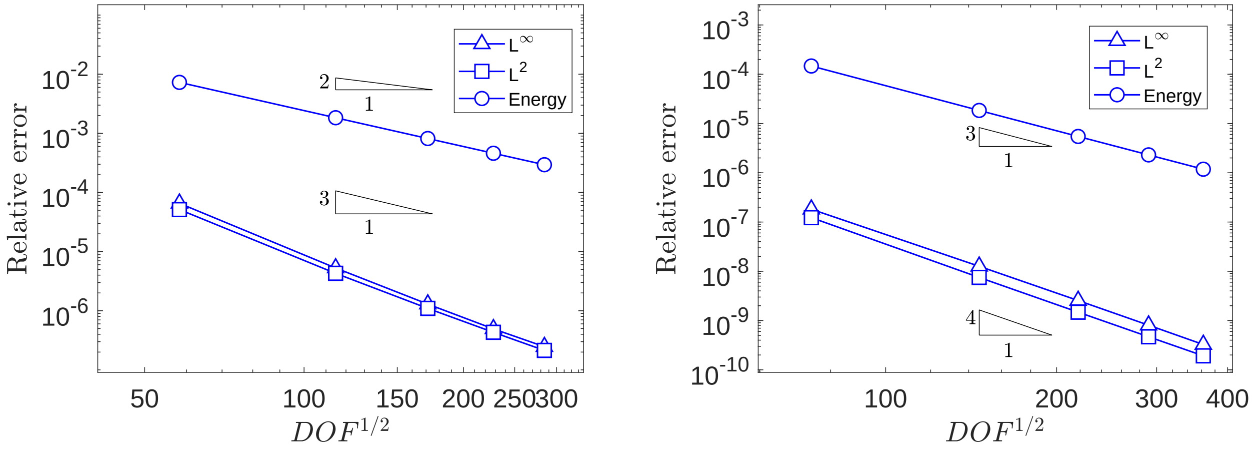

(a) (b)

FIGURE 4.15. Convergence curves of serendipity VEM on nonconvex meshes for sinusoidal loaded beam problem. (a) $k = 2$ and (b) $k = 3$.

domains with curved edges. We see this result in Figure 4.17, where both the second- and third-order methods failed to attain the optimal convergence rates. With this result, it is natural to look into the extension of stabilization free methods onto elements with curved edges.

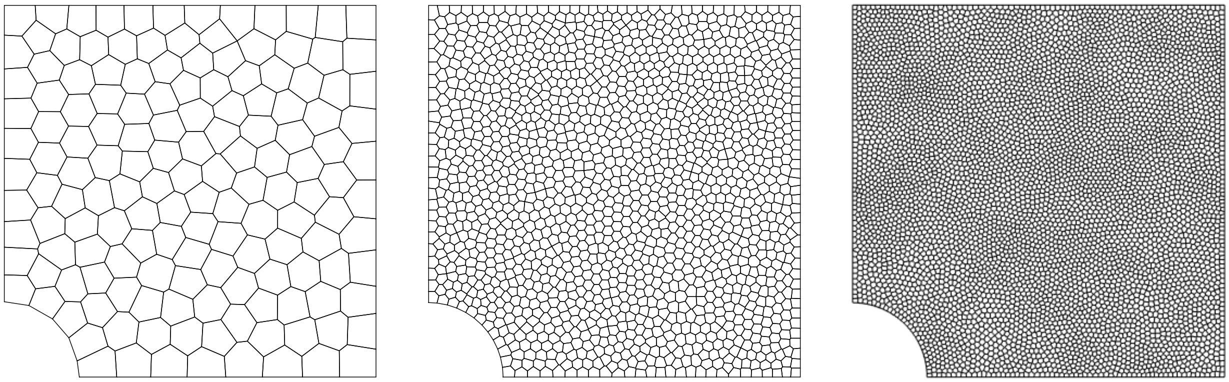

(a) (b) (c)

FIGURE 4.16. Polygonal meshes for the plate with a circular hole problem. (a) 250 elements, (b) 1500 elements, and (c) 6000 elements.

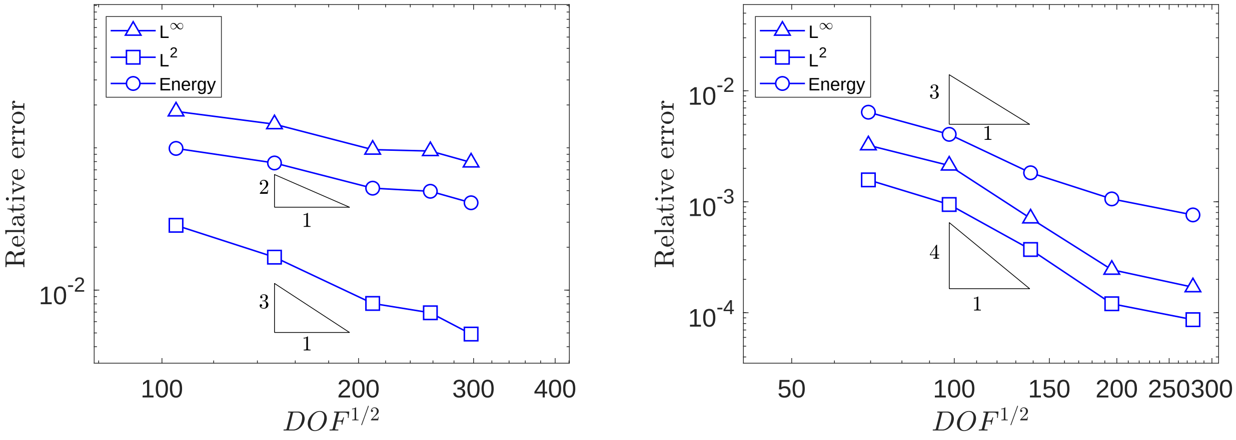

(a) (b)

FIGURE 4.17. Convergence curves of serendipity VEM for plate with a circular hole problem. (a) $k = 2$ and (b) $k = 3$.

CHAPTER 5

Stress-Hybrid Virtual Element Method on Quadrilateral Meshes

In computational mechanics, it is known that many standard displacement-based finite or virtual element methods will suffer from volumetric locking as the material approaches the incompressible limit and from shear locking in bending-dominated problems. One technique to reduce this locking is by using a stress-based hybrid formulation first introduced in [89]. Starting with the Hellinger–Reissner two-field functional, the stress and displacement fields can be independently varied and chosen to retain stability and have optimal bending properties. The stress field is then condensed on each element so that the method is purely displacement based. By following the developments in [43, 89, 90], we introduce a stress-hybrid approach with a five-parameter stress field to construct a stabilization-free virtual element method for quadrilateral elements. Although the virtual element method is applicable to very general polygonal and polyhedral meshes, the majority of current industrial applications still rely on standard finite element meshes (triangles and quadrilaterals in two dimensions). Therefore, in this chapter we focus on formulating the stress-hybrid VEM on general quadrilateral meshes and in the next chapter we extend this approach to six-noded triangular meshes.

In this chapter, we first present the Hellinger–Reissner variational principle, then apply it to construct the weak formulation and a stress projection operator. Following the procedure in Section 3.2, we define an enhanced virutal element space. Next, we discuss the choice of stress basis functions and describe the numerical implementation of the method. Finally, numerical results comparing the SH-VEM to the B-bar VEM [85] are presented on a series of benchmark problems with $\nu \to 0.5$ (nearly-incompressible): bending of a thin cantilever bean, Cook's membrane under shear load, infinite plate with a hole, pressurized cylinder and the flat punch.

This chapter is based on the work published in [38].

5.1. Hellinger–Reissner variational principle

In the previous chapters, we constructed the weak form directly from the governing boundary-value problem; however, for more general applications, it is useful to start from a variational principle. In the next two chapters, we utilize the Hellinger–Reissner variational formulation for linear elasticity. The Hellinger–Reissner formulation assumes that the displacement field and the stress field are independent and that the stress field does not satisfy the constitutive relation pointwise. This gives more flexibility in choosing an approximation for the displacement and stress spaces to avoid locking. The weak form is recovered by finding the stationary values of the Hellinger–Reissner functional given by:

$$\Pi_{\mathrm{HR}}[\boldsymbol{u}, \boldsymbol{\sigma}] = -\frac{1}{2}\int_{\Omega} \boldsymbol{\sigma} : \mathbb{C}^{-1} : \boldsymbol{\sigma}\, d\boldsymbol{x} + \int_{\Omega} \boldsymbol{\sigma} : \nabla_s \boldsymbol{u}\, d\boldsymbol{x} - \int_{\Omega} \boldsymbol{b} \cdot \boldsymbol{u}\, d\boldsymbol{x} - \int_{\Gamma_t} \bar{\boldsymbol{t}} \cdot \boldsymbol{u}\, ds. \tag{5.1}$$

After taking the first variation and requiring it to be stationary, we obtain the expression

$$\begin{aligned}\delta\Pi_{\mathrm{HR}}[\boldsymbol{u}, \boldsymbol{\sigma}; \delta\boldsymbol{u}, \delta\boldsymbol{\sigma}] = \int_{\Omega} \delta\boldsymbol{\sigma} : \left(\nabla_s \boldsymbol{u} - \mathbb{C}^{-1} : \boldsymbol{\sigma}\right)\, d\boldsymbol{x} + \int_{\Omega} \boldsymbol{\sigma} : \nabla_s(\delta\boldsymbol{u})\, d\boldsymbol{x} - \int_{\Omega} \boldsymbol{b} \cdot \delta\boldsymbol{u}\, d\boldsymbol{x} \\ - \int_{\Gamma_t} \bar{\boldsymbol{t}} \cdot \delta\boldsymbol{u}\, ds = 0 \quad \forall \delta\boldsymbol{u} \in \mathcal{V}_u,\ \delta\boldsymbol{\sigma} \in \mathcal{V}_\sigma,\end{aligned} \tag{5.2}$$

where $\mathcal{V}_u$ contains vector-valued functions in the Hilbert space $[H^1(\Omega)]^2$ that also vanish on Γ_u, whereas $\mathcal{V}_\sigma$ contains functions in $(L^2)^{2\times 2}_{\mathrm{sym}}$. This gives us the weak statement of the equilibrium equations and strain-displacement relations:

$$\int_{\Omega} \boldsymbol{\sigma} : \nabla_s(\delta\boldsymbol{u})\, d\boldsymbol{x} - \int_{\Omega} \boldsymbol{b} \cdot \delta\boldsymbol{u}\, d\boldsymbol{x} - \int_{\Gamma_t} \bar{\boldsymbol{t}} \cdot \delta\boldsymbol{u}\, ds = 0 \quad \forall \delta\boldsymbol{u} \in \mathcal{V}_u, \tag{5.3a}$$

$$\int_{\Omega} \delta\boldsymbol{\sigma} : \left(\nabla_s \boldsymbol{u} - \mathbb{C}^{-1} : \boldsymbol{\sigma}\right)\, d\boldsymbol{x} = 0 \quad \forall \delta\boldsymbol{\sigma} \in \mathcal{V}_\sigma. \tag{5.3b}$$

5.2. Virtual element discretization

Let $\mathcal{T}^h$ be a decomposition of Ω into nonoverlapping quadrilaterals (see Figure 5.1). For each quadrilateral $E \in \mathcal{T}^h$, let h_E denote its diameter, $\boldsymbol{x}_E$ its centroid, and $\boldsymbol{x}_i = (x_i, y_i)$ the coordinate of the i-th vertex.

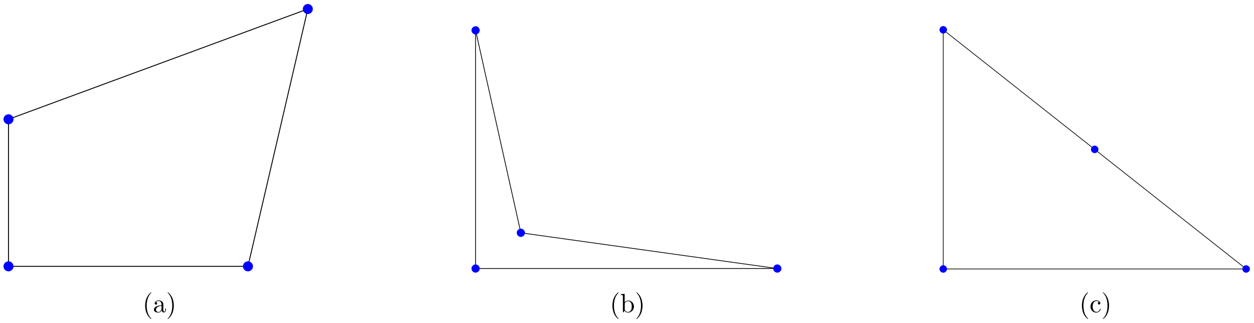
(a) (b) (c)

FIGURE 5.1. Examples of admissible elements in the stress-hybrid virtual element method (a) convex quadrilateral, (b) nonconvex quadrilateral and (c) degenerate quadrilateral.

5.2.1. Stress-hybrid projection operator. We now define the projection operator for the stress-hybrid formulation. On choosing $\delta\boldsymbol{\sigma} = \mathbb{P} \in [\mathbb{P}_\ell(E)]^{2\times 2}_{\text{sym}}$ and $\boldsymbol{\sigma} \in [\mathbb{P}_\ell(E)]^{2\times 2}_{\text{sym}}$ in (5.3b), we have

$$\int_E \mathbb{P} : \left(\nabla_s \boldsymbol{u} - \mathbb{C}^{-1} : \boldsymbol{\sigma}\right) \, d\boldsymbol{x} = 0.$$

This condition is true for all $\mathbb{P} \in [\mathbb{P}_\ell(E)]^{2\times 2}_{\text{sym}}$, so we can view $\mathbb{C}^{-1} : \boldsymbol{\sigma}$ as a projection of $\nabla_s \boldsymbol{u}$ with respect to the space $[\mathbb{P}_\ell(E)]^{2\times 2}_{\text{sym}}$. Now, let the assumed stress field be taken as $\sigma := \Pi_\beta \sigma$, where Π_β is the stress projection operator. Then, the orthogonality condition becomes

$$\int_E \mathbb{P} : \left(\nabla_s \boldsymbol{u} - \mathbb{C}^{-1} : \Pi_\beta \boldsymbol{\sigma}\right) \, d\boldsymbol{x} = 0 \quad \forall \mathbb{P} \in [\mathbb{P}_\ell(E)]^{2\times 2}_{\text{sym}}, \tag{5.4a}$$

or equivalently

$$\int_E \mathbb{P} : \mathbb{C}^{-1} : \Pi_\beta \boldsymbol{\sigma} \, d\boldsymbol{x} = \int_E \mathbb{P} : \nabla_s \boldsymbol{u} \, d\boldsymbol{x} \quad \forall \mathbb{P} \in [\mathbb{P}_\ell(E)]^{2\times 2}_{\text{sym}}. \tag{5.4b}$$

After applying the divergence theorem and simplifying, we obtain

$$\int_E \mathbb{P} : \mathbb{C}^{-1} : \Pi_\beta \boldsymbol{\sigma} \, d\boldsymbol{x} = \int_{\partial E} (\mathbb{P} \cdot \boldsymbol{n}) \cdot \boldsymbol{u} \, ds - \int_E (\nabla \cdot \mathbb{P}) \cdot \boldsymbol{u} \, d\boldsymbol{x}, \tag{5.5}$$

where $\boldsymbol{n} = (n_x, n_y)^T$ is the outward unit normal along ∂E. For later implementation, we convert this expression into the associated matrix-vector form. Let $\overline{\mathbb{P}}$, $\overline{\Pi_\beta \boldsymbol{\sigma}}$ be the Voigt representation of $\mathbb{P}$ and $\Pi_\beta \boldsymbol{\sigma}$, respectively. Then, (5.5) can be written as

$$\int_E \overline{\mathbb{P}}^T \boldsymbol{C}^{-1} \overline{\Pi_\beta \boldsymbol{\sigma}} \, d\boldsymbol{x} = \int_{\partial E} \overline{\mathbb{P}}^T \boldsymbol{N}^{\partial E} \boldsymbol{u} \, ds - \int_E \left(\boldsymbol{\partial} \overline{\mathbb{P}}\right)^T \boldsymbol{u} \, d\boldsymbol{x} \quad \forall \mathbb{P} \in [\mathbb{P}_\ell(E)]^{2\times 2}_{\text{sym}}, \tag{5.6a}$$

where $\boldsymbol{N}^{\partial E}$ is the representation of the outward normals and $\boldsymbol{\partial}$ is the matrix divergence operator that are given by

$$\boldsymbol{N}^{\partial E} := \begin{bmatrix} n_x & 0 \\ 0 & n_y \\ n_y & n_x \end{bmatrix}, \quad \boldsymbol{\partial} := \begin{bmatrix} \frac{\partial}{\partial x} & 0 & \frac{\partial}{\partial y} \\ 0 & \frac{\partial}{\partial y} & \frac{\partial}{\partial x} \end{bmatrix}. \tag{5.6b}$$

5.2.2. Virtual element space. Following Section 3.2 with $\ell = 1$, we define the first-order vector-valued virtual element space on an element E as [2, 9]:

$$\boldsymbol{V}_h(E) = \Big\{ \boldsymbol{v}_h \in [H^1(E)]^2 : \Delta \boldsymbol{v}_h \in [\mathbb{P}_1(E)]^2,\ \boldsymbol{v}_h|_e \in [\mathbb{P}_1(e)]^2\ \forall e \in \partial E,\ \boldsymbol{v}_h|_{\partial E} \in [C^0(\partial E)]^2, \\ \int_E \boldsymbol{v}_h \cdot \boldsymbol{p}\, d\boldsymbol{x} = \int_E \Pi^\varepsilon \boldsymbol{v}_h \cdot \boldsymbol{p}\, d\boldsymbol{x} \quad \forall \boldsymbol{p} \in [\mathbb{P}_0(E)]^2 \Big\}, \tag{5.7}$$

where Δ is the vector Laplacian operator and Π^ε is the energy projection operator defined in (3.6). On this space, the vector-valued functions are continuous on the boundary and affine along each edge e, so we can choose the degrees of freedom (DOFs) to be the function values at the vertices of E. Each element has a total of eight displacement DOFs. For each element E we also assign a basis for the local space $\boldsymbol{V}_h(E)$. Let $\{\phi_i\}$ be the standard scalar basis functions in standard VEM [9] that satisfy the property $\phi_i(\boldsymbol{x}_j) = \delta_{ij}$. Using the scalar basis, we define the matrix of vector-valued basis functions by

$$\boldsymbol{\varphi} = \begin{bmatrix} \phi_1 & \phi_2 & \phi_3 & \phi_4 & 0 & 0 & 0 & 0 \\ 0 & 0 & 0 & 0 & \phi_1 & \phi_2 & \phi_3 & \phi_4 \end{bmatrix} := \begin{bmatrix} \boldsymbol{\varphi}_1 & \boldsymbol{\varphi}_2 & \ldots \boldsymbol{\varphi}_8 \end{bmatrix}, \tag{5.8a}$$

then any function $\boldsymbol{v}_h \in \boldsymbol{V}_h(E)$ can be represented as:

$$\boldsymbol{v}_h(\boldsymbol{x}) = \sum_{i=1}^{8} \boldsymbol{\varphi}_i(\boldsymbol{x}) v_i = \boldsymbol{\varphi}\boldsymbol{d}, \tag{5.8b}$$

where v_i is the i-th degree of freedom of $\boldsymbol{v}_h$.

REMARK 5.2.1. *In the current and the next chapters, we use a different notation to represent the matrix of basis functions. The matrix* $\boldsymbol{N}^v$ *given in* (3.21b) *is defined for elements with arbitrary many vertices, while in this chapter and the next, the number of vertices is fixed to* $N_E = 4$ *and*

$N_E = 6$, respectively. Therefore, to differentiate between the two cases, we use the notation $\boldsymbol{\varphi}$ to denote the matrix with either 8 or 12 basis functions.

5.3. Numerical implementation

5.3.1. Matrix representation of the stress-hybrid projection. We present the matrix representation of the SH-VEM projection, which relies on the rotated coordinates introduced by Cook [**43**] (see Figure 5.2). In the SH-VEM, an assumed stress ansatz is first defined on E' (rotated element) and then transformed to E using the stress transformation equations. The computation of the element stiffness matrix is carried out on E.

5.3.1.1. *Rotated coordinates.* It is known that using global Cartesian coordinates to construct a 5-term expansion of the stress field leads to an incomplete stress approximation and the resulting element stiffness matrix is not rotationally invariant [**43**, **90**, **93**]. We follow the modification proposed by Cook [**43**] to construct a local coordinate system for each element E. Let $\boldsymbol{x}_P, \boldsymbol{x}_Q, \boldsymbol{x}_R, \boldsymbol{x}_S$ be the midpoints of the edges of element E (see Figure 5.2). Define L_1 and L_2 as the length of the line segments PQ and RS, respectively. Then, we compute the angles

$$\theta_1 = \arctan\left(\frac{y_Q - y_P}{x_Q - x_P}\right), \quad \theta_2 = \arctan\left(\frac{x_R - x_S}{y_S - y_R}\right), \quad \theta = \frac{L_1\theta_1 + L_2\theta_2}{L_1 + L_2}. \tag{5.9}$$

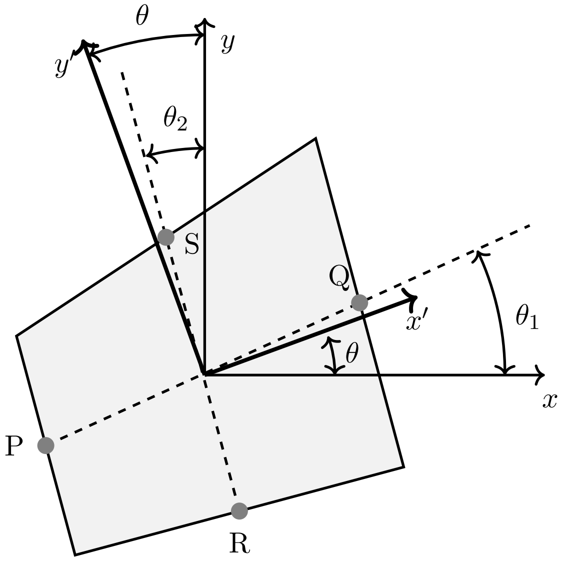

FIGURE 5.2. Construction of the local coordinate system for a distorted quadrilateral.

On using the angle θ, we define the rotated coordinates (x', y') via the transformation

$$\boldsymbol{x}' := \begin{Bmatrix} x' \\ y' \end{Bmatrix} = \begin{bmatrix} c & s \\ -s & c \end{bmatrix} \begin{Bmatrix} x \\ y \end{Bmatrix} := \boldsymbol{Q}\boldsymbol{x}, \quad c = \cos\theta,\ s = \sin\theta. \tag{5.10}$$

5.3.1.2. *Stress-hybrid virtual element formulation.* We now present the stress-hybrid approach, which constructs the stress basis functions and stiffness matrix over the distorted element E. For a quadrilateral element, using the complete linear stress basis given in (3.2) ($\ell = 1$) results in an overly stiff element; therefore, we only use a five-dimensional subset of this basis. On a square, the selection of the stress basis in the stress-hybrid finite element method as [90]

$$\boldsymbol{M}_{5\beta} = \left[\begin{Bmatrix} 1 \\ 0 \\ 0 \end{Bmatrix}, \begin{Bmatrix} 0 \\ 1 \\ 0 \end{Bmatrix}, \begin{Bmatrix} 0 \\ 0 \\ 1 \end{Bmatrix}, \begin{Bmatrix} y \\ 0 \\ 0 \end{Bmatrix}, \begin{Bmatrix} 0 \\ x \\ 0 \end{Bmatrix} \right]$$

ensures that uniform stress states as well as pure bending can be exactly represented. To tailor this approach to VEM, we use this 5β stress expansion in a local coordinate system (E is rotated) and then apply the stress transformation equations to obtain the stress ansatz on E.

Let E' be the rotated element with vertices (x_i', y_i'), centroid $\boldsymbol{x}'_{E'}$ and diameter $h'_{E'}$. In a rotated element E', we assume the stress expansion $\overline{\Pi_\beta \boldsymbol{\sigma}'} = \boldsymbol{P}'\boldsymbol{\beta}'$, where $\boldsymbol{P}'$ is given by

$$\boldsymbol{P}' = \begin{bmatrix} 1 & 0 & 0 & \eta' & 0 \\ 0 & 1 & 0 & 0 & \xi' \\ 0 & 0 & 1 & 0 & 0 \end{bmatrix} = \begin{bmatrix} \boldsymbol{P}_1' & \boldsymbol{P}_2' & \boldsymbol{P}_3' & \boldsymbol{P}_4' & \boldsymbol{P}_5' \end{bmatrix}, \tag{5.11a}$$

and the rotated scaled monomials are

$$\xi' = \frac{x' - x'_{E'}}{h'_{E'}}, \quad \eta' = \frac{y' - y'_{E'}}{h'_{E'}}. \tag{5.11b}$$

On viewing each column $\boldsymbol{P}_i'$ of the matrix $\boldsymbol{P}'$ as an equivalent tensor $\boldsymbol{\mathcal{P}}_i'$, we apply the rotation matrix $\boldsymbol{Q}$ given in (5.10) to obtain a transformed tensor $\boldsymbol{\mathcal{P}}_i$:

$$\boldsymbol{\mathcal{P}}_i = \boldsymbol{Q}^T \boldsymbol{\mathcal{P}}_i' \boldsymbol{Q}. \tag{5.12}$$

After computing each tensor $\boldsymbol{\mathcal{P}}_i$ and rewriting them in terms of 3×1 vectors $\boldsymbol{P}_i$, we define the matrix $\boldsymbol{P}^*$ by [43]

$$\boldsymbol{P}^* = \begin{bmatrix} \boldsymbol{P}_1 & \boldsymbol{P}_2 & \boldsymbol{P}_3 & \boldsymbol{P}_4 & \boldsymbol{P}_5 \end{bmatrix} = \begin{bmatrix} c^2 & s^2 & -2cs & c^2(c\eta - s\xi) & s^2(c\xi + s\eta) \\ s^2 & c^2 & 2cs & s^2(c\eta - s\xi) & c^2(c\xi + s\eta) \\ cs & -cs & c^2 - s^2 & cs(c\eta - s\xi) & -cs(c\xi + s\eta) \end{bmatrix}, \tag{5.13}$$

where c and s are given in (5.10). Without loss of generality, we choose an orthogonal basis for terms representing constant stresses, which results in the matrix

$$\boldsymbol{P} = \begin{bmatrix} 1 & 0 & 0 & c^2(c\eta - s\xi) & s^2(c\xi + s\eta) \\ 0 & 1 & 0 & s^2(c\eta - s\xi) & c^2(c\xi + s\eta) \\ 0 & 0 & 1 & cs(c\eta - s\xi) & -cs(c\xi + s\eta) \end{bmatrix}. \tag{5.14}$$

We now construct the stress-hybrid projection operator on the space $\boldsymbol{V}_h(E)$ over the original element E with respect to the basis $\boldsymbol{P}$. From (5.6a), we have the relation:

$$\int_E \overline{\mathbb{P}}^T \boldsymbol{C}^{-1} \overline{\Pi_\beta \boldsymbol{\sigma}} \, d\boldsymbol{x} = \int_{\partial E} \overline{\mathbb{P}}^T \boldsymbol{N}^{\partial E} \boldsymbol{u}_h \, ds - \int_E \left(\boldsymbol{\partial} \overline{\mathbb{P}}\right)^T \boldsymbol{u}_h \, d\boldsymbol{x}.$$

Expanding $\boldsymbol{u}_h$ in terms of the basis in $\boldsymbol{V}_h(E)$, we have $\boldsymbol{u}_h = \boldsymbol{\varphi} \boldsymbol{d}$, where $\boldsymbol{d}$ is the displacement vector. We also expand $\overline{\Pi_\beta \boldsymbol{\sigma}}$ in terms of $\boldsymbol{P}$: $\overline{\Pi_\beta \boldsymbol{\sigma}} = \boldsymbol{P}\boldsymbol{\beta}$, and since $\mathbb{P}$ is arbitrary we take $\overline{\mathbb{P}} = \boldsymbol{P}_i \ \ (i = 1, 2, \dots, 5)$. After substituting in (5.6a) for each $i = 1, 2, \dots, 5$ and simplifying, we obtain the system:

$$\left(\int_E \boldsymbol{P}^T \boldsymbol{C}^{-1} \boldsymbol{P} \, d\boldsymbol{x} \right) \boldsymbol{\beta} = \left(\int_{\partial E} \boldsymbol{P}^T \boldsymbol{N}^{\partial E} \boldsymbol{\varphi} \, ds - \int_E (\boldsymbol{\partial} \boldsymbol{P})^T \boldsymbol{\varphi} \, d\boldsymbol{x} \right) \boldsymbol{d}. \tag{5.15}$$

For this choice of $\boldsymbol{P}$, we have $\boldsymbol{\partial}\boldsymbol{P} = \boldsymbol{0}$ (divergence-free), so we obtain

$$\left(\int_E \boldsymbol{P}^T \boldsymbol{C}^{-1} \boldsymbol{P} \, d\boldsymbol{x} \right) \boldsymbol{\beta} = \left(\int_{\partial E} \boldsymbol{P}^T \boldsymbol{N}^{\partial E} \boldsymbol{\varphi} \, ds \right) \boldsymbol{d}. \tag{5.16}$$

Now define the corresponding matrices $\boldsymbol{H}$ and $\boldsymbol{L}$ by

$$\boldsymbol{H} = \int_E \boldsymbol{P}^T \boldsymbol{C}^{-1} \boldsymbol{P} \, d\boldsymbol{x}, \quad \boldsymbol{L} = \int_{\partial E} \boldsymbol{P}^T \boldsymbol{N}^{\partial E} \boldsymbol{\varphi} \, ds, \tag{5.17a}$$

and then the stress coefficients are given by

$$\boldsymbol{\beta} = \boldsymbol{H}^{-1} L \boldsymbol{d} := \boldsymbol{\Pi}_\beta \boldsymbol{d}, \tag{5.17b}$$

where $\mathbf{\Pi}_\beta$ is the matrix representation of the stress-hybrid projection operator with respect to the symmetric tensor polynomial basis $\boldsymbol{P}$.

5.3.2. Element stiffness matrix and element force vector. Following the structure of (5.3a), we define the discrete system using the projection operator $\Pi_\beta \boldsymbol{\sigma}$ by:

$$a_h^E(\boldsymbol{u}_h, \delta \boldsymbol{u}_h) = \ell_h^E(\delta \boldsymbol{u}_h),$$

where

$$\begin{aligned} a_h^E(\boldsymbol{u}_h, \delta \boldsymbol{u}_h) &:= \int_E \overline{\Pi_\beta \boldsymbol{\sigma}(\delta \boldsymbol{u}_h)}^T \boldsymbol{C}^{-1} \overline{\Pi_\beta \boldsymbol{\sigma}(\boldsymbol{u}_h)} \, d\boldsymbol{x}, \\ \ell_h^E(\delta \boldsymbol{u}_h) &:= \int_E (\delta \boldsymbol{u}_h)^T \boldsymbol{b} \, d\boldsymbol{x} + \int_{\Gamma_t \cap \partial E} (\delta \boldsymbol{u}_h)^T \bar{\boldsymbol{t}} \, ds. \end{aligned}$$

Expanding $\overline{\Pi_\beta \boldsymbol{\sigma}}$ in terms of β and applying (5.17b), we obtain

$$a_h^E(\boldsymbol{u}_h, \delta \boldsymbol{u}_h) = (\delta \boldsymbol{d})^T (\mathbf{\Pi}_\beta)^T \left(\int_E \boldsymbol{P}^T \boldsymbol{C}^{-1} \boldsymbol{P} \, d\boldsymbol{x} \right) \mathbf{\Pi}_\beta \boldsymbol{d} := (\delta \boldsymbol{d})^t \boldsymbol{K}_E \boldsymbol{d}, \tag{5.19}$$

where we identify the element stiffness matrix for SH-VEM as

$$\boldsymbol{K}_E = (\mathbf{\Pi}_\beta)^T \left(\int_E \boldsymbol{P}^T \boldsymbol{C}^{-1} \boldsymbol{P} \, d\boldsymbol{x} \right) \mathbf{\Pi}_\beta = \mathbf{\Pi}_\beta^T \boldsymbol{H} \mathbf{\Pi}_\beta. \tag{5.20}$$

In Appendix A, we give an alternate stress-hybrid virtual element formulation based on Cook's approach [43], and show that it is identical to the stress-hybrid element stiffness matrix that is obtained using $\boldsymbol{P}^*$ in (5.13).

Now for every element E, the element force vector is given by

$$\boldsymbol{f}_E := \int_E \boldsymbol{\varphi}^T \boldsymbol{b} \, d\boldsymbol{x} + \int_{\Gamma_t \cap \partial E} \boldsymbol{\varphi}^T \bar{\boldsymbol{t}} \, ds. \tag{5.21}$$

For a low-order method, the first term in (5.21) is approximated by taking the nodal average of the basis functions $\boldsymbol{\varphi}$ and then using a single-point quadrature to compute the integral [37]. The second term is computed using Gauss quadrature over the element edges.

5.3.3. B-bar VEM. The B-bar finite element method [94] is a well-established technique to alleviate volumetric locking for nearly incompressible materials. Recently, a B-bar virtual element formulation has been proposed in [85]. The method was shown to be robust for nearly incompressible problems and delivered more accurate results than the B-bar finite element method. For later numerical tests, we compare the results of the SH-VEM to a B-bar VEM. Following Park et at. [85], we first decompose the material moduli matrix $\boldsymbol{C}$ in terms of its eigenvectors:

$$\boldsymbol{C} = \sum_{i=1}^{3} \lambda_i \boldsymbol{p}_i \boldsymbol{p}_i^T, \tag{5.22}$$

where $(\lambda_i, \boldsymbol{p}_i)$ is the i-th eigenpair of $\boldsymbol{C}$. It is known for plane elasticity that $\boldsymbol{p}_1 = \frac{1}{\sqrt{2}}[1, 1, 0]^T$ and $\lambda_1 = 2\kappa + \frac{2\mu}{3}$, where κ is the bulk modulus and μ is the shear modulus. We express (5.22) as

$$\boldsymbol{C} = \lambda_1 \boldsymbol{p}_1 \boldsymbol{p}_1^T + \sum_{i=2}^{3} \lambda_i \boldsymbol{p}_i \boldsymbol{p}_i^T := \boldsymbol{C}_{\text{dil}} + \boldsymbol{C}_{\text{dev}}. \tag{5.23}$$

The element stiffness matrix in the B-bar formulation is the sum of a consistency matrix and a stabilization matrix. For the consistency matrix $\boldsymbol{K}^c$, we have after simplification:

$$\begin{aligned} \boldsymbol{K}^c &= (\boldsymbol{\Pi}_*^{\boldsymbol{\varepsilon}})^T \left(\int_E (\boldsymbol{S}\boldsymbol{M})^T \boldsymbol{C} (\boldsymbol{S}\boldsymbol{M}) \, d\boldsymbol{x} \right) \boldsymbol{\Pi}_*^{\boldsymbol{\varepsilon}} \\ &= (\boldsymbol{\Pi}_*^{\boldsymbol{\varepsilon}})^T \left(\int_E (\boldsymbol{S}\boldsymbol{M})^T \boldsymbol{C}_{\text{dil}} (\boldsymbol{S}\boldsymbol{M}) \, d\boldsymbol{x} \right) \boldsymbol{\Pi}_*^{\boldsymbol{\varepsilon}} + (\boldsymbol{\Pi}_*^{\boldsymbol{\varepsilon}})^T \left(\int_E (\boldsymbol{S}\boldsymbol{M})^T \boldsymbol{C}_{\text{dev}} (\boldsymbol{S}\boldsymbol{M}) \, d\boldsymbol{x} \right) \boldsymbol{\Pi}_*^{\boldsymbol{\varepsilon}} \\ &:= \boldsymbol{K}_{\text{dil}}^c + \boldsymbol{K}_{\text{dev}}^c, \end{aligned} \tag{5.24}$$

where $\boldsymbol{S}$ is defined in (2.129b), $\boldsymbol{\Pi}_*^{\boldsymbol{\varepsilon}}$ is given in (3.34) and $\boldsymbol{M}$ is:

$$\boldsymbol{M} = \begin{bmatrix} 1 & 0 & -\eta & \eta & \xi & 0 \\ 0 & 1 & \xi & \xi & 0 & \eta \end{bmatrix}.$$

The expression for the stabilization matrix is:

$$\boldsymbol{K}^s = (\boldsymbol{I} - \boldsymbol{\Pi}^{\boldsymbol{\varepsilon}})^T \boldsymbol{\Lambda} (\boldsymbol{I} - \boldsymbol{\Pi}^{\boldsymbol{\varepsilon}}), \tag{5.25a}$$

where $\mathbf{\Pi}^{\varepsilon}$ is the representation of the energy projection with respect to the basis functions $\boldsymbol{\varphi}$ defined by $\mathbf{\Pi}^{\varepsilon} = \boldsymbol{D}\mathbf{\Pi}^{\varepsilon}_{*}$, with

$$\boldsymbol{D} = \begin{bmatrix} \boldsymbol{m}_1(\boldsymbol{x}_1) & \boldsymbol{m}_2(\boldsymbol{x}_1) & \dots & \boldsymbol{m}_6(\boldsymbol{x}_1) \\ \boldsymbol{m}_1(\boldsymbol{x}_2) & \boldsymbol{m}_2(\boldsymbol{x}_2) & \dots & \boldsymbol{m}_6(\boldsymbol{x}_2) \\ \cdots & \cdots & \cdots & \cdots \\ \boldsymbol{m}_1(\boldsymbol{x}_4) & \boldsymbol{m}_2(\boldsymbol{x}_4) & \dots & \boldsymbol{m}_6(\boldsymbol{x}_4) \end{bmatrix}, \tag{5.25b}$$

and $\mathbf{\Lambda}$ is a diagonal matrix with components

$$\mathbf{\Lambda}_{ii} = \max\left((\boldsymbol{K}^{c}_{\text{dev}})_{ii}, \frac{\mu}{2} \right). \tag{5.25c}$$

5.4. Numerical results for SH-VEM on quadrilateral elements

We present a collection of two-dimensional numerical examples for linear elasticity under plane strain conditions. We examine the errors of the displacements in the L^2 norm and energy seminorm, and the L^2 error of the hydrostatic stress. The exact hydrostatic stress (denoted by $\tilde{p}$) and its numerical approximation are computed as:

$$\tilde{p} = \frac{\text{trace}\,(\boldsymbol{\sigma})}{3}, \quad \tilde{p}_h = \frac{1+\nu}{3}\left(\left(\overline{\Pi_\beta \boldsymbol{\sigma}}\right)_1 + \left(\overline{\Pi_\beta \boldsymbol{\sigma}}\right)_2 \right), \tag{5.26}$$

where $\left(\overline{\Pi_\beta \boldsymbol{\sigma}}\right)_i$ is the i-th component of $\overline{\Pi_\beta \boldsymbol{\sigma}}$. The convergence rates are computed using the following discrete error measures:

$$\|\boldsymbol{u} - \boldsymbol{u}_h\|_{\boldsymbol{L}^2(\Omega)} = \sqrt{\sum_E \int_E |\boldsymbol{u} - \Pi^{\varepsilon}\boldsymbol{u}_h|^2 \, d\boldsymbol{x}}, \tag{5.27a}$$

$$\|\tilde{p} - \tilde{p}_h\|_{\boldsymbol{L}^2(\Omega)} = \sqrt{\sum_E \int_E |\tilde{p} - \tilde{p}_h|^2 \, d\boldsymbol{x}}, \tag{5.27b}$$

$$\|\boldsymbol{u} - \boldsymbol{u}_h\|_a = \sqrt{\sum_E \int_E (\overline{\boldsymbol{\sigma}} - \overline{\Pi_\beta \boldsymbol{\sigma}})^T \boldsymbol{C}^{-1} (\overline{\boldsymbol{\sigma}} - \overline{\Pi_\beta \boldsymbol{\sigma}}) \, d\boldsymbol{x}}. \tag{5.27c}$$

5.4.1. Eigenvalue analysis. We first examine the stability of the SH-VEM for rotated elements through an eigenanalysis. From Cook [43], it is known that for a noninvariant method, a rectangular element rotated by $\frac{\pi}{4}$ will contain spurious zero-energy modes. For this test, we take a unit square and rotate it by angle $\gamma = 0, \frac{\pi}{6}, \frac{\pi}{4}, \frac{\pi}{3}$, and then compute the eigenvalues of the element stiffness matrix. The material has Young's modulus $E_Y = 1$ psi and Poisson's ratio $\nu = 0.4999999$.

Three formulations are considered: an unrotated 5β, rotated 5β and an unrotated 7β. In the unrotated formulations, the projection matrix is computed on the original element E without applying the rotated coordinate transformation given in (5.10), and for the 7β formulation a 7-term expansion is used for$\boldsymbol{P}$:

$$\boldsymbol{P} = \begin{bmatrix} 1 & 0 & 0 & \eta & 0 & 0 & \xi \\ 0 & 1 & 0 & 0 & \xi & \eta & 0 \\ 0 & 0 & 1 & 0 & 0 & -\xi & -\eta \end{bmatrix}.$$

Every method has three physical zero eigenvalues that correspond to the zero-energy modes. For a method to be stable the next lowest eigenvalue must be positive and not close to zero. In Table 5.1, we indicate the fourth smallest eigenvalue of the element stiffness matrix for the three formulations. The table shows that both the rotated 5β and the unrotated 7β have their eigenvalues unaffected for any angle γ. However, as γ is increased to $\gamma = \frac{\pi}{4}$, the next lowest eigenvalue of the unrotated 5β formulation becomes zero. This shows that the 5β SH-VEM in global coordinates is not rotationally invariant. Numerical tests also reveal that the 7β formulation ameliorates volumetric locking but is much stiffer for pure bending problems, and therefore both unrotated 5β and 7β formulations are not considered in the remainder of this paper.

Method	$\gamma = 0$	$\gamma = \frac{\pi}{6}$	$\gamma = \frac{\pi}{4}$	$\gamma = \frac{\pi}{3}$
Unrotated 5β	0.444	0.111	0.000	0.111
Rotated 5β	0.444	0.444	0.444	0.444
Unrotated 7β	0.444	0.444	0.444	0.444

TABLE 5.1. Comparison of the fourth-lowest eigenvalue on a square that is rotated by angle γ for three stress-hybrid VEMs.

To further test the stability of the SH-VEM on different convex and nonconvex element types, we consider two additional tests. For the second test, we study the effects of perturbing a vertex of a unit square. We construct quadrilaterals with coordinates $\{(0,0),\ (1,0),\ (\gamma_1,\gamma_2),\ (0,1)\}$, where $\gamma_1, \gamma_2 \in (0.05, 10)$. For every combination of γ_1 and γ_2 we compute the element stiffness matrix on this quadrilateral and then determine its fourth smallest eigenvalue. A few representative elements and a contour plot of the eigenvalues are shown in Figure 5.3. The contour plot reveals that deviations from the unit square decreases the value of the fourth smallest eigenvalue; however, the eigenvalue remains positive and away from zero (greater than 0.003) in all cases. This test shows that no spurious zero eigenvalues appear even for large perturbations of the unit square.

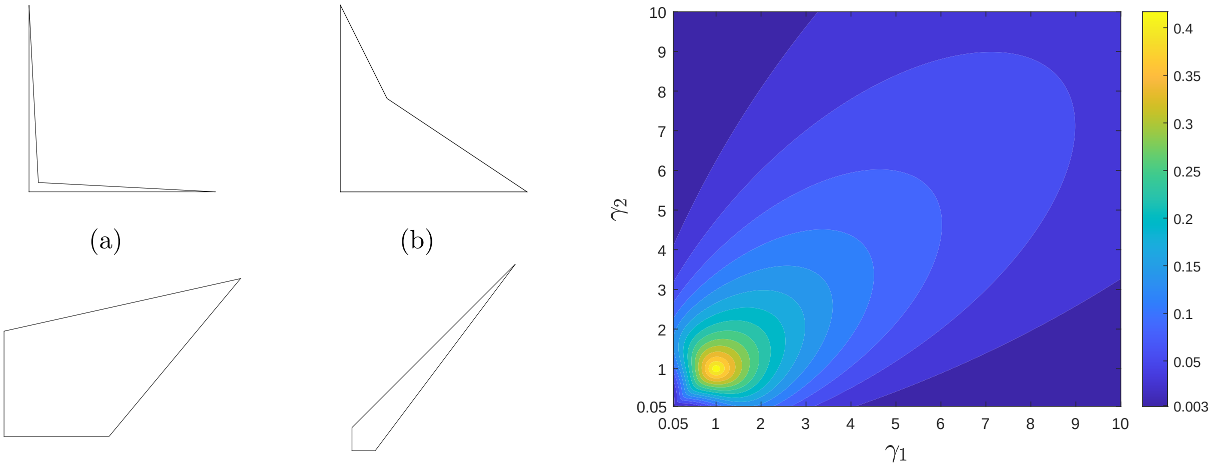

(a) (b) (c) (d) (e)

FIGURE 5.3. (a)–(d) First sequence of distorted quadrilaterals, where the fourth vertex is located at (γ_1, γ_2), and (e) contour plot of the fourth-lowest eigenvalue as a function of γ_1 and γ_2.

In the third test, we examine the effects of varying the angles of a unit square by constructing quadrilaterals with coordinates $\{(0,0), (\cos\gamma_1, -\sin\gamma_1), (1,1), (-\sin\gamma_2, \cos\gamma_2)\}$, where $\gamma_1, \gamma_2 \in \left[-\frac{\pi}{4}, \frac{\pi}{2}\right]$. We again compute the eigenvalues of the element stiffness matrix for different combinations of γ_1 and γ_2. Figure 5.4 shows a few representative elements and a contour plot of the fourth smallest eigenvalue. The contour plot shows that the smallest nonzero eigenvalue remains positive and away from zero (greater than 0.004) for any combination of $\gamma_1, \gamma_2 \in \left[-\frac{\pi}{4}, \frac{\pi}{2}\right]$, and hence demonstrates that distorting a quadrilateral by varying its angle does not affect the stability of SH-VEM.

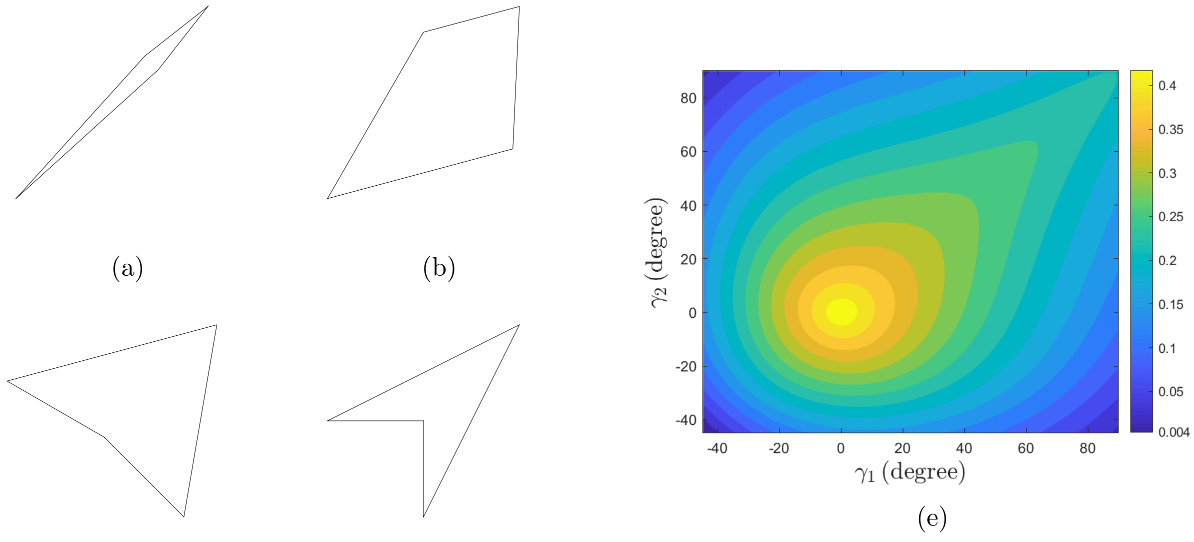
(a) (b) (c) (d) (e)

FIGURE 5.4. (a)–(d) Second sequence of distorted quadrilaterals, where the two vertices that are varied are located at $(\cos\gamma_1, -\sin\gamma_1)$ and $(-\sin\gamma_2, \cos\gamma_2)$, and (e) contour plot of the fourth-lowest eigenvalue as a function of γ_1 and γ_2.

5.4.2. Manufactured problem. We examine the effects of increasing the Poisson ratio to the incompressible limit ($\nu \to 0.5$) on a manufactured problem with a known solution [3]. The problem domain is the unit square and the Young's modulus $E_Y = 1$ psi and the Poisson's ratio $\nu \in \{0.3, 0.4, 0.4999, 0.4999999\}$. The exact solution with associated loading is given by:

$$u(\boldsymbol{x}) = -\cos(\pi x)\sin(\pi y) \quad \text{and} \quad v(\boldsymbol{x}) = \sin(\pi x)\cos(\pi y), \qquad \boldsymbol{b}(\boldsymbol{x}) = \frac{\pi^2}{1+\nu}\begin{Bmatrix} \cos(\pi x)\sin(\pi y) \\ -\sin(\pi x)\cos(\pi y) \end{Bmatrix}.$$

In Figure 5.5, we show a few sample meshes for the unit square, and in Figure 5.6 we show the convergence rates in L^2 error of displacement and the energy seminorm as ν is varied. We assess five formulations: standard VEM [11], SF-VEM [37], second-order stabilization-free serendipity VEM (SFS-VEM) [36], B-bar VEM [85], and SH-VEM. From these plots, we observe that as ν is increased, the standard VEM and SF-VEM fail to converge, while both B-bar VEM and SH-VEM converge with rates that are in agreement with theory. For the SFS-VEM, the rates of convergence in the compressible regime is one order higher in the L^2 error of displacement and energy seminorm than the first-order methods, as expected. However, we find that as ν increases, the rates of convergence become suboptimal and the accuracy of the solution deteriorates. This shows that the SFS-VEM also suffers from volumetric locking.

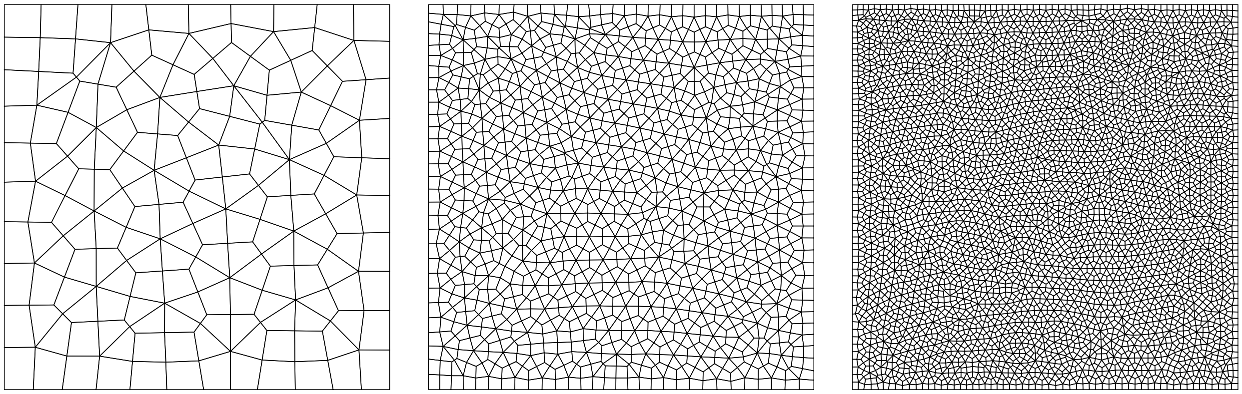

(a) (b) (c)

FIGURE 5.5. Quadrilateral meshes for the manufactured problem. (a) 150 elements, (b) 1500 elements and (c) 6000 elements.

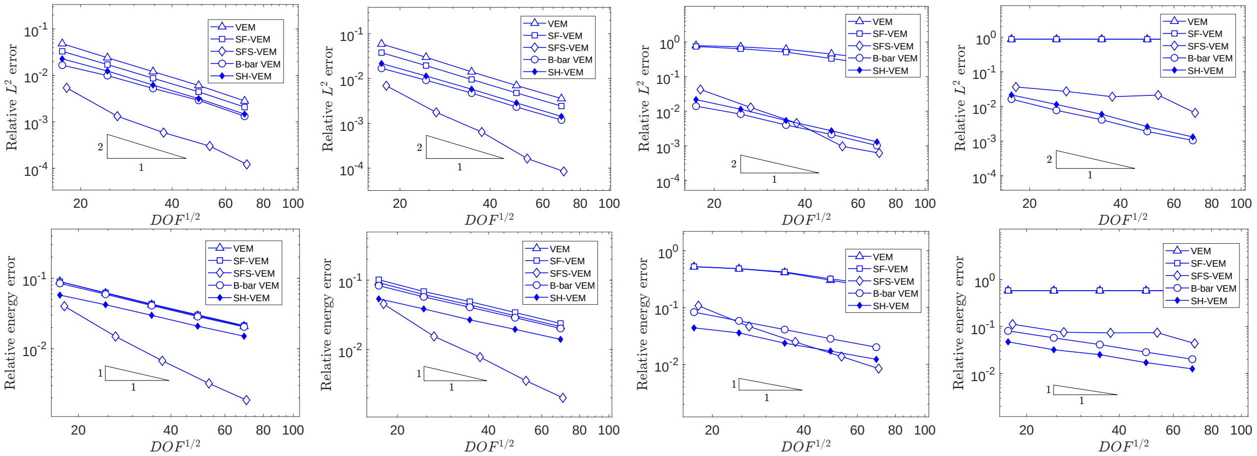

(a) (b) (c) (d)

FIGURE 5.6. Comparison of the convergence of standard VEM, stabilization-free VEM, stabilization-free serendipity VEM, B-bar VEM and SH-VEM for the manufactured problem on unstructured meshes (see Figure 5.5). Each column represents a different value of ν. (a) $\nu = 0.3$, (b) $\nu = 0.4$, (c) $\nu = 0.4999$ and (d) $\nu = 0.4999999$.

We also test this problem on noncovex meshes. We begin with a uniform rectangular mesh and then split each element into a convex and a nonconvex quadrilateral. A few sample meshes are shown in Figure 5.7. Numerical results are presented in Figure 5.8, which reveal that even on nonconvex meshes B-bar VEM and SH-VEM retain optimal rates of convergence, while the SFS-VEM still converges suboptimally in the incompressible limit.

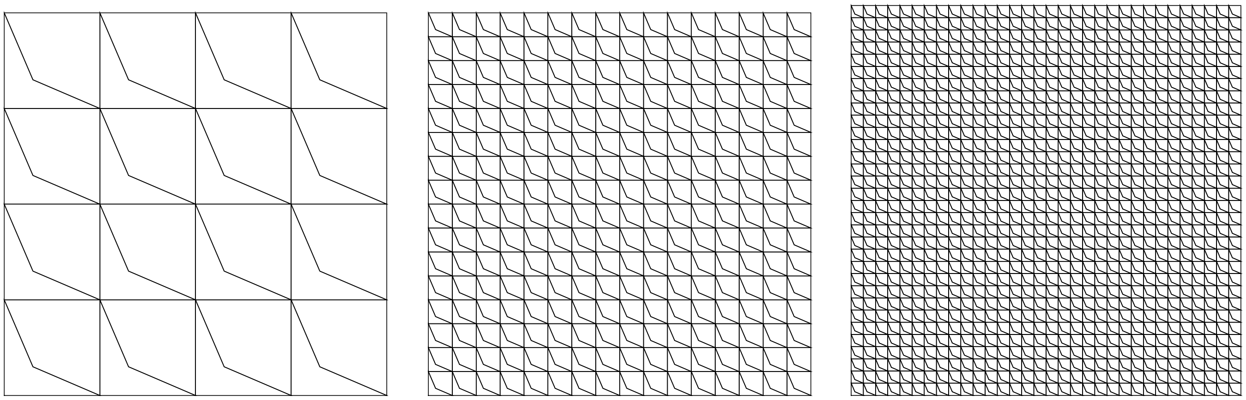

(a) (b) (c)

FIGURE 5.7. Nonconvex quadrilateral meshes for the manufactured problem. (a) 32 elements, (b) 512 elements and (c) 2048 elements.

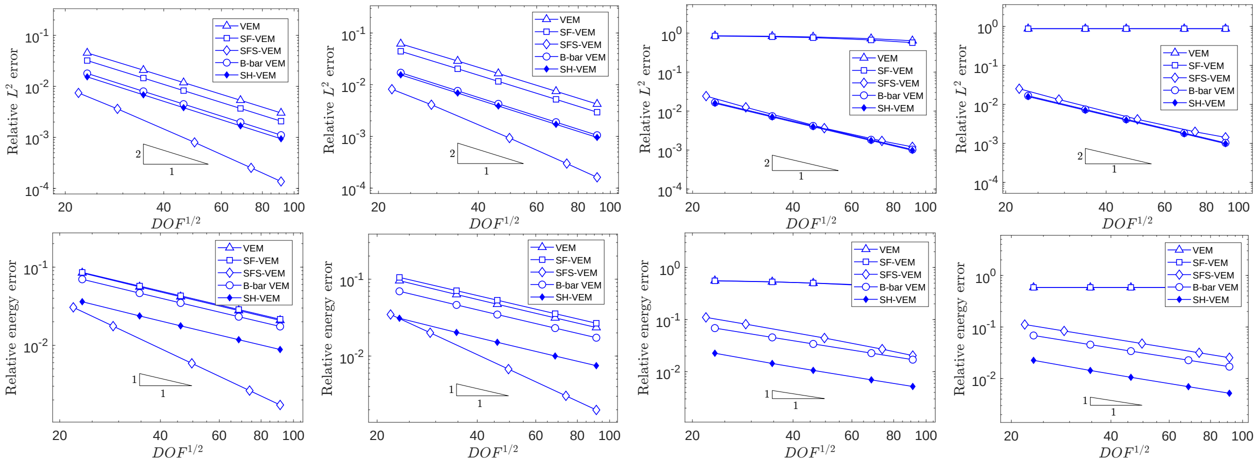

(a) (b) (c) (d)

FIGURE 5.8. Comparison of the convergence of standard VEM, stabilization-free VEM, stabilization-free serendipity VEM, B-bar VEM and SH-VEM for the manufactured problem on nonconvex meshes (see Figure 5.7). Each column represents a different value of ν. (a) $\nu = 0.3$, (b) $\nu = 0.4$, (c) $\nu = 0.4999$ and (d) $\nu = 0.4999999$.

Lastly, we examine the conditioning of the global stiffness matrix to ensure that increasing the Poisson's ratio and varying the element shapes and refinement does not lead to ill-conditioning. In Figure 5.9, we show the condition number of the five methods as $\nu \to 0.5$ on both unstructured and nonconvex meshes. From the plot, we observe that the condition number of SH-VEM is comparable to the other four methods for compressible materials. As the material becomes nearly incompressible, the condition number increases for all methods on the coarsest mesh. However, we observe that the growth of the condition number with refinement for B-bar VEM and SH-VEM is similar to the case when $\nu = 0.3$, which is in agreement with the $\mathcal{O}(h^{-2})$ increase of the stiffness matrix condition number in the finite element method.

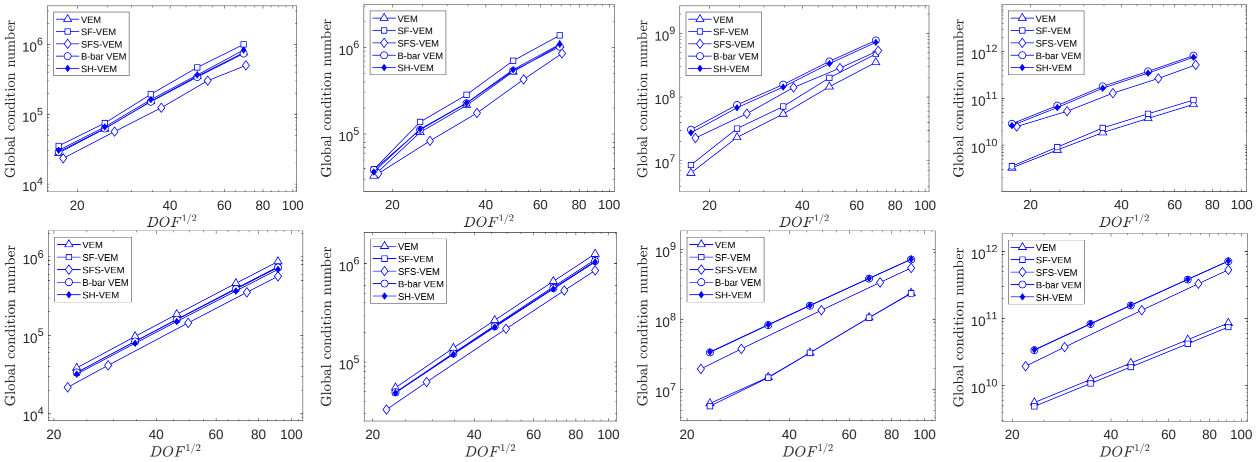

(a) (b) (c) (d)

FIGURE 5.9. Comparison of the conditioning of the global stiffness matrix of the standard VEM, stabilization-free VEM, stabilization-free serendipity VEM, B-bar VEM and SH-VEM for the manufactured problem. The first row is for the unstructured quadrilateral mesh (see Figure 5.5), the second row is for the nonconvex mesh (see Figure 5.7). Each column represents a different value of ν. (a) $\nu = 0.3$, (b) $\nu = 0.4$, (c) $\nu = 0.4999$ and (d) $\nu = 0.4999999$.

5.4.3. Thin cantilever beam. We consider the benchmark problem of a thin cantilever beam under a shear end load [109]. The material has Young's modulus $E_Y = 1 \times 10^5$ psi and $\nu = 0.49995$. The beam has length $L = 32$ inch, height $D = 1$ inch and unit thickness. The left boundary is fixed and a shear end load of $P = -100$ lbf is applied on the right boundary. We use a regular rectangular mesh with $N \in \{1, 2, 4, 8, 16\}$ elements along the height and $10N$ elements along the length. In Figure 5.10, we show a few representative meshes and in Figure 5.11 we compare the rates of convergence of B-bar VEM to SH-VEM in the three error norms. In Figure 5.12, we plot the end displacement of the three methods and contours of the hydrostatic stress for SH-VEM. From these results, we observe that the accuracy of SH-VEM is far superior to B-bar VEM and the displacements in the SH-VEM display superconvergence (close to the exact solution) on coarse rectangular meshes.

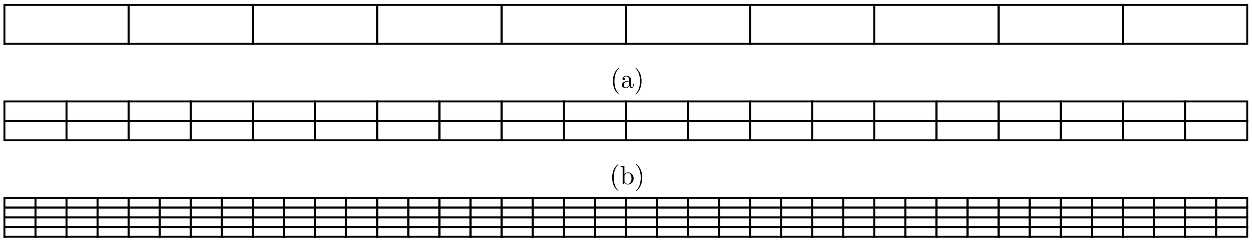

(a)

(b)

(c)

FIGURE 5.10. Rectangular meshes for the cantilever beam problem. (a) 10 elements, (b) 40 elements and (c) 160 elements.

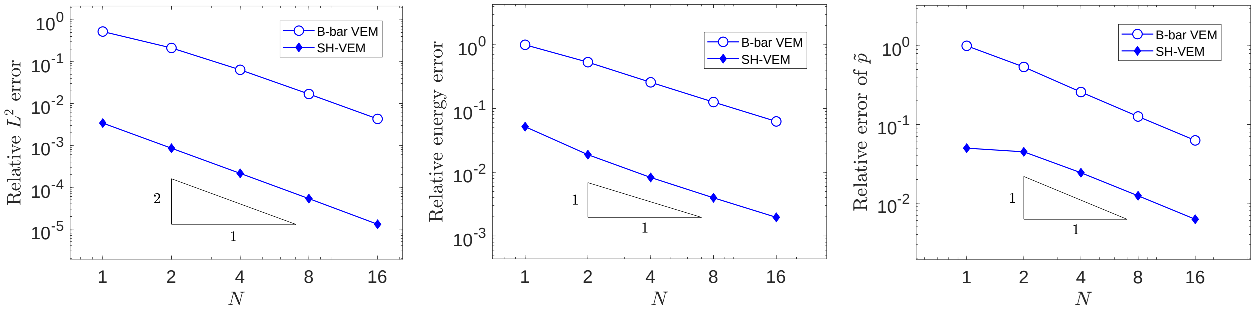

(a) (b) (c)

FIGURE 5.11. Comparison of B-bar VEM and SH-VEM for the thin cantilever beam problem on structured meshes (see Figure 5.10). (a) L^2 error of displacement, (b) energy error and (c) L^2 error of hydrostatic stress, where N is the number of elements along the height of the beam.

We consider another test for the cantilever beam problem using a mesh with either one or two elements along the height and M elements along the length. We choose the number of elements $M \in \{2, 4, 8, 16\}$. The meshes are depicted in Figure 5.13 and the convergence of the tip displacement for the two cases is presented in Figure 5.14. The plots reveal that SH-VEM is accurate even for high aspect ratio elements and is free of shear locking. However, for one element along the height and with refinement along the length, we observe that B-bar VEM converges to a value below the exact value (see Figure 5.14a) and for the case of two elements along the height, the end displacement is not accurate (see Figure 5.14b).

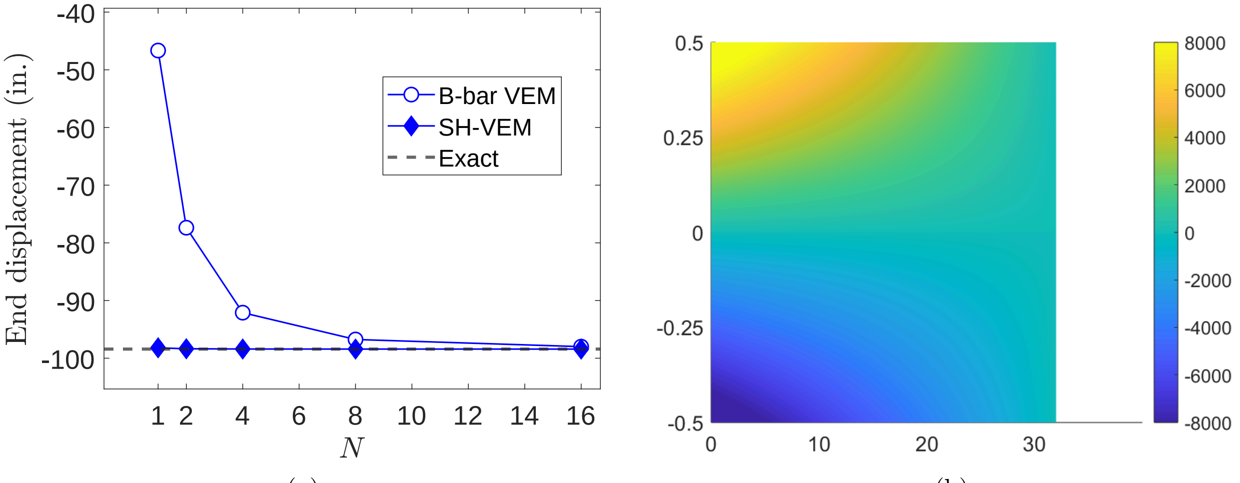

(a)

(b)

FIGURE 5.12. (a) Convergence of the end displacement for the cantilever beam problem. The mesh consists of $10N \times N$ rectangular elements, where N is the number of elements along the height of the beam (see Figure 5.10), (b) contour plot of hydrostatic stress for SH-VEM.

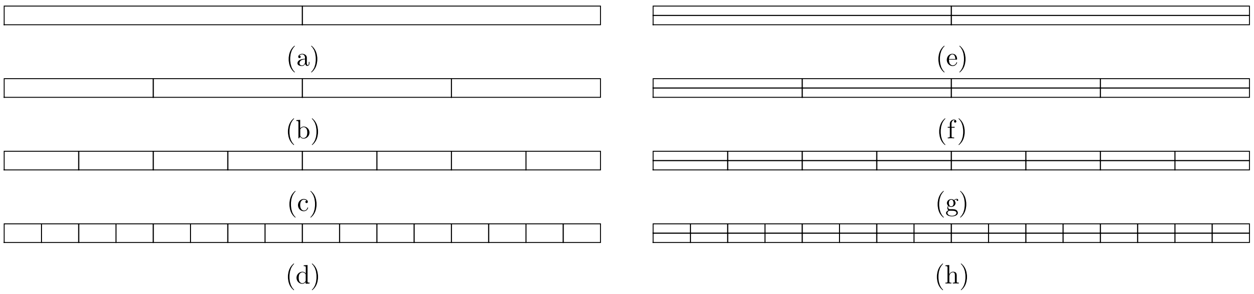

(a)

(b)

(c)

(d)

(e)

(f)

(g)

(h)

FIGURE 5.13. Rectangular meshes for the cantilever beam problem with fixed length to height ratio for each element. (a), (b), (c), (d) 16:1, 8:1, 4:1 and 2:1; and (e), (f), (g), (h) 32:1, 16:1, 8:1 and 4:1.

It is known that distortions of a rectangular mesh can lead to shear locking in the thin beam problem [76]. We study this issue on perturbed trapezoidal meshes that are shown in Figure 5.15. In Figure 5.16, we present the convergence of the end displacement. The plot shows that on such meshes SH-VEM is convergent but with reduced accuracy; however, note that the B-bar formulation fails to converge to the exact end displacement for the case $N = 1$ (see Figure 5.16a).

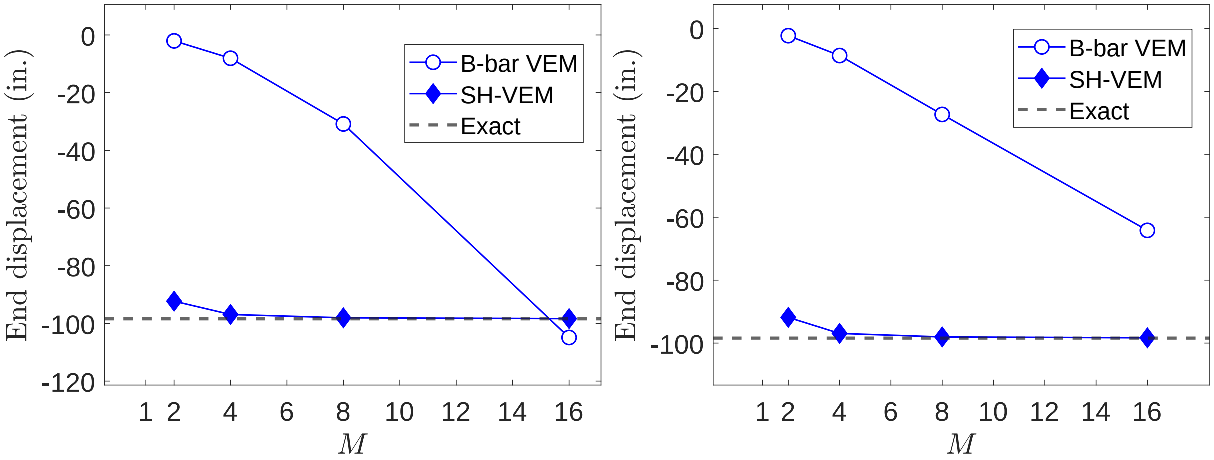

(a) (b)

FIGURE 5.14. Convergence of the end displacement for the cantilever beam problem. The mesh consists of $M \times N$ quadrilaterals, where M is the number of elements along the length of the beam (see Figure 5.13). (a) $N = 1$ and (b) $N = 2$.

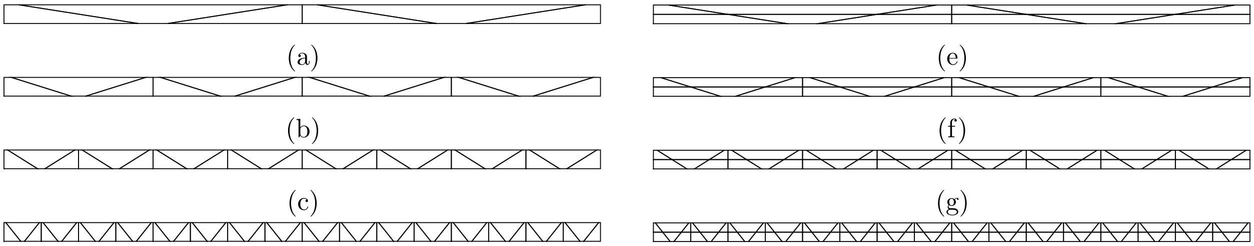

(a) (e) (b) (f) (c) (g) (d) (h)

FIGURE 5.15. Trapezoidal meshes for the cantilever beam problem. Mesh is refined along the length with (a) 1 element along the height and (b) 2 elements along the height.

We also solve the cantilever beam problem on nearly degenerate quadrilateral meshes. We start with a regular rectangular mesh, and then split each element into four quadrilaterals with two of the elements have collapsing edges. A few sample meshes are shown in Figure 5.17. In Figure 5.18, we compare the convergence rates of B-bar VEM and SH-VEM in the three norms, and in Figure 5.19 we present the convergence of the tip displacement as well as the contour plot of the hydrostatic stress using SH-VEM. The plots reveal that B-bar VEM and SH-VEM retain optimal convergence rates. Furthermore, the convergence of SH-VEM is monotonic; however its accuracy is worse when compared to the uniform mesh case. This decrease in accuracy can be attributed to the poor shape (near-degeneracy) quality of the elements.

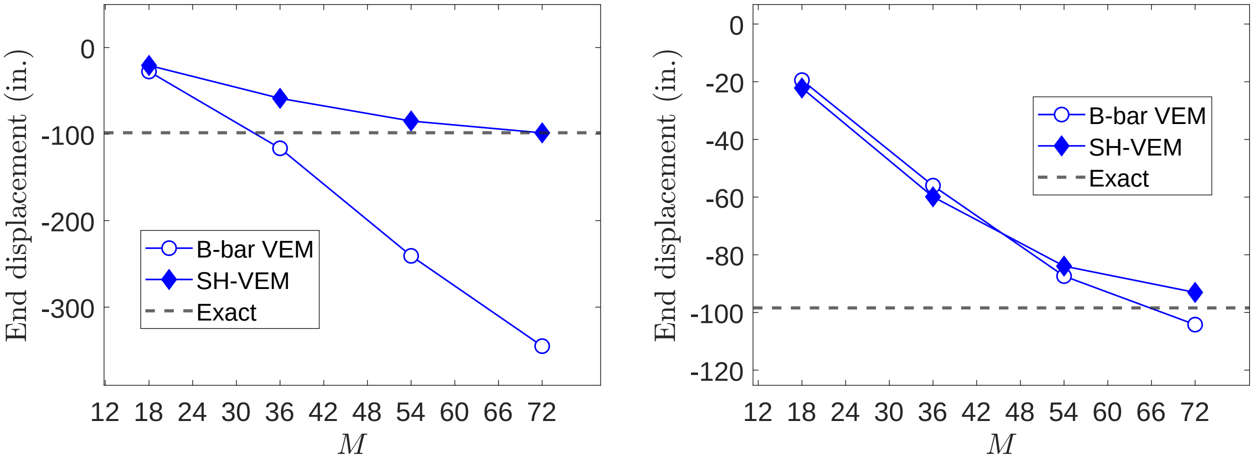

(a)

(b)

FIGURE 5.16. Convergence of the end displacement for the cantilever beam problem. The mesh consists of $M \times N$ trapezoids, where M is the number of elements along the length of the beam (see Figure 5.15). (a) $N = 1$ and $N = 2$.

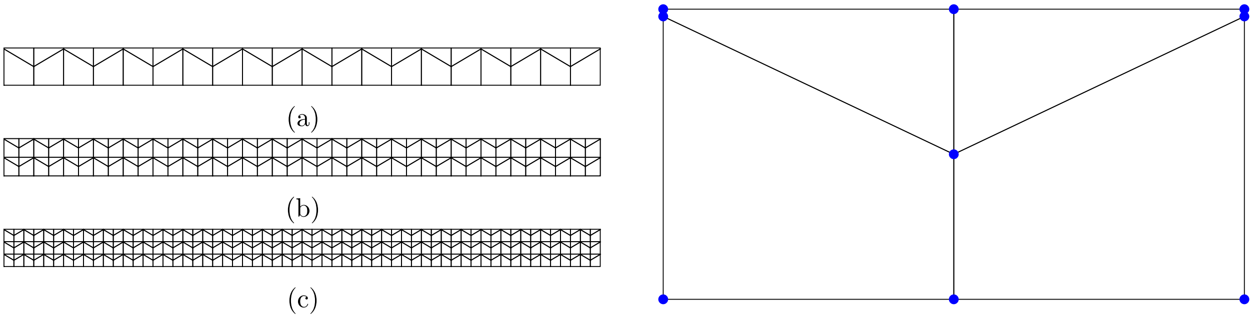

(a)

(b)

(c)

(d)

FIGURE 5.17. Nearly degenerate meshes used for the cantilever beam problem. (a) 40 elements, (b) 160 elements (c) 360 elements, and (d) magnification of a single element split into four quadrilaterals.

5.4.4. Cook's membrane. Here we consider the Cook's membrane problem under shear load [43] (see Figure 5.20). This problem is commonly used to test a combination of bending and shear for nearly-incompressible materials. The material has Young's modulus $E_Y = 250$ psi and Poisson's ratio $\nu = 0.4999999$. The left edge of the membrane is fixed and the right edge has an applied shear load of $F = 6.25$ lbf per unit length. This problem does not have an exact solution; a reference solution for the vertical displacement at the tip of the membrane is $v = 7.769$ inch [85]. We first test this problem on an unstructured quadrilateral mesh. A few sample meshes are shown in Figure 5.20. In Figure 5.21, the convergence of the tip displacement and that of the hydrostatic

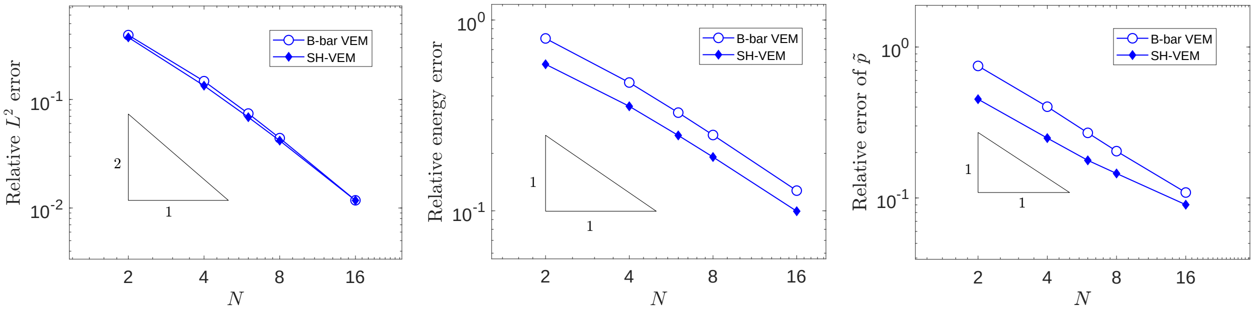

(a) (b) (c)

FIGURE 5.18. Comparison of B-bar VEM and SH-VEM for the thin cantilever beam problem on nearly degenerate meshes (see Figure 5.17). (a) L^2 error of displacement, (b) energy error and (c) L^2 error of hydrostatic stress, where N is the number of elements along the height of the beam.

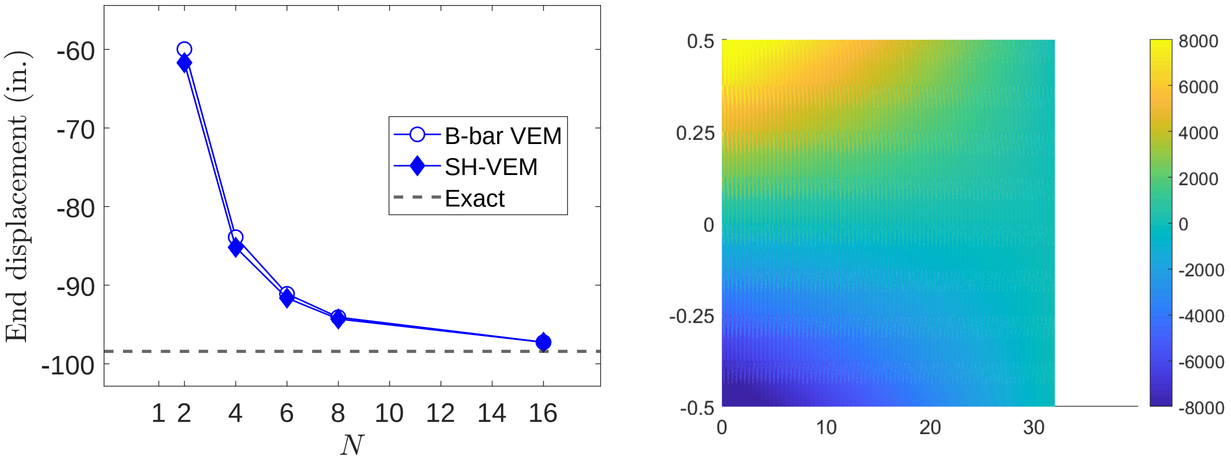

(a) (b)

FIGURE 5.19. (a) Convergence of the end displacement for the cantilever beam problem. The mesh consists of $10N \times N$ nearly degenerate quadrilaterals, where N is the number of elements along the height of the beam (see Figure 5.17), (b) contour plot of hydrostatic stress for SH-VEM.

stress are presented. The plot shows that the B-bar VEM and SH-VEM have comparable accuracy and convergence for the tip displacement. In addition, SH-VEM is able to produce a relatively smooth hydrostatic stress field on an unstructured mesh.

Next, the SH-VEM is now assessed for the Cook's membrane problem on nonconvex meshes. We begin with an unstructured quadrilateral mesh, and then each element is split into a convex and a nonconvex quadrilateral. A few representative meshes are shown in Figure 5.22. The plots of the convergence of tip displacement and the contour of the hydrostatic stress are presented in Figure 5.23. The plots show that even on nonconvex meshes, the convergence of the tip displacement

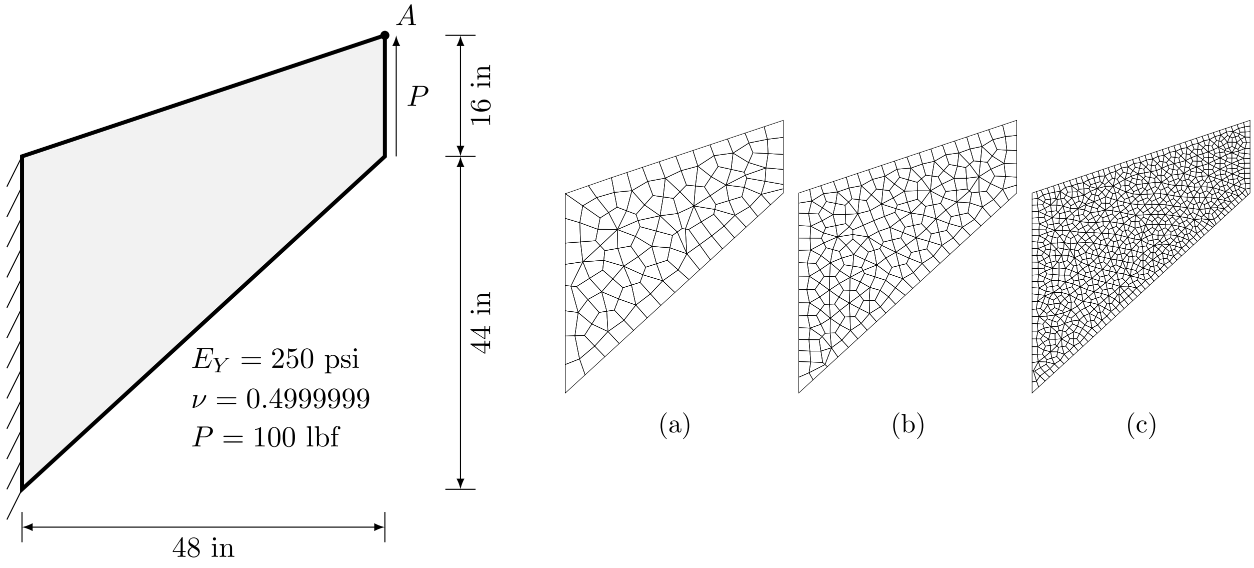

(a) (b) (c)

FIGURE 5.20. (a) Cook's membrane problem. (b), (c), (d) Unstructured quadrilateral meshes with 100 elements, 300 elements and 1000 elements, respectively.

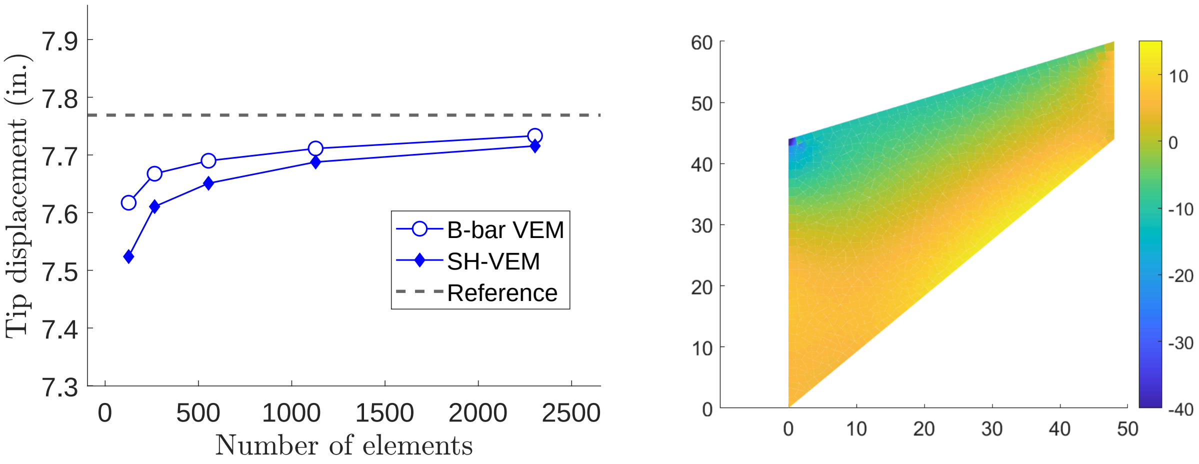

(a) (b)

FIGURE 5.21. (a) Convergence of the tip displacement for Cook's membrane problem. The mesh consists of unstructured quadrilaterals (see Figure 5.20). (b) Contour plot of the hydrostatic stress for SH-VEM.

of B-bar VEM and SH-VEM are proximal, and the contours of the hydrostatic stress for SH-VEM remains relatively smooth.

5.4.5. Plate with a circular hole. We revisit the infinite plate with a circular hole problem used in the previous two chapters (see Section 3.5.4) but now in the incompressible limit. The material has Young's modulus $E_Y = 2 \times 10^7$ psi and Poisson's ratio $\nu = 0.4999999$. We first

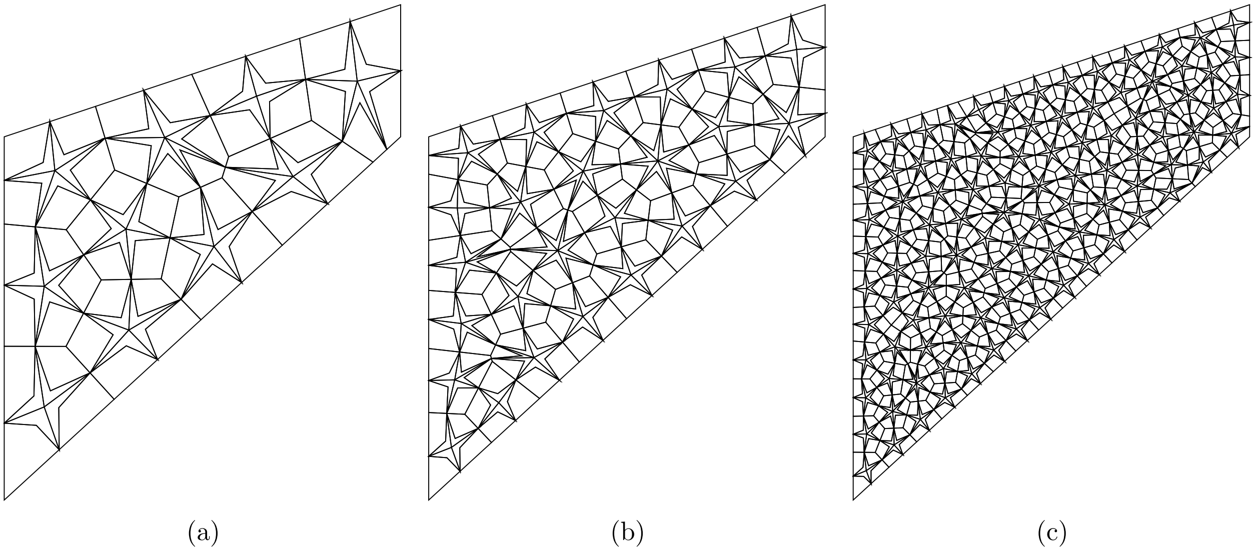
(a) (b) (c)

FIGURE 5.22. Nonconvex quadrilateral meshes for the Cook's membrane problem. (a) 100 elements, (b) 250 elements and (c) 1000 elements.

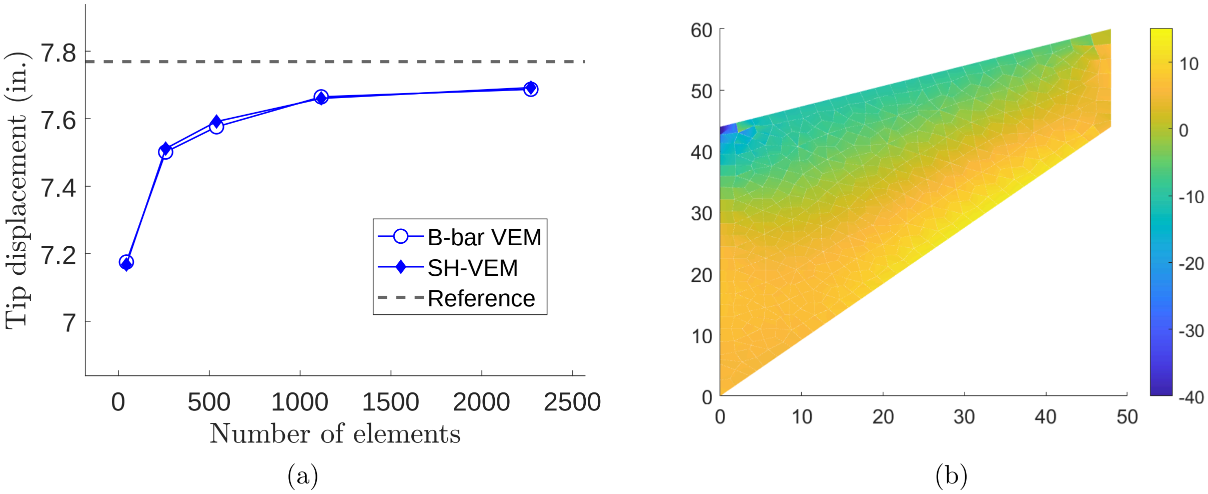

(a) (b)

FIGURE 5.23. (a) Convergence of the tip displacement for Cook's membrane. The mesh consists of nonconvex quadrilaterals (see Figure 5.22). (b) Contour plot of the hydrostatic stress for SH-VEM.

test this problem on structured quadrilateral meshes; a few representative meshes are shown in Figure 5.24. In Figure 5.25, we compare the convergence results of the B-bar formulation and the SH-VEM, and find that both methods deliver optimal convergence rates. In Figure 5.26, we also compare the contours of the hydrostatic stress by the two methods and find that they both are smooth and have comparable accuracy.

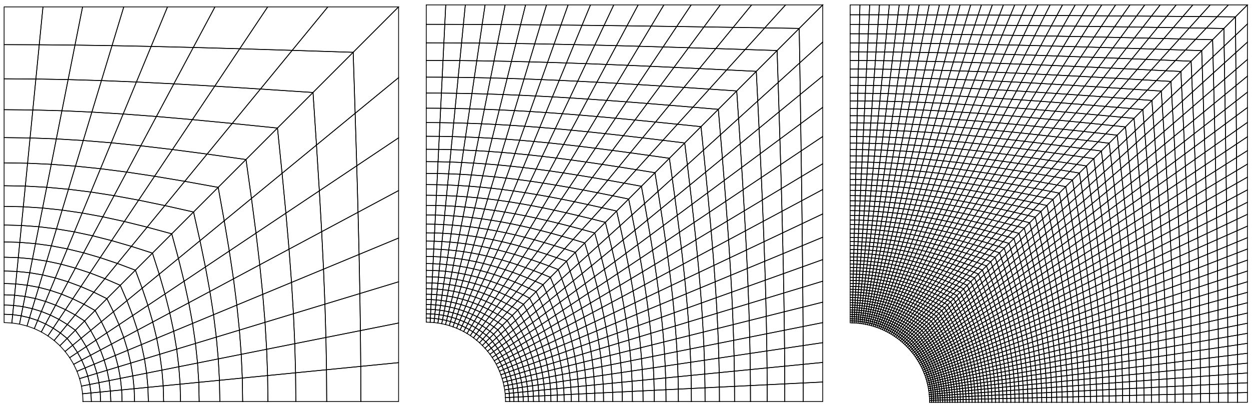

(a) (b) (c)

Figure 5.24. Structured quadrilateral meshes for the plate with a hole problem. (a) 256 elements, (b) 1024 elements and (c) 4096 elements.

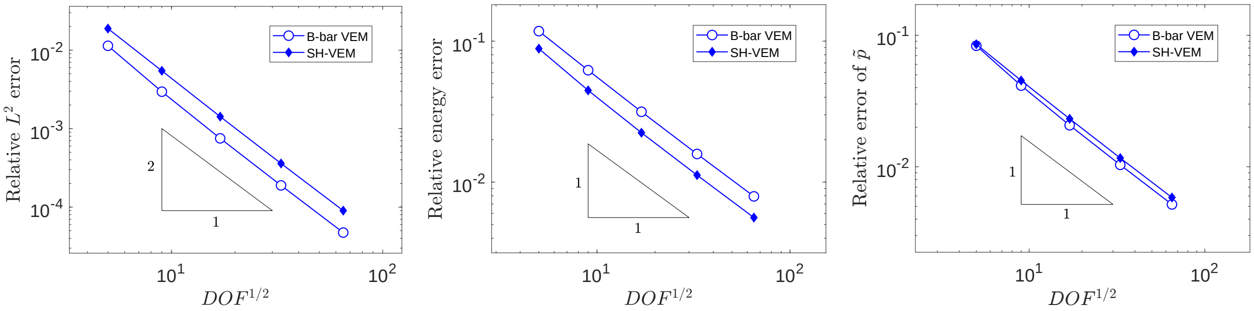

(a) (b) (c)

Figure 5.25. Comparison of SH-VEM and B-bar VEM for the plate with a circular hole problem on structured meshes (see Figure 5.24). (a) L^2 error of displacement, (b) energy error and (c) L^2 error of the hydrostatic stress.

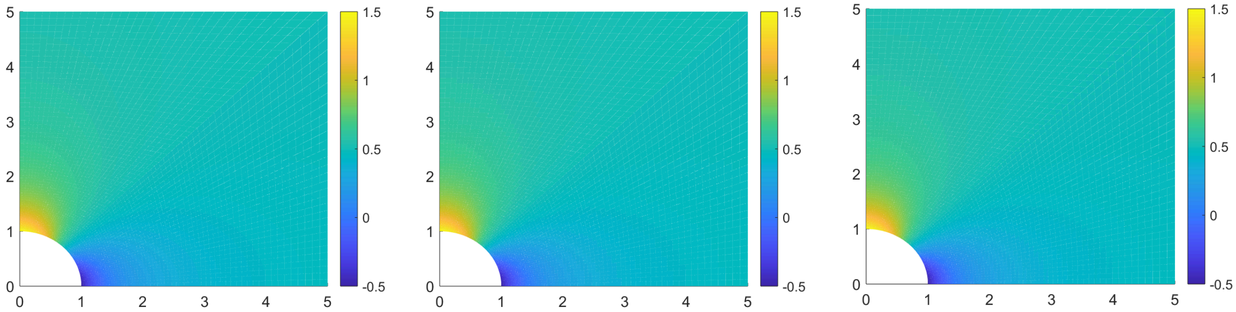

(a) (b) (c)

Figure 5.26. Contour plots of the hydrostatic stress on structured meshes (see Figure 5.24) for the plate with a circular hole problem. (a) exact solution, (b) B-bar VEM, (c) SH-VEM.

We now consider the plate with a circular hole problem on a perturbed mesh. We start with a structured mesh, then for each internal node we perturb its location. Representative meshes are shown in Figure 5.27. In Figure 5.28, we show the convergence rates of the two methods and find that both methods retain optimal convergence on the perturbed mesh. In Figure 5.29, the exact hydrostatic stress and contour plots of the error, $\tilde{p} - \tilde{p}_h$, are shown. The plots reveal that both methods produce relatively smooth error distributions of the hydrostatic stress field, with the B-bar VEM having smaller pointwise error than SH-VEM.

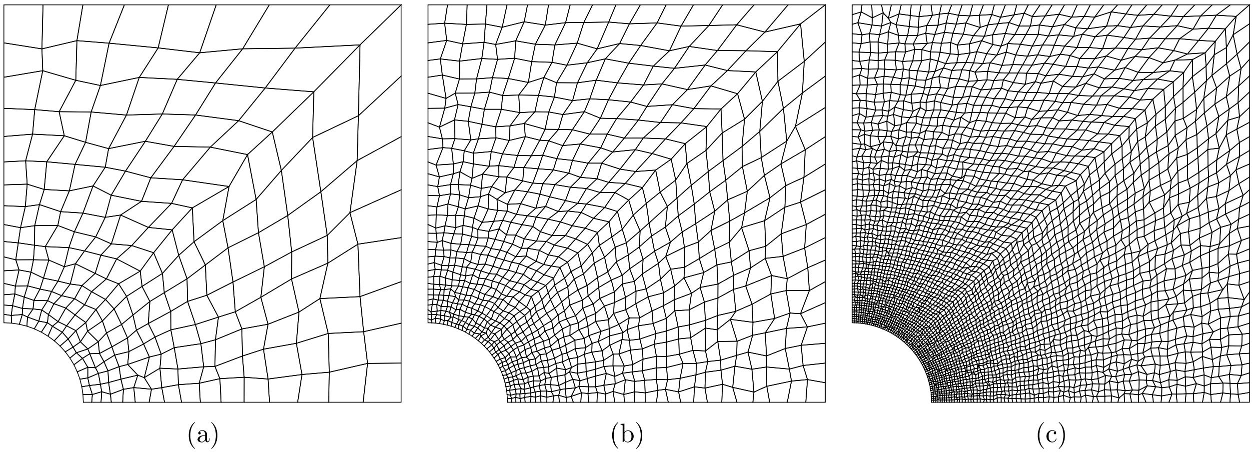

(a) (b) (c)

Figure 5.27. Perturbed quadrilateral meshes for the plate with a hole problem. (a) 256 elements, (b) 1024 elements and (c) 4096 elements.

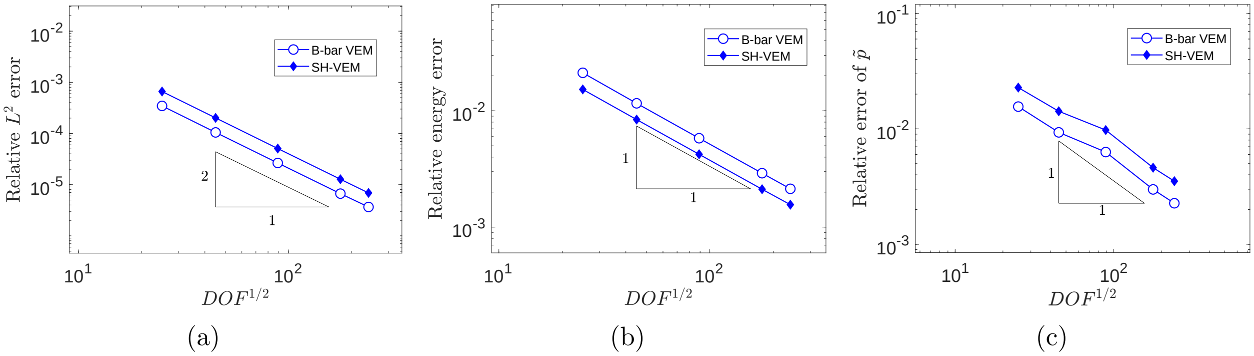

Figure 5.28. Comparison of SH-VEM and B-bar VEM for the plate with a circular hole problem on perturbed meshes (see Figure 5.27). (a) L^2 error of displacement, (b) energy error and (c) L^2 error of hydrostatic stress.

5.4.6. Hollow cylinder under internal pressure. We again consider the problem of a hollow cylinder with inner radius $a = 1$ inch and outer radius $b = 5$ inch under internal pressure [109].

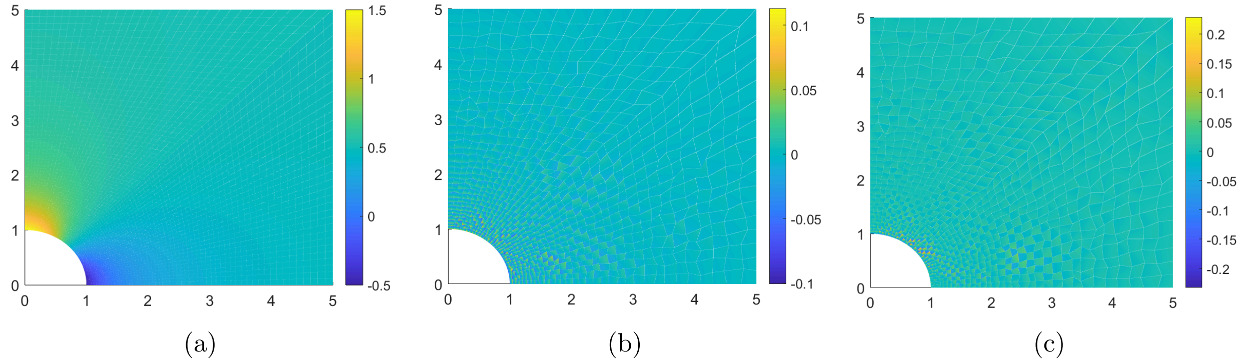

(a) (b) (c)

FIGURE 5.29. Contour plots of the hydrostatic stress for the plate with a circular hole problem on perturbed meshes (see Figure 5.27). (a) exact solution, and error in the hydrostatic stress field, $\tilde{p} - \tilde{p}_h$ for (b) B-bar VEM and (c) SH-VEM.

However, due to symmetry, we model this problem as a quarter cylinder. A uniform pressure of $p = 10^5$ psi is applied on the inner radius, while the outer radius is kept traction-free. The material has Young's modulus $E_Y = 2 \times 10^5$ psi and Poisson's ratio $\nu = 0.4999999$. For this example, the hydrostatic stress field is constant; therefore, we use an element averaged approximation to compute the hydrostatic stress $\tilde{p}_h$. We first examine this problem on structured quadrilateral meshes; a few representative meshes are presented in Figure 5.30. In Figure 5.31, the convergence rates of B-bar VEM and SH-VEM are shown. For both methods, convergence in L^2 norm and energy seminorm is optimal. The contour plots in Figure 5.32 show that both methods are able to reproduce the constant exact hydrostatic stress field on a uniform mesh.

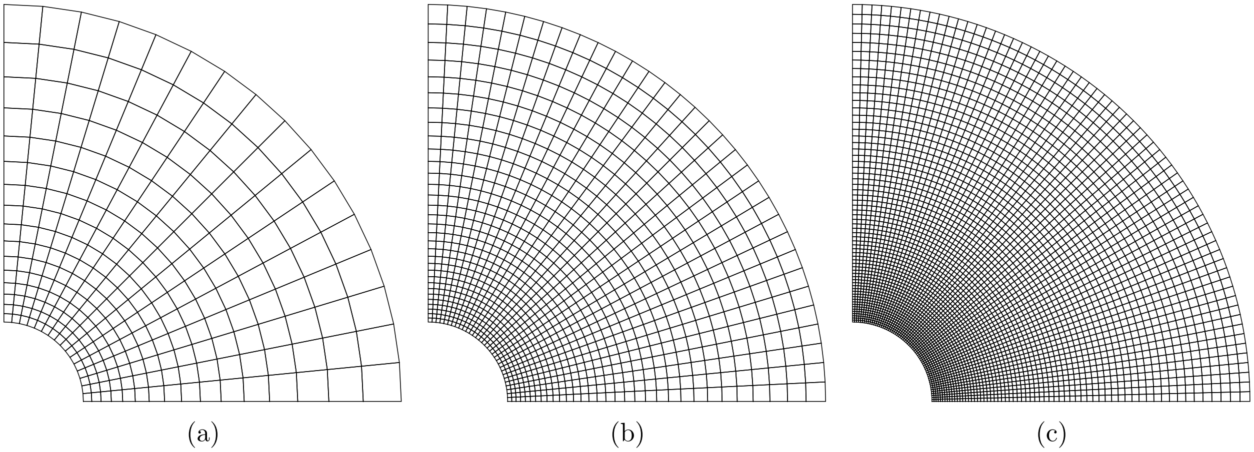

(a) (b) (c)

FIGURE 5.30. Uniform quadrilateral meshes for the hollow cylinder problem. (a) 256 elements, (b) 1024 elements and (c) 4096 elements.

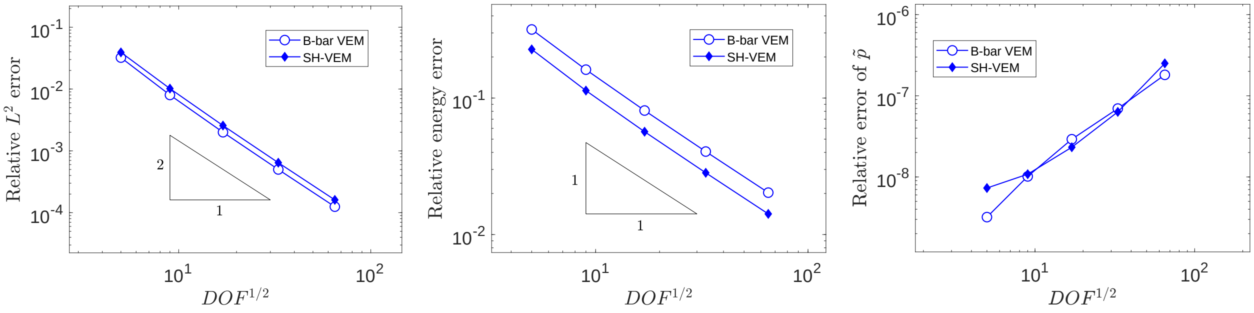

(a) (b) (c)

Figure 5.31. Comparison of B-bar VEM and SH-VEM for the hollow cylinder problem on structured meshes (see Figure 5.30). (a) L^2 error of displacement, (b) energy error and (c) L^2 error of hydrostatic stress.

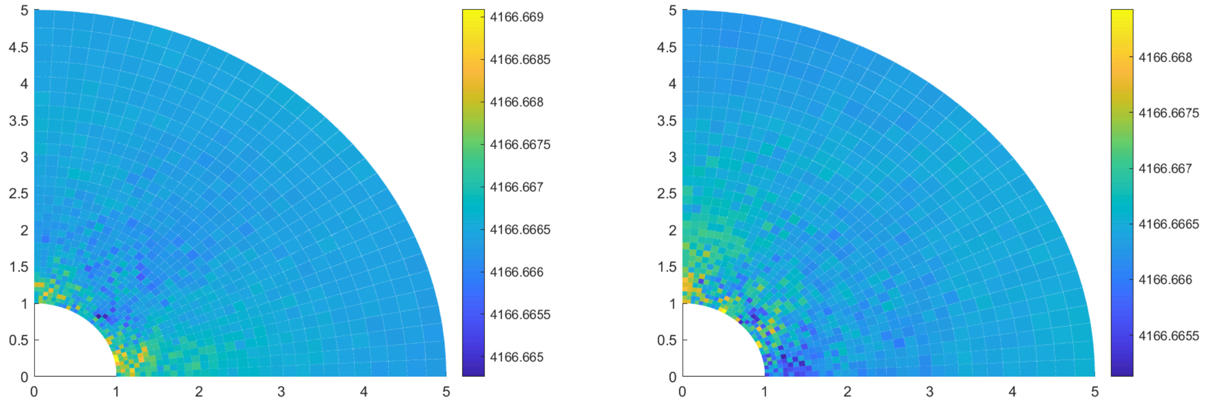

(a) (b)

Figure 5.32. Contour plots of the hydrostatic stress field on structured meshes (see Figure 5.30) for the hollow pressurized cylinder problem. The exact hydrostatic stress is 4166.6666 psi. (a) B-bar VEM and (b) SH-VEM.

Now we solve the pressurized cylinder problem on a sequence of nonconvex meshes; a few representation meshes are shown in Figure 5.33. Figure 5.34 shows that both the B-bar VEM and the SH-VEM deliver optimal convergence rates; however unlike the uniform mesh case, the hydrostatic stress field is not exactly reproduced by either method. In Figure 5.35, we compare the contour plots of the error in the hydrostatic stress field for the two methods. We observe that both methods are very accurate away from the inner circular boundary but produce much larger errors in its vicinity (see Figures 5.35b and 5.35d). The maximum error of the SH-VEM is 30 percent, whereas that of B-bar VEM is markedly worse at 55 percent. Compared to Figure 5.33c, if the nonconvex quadrilateral is distorted even more, we find from our simulations that the maximum error in the hydrostatic stress for SH-VEM increases to 35 percent, whereas the maximum error using B-bar VEM has a 10-fold increase.

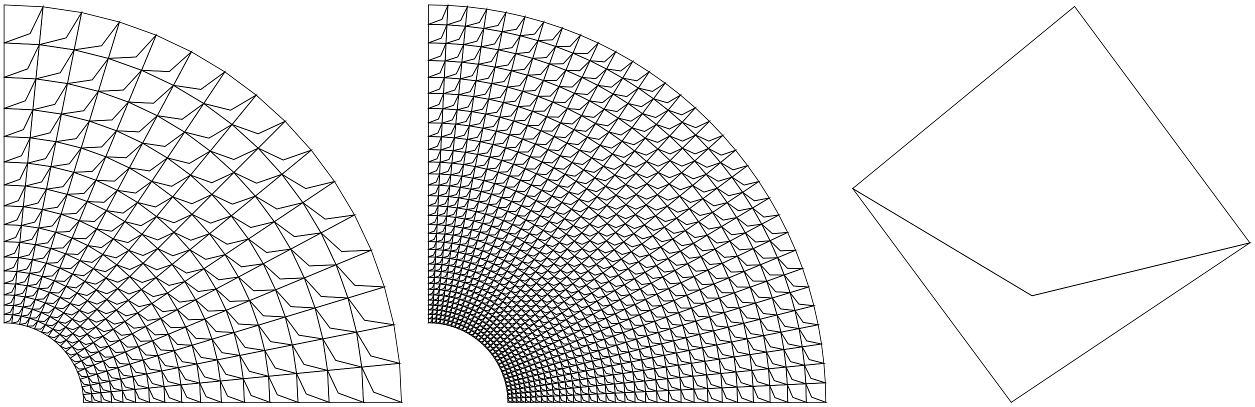
(a) (b) (c)

Figure 5.33. Nonconvex quadrilateral meshes for the hollow cylinder problem. (a) 512 elements, (b) 2048 elements and (c) magnification of a single element split into convex and nonconvex partitions.

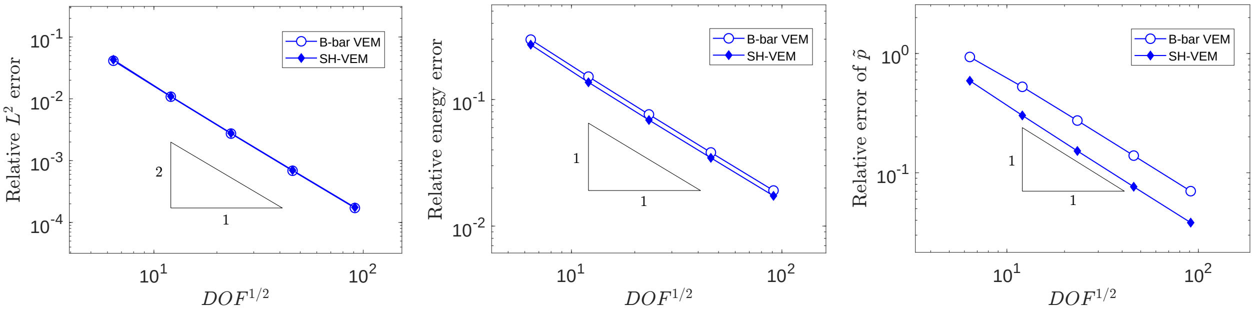

(a) (b) (c)

Figure 5.34. Comparison of B-bar VEM and SH-VEM for the hollow cylinder problem on nonconvex meshes (see Figure 5.33). (a) L^2 error of displacement, (b) energy error and (c) L^2 error of hydrostatic stress.

5.4.7. Flat punch.

Finally, we consider the problem of a flat punch as described in Park et al. [85] and shown in Figure 5.36. The domain is the unit square and we choose $E_Y = 250$ psi and $\nu = 0.4999999$. The left, right and bottom edges are constrained in the direction normal to the edges, and the top has a constant vertical displacement of $v = -0.03$ applied on the middle third of the edge. A sequence of unstructured quadrilateral (see Figure 5.5) is used to solve this problem. The hydrostatic stress field from both methods are presented in Figure 5.37. The plots show that both methods produce relatively smooth hydrostatic stress fields of comparable accuracy.

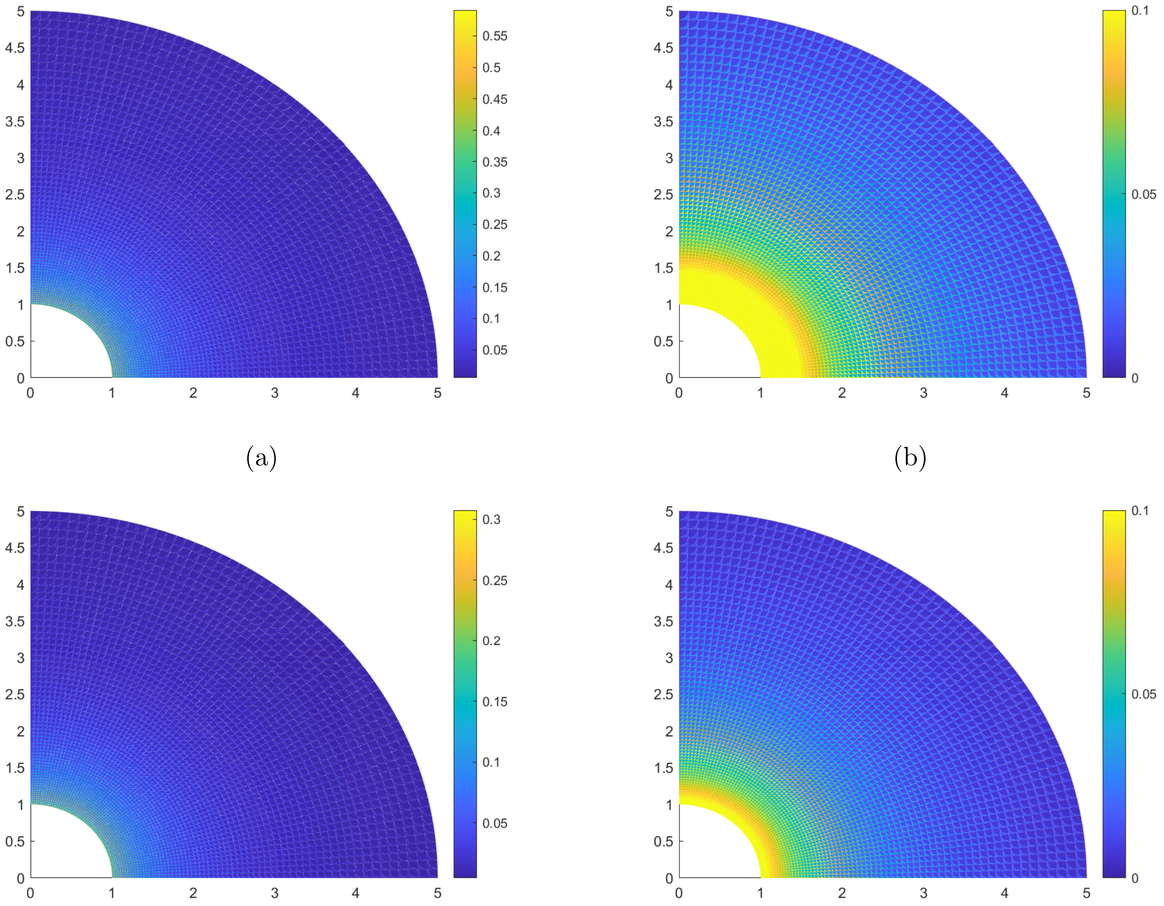

(a)

(b)

(c)

(d)

FIGURE 5.35. Contour plots of the relative error in the hydrostatic stress on nonconvex meshes (see Figure 5.33) for the hollow pressurized cylinder problem. The exact hydrostatic stress is 4166.6666 psi. (a) B-bar VEM, (b) B-bar VEM (color scale for error is between 0 and 10 percent), (c) SH-VEM and (d) SH-VEM (color scale for error is between 0 and 10 percent.

In Figure 5.38, plots of the trace of the strain field are shown for B-bar VEM and SH-VEM, and we find that consistent with the exact solution the numerically computed strain field is nearly traceless.

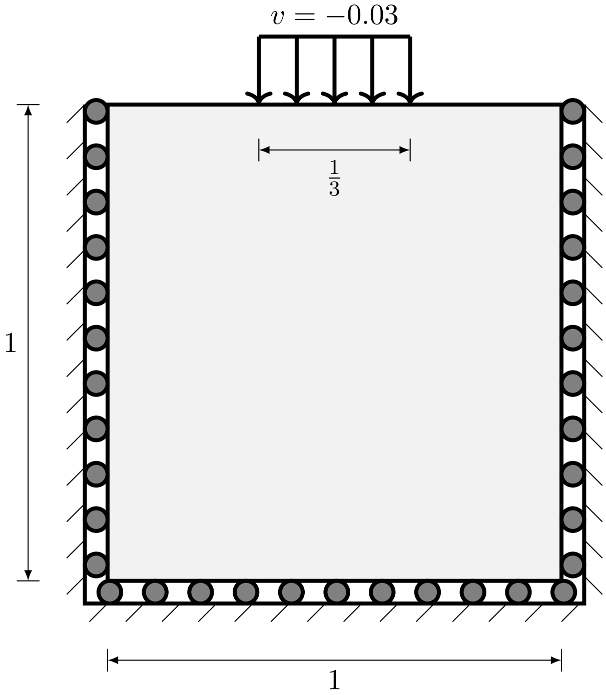

Figure 5.36. Flat punch problem.

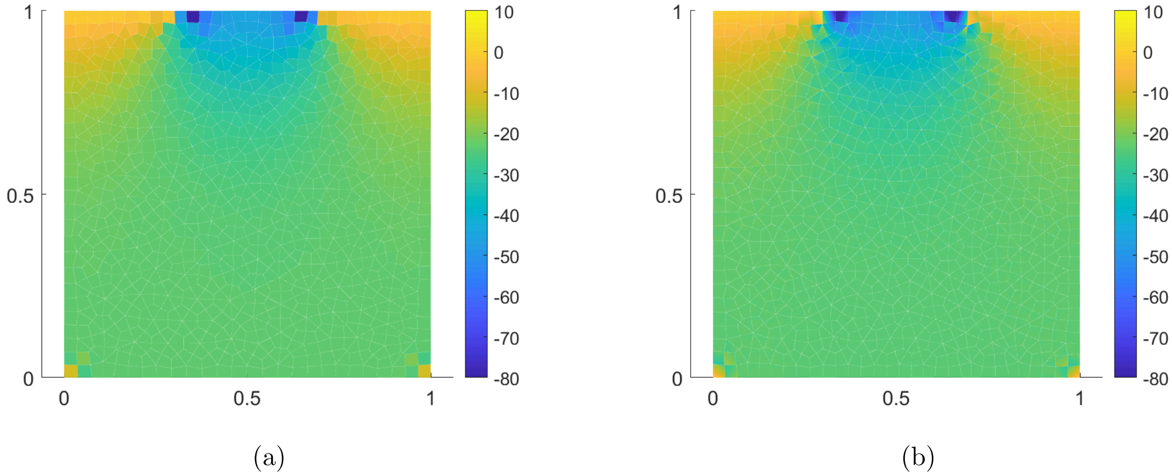

(a)

(b)

Figure 5.37. Contour plots of the hydrostatic stress on unstructured meshes (see Figure 5.5) for the flat punch problem. (a) B-bar VEM and (b) SH-VEM.

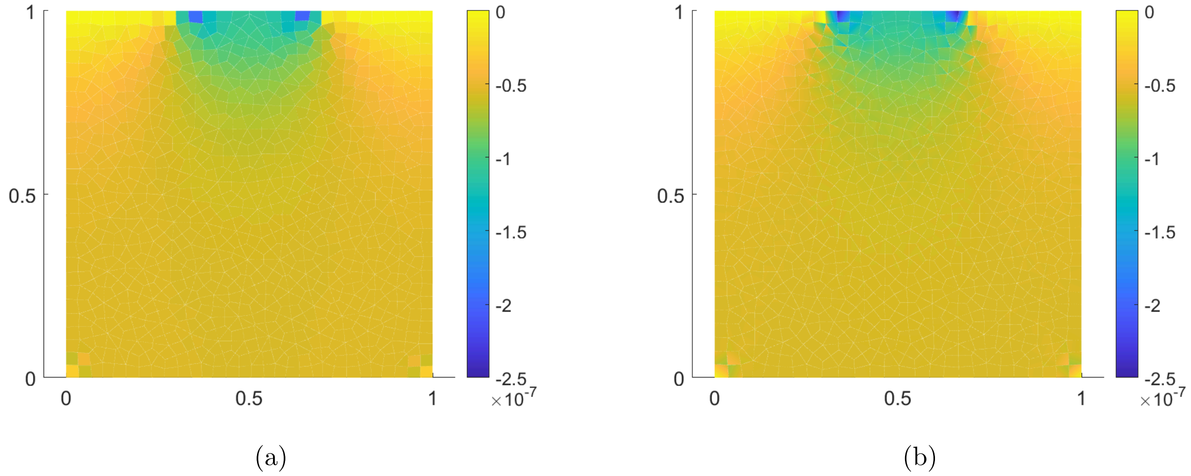

FIGURE 5.38. Contour plots of the trace of the strain field on unstructured meshes (see Figure 5.5) for the flat punch problem. (a) B-bar VEM and (b) SH-VEM.

CHAPTER 6

Stress-Hybrid Virtual Element Method on Six-Noded Triangular Meshes

In many applications with complex geometries, the standard quadrilateral and hexahedral elements used in FEM are not easily generated. Triangular and tetrahedral meshes can be automatically generated for very general geometries using robust and well-established meshing algorithms. However, the majority of triangular and tetrahedral elements are overly stiff in bending problems and suffer from volumetric locking in the incompressible limit. Many of the techniques developed in finite elements to alleviate locking are applicable to only quadrilateral elements, although there has been progress in constructing robust and accurate triangular elements. Using the foundation of the virtual element method, we seek a method that is locking-free on triangular meshes. Following the approach of Chapter 5, we examine a stress-hybrid formulation for six-noded elements using equilibrated stress fields, and by applying the ideas of [116, 117], we introduce a penalty stress-hybrid approach.

In this chapter, we revisit the Hellinger–Reissner variational formulation and use it to construct the stress-hybrid projection operator. We then examine the different choices of stress basis functions and show the aspects of numerical implementation. Next, we introduce an alternative method using an equilibrium penalty term. This approach is refered to as the Penalty Stress-Hybrid Virtual Element Method (PSH-VEM). To conclude the chapter, we present results comparing the Composite triangle FEM (CT FEM) [60], B-bar VEM [85], SH-VEM, and the PSH-VEM. The four methods are used to solve a series of benchmark problems in the nearly-incompressible limit: bending of a thin cantilever beam, Cook's membrane, infinite plate with a circular hole, pressurized cylinder, a manufactured problem with a sinusoidal solution, and the punch problem.

This chapter is based on the work published in [35].

6.1. Stress-hybrid virtual elements for triangular elements

Let $\mathcal{T}^h$ be a decomposition of Ω into six-noded elements (see Figure 6.1). For each element E, denote its diameter by h_E, its centroid by $\boldsymbol{x}_E$ and the coordinate of the i-th vertex by $\boldsymbol{x}_i = (x_i, y_i)$.

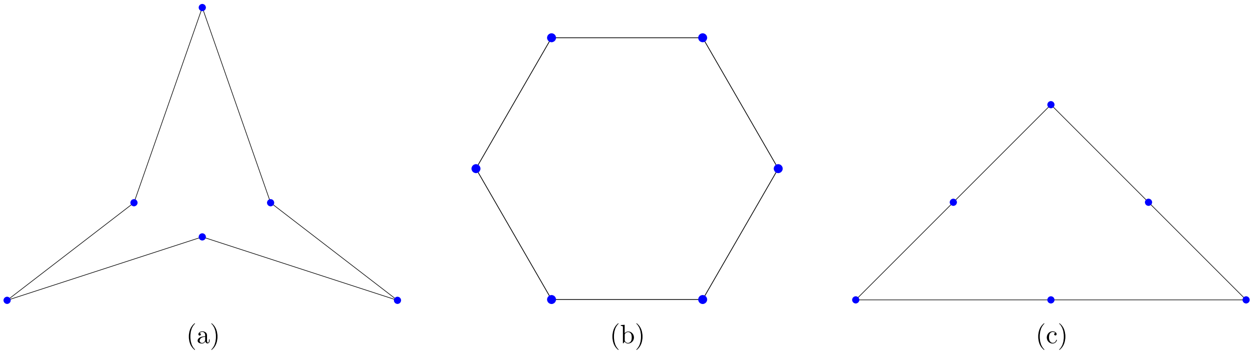
(a) (b) (c)

FIGURE 6.1. Examples of admissible six-noded elements (a) nonconvex element, (b) hexagonal element and (c) six-noded triangular element.

6.1.1. Variational formulation. Following (5.1), we write the Hellinger–Reissner functional for linear elasticity:

$$\Pi_{\mathrm{HR}}[\boldsymbol{u}, \boldsymbol{\sigma}] = -\frac{1}{2}\int_\Omega \boldsymbol{\sigma} : \mathbb{C}^{-1} : \boldsymbol{\sigma}\, d\boldsymbol{x} + \int_\Omega \boldsymbol{\sigma} : \nabla_s \boldsymbol{u}\, d\boldsymbol{x} - \int_\Omega \boldsymbol{b} \cdot \boldsymbol{u}\, d\boldsymbol{x} - \int_{\Gamma_t} \bar{\boldsymbol{t}} \cdot \boldsymbol{u}\, ds.$$

After taking the first variation of $\Pi_{\mathrm{HR}}(\cdot,\cdot)$ and requiring it to be stationary, we obtain the weak statement of the equilibrium equations and strain-displacement relations:

$$\int_\Omega \boldsymbol{\sigma} : \nabla_s(\delta \boldsymbol{u})\, d\boldsymbol{x} - \int_\Omega \boldsymbol{b} \cdot \delta\boldsymbol{u}\, d\boldsymbol{x} - \int_{\Gamma_t} \bar{\boldsymbol{t}} \cdot \delta\boldsymbol{u}\, ds = 0 \quad \forall \delta\boldsymbol{u} \in \mathcal{V}_u, \tag{6.1a}$$

$$\int_\Omega \delta\boldsymbol{\sigma} : \left(\nabla_s \boldsymbol{u} - \mathbb{C}^{-1} : \boldsymbol{\sigma}\right) d\boldsymbol{x} = 0 \quad \forall \delta\boldsymbol{\sigma} \in \mathcal{V}_\sigma, \tag{6.1b}$$

where $\mathcal{V}_u \subset [H^1(\Omega)]^2$ contains vector-valued functions that vanish on Γ_u and $\mathcal{V}_\sigma$ contains symmetric tensor-valued functions in $[L^2(\Omega)]^{2\times 2}_{\mathrm{sym}}$.

6.1.2. Stress-hybrid projection. Let $\ell \in \mathbb{N}$ be the largest degree of the polynomials used for the stress approximation on an element. Then following (5.4), define the projection operator $\Pi_\beta \boldsymbol{\sigma}$ for the stress-hybrid formulation by the condition

$$\int_E \mathbb{P} : \left(\nabla_s \boldsymbol{u}_h - \mathbb{C}^{-1} : \Pi_\beta \boldsymbol{\sigma}\right) d\boldsymbol{x} = 0 \quad \forall \mathbb{P} \in [\mathbb{P}_\ell(E)]^{2\times 2}_{\mathrm{sym}},$$

which is rewritten as

$$\int_E \mathbb{P} : \mathbb{C}^{-1} : \Pi_\beta \boldsymbol{\sigma}\, d\boldsymbol{x} = \int_E \mathbb{P} : \nabla_s \boldsymbol{u}_h \, d\boldsymbol{x} \quad \forall \mathbb{P} \in [\mathbb{P}_\ell(E)]^{2\times 2}_{\mathrm{sym}}.$$

Now applying the divergence theorem and simplifying, we obtain

$$\int_E \mathbb{P} : \mathbb{C}^{-1} : \Pi_\beta \boldsymbol{\sigma}\, d\boldsymbol{x} = \int_{\partial E} (\mathbb{P} \cdot \boldsymbol{n}) \cdot \boldsymbol{u}_h \, ds - \int_E (\nabla \cdot \mathbb{P}) \cdot \boldsymbol{u}_h \, d\boldsymbol{x}, \tag{6.3}$$

Let $\overline{\mathbb{P}}$, $\overline{\Pi_\beta \boldsymbol{\sigma}}$ be the Voigt representation of $\mathbb{P}$ and $\Pi_\beta \boldsymbol{\sigma}$, respectively. Then, (6.3) can be written as

$$\int_E \overline{\mathbb{P}}^T \boldsymbol{C}^{-1} \overline{\Pi_\beta \boldsymbol{\sigma}}\, d\boldsymbol{x} = \int_{\partial E} \overline{\mathbb{P}}^T \boldsymbol{N}^{\partial E} \boldsymbol{u}_h \, ds - \int_E \left(\boldsymbol{\partial} \overline{\mathbb{P}}\right)^T \boldsymbol{u}_h \, d\boldsymbol{x} \quad \forall \mathbb{P} \in [\mathbb{P}_\ell(E)]^{2\times 2}_{\mathrm{sym}}, \tag{6.4a}$$

where $\boldsymbol{N}^{\partial E}$ is the matrix representation of the outward normals along the boundary of E, and $\boldsymbol{\partial}$ is the matrix divergence operator that are given by

$$\boldsymbol{N}^{\partial E} := \begin{bmatrix} n_x & 0 \\ 0 & n_y \\ n_y & n_x \end{bmatrix}, \quad \boldsymbol{\partial} := \begin{bmatrix} \frac{\partial}{\partial x} & 0 & \frac{\partial}{\partial y} \\ 0 & \frac{\partial}{\partial y} & \frac{\partial}{\partial x} \end{bmatrix}. \tag{6.4b}$$

6.1.3. Choice of stress basis for a hybrid formulation. Now that we have a projection operator for the stress, we need to choose a suitable polynomial basis for the stress field. Using too few basis functions will result in an unstable element; while using too many will lead to overstiff elements. It is known that for a stress-based method, using a stress approximation that satisfies the element equilibrium condition results in more accurate stress distributions for homogeneous problems [**62**,**104**,**105**,**116**]. For plane isotropic elasticity, a convenient set of suitable stresses that satisfy the equilibrium equations with zero body force are derived from the Airy stress functions [**34**, **59**, **96**]. A collection of fifteen potential stress fields is given in Voigt representation by [**34**]:

$$\boldsymbol{P} = \begin{bmatrix} 1 & 0 & 0 & \eta & 0 & \xi & 0 & 0 & 2\xi\eta & -\eta^2 & \xi^2-\eta^2 & \xi(\xi^2-6\eta^2) & \xi^3 & 3\xi^2\eta & \eta(3\xi^2-2\eta^2) \\ 0 & 1 & 0 & 0 & \xi & 0 & \eta & 2\xi\eta & 0 & \xi^2 & \eta^2-\xi^2 & 3\xi\eta^2 & -\xi(2\xi^2-3\eta^2) & -\eta(6\xi^2-\eta^2) & \eta^3 \\ 0 & 0 & 1 & 0 & 0 & -\eta & -\xi & -\xi^2 & -\eta^2 & 0 & -2\xi\eta & -\eta(3\xi^2-2\eta^2) & -3\xi^2\eta & \xi(2\xi^2-3\eta^2) & -3\xi\eta^2 \end{bmatrix}. \tag{6.5}$$

For a six-noded element, there are twelve displacement degrees of freedom and three rigid-body modes, so a minimum of nine terms are needed for the stress approximation [**92**]. However, it is also known that using an incomplete stress approximation will result in a stiffness matrix that is not rotationally invariant [**43**, **90**], or result in elements with inaccurate stress distributions [**116**].

Therefore, we only consider the complete bases with the first eleven terms of (6.5) and all fifteen terms. We denote any stress basis with k independent terms by $k\beta$.

Remark 6.1.1. *The set of stress basis in* (6.5) *is an extension of the* 5β *hybrid-stress basis introduced in [89] and the* 15β *basis introduced in [105]. In [54], a similar collection of divergence-free polynomials is used as a basis for the enhanced strain VEM.*

We also examine a basis similar to the hybrid basis given in [54], which uses a mix of nine uncoupled constant and linear polynomials and four divergence-free quadratic polynomials:

$$\boldsymbol{P}^* = \begin{bmatrix} 1 & 0 & 0 & \xi & 0 & 0 & \eta & 0 & 0 & 0 & 2\xi\eta & -\eta^2 & \xi^2-\eta^2 \\ 0 & 1 & 0 & 0 & \xi & 0 & 0 & \eta & 0 & 2\xi\eta & 0 & \xi^2 & \eta^2-\xi^2 \\ 0 & 0 & 1 & 0 & 0 & \xi & 0 & 0 & \eta & -\xi^2 & -\eta^2 & 0 & -2\xi\eta \end{bmatrix}. \tag{6.6}$$

6.1.4. Virtual element space. Similar to the previous chapters, the standard virtual element space is not sufficient to compute the projection $\overline{\Pi_\beta \boldsymbol{\sigma}}$ for arbitrary ℓ without adding additional degrees of freedom; therefore, we reuse the enhanced virtual element space given in (3.19) for each element E:

$$\begin{aligned} \boldsymbol{V}_h(E) = \Big\{ & \boldsymbol{v}_h \in [H^1(E)]^2 : \Delta \boldsymbol{v}_h \in [\mathbb{P}_{\ell-1}(E)]^2,\ \boldsymbol{v}_h|_e \in [\mathbb{P}_1(e)]^2\ \forall e \in \partial E, \\ & \boldsymbol{v}_h|_{\partial E} \in [C^0(\partial E)]^2,\ \int_E \boldsymbol{v}_h \cdot \boldsymbol{p}\, d\boldsymbol{x} = \int_E \Pi^\varepsilon \boldsymbol{v}_h \cdot \boldsymbol{p}\, d\boldsymbol{x} \quad \forall \boldsymbol{p} \in [\mathbb{P}_{\ell-1}(E)]^2 \Big\}, \end{aligned} \tag{6.7}$$

where Δ is the vector Laplacian operator and e is an edge of the element. We note that for a stress basis that uses degree ℓ polynomials, the space requires the enhancing property $\int_E \boldsymbol{v}_h \cdot \boldsymbol{p}\, d\boldsymbol{x} = \int_E \Pi^\varepsilon \boldsymbol{v}_h \cdot \boldsymbol{p}\, d\boldsymbol{x}$ to hold for all vectorial polynomials up to degree $\ell - 1$. For each element E we also assign a basis for the local space $\boldsymbol{V}_h(E)$. Let $\{\phi_i\}$ be the scalar polygonal basis functions in standard VEM [9] that satisfy the Kronecker-delta property $\phi_i(\boldsymbol{x}_j) = \delta_{ij}$. Using the scalar basis, we define the matrix of vector-valued basis functions by

$$\boldsymbol{\varphi} = \begin{bmatrix} \phi_1 & \phi_2 & \phi_3 & \cdots & \phi_6 & 0 & 0 & 0 & \cdots & 0 \\ 0 & 0 & 0 & \cdots & 0 & \phi_1 & \phi_2 & \phi_3 & \cdots & \phi_6 \end{bmatrix} := \begin{bmatrix} \boldsymbol{\varphi}_1 & \boldsymbol{\varphi}_2 & \dots & \boldsymbol{\varphi}_{12} \end{bmatrix}, \tag{6.8a}$$

then any function $\boldsymbol{v}_h \in \boldsymbol{V}_h(E)$ can be represented as:

$$\boldsymbol{v}_h(\boldsymbol{x}) = \sum_{i=1}^{12} \boldsymbol{\varphi}_i(\boldsymbol{x}) v_i = \boldsymbol{\varphi}\boldsymbol{d}, \tag{6.8b}$$

where v_i is the i-th degree of freedom of $\boldsymbol{v}_h$ and $\boldsymbol{d}$ is the displacement vector with components v_i.

6.1.5. Implementation of the stress-hybrid projection. From (6.4a) we have the weak discrete relation given by:

$$\int_E \overline{\mathbb{P}}^T \boldsymbol{C}^{-1} \overline{\Pi_\beta \boldsymbol{\sigma}} \, d\boldsymbol{x} = \int_{\partial E} \overline{\mathbb{P}}^T \boldsymbol{N}^{\partial E} \boldsymbol{u}_h \, ds - \int_E \left(\boldsymbol{\partial}\overline{\mathbb{P}}\right)^T \boldsymbol{u}_h \, d\boldsymbol{x}. \tag{6.9a}$$

The last term in (6.9a) is not computable for general $\overline{\mathbb{P}}$; however since the elements of $\boldsymbol{\partial}\overline{\mathbb{P}}$ are polynomials of degree at most $\ell - 1$, we apply the definition of the virtual element space (6.7) to rewrite as

$$\int_E \overline{\mathbb{P}}^T \boldsymbol{C}^{-1} \overline{\Pi_\beta \boldsymbol{\sigma}} \, d\boldsymbol{x} = \int_{\partial E} \overline{\mathbb{P}}^T \boldsymbol{N}^{\partial E} \boldsymbol{u}_h \, ds - \int_E \left(\boldsymbol{\partial}\overline{\mathbb{P}}\right)^T \Pi^{\varepsilon} \boldsymbol{u}_h \, d\boldsymbol{x}. \tag{6.9b}$$

Expanding $\boldsymbol{u}_h$ in terms of the basis in $\boldsymbol{V}_h(E)$, we have $\boldsymbol{u}_h = \boldsymbol{\varphi}\boldsymbol{d}$, where $\boldsymbol{d}$ is the displacement vector. We also expand $\overline{\Pi_\beta \boldsymbol{\sigma}}$ in terms of $\boldsymbol{P}$: $\overline{\Pi_\beta \boldsymbol{\sigma}} = \boldsymbol{P}\boldsymbol{\beta}$, and since $\mathbb{P}$ is arbitrary we take $\overline{\mathbb{P}} = \boldsymbol{P}_i$ $(i = 1, 2, \ldots, 15)$. After substituting in (6.9b) for each $i = 1, 2, \ldots, 15$ and simplifying, we obtain the system:

$$\left(\int_E \boldsymbol{P}^T \boldsymbol{C}^{-1} \boldsymbol{P} \, d\boldsymbol{x}\right) \boldsymbol{\beta} = \left(\int_{\partial E} \boldsymbol{P}^T \boldsymbol{N}^{\partial E} \boldsymbol{\varphi} \, ds - \int_E \left(\boldsymbol{\partial}\boldsymbol{P}\right)^T \Pi^{\varepsilon} \boldsymbol{\varphi} \, d\boldsymbol{x}\right) \boldsymbol{d}. \tag{6.10}$$

For any choice of $\boldsymbol{P}$ in (6.5), we have the divergence-free condition $\boldsymbol{\partial}\boldsymbol{P} = \boldsymbol{0}$, so we obtain

$$\left(\int_E \boldsymbol{P}^T \boldsymbol{C}^{-1} \boldsymbol{P} \, d\boldsymbol{x}\right) \boldsymbol{\beta} = \left(\int_{\partial E} \boldsymbol{P}^T \boldsymbol{N}^{\partial E} \boldsymbol{\varphi} \, ds\right) \boldsymbol{d}. \tag{6.11}$$

Now define the corresponding matrices $\boldsymbol{H}$ and $\boldsymbol{L}$ by

$$\boldsymbol{H} = \int_E \boldsymbol{P}^T \boldsymbol{C}^{-1} \boldsymbol{P} \, d\boldsymbol{x}, \quad \boldsymbol{L} = \int_{\partial E} \boldsymbol{P}^T \boldsymbol{N}^{\partial E} \boldsymbol{\varphi} \, ds. \tag{6.12a}$$

Since $\boldsymbol{P}$ has linearly independent columns and $\boldsymbol{C}^{-1}$ is symmetric positive-definite, the matrix $\boldsymbol{H}$ is invertible. Then the stress coefficients are given by

$$\boldsymbol{\beta} = \boldsymbol{H}^{-1} \boldsymbol{L} \boldsymbol{d} := \boldsymbol{\Pi}_\beta \boldsymbol{d}, \tag{6.12b}$$

where $\mathbf{\Pi}_\beta$ is the matrix representation of the stress-hybrid projection operator with respect to the symmetric tensor polynomial basis $\boldsymbol{P}$.

Remark 6.1.2. *For a nondivergence-free basis, the use of* (6.9b) *can lead to an overly stiff element. An alternate approach used in [54, 70], is to introduce additional internal moment degrees of freedom to compute the last integral in* (6.9a)*. These additional DOFs result in better performing elements but require an additional static condensation on the element stiffness matrix. Another approach is to follow the idea of using composite elements [60] to compute the stress projection operator. For each element, we construct a sub-triangulation and assume the displacement field (displacement projection) is affine on each subtriangle. This piecewise displacement field can then be used to compute the integral in* (6.9a)*. We tested a virtual element formulation based on composite elements and found that the resulting elements were more flexible but still suffered from volumetric locking.*

6.1.6. Element stiffness and forcing. Following the procedure of Section 5.3.2, we define the discrete system:

$$a_h^E(\boldsymbol{u}_h, \delta\boldsymbol{u}_h) = \ell_h^E(\delta\boldsymbol{u}_h),$$

where

$$\begin{aligned} a_h^E(\boldsymbol{u}_h, \delta\boldsymbol{u}_h) &:= \int_E \overline{\Pi_\beta \boldsymbol{\sigma}(\delta\boldsymbol{u}_h)}^T \boldsymbol{C}^{-1} \overline{\Pi_\beta \boldsymbol{\sigma}(\boldsymbol{u}_h)}\, d\boldsymbol{x}, \\ \ell_h^E(\delta\boldsymbol{u}_h) &:= \int_E (\delta\boldsymbol{u}_h)^T \boldsymbol{b}\, d\boldsymbol{x} + \int_{\Gamma_t \cap \partial E} (\delta\boldsymbol{u}_h)^T \bar{\boldsymbol{t}}\, ds. \end{aligned}$$

After expanding $\overline{\Pi_\beta \boldsymbol{\sigma}}$ and simplifying, we construct the element stiffness matrix

$$\boldsymbol{K}_E = (\mathbf{\Pi}_\beta)^T \left(\int_E \boldsymbol{P}^T \boldsymbol{C}^{-1} \boldsymbol{P}\, d\boldsymbol{x} \right) \mathbf{\Pi}_\beta = \mathbf{\Pi}_\beta^T \boldsymbol{H} \mathbf{\Pi}_\beta. \tag{6.14}$$

Similarly, for every element E, the element force vector is given by

$$\boldsymbol{f}_E := \int_E \boldsymbol{\varphi}^T \boldsymbol{b}\, d\boldsymbol{x} + \int_{\Gamma_t \cap \partial E} \boldsymbol{\varphi}^T \bar{\boldsymbol{t}}\, ds. \tag{6.15}$$

6.2. Equilibrium penalty stress-hybrid method

In the original stress-hybrid approach, we used a set of stress basis functions that satisfy the equilibrium equations without body force. In general, this is difficult or not possible for nonlinear, anisotropic and three-dimensional problems. It was also found in our numerical tests that many higher order polynomial terms were needed in order to preserve the stability without using a stabilization term. This requirement increases the cost of integration and results in stiffer solutions. An alternative method is to adapt the approach by [116]. It was found that for distorted elements, the original Pian-Sumihara element does not satisfy elementwise equilibrium; this resulted in shear locking and large errors in pure bending problems on distorted meshes. The remedy suggested in [116, 117] is to add an additional term which penalizes the functional when the stress basis functions are not in equilibrium. In the limit as the penalty term approaches infinity, the equilibrium conditions are exactly satisfied. This formulation was shown to mitigate shear locking in the Pian-Sumihara element and to improve performance in axisymmetric problems [116, 117]. A similar method was developed in [106], which uses carefully selected scaling parameters to eliminate excess shear stresses rather than enforce equilibrium. Later, the penalty equilibrium formulation was applied to fracture mechanics [118] and extended to the Hu–Washizu variational principle [32, 33]. The addition of an equilibrium penalty term is also used in [22, 112] to construct superconvergent stress recovery methods. In this section, we utilize the penalty approach to weakly enforce equilibrium conditions on a set of non-equilibrated stress basis functions. We first introduce a Hellinger–Reissner functional with an additional penalty term, then define a penalized stress-hybrid projection operator from the associated weak strain-displacement relation. Finally we construct the element stiffness matrix, forcing vector and discuss a choice for the penalty parameter and basis functions.

We start with a modified Hellinger–Reissner functional with an equilibrium penalty term:

$$\begin{aligned}\Pi_{\mathrm{HR}^*}[\boldsymbol{u},\boldsymbol{\sigma}] = -\frac{1}{2}\int_\Omega \boldsymbol{\sigma} : \mathbb{C}^{-1} : \boldsymbol{\sigma}\, d\boldsymbol{x} + \int_\Omega \boldsymbol{\sigma} : \nabla_s \boldsymbol{u}\, d\boldsymbol{x} - \int_\Omega \boldsymbol{b}\cdot\boldsymbol{u}\, d\boldsymbol{x} - \int_{\Gamma_t} \bar{\boldsymbol{t}}\cdot\boldsymbol{u}\, ds \\ -\frac{\alpha}{2}\int_\Omega (\nabla\cdot\boldsymbol{\sigma}+\boldsymbol{b})\cdot(\nabla\cdot\boldsymbol{\sigma}+\boldsymbol{b})\, d\boldsymbol{x},\end{aligned} \tag{6.16}$$

where $\alpha > 0$ is a penalty parameter. After taking the first variation, the stationary condition results in the weak equilibrium equations and modified strain-displacement relations:

$$\int_\Omega \boldsymbol{\sigma} : \nabla_s(\delta \boldsymbol{u})\, d\boldsymbol{x} - \int_\Omega \boldsymbol{b} \cdot \delta \boldsymbol{u}\, d\boldsymbol{x} - \int_{\Gamma_t} \bar{\boldsymbol{t}} \cdot \delta \boldsymbol{u}\, ds = 0 \quad \forall \delta \boldsymbol{u} \in \mathcal{V}_u, \tag{6.17a}$$

$$\int_\Omega \delta\boldsymbol{\sigma} : \left(\nabla_s \boldsymbol{u} - \mathbb{C}^{-1} : \boldsymbol{\sigma}\right)\, d\boldsymbol{x} - \alpha \int_\Omega (\nabla \cdot \delta\boldsymbol{\sigma}) \cdot (\nabla \cdot \boldsymbol{\sigma} + \boldsymbol{b})\, d\boldsymbol{x} = 0 \quad \forall \delta\boldsymbol{\sigma} \in \mathcal{V}_\sigma. \tag{6.17b}$$

6.2.1. Penalty stress-hybrid projection and implementation. We first construct the penalized stress-hybrid projection operator on an element E from the modified strain-displacement relation. By modifying (6.17b), we define the projection by the condition:

$$\int_E \mathbb{P} : \left(\nabla_s \boldsymbol{u}_h - \mathbb{C}^{-1} : \Pi_\beta \boldsymbol{\sigma}\right)\, d\boldsymbol{x} - \alpha \int_E (\nabla \cdot \mathbb{P}) \cdot (\nabla \cdot \Pi_\beta \boldsymbol{\sigma} + \boldsymbol{b})\, d\boldsymbol{x} = 0,$$

which can be rewritten as

$$\int_E \mathbb{P} : \mathbb{C}^{-1} : \Pi_\beta \boldsymbol{\sigma}\, d\boldsymbol{x} + \alpha \int_E (\nabla \cdot \mathbb{P}) \cdot (\nabla \cdot \Pi_\beta \boldsymbol{\sigma})\, d\boldsymbol{x} = \int_E \mathbb{P} : \nabla_s \boldsymbol{u}_h\, d\boldsymbol{x} - \alpha \int_E (\nabla \cdot \mathbb{P}) \cdot \boldsymbol{b}\, d\boldsymbol{x}.$$

After applying the divergence theorem, we get

$$\begin{aligned}\int_E \mathbb{P} : \mathbb{C}^{-1} : \Pi_\beta \boldsymbol{\sigma}\, d\boldsymbol{x} + \alpha \int_E (\nabla \cdot \mathbb{P}) \cdot (\nabla \cdot \Pi_\beta \boldsymbol{\sigma})\, d\boldsymbol{x} \\ = \int_{\partial E} (\mathbb{P} \cdot \boldsymbol{n}) \cdot \boldsymbol{u}_h\, ds - \int_E (\nabla \cdot \mathbb{P}) \cdot \boldsymbol{u}_h\, d\boldsymbol{x} - \alpha \int_E (\nabla \cdot \mathbb{P}) \cdot \boldsymbol{b}\, d\boldsymbol{x}.\end{aligned} \tag{6.19}$$

Using Voigt notation, we rewrite (6.19) in terms of matrix-vector operations

$$\begin{aligned}\int_E \overline{\mathbb{P}}^T \boldsymbol{C}^{-1} \overline{\Pi_\beta \boldsymbol{\sigma}}\, d\boldsymbol{x} + \alpha \int_E (\boldsymbol{\partial} \overline{\mathbb{P}})^T \boldsymbol{\partial} \overline{\Pi_\beta \boldsymbol{\sigma}}\, d\boldsymbol{x} = \int_{\partial E} \overline{\mathbb{P}}^T \boldsymbol{N}^{\partial E} \boldsymbol{u}_h\, ds - \int_E (\boldsymbol{\partial} \overline{\mathbb{P}})^T \boldsymbol{u}_h\, d\boldsymbol{x} \\ - \alpha \int_E (\boldsymbol{\partial} \overline{\mathbb{P}})^T \boldsymbol{b}\, d\boldsymbol{x}.\end{aligned} \tag{6.20a}$$

The second term on the right-hand side is not computable from the element DOF's; however, by applying the definition of the virtual element space (6.7), we rewrite the relation in a computable form

$$\begin{aligned}\int_E \overline{\mathbb{P}}^T \boldsymbol{C}^{-1} \overline{\Pi_\beta \boldsymbol{\sigma}}\, d\boldsymbol{x} + \alpha \int_E (\boldsymbol{\partial} \overline{\mathbb{P}})^T \boldsymbol{\partial} \overline{\Pi_\beta \boldsymbol{\sigma}}\, d\boldsymbol{x} = \int_{\partial E} \overline{\mathbb{P}}^T \boldsymbol{N}^{\partial E} \boldsymbol{u}_h\, ds - \int_E (\boldsymbol{\partial} \overline{\mathbb{P}})^T \Pi^\varepsilon \boldsymbol{u}_h\, d\boldsymbol{x} \\ - \alpha \int_E (\boldsymbol{\partial} \overline{\mathbb{P}})^T \boldsymbol{b}\, d\boldsymbol{x}.\end{aligned} \tag{6.20b}$$

Letting $\overline{\mathbb{P}} = \boldsymbol{P}, \overline{\Pi_\beta \boldsymbol{\sigma}} = \boldsymbol{P}\boldsymbol{\beta}$ and $\boldsymbol{u}_h = \boldsymbol{\varphi}\boldsymbol{d}$, we obtain the system of equations:

$$\begin{aligned}\left(\int_E \boldsymbol{P}^T \boldsymbol{C}^{-1} \boldsymbol{P}\, d\boldsymbol{x} + \alpha \int_E (\boldsymbol{\partial P})^T \boldsymbol{\partial P}\, d\boldsymbol{x}\right)\boldsymbol{\beta} \\ = \left(\int_{\partial E} \boldsymbol{P}^T \boldsymbol{N}^{\partial E} \boldsymbol{\varphi}\, ds - \int_E (\boldsymbol{\partial P})^T \Pi^\varepsilon \boldsymbol{\varphi}\, d\boldsymbol{x}\right)\boldsymbol{d} - \alpha \int_E (\boldsymbol{\partial P})^T \boldsymbol{b}\, d\boldsymbol{x}.\end{aligned} \tag{6.21}$$

Define the corresponding matrices by

$$\boldsymbol{H} = \int_E \boldsymbol{P}^T \boldsymbol{C}^{-1} \boldsymbol{P}\, d\boldsymbol{x}, \quad \boldsymbol{H}_p = \int_E (\boldsymbol{\partial P})^T \boldsymbol{\partial P}\, d\boldsymbol{x}, \tag{6.22a}$$

$$\boldsymbol{L} = \int_{\partial E} \boldsymbol{P}^T \boldsymbol{N}^{\partial E} \boldsymbol{\varphi}\, ds - \int_E (\boldsymbol{\partial P})^T \Pi^\varepsilon \boldsymbol{\varphi}\, d\boldsymbol{x}, \quad \boldsymbol{L}_p = \int_E (\boldsymbol{\partial P})^T \boldsymbol{b}\, d\boldsymbol{x}. \tag{6.22b}$$

Then the stress coefficients are given as

$$\boldsymbol{\beta} = (\boldsymbol{H} + \alpha \boldsymbol{H}_p)^{-1} (\boldsymbol{L}\boldsymbol{d} - \alpha \boldsymbol{L}_p). \tag{6.22c}$$

6.2.2. Element stiffness and forcing. The element stiffness matrix can be constructed by using the the discrete equilibrium equations based on (6.17a)

$$\int_E \overline{\Pi_\beta \boldsymbol{\sigma}(\boldsymbol{u}_h)}^T \nabla_s(\delta \boldsymbol{u}_h)\, d\boldsymbol{x} = \int_E \boldsymbol{b}^T \delta \boldsymbol{u}_h\, d\boldsymbol{x} + \int_{\Gamma_t} \bar{\boldsymbol{t}}^T \delta \boldsymbol{u}_h\, ds.$$

On applying (6.17b) and simplifying, we rewrite the first integral as

$$\begin{aligned}\int_E \overline{\Pi_\beta \boldsymbol{\sigma}(\boldsymbol{u}_h)}^T \nabla_s(\delta \boldsymbol{u}_h)\, d\boldsymbol{x} = \int_E \overline{\Pi_\beta \boldsymbol{\sigma}(\boldsymbol{u}_h)}^T \boldsymbol{C}^{-1} \overline{\Pi_\beta \boldsymbol{\sigma}(\delta \boldsymbol{u}_h)}\, d\boldsymbol{x} \\ + \alpha \int_E (\boldsymbol{\partial} \overline{\Pi_\beta \boldsymbol{\sigma}(\boldsymbol{u}_h)})^T (\boldsymbol{\partial} \overline{\Pi_\beta \boldsymbol{\sigma}(\delta \boldsymbol{u}_h)} + \boldsymbol{b})\, d\boldsymbol{x}.\end{aligned} \tag{6.23}$$

Now we have the equation

$$\begin{aligned}\int_E \overline{\Pi_\beta \boldsymbol{\sigma}(\boldsymbol{u}_h)}^T \boldsymbol{C}^{-1} \overline{\Pi_\beta \boldsymbol{\sigma}(\delta \boldsymbol{u}_h)}\, d\boldsymbol{x} + \alpha \int_E (\boldsymbol{\partial} \overline{\Pi_\beta \boldsymbol{\sigma}(\boldsymbol{u}_h)})^T (\boldsymbol{\partial} \overline{\Pi_\beta \boldsymbol{\sigma}(\delta \boldsymbol{u}_h)} + \boldsymbol{b})\, d\boldsymbol{x} \\ = \int_E \boldsymbol{b}^T \delta \boldsymbol{u}_h\, d\boldsymbol{x} + \int_{\Gamma_t \cap \partial E} \bar{\boldsymbol{t}}^T \delta \boldsymbol{u}_h\, ds.\end{aligned} \tag{6.24}$$

After expanding $\overline{\Pi_\beta \boldsymbol{\sigma}} = \boldsymbol{P}\boldsymbol{\beta}$ and simplifying, we construct the element stiffness matrix

$$\boldsymbol{K}_E = \boldsymbol{L}^T \big(\boldsymbol{H} + \alpha \boldsymbol{H}_p\big)^{-1} \boldsymbol{L}, \tag{6.25a}$$

and the element force vector is given by

$$\boldsymbol{f}_E = \int_E \boldsymbol{\varphi}^T \boldsymbol{b}\, d\boldsymbol{x} + \int_{\Gamma_t \cap \partial E} \boldsymbol{\varphi}^T \bar{\boldsymbol{t}}\, ds + \alpha \boldsymbol{L}^T \left(\boldsymbol{H} + \alpha \boldsymbol{H}_p\right)^{-1} \boldsymbol{L}_p, \tag{6.25b}$$

where $\boldsymbol{H}, \boldsymbol{H}_p, \boldsymbol{L}, \boldsymbol{L}_p$ are given in (6.22).

6.2.3. Choice of penalty parameter. Similar to the stabilized virtual element method, one drawback of the penalty equilibrium method is the need for a properly designed penalty parameter α. In [116], $\alpha = \frac{\kappa}{E_Y}$, where E_Y is the Young's modulus and $\kappa > 10^3$ is a large dimensionless number, is suggested. However, we found that this can result in the loss of stability for problems with highly distorted meshes. It is suggested in [32], that the penalty term should be scaled by a term that depends on the geometry in order to attain consistent units. In particular, α is chosen to be of the form $\alpha = \frac{\kappa \ell_0^2}{E_Y}$, where ℓ_0 is a characteristic length that is dependent on the element geometry. In our tests, we let ℓ_0 be the minimum length from the element centroid to the nodes and $\kappa = 10^4$. From our numerical experiments on benchmark problems, we found that using the penalty parameter $\alpha = \frac{\kappa \ell_0^2}{E_Y}$ resulted in higher accuracy and superconvergence on sufficiently refined uniform meshes. However, in the case when E_Y is small (α too large), low energy modes appear in the element stiffness matrix. From [74], it is suggested that a reasonable value of $\frac{\kappa}{E_Y}$ is between 10 and 100; therefore, we fix an arbitrary upper bound of 10 in our tests. That is, we use

$$\alpha = \min\left\{10, \frac{\kappa}{E_Y}\right\} \ell_0^2. \tag{6.26}$$

For the penalty equilibrium stress-hybrid method, we do not require the equilibrated stress basis functions given in (6.5). Instead, we seek the smallest number of stress basis functions that still retains stability and is not overly stiff in bending. For a six-noded element, a minimum of nine terms are needed; but it was found in [37] that the 9β complete linear basis is not sufficient for stability. We choose the 12β expansion with complete bilinear polynomials given by

$$\boldsymbol{P} = \begin{bmatrix} 1 & 0 & 0 & \xi & 0 & 0 & \eta & 0 & 0 & \xi\eta & 0 & 0 \\ 0 & 1 & 0 & 0 & \xi & 0 & 0 & \eta & 0 & 0 & \xi\eta & 0 \\ 0 & 0 & 1 & 0 & 0 & \xi & 0 & 0 & \eta & 0 & 0 & \xi\eta \end{bmatrix}. \tag{6.27}$$

6.3. Numerical results for SH-VEM on triangular elements

We present a series of numerical examples in linear elasticity under plane strain conditions on a variety of meshes. The unstructured triangular meshes used in these examples are generated using DistMesh [88]. We compute the errors of the displacement in the L^2 norm and energy seminorm, and the L^2 error of the hydrostatic stress (denoted by $\tilde{p}$). The convergence rates of CT FEM, B-bar VEM, SH-VEM, and PSH-VEM are computed using the discrete error measures given in (5.27). Similar to the previous sections, we use the scaled boundary cubature (SBC) method [41] to compute the matrices $\boldsymbol{H}$ in (6.12a), $\boldsymbol{H}_p$, $\boldsymbol{L}$ and $\boldsymbol{L}_p$ in (6.22), and the integrals appearing in (5.27). The matrices $\boldsymbol{H}$, $\boldsymbol{H}_p$ and $\boldsymbol{L}$ are integrals of polynomial functions and are exactly computed by the SBC method. The integrals in (5.27) are in general not integrals of polynomials but they can be computed to arbitrary accuracy with the SBC method.

6.3.1. Eigenvalue analysis.

We examine the eigenvalues of the SH-VEM for general triangular elements to determine the stability of the method. The material has Young's modulus $E_Y = 1$ psi and Poisson's ratio $\nu = 0.49995$. We assess the eigenvalues of the standard VEM [11], B-bar VEM [85], composite triangle FEM [60] and the three formulations: a 11β and 15β that is based on the Airy stress function basis given in (6.5), and a 13β hybrid formulation given in (6.6). For a stable method, the element stiffness matrix should have three zero eigenvalues that correspond to the zero-energy modes and the next smallest eigenvalue should be positive and bounded away from zero. For this test, we construct six-noded triangular elements with vertices at $\{(-1, 0), (1, 0), (\gamma_1, \gamma_2)\}$, where $\gamma_1 \in [-10, 10]$, $\gamma_2 \in [.05, 10]$, and then nodes are placed at the midpoints of each edge (see Figure 6.2). For each combination of γ_1 and γ_2, we compute the first non-rigid body eigenvalue, which corresponds to the fourth smallest eigenvalue of the element stiffness matrix. The contour plots of the first non-rigid body eigenvalue are given in Figure 6.3. The plots show that the 11β formulation will develop spurious modes as the elements become highly distorted. The 15β SH-VEM and B-bar VEM produced similar ranges for their eigenvalues and both do not produce any spurious zero-energy modes. The eigenvalue in the 13β formulation had a similar range to the standard VEM and further numerical tests show that the 13β formulation locks in the incompressible limit. Therefore both the 11β Airy stress and 13β hybrid formulations are not considered in the remaining examples. The 15β SH-VEM will be denoted as SH-VEM in the later examples.

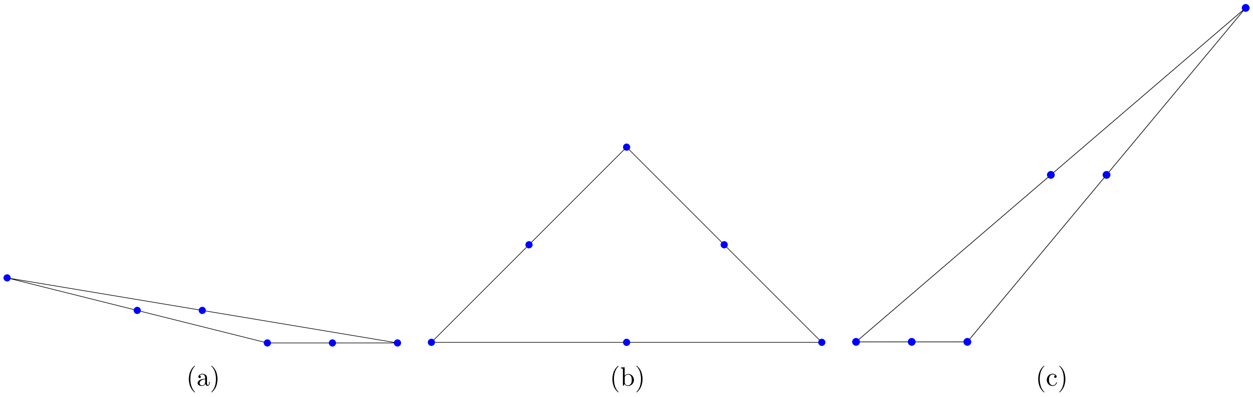
(a) (b) (c)

FIGURE 6.2. (a)-(c) Sequence of six-noded triangular elements with vertices at $\{(-1,0),\ (1,0),\ (\alpha,\beta)\}$ and nodes placed at the midpoint of each edge.

6.3.2. Eigenvalue analysis of the penalty formulation. We test the stability of the PSH-VEM with different values of the penalty parameter α. The material has Young's modulus $E_Y = 1$ psi and Poisson's ratio $\nu = 0.49995$. We choose four penalty parameters $\alpha \in \left\{\frac{\ell_0^2}{10}, \ell_0^2, 10\ell_0^2, 100\ell_0^2\right\}$ and examine the first non-rigid body eigenvalue of the element stiffness matrix of the penalty stress-hybrid formulation. For each α, we repeat the eigenvalue analysis presented in the previous section. In Figure 6.4, the countour plots of the the first non-rigid body eigenvalue as a function of (γ_1, γ_2) are shown. The plots reveal that as α increases, the maximum value of the eigenvalue decreases. This implies as $\alpha \to \infty$, the element stiffness matrix will be rank-deficient and lose stability. However, for the tested values of α, no spurious eigenvalues appear even for highly distorted elements.

6.3.3. Eigenvalue analysis for near incompressibility. It is known that in the incompressible limit ($\nu \to 0.5$) that the element stiffness matrix should only have one eigenvalue that tends to infinity [101]. Elements with more than one infinite eigenvalue will experience volumetric locking. We examine the eigenvalues of the element stiffness matrix for the standard VEM, CT FEM, B-bar VEM, 15β SH-VEM, and 12β PSH-VEM on a single element. The material has Youngs modulus $E_Y = 1$ psi and Poisson's ratio $\nu = 0.4999999$. In Table 6.1, the five largest eigenvalues of each method is presented for a regular six-noded triangular element (see Figure 6.1c) and Table 6.2 shows the eigenvalues for a six-noded nonconvex element (see Figure 6.1a). The tables show that the standard virtual element approach has all five largest eigenvalues tending to infinity, which leads to severe volumetric locking. The composite element has three diverging eigenvalues, which

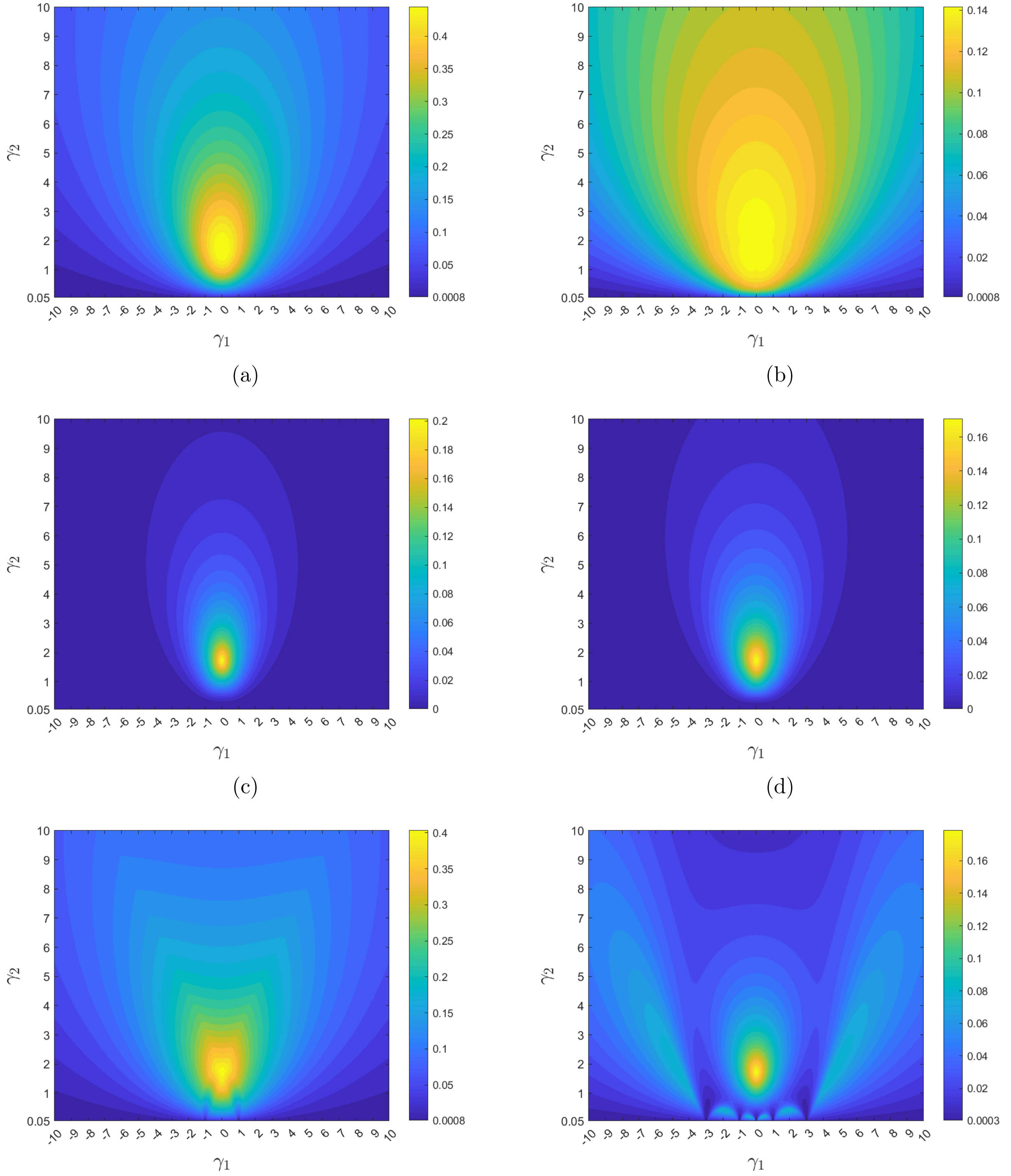

(a) (b) (c) (d) (e) (f)

FIGURE 6.3. Contour plots of the fourth-lowest eigenvalue as a function of (γ_1, γ_2) for (a) standard VEM, (b) B-bar VEM, (c) CT FEM, (d) 11β SH-VEM, (e) 13β SH-VEM, and (f) 15β SH-VEM.

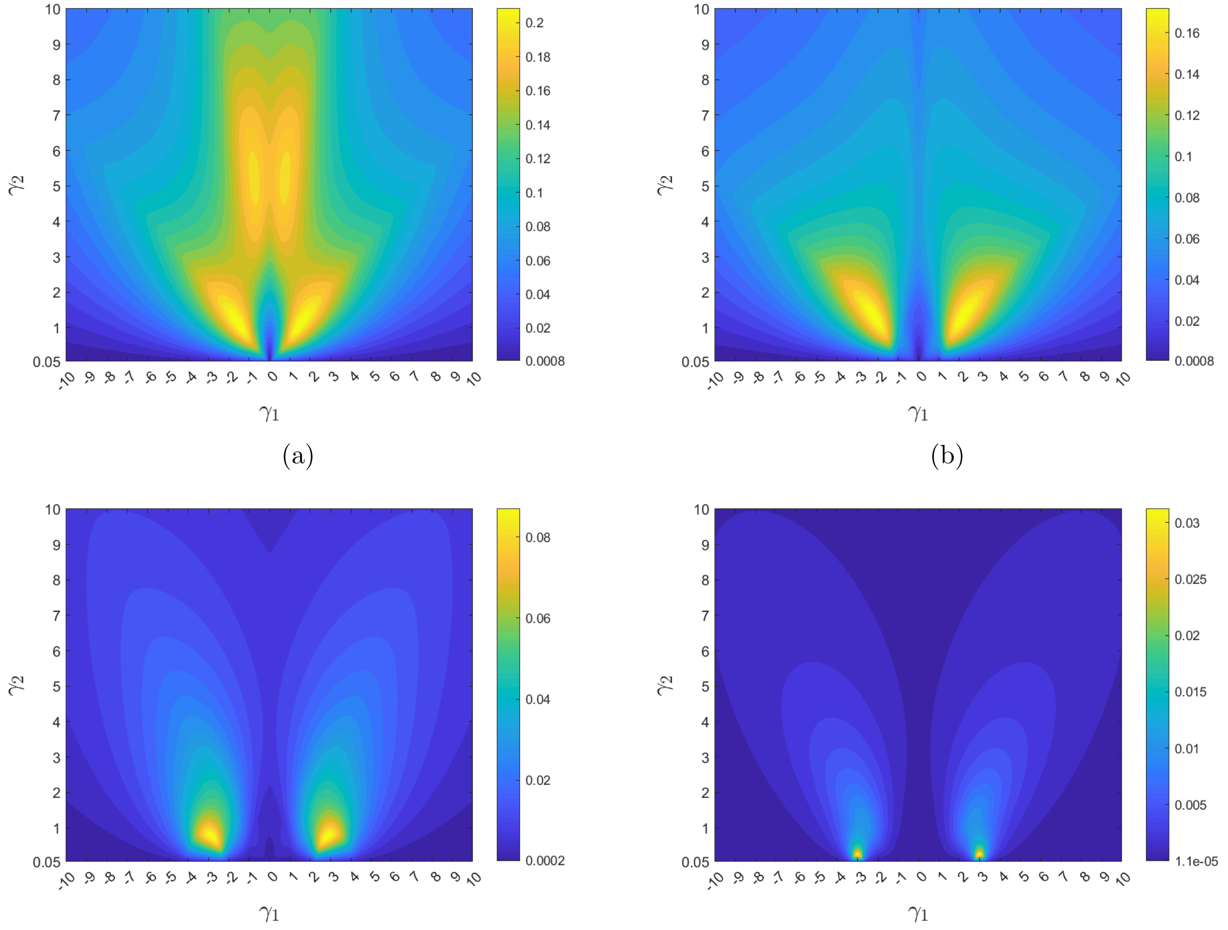

(a) (b)

(c) (d)

FIGURE 6.4. Contour plots of the fourth smallest eigenvalue as a function of (γ_1, γ_2) using the penalty parameters (a) $\alpha = \frac{\ell_0^2}{10}$, (b) $\alpha = \ell_0^2$, (c) $\alpha = 10\ell_0^2$, and (d) $\alpha = 100\ell_0^2$.

can result in the mild locking behavior. The B-bar VEM, SH-VEM, and PSH-VEM have only a single large eigenvalue for both the regular and the nonconvex element.

VEM	CT FEM	B-bar VEM	15β SH-VEM	12β PSH-VEM
1.1×10^6	8.1×10^{-1}	2.1×10^{-1}	6.3×10^{-1}	4.3×10^{-1}
1.2×10^6	1.2×10^0	2.2×10^{-1}	8.8×10^{-1}	8.2×10^{-1}
1.7×10^6	3.7×10^5	7.5×10^{-1}	1.9×10^0	8.4×10^{-1}
1.8×10^6	4.2×10^5	9.6×10^{-1}	4.5×10^1	2.8×10^0
5.0×10^6	4.6×10^5	4.2×10^6	4.2×10^6	4.2×10^6

TABLE 6.1. Comparison of the five largest eigenvalues of the element stiffness matrix on a six-noded triangular element.

VEM	CT FEM	B-bar VEM	15β SH-VEM	12β PSH-VEM
1.2×10^6	5.8×10^{-1}	2.9×10^{-1}	5.3×10^{-1}	3.6×10^{-1}
1.3×10^6	1.9×10^0	3.9×10^{-1}	1.5×10^0	1.3×10^0
5.8×10^6	4.8×10^5	2.1×10^0	6.6×10^0	2.0×10^0
5.9×10^6	5.6×10^5	2.2×10^0	1.8×10^1	5.1×10^0
1.2×10^7	6.8×10^6	6.7×10^6	6.7×10^6	6.7×10^6

TABLE 6.2. Comparison of the five largest eigenvalues of the element stiffness matrix on a six-noded nonconvex element.

6.3.4. Thin cantilever beam. We revisit the problem of a nearly incompressible thin cantilever beam subjected to a shear end load as described in Section 5.4.3. The material properties are given by $E_Y = 1 \times 10^5$ psi and $\nu = 0.49995$. We first use a set of unstructured triangular meshes. In Figure 6.5, we show examples of the unstructred meshes and in Figure 6.6 we show the convergence of the four methods in the displacement L^2 norm, energy seminorm, and L^2 norm of hydrostatic stress. Figure 6.7 shows the convergence of the end displacement and the contour plot of hydrostatic stress for the SH-VEM. For methods that experience volumetric locking, non-physical oscillations will appear in the hydrostatic stress field. The plots reveal that the two stress-hybrid approaches yield better results, with the PSH-VEM having superior convergence and accuracy in the displacement, energy, and hydrostatic stress.

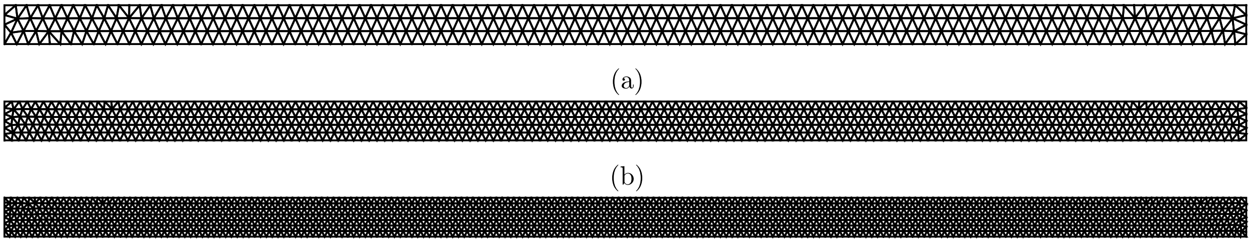
(a)

(b)

(c)

FIGURE 6.5. Unstructured triangular meshes for the cantilever beam problem. (a) 600 elements, (b) 1600 elements, and (c) 3000 elements.

In the following tests, we examine the four methods on meshes with $N = 1$ and $N = 2$ elements along the height of the beam. For many formulations, these meshes will lead to overly stiff displacements and shear locking. The first set of meshes is constructed by taking a uniform quadrilateral mesh and splitting each element into two right triangles (see Figure 6.8). The convergence of the end displacement of the four methods is presented in Figure 6.9. For $N = 1$, the two stress-hybrid methods are converging to the exact solution, while CT FEM experiences shear locking and B-bar

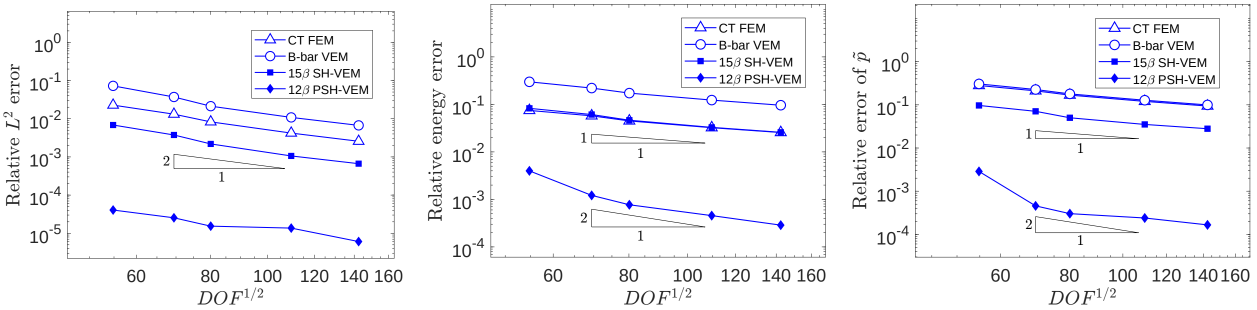

(a) (b) (c)

Figure 6.6. Comparison of CT FEM, B-bar VEM, SH-VEM and PSH-VEM for the thin cantilever beam problem on unstructured meshes. (a) L^2 error of displacement, (b) energy error, and (c) L^2 error of hydrostatic stress.

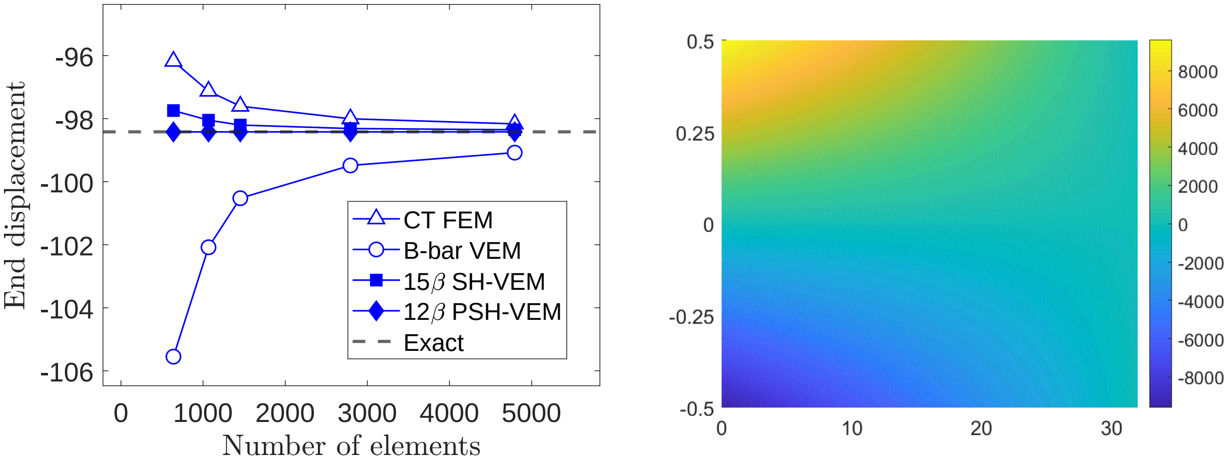

(a) (b)

Figure 6.7. (a) Convergence of the end displacement for the cantilever beam problem. The mesh consists of unstructured triangles. (b) Contour plot of the hydrostatic stress for PSH-VEM.

VEM diverges from the exact solution (see Figure 6.9a) and for $N = 2$, B-bar VEM is still overly flexible (see Figure 6.9b). In both cases, the PSH-VEM shows far superior accuracy in displacement even on coarse meshes.

The second set of meshes is constructed by taking a uniform quadrilateral mesh and splitting each element along the two diagonals to form four triangles. The meshes are shown in Figure 6.10 and the convergence of the end displacement is depicted in Figure 6.11. The plots show that SH-VEM and PSH-VEM converge to the exact solution for both $N = 1$ and $N = 2$; however, the SH-VEM is much stiffer and less accurate than the penalty approach. CT FEM suffers from locking, while B-bar fails to converge for the case of a single element along the height.

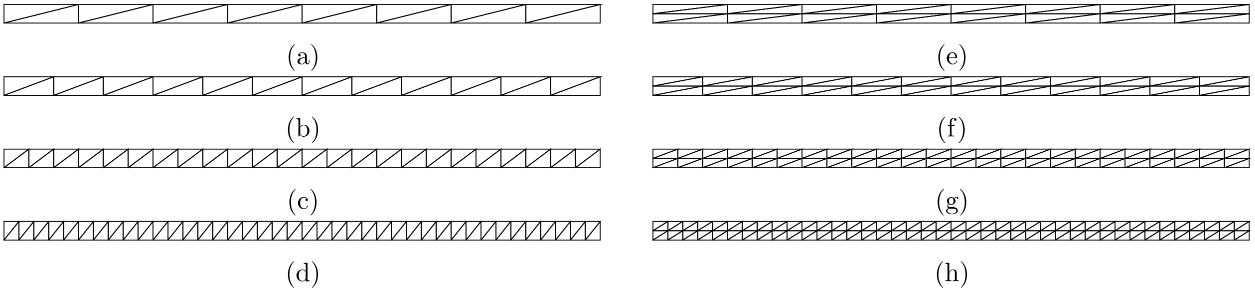

Figure 6.8. Structured meshes for the cantilever beam problem. Mesh is refined along the length with (a)-(d) 1 element along the height and (e)-(h) 2 elements along the height.

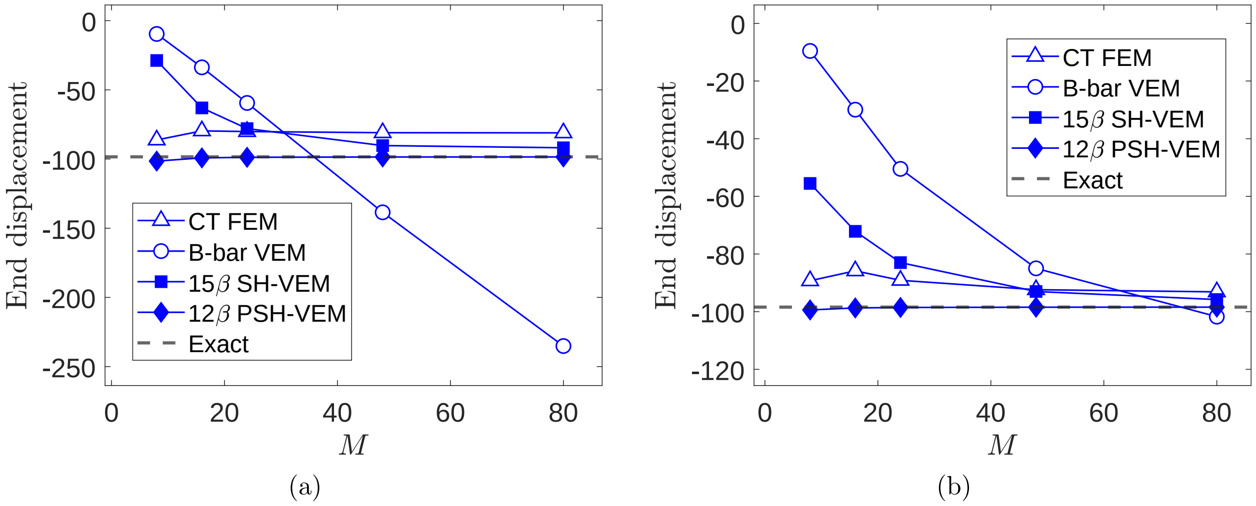

Figure 6.9. Convergence of the end displacement for the cantilever beam problem. The mesh consists of $M \times N$ right triangles, where M is the number of elements along the length of the beam. (a) $N = 1$ and (b) $N = 2$.

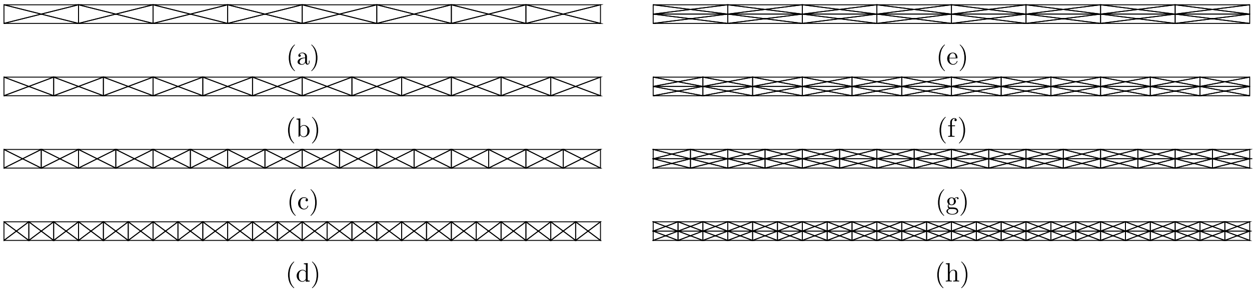

Figure 6.10. Structured meshes for the cantilever beam problem. Mesh is refined along the length with (a)-(d) 1 element along the height and (e)-(h) 2 elements along the height.

The third set of meshes is constructed by taking the previous mesh and collapsing one of the triangles to a nearly degenerate triangle (see Figure 6.12). The plots showing the convergence of the

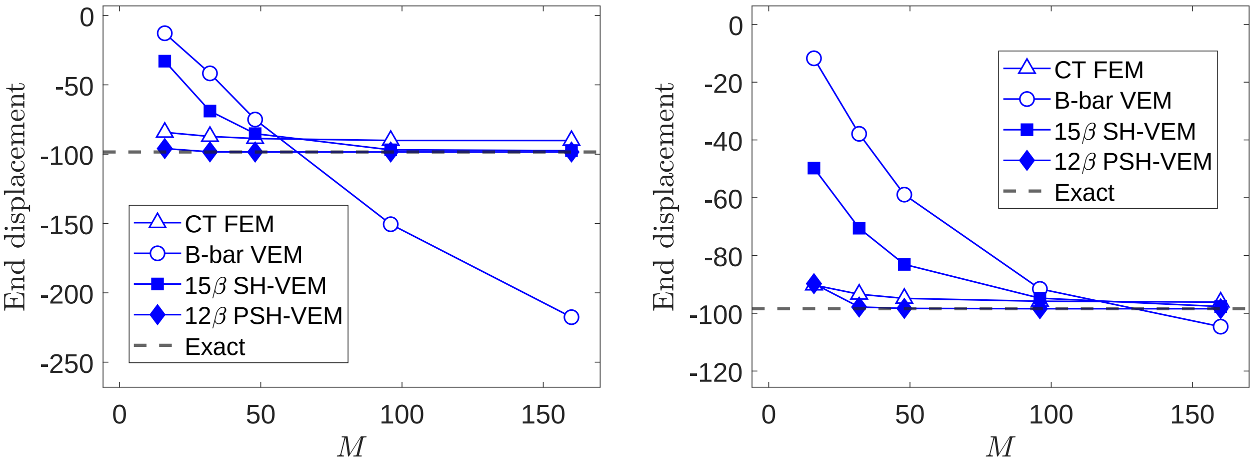

(a)

(b)

FIGURE 6.11. Convergence of the end displacement for the cantilever beam problem. The mesh consists of $M \times N$ triangles, where M is the number of elements along the length of the beam. (a) $N = 1$ and (b) $N = 2$.

end displacement is given in Figure 6.13. The plots reveal that for these meshes, the stress-hybrid methods are converging to the exact solution, while CT FEM and B-bar VEM do not converge in the case of a single element along the height. When using two elements along the height, the B-bar formulation is tending to the exact solution but is not accurate, while CT FEM still suffers from locking and does not converge. The PSH-VEM again attains a much more accurate solution than the other methods; however, it appears to be stiff for the coarsest mesh when $N = 2$.

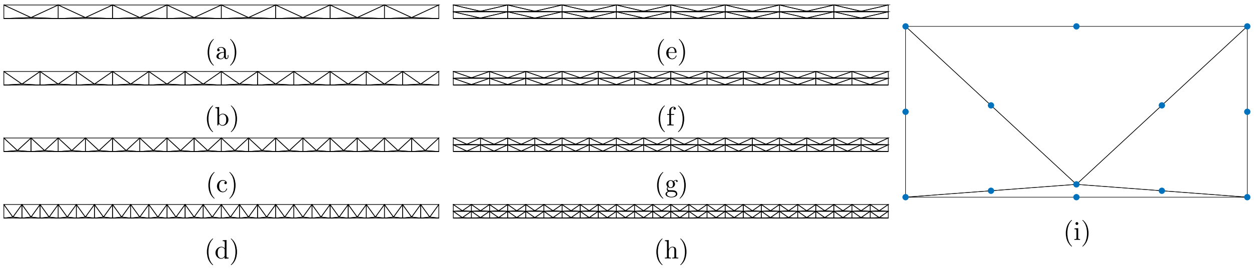

(a)

(b)

(c)

(d)

(e)

(f)

(g)

(h)

(i)

FIGURE 6.12. Structured nearly degenerate meshes for the cantilever beam problem. Mesh is refined along the length with (a)-(d) 1 element along the height and (e)-(h) 2 elements along the height. (i) Magnification of a single element split into four six-noded triangles.

One benefit of the virtual element formulation is that it allows for very general element shapes. In particular, for the final set of meshes we use a mixture of distorted nonconvex hexagons and convex hexagons. A few representative meshes are shown in Figure 6.14. In Figure 6.15, we present

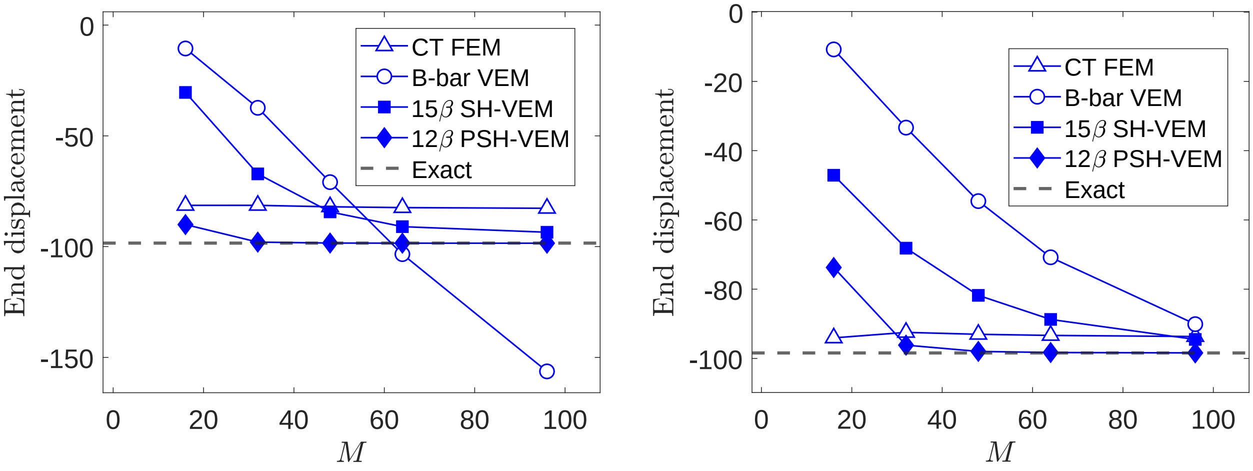

(a) (b)

FIGURE 6.13. Convergence of the end displacement for the cantilever beam problem. The mesh consists of $M \times N$ triangles with some nearly degenerate, where M is the number of elements along the length of the beam. (a) $N = 1$ and (b) $N = 2$.

the convergence of the end displacement for the four methods. In both cases $N = 1$ and $N = 2$, SH-VEM and PSH-VEM are convergent, but CT FEM is overly stiff.

REMARK 6.3.1. *The solutions produced by* 15β *SH-VEM are much stiffer than those found using the* 5β *formulation on quadrilaterals in* [38]. *In particular, for uniform rectangular meshes with* $N = 1$, *the* 5β *SH-VEM converges to nearly the exact solution with just* $M = 8$ *elements along the length of the beam. However, the PSH-VEM offers coarse mesh accuracy that is similar to the* 5β *SH-VEM.*

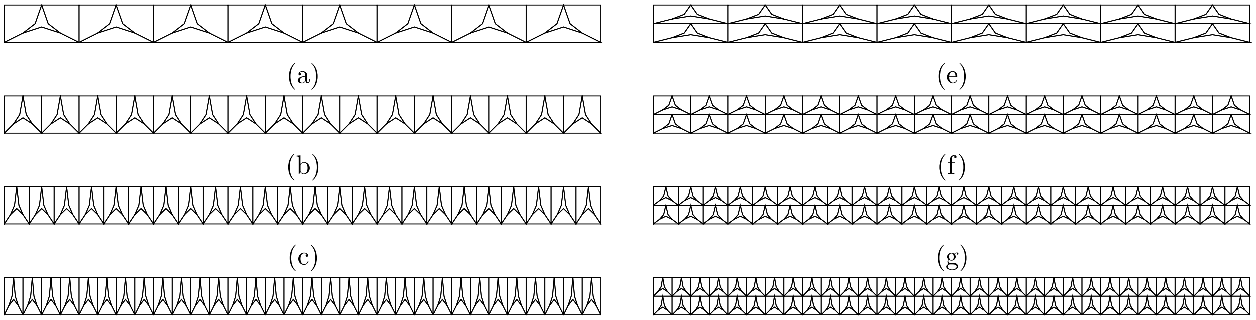

(a) (e)

(b) (f)

(c) (g)

(d) (h)

FIGURE 6.14. Meshes with nonconvex elements for the cantilever beam problem. Mesh is refined along the length with (a)-(d) 1 element along the height and (e)-(h) 2 elements along the height.

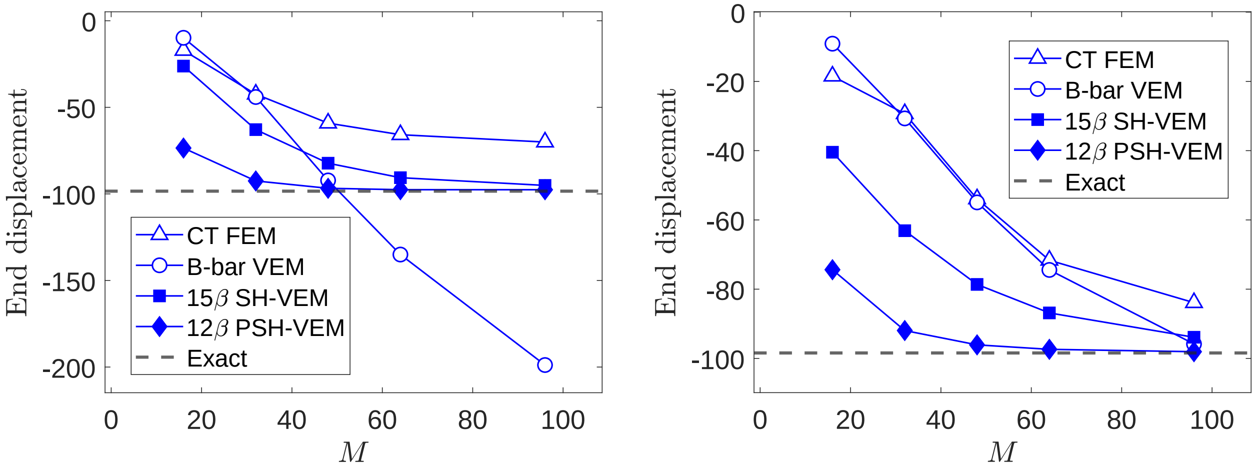

(a) (b)

FIGURE 6.15. Convergence of the end displacement for the cantilever beam problem. The mesh consists of $M \times N$ convex and nonconvex elements, where M is the number of elements along the length of the beam. (a) $N = 1$ and (b) $N = 2$.

The penalty stress-hybrid approach provides the best accuracy for the cantilever beam problem; however, it relies on the choice of a suitable penalty parameter α. Therefore, we examine the sensitivity of the bending solution of PSH-VEM to the penalty parameter. For this test, we use the same material properties $E_Y = 1 \times 10^5$ psi and $\nu = 0.49995$. The problem is solved on a mesh consisting of $M \times 1$ right triangles (see Figure 6.8). The default penalty parameter is given by $\alpha = \frac{10^4 \ell_0^2}{E_Y} = 10^{-1}\ell_0^2$. To test the sensitivity of the parameter, we vary the penalty parameter three orders of magnitude on each side. That is, α is varied from $10^{-4}\ell_0^2$ to $10^2\ell_0^2$. In Figure 6.16, the convergence of the end displacements for different values of α is presented. The plot shows that increasing α above the value $10^{-1}\ell_0^2$ does not greatly affect the solution; however, decreasing α makes the solution stiffer. If we decrease the value of α by three orders of magnitude to $\alpha = 10^{-4}\ell_0^2$, the solution becomes overly stiff and produces much larger errors than the other values of α.

6.3.5. Cook's membrane. Next, we consider the problem of the Cook's membrane under shear load as described in Section 5.4.4. The material has Youngs modulus $E_Y = 250$ psi and Poisson's ratio $\nu = 0.49995$. The first set of meshes comprise of structured triangular meshes; a few sample meshes are shown in Figure 6.17. Figure 6.18 presents the convergence of the tip displacement of the four methods and the hydrostatic stress of the PSH-VEM. The plot in Figure 6.18a

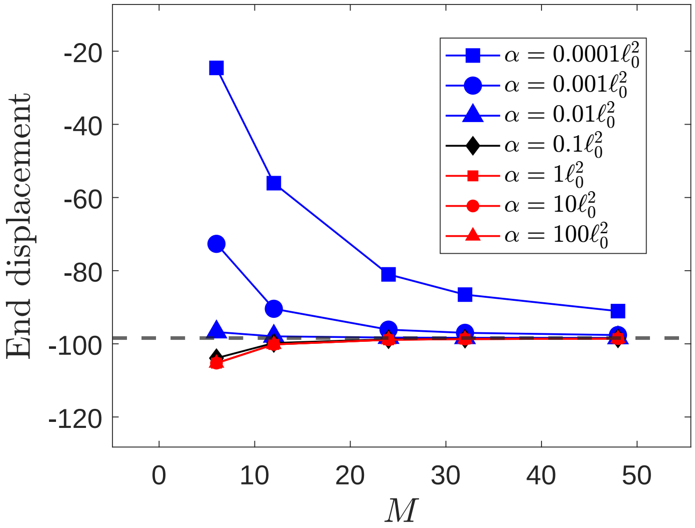

FIGURE 6.16. Comparison of the convergence of end displacement for PSH-VEM when using different choices of penalty parameter α. The mesh consists of $M \times 1$ right triangles, where M is the number of elements along the length of the beam.

shows that, unlike in the cantilever beam problem, the CT FEM, SH-VEM, and PSH-VEM all perform worse than the B-bar formulation. Figure 6.18b shows that the PSH-VEM is able to produce a relatively smooth hydrostatic stress field with no visible signs of volumetric locking.

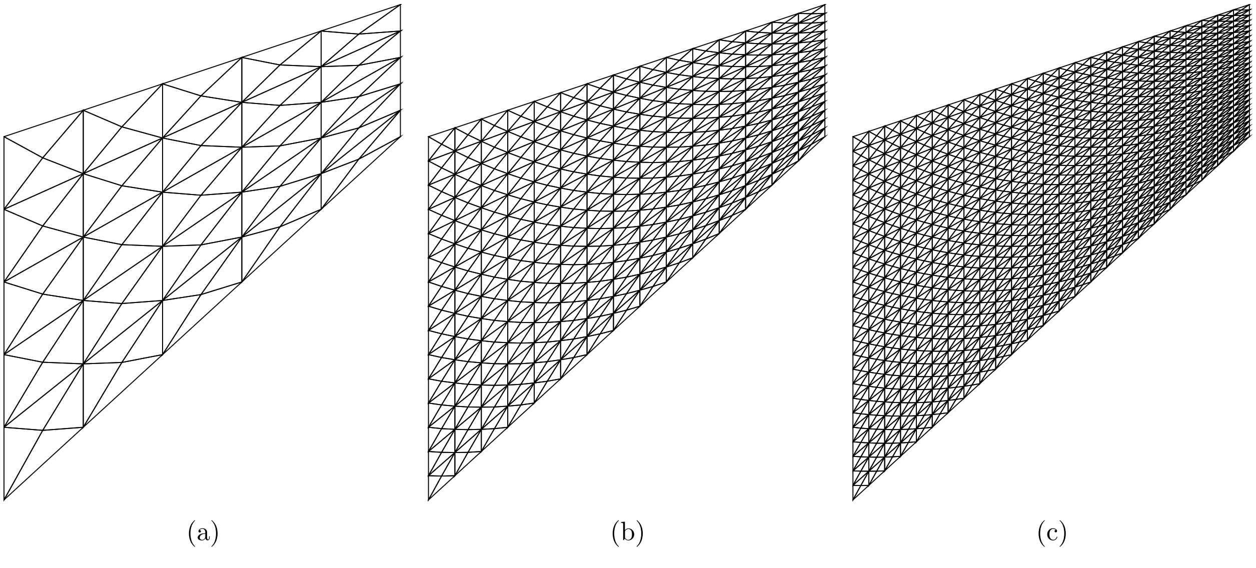

(a)

(b)

(c)

FIGURE 6.17. Structured triangular meshes for the Cook's membrane problem. (a) 100 elements, (b) 1000 elements, and (c) 2500 elements.

The second set of meshes that we test consists of unstructured triangles. In Figure 6.19, sample meshes are shown. The convergence of tip displacement and the contour plot of PSH-VEM is given

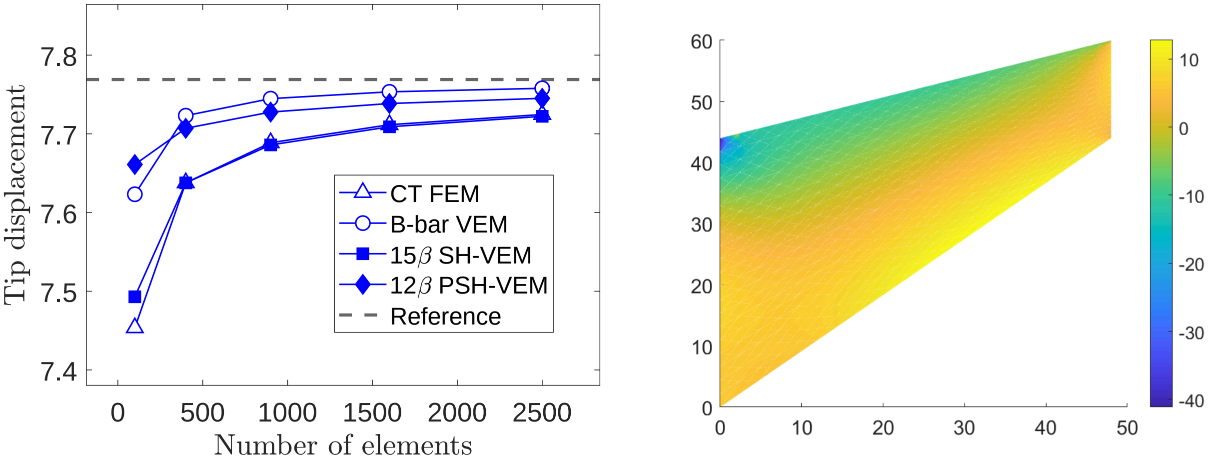

(a) (b)

FIGURE 6.18. (a) Convergence of the tip displacement for Cook's membrane problem. The mesh consists of structured triangles. (b) Contour plot of the hydrostatic stress for PSH-VEM.

in Figure 6.20. The plots show that for the unstructured mesh, SH-VEM and PSH-VEM have the fastest convergence, while B-Bar VEM becomes very flexible and converges from above. The hydrostatic stress contours of PSH-VEM remain smooth and agree with the contours found on structured meshes.

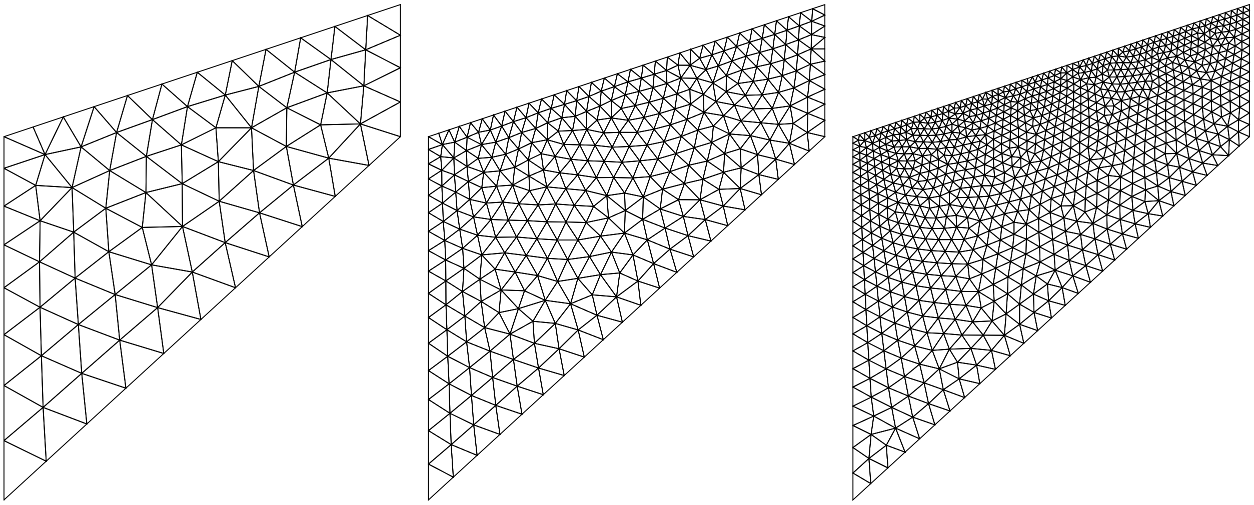

(a) (b) (c)

FIGURE 6.19. Unstructured triangular meshes for the Cook's membrane problem. (a) 100 elements, (b) 700 elements, and (c) 2000 elements.

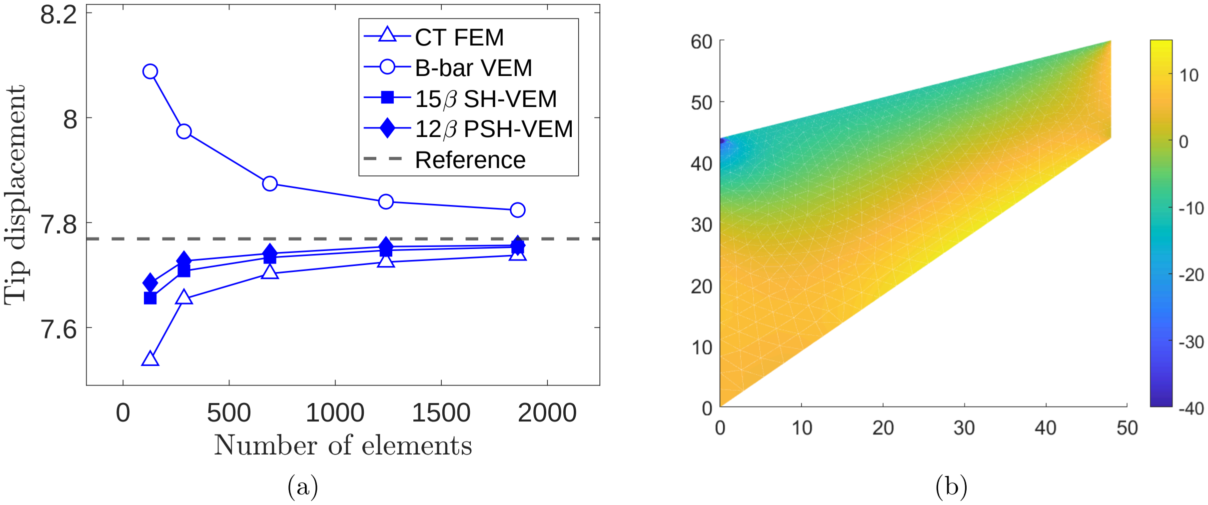

FIGURE 6.20. (a) Convergence of the tip displacement for Cook's membrane problem. The mesh consists of unstructured triangles. (b) Contour plot of the hydrostatic stress for PSH-VEM.

6.3.6. Plate with a circular hole. We consider the problem of an infinite plate with a circular hole of radius $a = 1$ inch under uniform tension as given in Section 5.4.5. The material has Young's modulus $E_Y = 2 \times 10^7$ psi and Poisson's ratio $\nu = 0.49995$. The first test of this problem is on unstructured triangular meshes with representative meshes shown in Figure 6.21. In Figure 6.22, we show the convergence results of the four methods that are tested and find that the three methods CT FEM, B-bar VEM, and SH-VEM all have optimal convergence rates. However, the penalty stress-hybrid method has third order superconvergence in the energy seminorm and L^2 norm of hydrostatic stress. In Figure 6.23, we plot the contours of the pointwise error $\tilde{p} - \tilde{p}_h$ of the hydrostatic stress. The plots reveal that the penalty stress-hybrid method has the smallest pointwise error and the remaining three methods produce similar error distributions.

We now solve the problem on perturbed meshes. In [3], it is shown that small perturbations of a regular triangular mesh can lead to locking and a reduction in the rate of convergence in the hydrostatic stress error. For this test, we start with a regular quadrilateral mesh and then cut along both diagonals to create four triangles. The point of intersection of the two diagonals are perturbed for each quadrilateral. Representative meshes are shown in Figure 6.24. In Figure 6.25, we plot the convergence of the four methods and find that CT FEM, B-bar VEM, and SH-VEM all still retain optimal rates of convergence. The penalty formulation exhibits second order superconvergence in the energy seminorm and L^2 norm of the hydrostatic stress. The contour plots in Figure 6.26 show

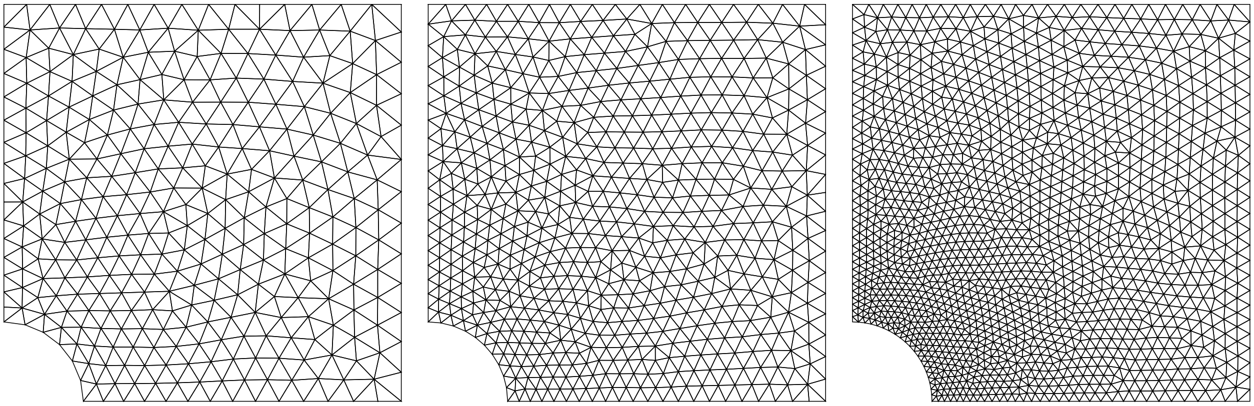

(a) (b) (c)

FIGURE 6.21. Unstructured triangular meshes for the plate with a hole problem. (a) 500 elements, (b) 1000 elements, and (c) 3000 elements.

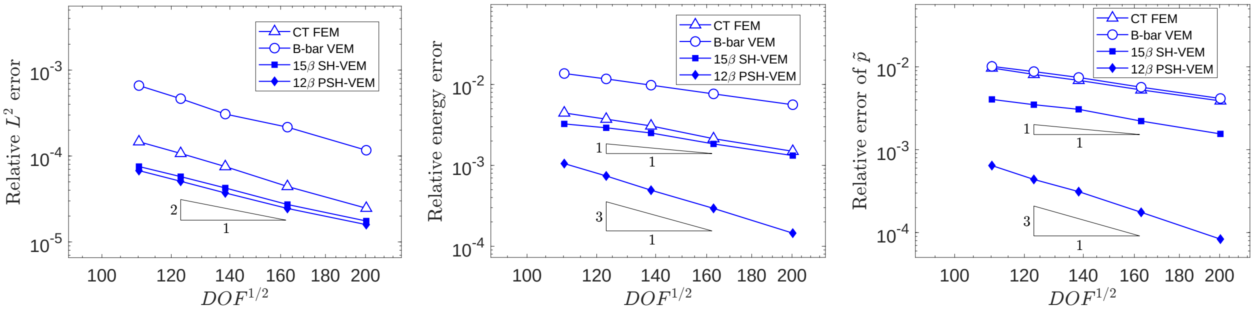

(a) (b) (c)

FIGURE 6.22. Comparison of CT FEM, B-bar VEM, SH-VEM, and PSH-VEM for the plate with a hole problem on unstructured meshes. (a) L^2 error of displacement, (b) energy error, and (c) L^2 error of hydrostatic stress.

that the four methods all have relatively smooth error distributions of the hydrostatic stress and display no signs of volumetric locking.

6.3.7. Hollow cylinder under internal pressure. Next, we consider a hollow cylinder subject to internal pressure. The description of the problem and boundary conditions are given in Section 5.4.6. The material properties are $E_Y = 2 \times 10^5$ psi and $\nu = 0.49995$. For this problem, the hydrostatic stress field is constant and we found that using nonconstant stress functions in the SH-VEM resulted in larger errors around the element corners. Therefore, we use an element averaged hydrostatic stress approximation for SH-VEM. We first solve the problem on structured triangular meshes; a few representative meshes are shown in Figure 6.27. In Figure 6.28, we show the rates of convergence in three error norms. The three methods CT FEM, B-bar VEM, and

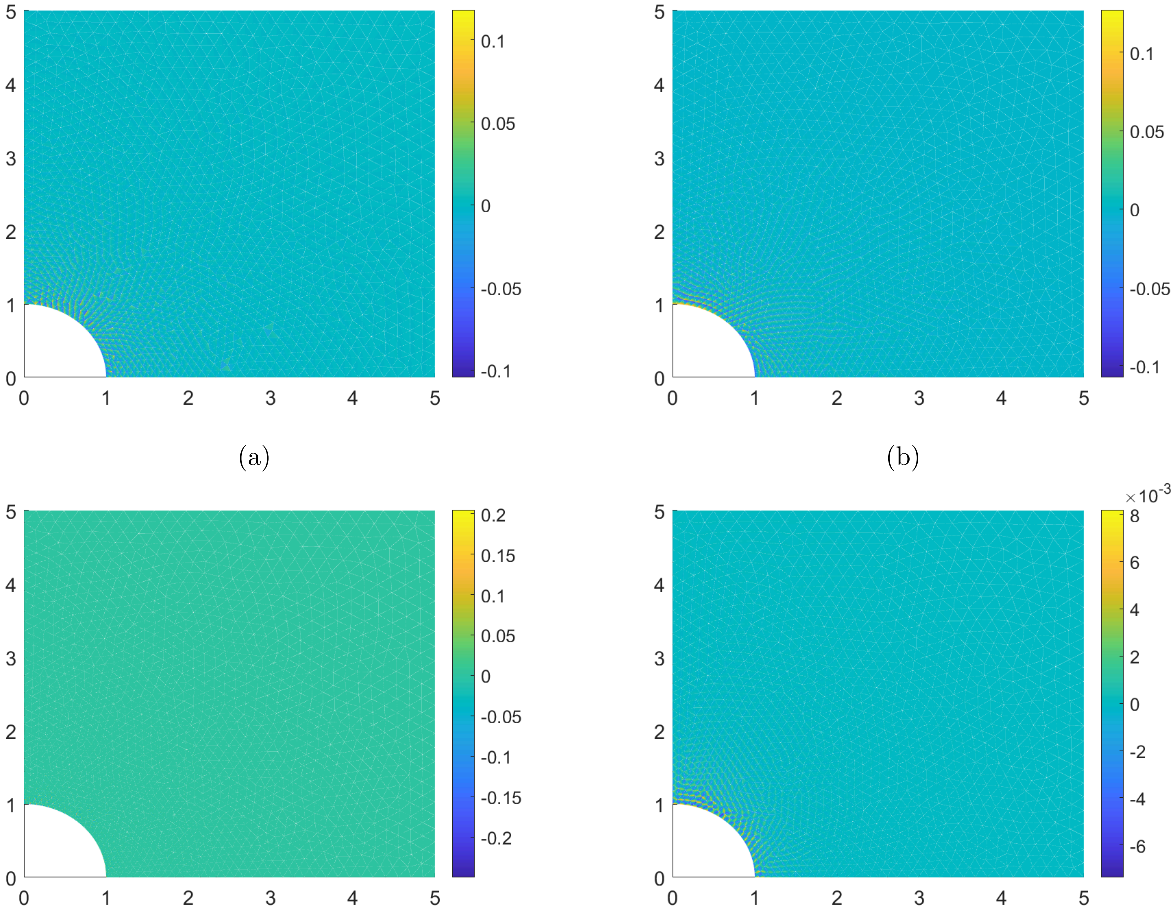

(a)

(b)

(c)

(d)

FIGURE 6.23. Contour plots of the error $\tilde{p}-\tilde{p}_h$ in hydrostatic stress on unstructured meshes for the plate with a circular hole problem. (a) CT FEM, (b) B-bar VEM, (c) SH-VEM, and (d) PSH-VEM.

SH-VEM produce optimal convergence in the displacement L^2 norm, L^2 norm of hydrostatic stress as well as in the energy seminorm; while the PSH-VEM has second order superconvergence in the energy seminorm and third order in the L^2 norm of the hydrostatic stress. In Figure 6.29, we plot the contours of the relative error in the hydrostatic stress field for the four methods. The plots show that the maximum errors concentrate along the inner radius and improves when away from the boundary. The SH-VEM and PSH-VEM produce the smallest relative errors, with a maximum of around 8 and 1.2 percent, respectively.

We now test the hollow cylinder problem on an unstuctured triangular mesh; a few representative meshes are presented in Figure 6.30. In Figure 6.31, the convergence results are given and

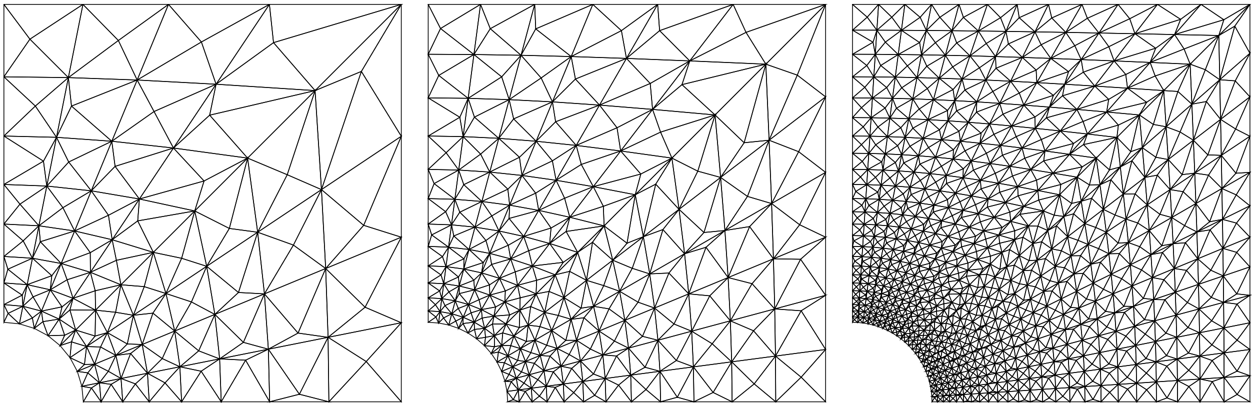
(a) (b) (c)

FIGURE 6.24. Perturbed triangular meshes for the plate with a hole problem. (a) 250 elements, (b) 500 elements, and (c) 2500 elements.

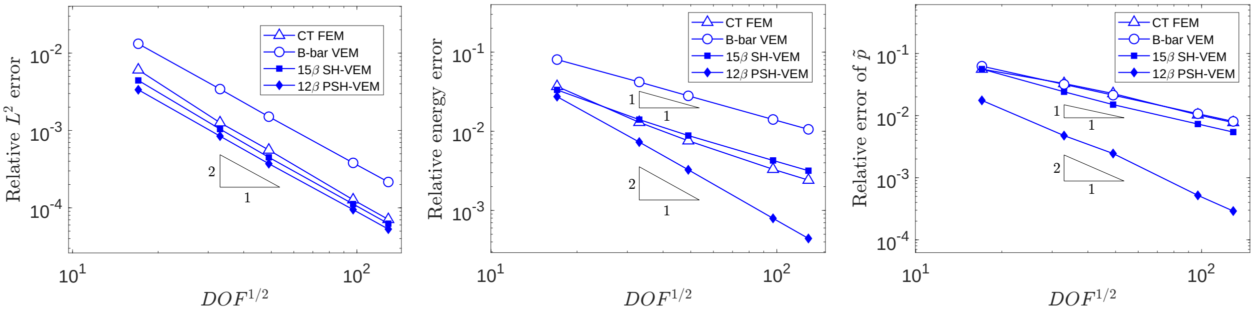

(a) (b) (c)

FIGURE 6.25. Comparison of CT FEM, B-bar VEM, SH-VEM, and PSH-VEM for the plate with a hole problem on perturbed meshes. (a) L^2 error of displacement, (b) energy error, and (c) L^2 error of hydrostatic stress.

again show that CT FEM, B-bar VEM, and SH-VEM deliver optimal rates. The penalty approach attains third and fourth order superconvergence in the energy seminorm and hydrostatic stress L^2 norm, respectively. The contour plots in Figure 6.32 show that for CT FEM, B-bar VEM, and SH-VEM, the errors are concentrated near the inner radius. The largest error from SH-VEM is 9 percent, while both CT FEM and B-bar VEM produce much larger errors of 70 and 60 percent, respectively. For PSH-VEM, the errors are much smaller, with a maximum relative error of 0.4 percent.

Next, we examine the effects of the penalty parameter on the convergence rates of the pressurized cylinder problem. For simplicity, the material properties are set to be $E_Y = 1 \times 10^4$ psi and $\nu = 0.49995$. The problem is solved on structured triangular meshes (see Figure 6.27). The initial

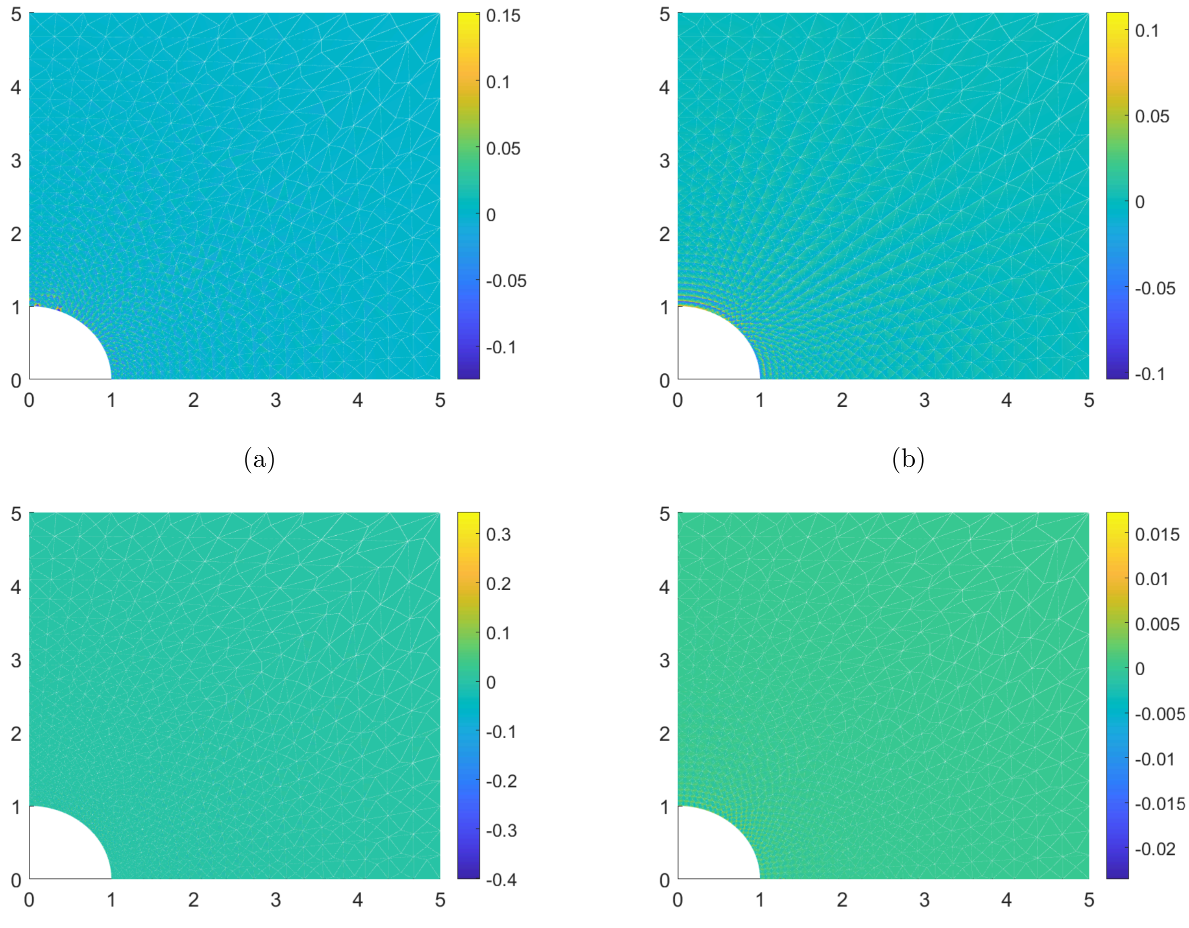

(a)

(b)

(c)

(d)

FIGURE 6.26. Contour plots of the error $\tilde{p} - \tilde{p}_h$ in hydrostatic stress on perturbed meshes for the plate with a circular hole problem. (a) CT FEM, (b) B-bar VEM, (c) SH-VEM, and (d) PSH-VEM.

penalty parameter is $\alpha = \frac{10^4 \ell_0^2}{E_Y} = \ell_0^2$, so we test α in the range of $10^{-3}\ell_0^2$ to $10^3\ell_0^2$. In Figure 6.33, we show the rates of convergence in the three error norms for different values of the penalty parameter α. The plots show that varying α did not affect the convergence of the displacement errors; however, the convergence of the energy seminorm is slightly affected and the rate of convergence in the L^2 norm of the hydrostatic stress is significantly reduced as α is decreased.

6.3.8. Manufactured problem. The basis functions derived from the Airy stress functions only satisfy the equilibrium conditions without a body force. Therefore, we test the convergence on a problem with a nonzero body force. We consider a manufactured problem given in [100] with

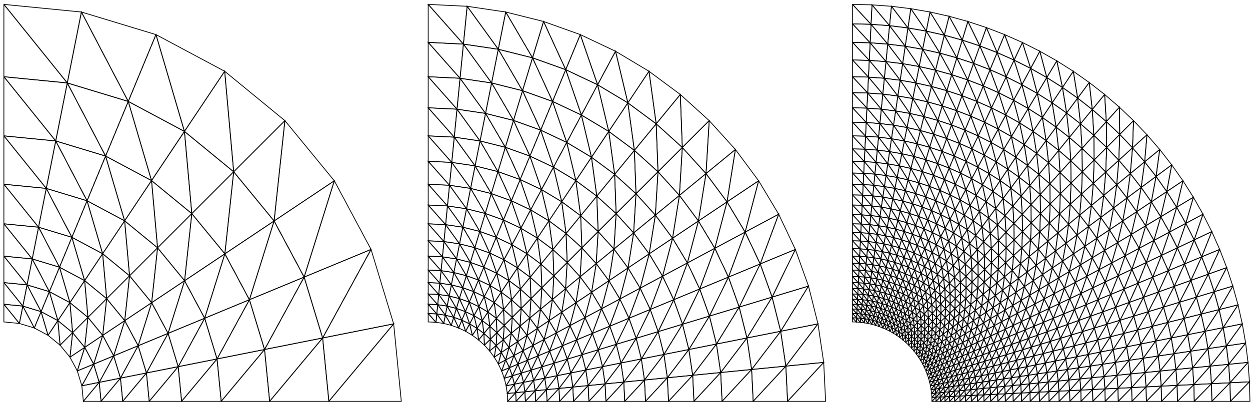

(a) (b) (c)

FIGURE 6.27. Structured triangular meshes for the hollow cylinder problem. (a) 128 elements, (b) 512 elements, and (c) 2048 elements.

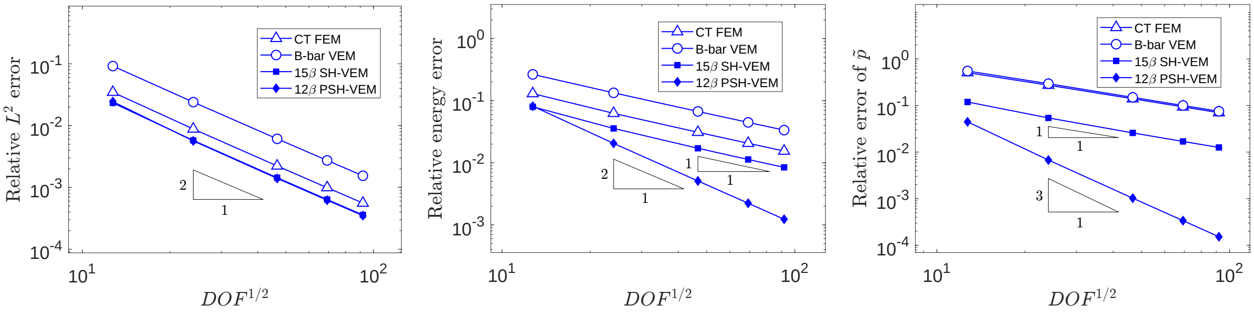

(a) (b) (c)

FIGURE 6.28. Comparison of CT FEM, B-bar VEM, SH-VEM, and PSH-VEM for the pressurized cylinder problem on structured meshes. (a) L^2 error of displacement, (b) energy error, and (c) L^2 error of hydrostatic stress.

the exact solution and loading given by:

$$
\begin{aligned}
u(\boldsymbol{x}) &= \sin 2\pi y(\cos 2\pi x - 1) + \frac{1}{1+\lambda}\sin \pi x \sin \pi y,\\
v(\boldsymbol{x}) &= \sin 2\pi x(1 - \cos 2\pi y) + \frac{1}{1+\lambda}\sin \pi x \sin \pi y,\\
\boldsymbol{b}(\boldsymbol{x}) &= -\pi^2 \left\{ \begin{matrix} \left(\frac{\lambda+\mu}{\lambda+1}\right)\cos \pi(x+y) - \mu(8\cos 2\pi x \sin 2\pi y - 4\sin 2\pi y + \frac{2}{\lambda+1}\sin \pi x \sin \pi y) \\ \left(\frac{\lambda+\mu}{\lambda+1}\right)\cos \pi(x+y) - \mu(-8\cos 2\pi y \sin 2\pi x + 4\sin 2\pi x + \frac{2}{\lambda+1}\sin \pi x \sin \pi y) \end{matrix} \right\},
\end{aligned}
$$

where λ and μ are the first and second Lamé parameters given by

$$
\lambda = \frac{E_Y \nu}{(1+\nu)(1-2\nu)}, \quad \mu = \frac{E_Y}{2(1+\nu)}.
$$

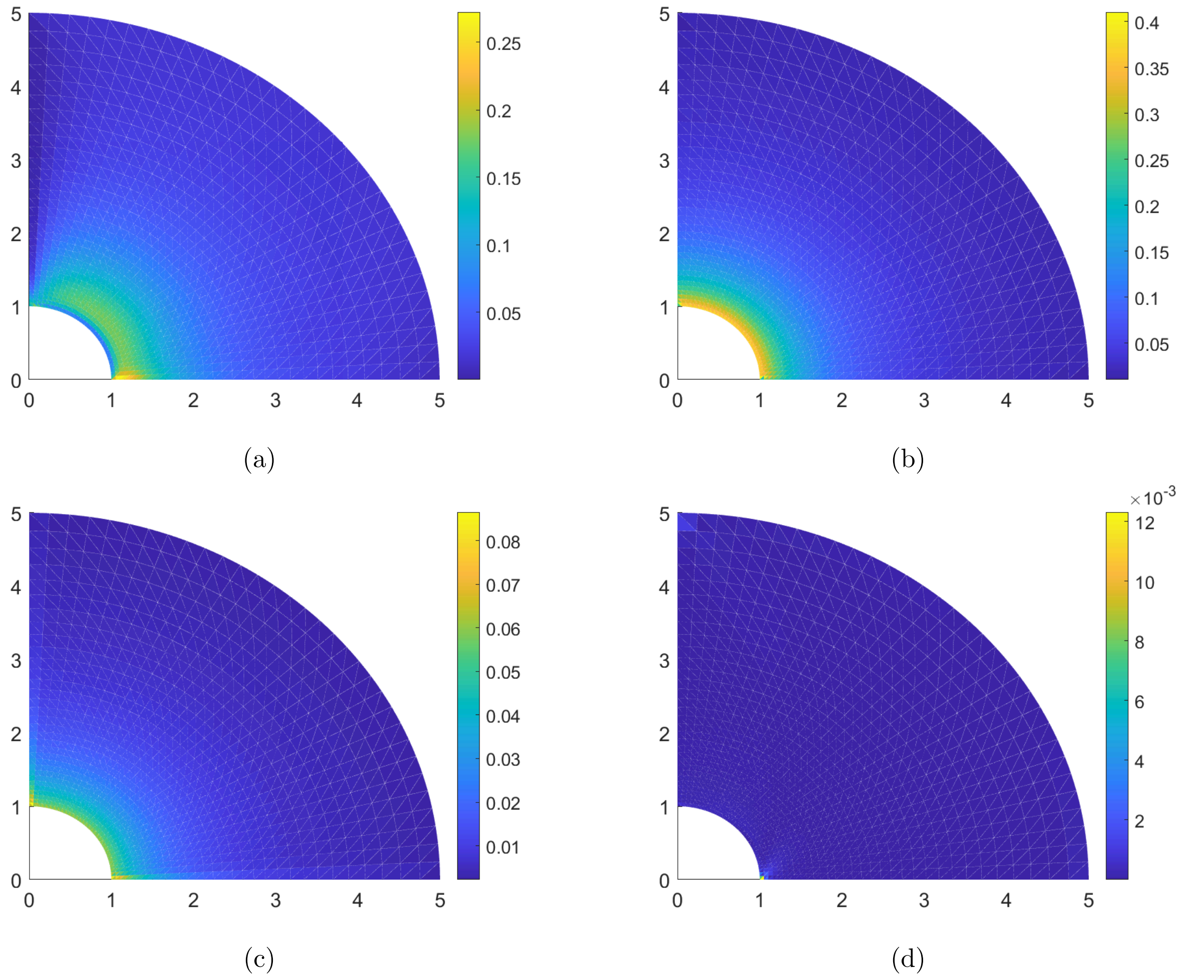

(a)

(b)

(c)

(d)

FIGURE 6.29. Contour plots of the relative error in the hydrostatic stress on structured meshes for the pressurized cylinder problem. The exact hydrostatic stress is 4166.528 psi. (a) CT FEM, (b) B-bar VEM, (c) SH-VEM, and (d) PSH-VEM.

For this problem, the material properties are set to $E_Y = 1$ psi and $\nu = 0.49995$. The first set of meshes we use is a perturbed unstructured triangular mesh. A few sample meshes are shown in Figure 6.34. The plots in Figure 6.35 show that the four methods converge optimally in displacement L^2 norm, energy seminorm, and hydrostatic stress L^2 norm. The PSH-VEM has smaller errors in both the energy and hydrostatic stress, but does not reach second order superconvergence. The contour plots in Figure 6.36 reveal that large errors in CT FEM appear along the boundary, while the other three methods have smooth hydrostatic stress fields.

Now, we solve the manufactured problem on a series of structured meshes. The meshes are generated by taking a uniform quadrilateral mesh, then splitting each element along the diagonal

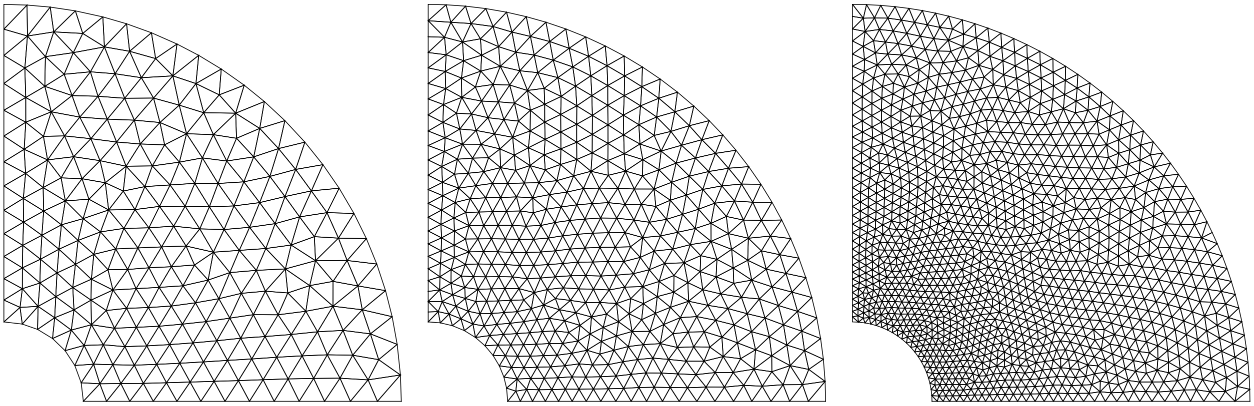

(a) (b) (c)

Figure 6.30. Unstructured triangular meshes for the hollow cylinder problem. (a) 500 elements, (b) 1000 elements, and (c) 2500 elements.

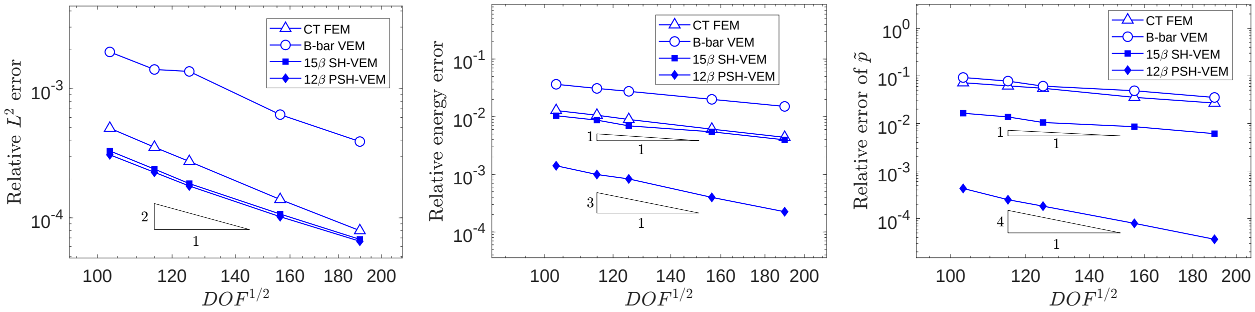

(a) (b) (c)

Figure 6.31. Comparison of CT FEM, B-bar VEM, SH-VEM, and PSH-VEM for the pressurized cylinder problem on unstructured meshes. (a) L^2 error of displacement, (b) energy error, and (c) L^2 error of hydrostatic stress.

into two triangles. Then each triangular element is split into three pieces; a few representative meshes are shown in Figure 6.37. As was the case with the perturbed meshes, Figure 6.38 shows that all four methods deliver optimal convergence rates. The PSH-VEM again has the smallest errors in energy and hydrostatic stress, while the SH-VEM has the largest errors in hydrostatic stress. The contour plots in Figure 6.39 are relatively smooth and do not show large errors along the boundary.

Remark 6.3.2. *From the sensitivity analysis of the beam and hollow cylinder, we know that if* α *is three orders of magnitude smaller than* $\frac{10^4 \ell_0^2}{E_Y}$*, then the convergence rates in energy seminorm and* L^2 *norm of the hydrostatic stress are affected. For this manufactured problem, when using a Young's modulus* $E_Y = 1$ *psi and* α *given in* (6.26)*, the penalty parameter is set to the minimum*

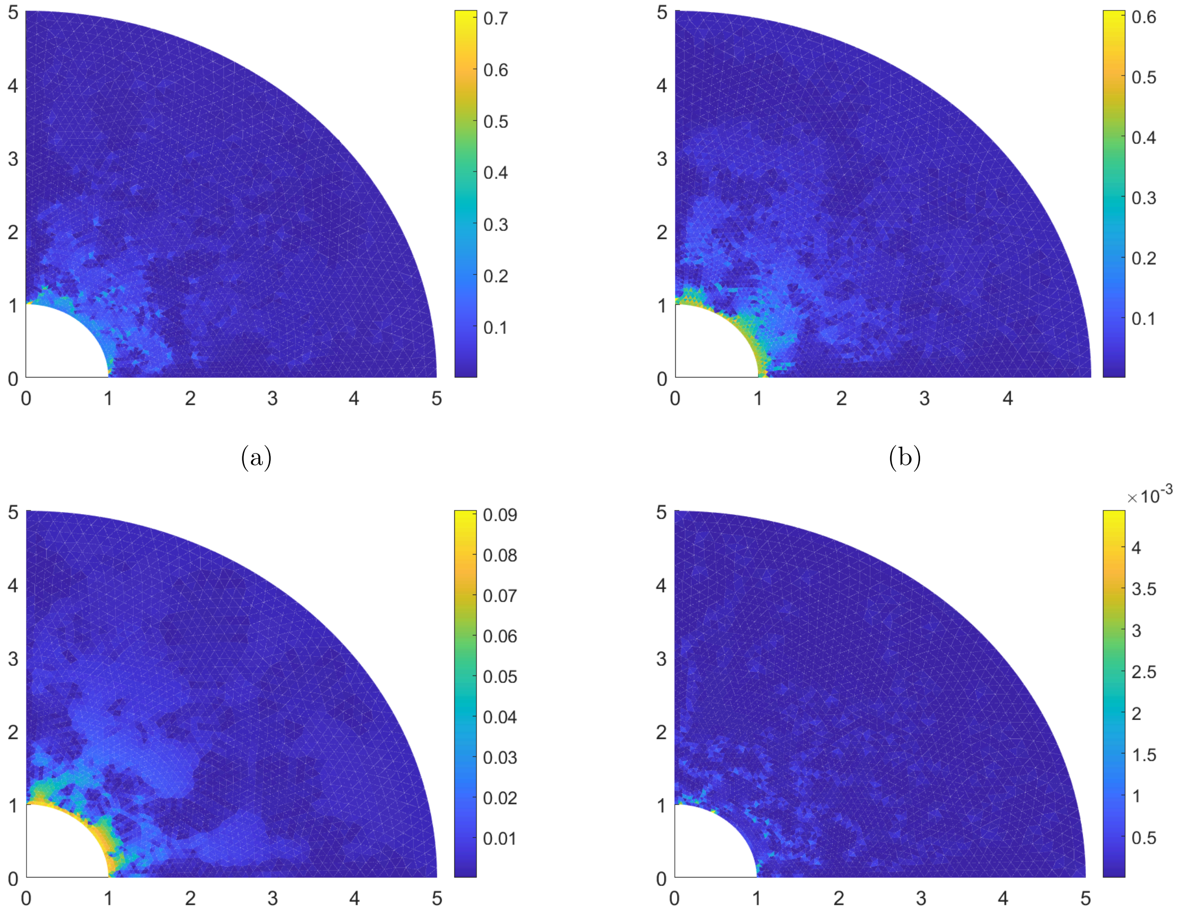

(a) (b)

(c) (d)

FIGURE 6.32. Contour plots of the relative error in the hydrostatic stress on unstructured meshes for the pressurized cylinder problem. The exact hydrostatic stress is 4166.528 psi. (a) CT FEM, (b) B-bar VEM, (c) SH-VEM, and (d) PSH-VEM.

value $\alpha = 10\ell_0^2$. *This value is three orders of magnitude less than* $\frac{10^4 \ell_0^2}{E_Y}$*; therefore, the errors of energy and hydrostatic stress are not expected to have higher order convergence rates even for uniform meshes. However, from our numerical tests, having a larger* E_Y *or increasing the upper bound on the penalty parameter* α *results in superconvergent solutions on sufficiently regular meshes.*

6.3.9. Punch problem. Next, we adapt the problem of a punch being driven into a solid as described in [114] for nearly incompressible hyperelastic materials. This problem is used in [114] to test the robustness of mixed virtual element methods for large deformations and to compare to standard mixed finite element formulations. In our tests, we assume a linearly elastic material and solve the problem on a unit square domain using $E_Y = 250$ psi and $\nu = 0.4999999$. The

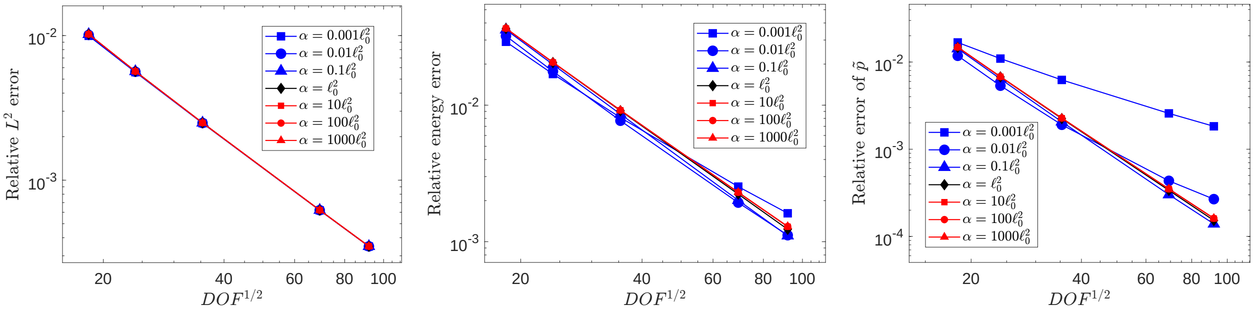

(a) (b) (c)

Figure 6.33. Comparison of the convergence of PSH-VEM for different choices of the penalty parameter α for the pressurized cylinder problem on structured meshes. (a) L^2 error of displacement, (b) energy error, and (c) L^2 error of hydrostatic stress.

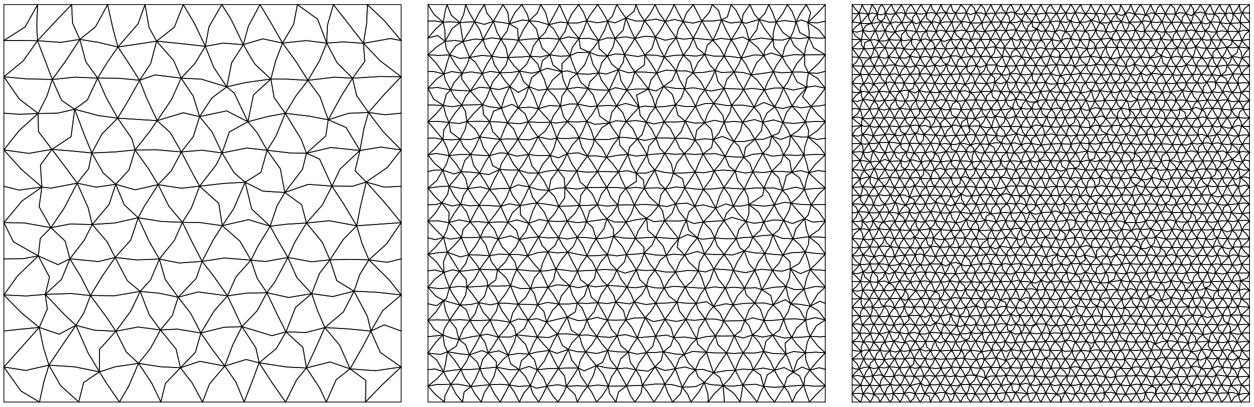

(a) (b) (c)

Figure 6.34. Perturbed triangular meshes for the manufactured problem. (a) 200 elements, (b) 1000 elements, and (c) 3600 elements.

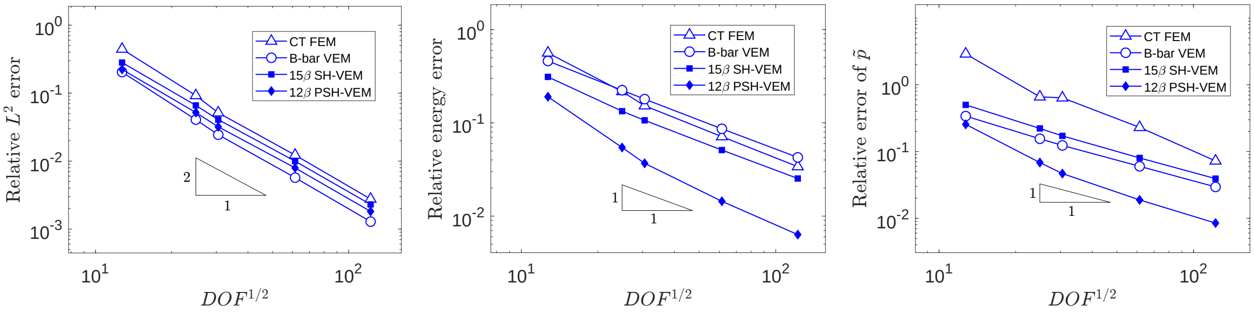

(a) (b) (c)

Figure 6.35. Comparison of CT FEM, B-bar VEM, SH-VEM, and PSH-VEM for the manufactured problem on perturbed meshes. (a) L^2 error of displacement, (b) energy error, and (c) L^2 error of hydrostatic stress.

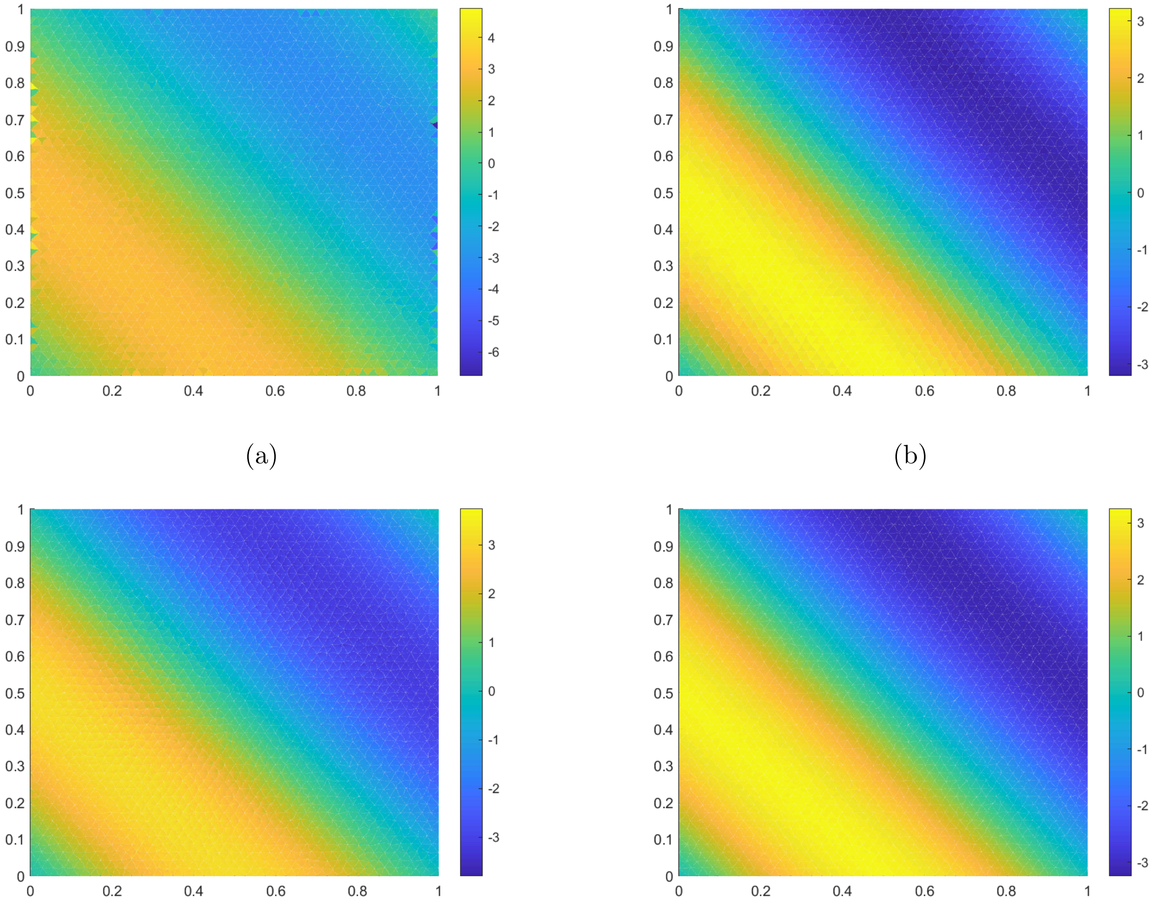

(a) (b)

(c) (d)

FIGURE 6.36. Contour plots of the hydrostatic stress on perturbed meshes for the manufactured problem. (a) CT FEM, (b) B-bar VEM, (c) SH-VEM, and (d) PSH-VEM.

left and top edges are horizontally constrained, while the bottom edge is vertically constrained. Along half of the top edge, a uniform load of $F = -250$ lbf per unit length is applied. For this problem, we examine the three methods B-bar VEM, SH-VEM, and PSH-VEM. We first use an unstructured triangular mesh (see Figure 6.40a) and plot the resulting contours of the hydrostatic stress in Figure 6.40. The contours are plotted on the deformed configuration. From the plots, we find that the three methods produced relatively smooth hydrostatic stress fields, with B-bar and PSH-VEM having a similar range. In Figure 6.41, plots of the trace of the strain field are shown on the undeformed configuration. The three methods yielded nearly traceless strain fields, which is consistent for a nearly incompressible material.

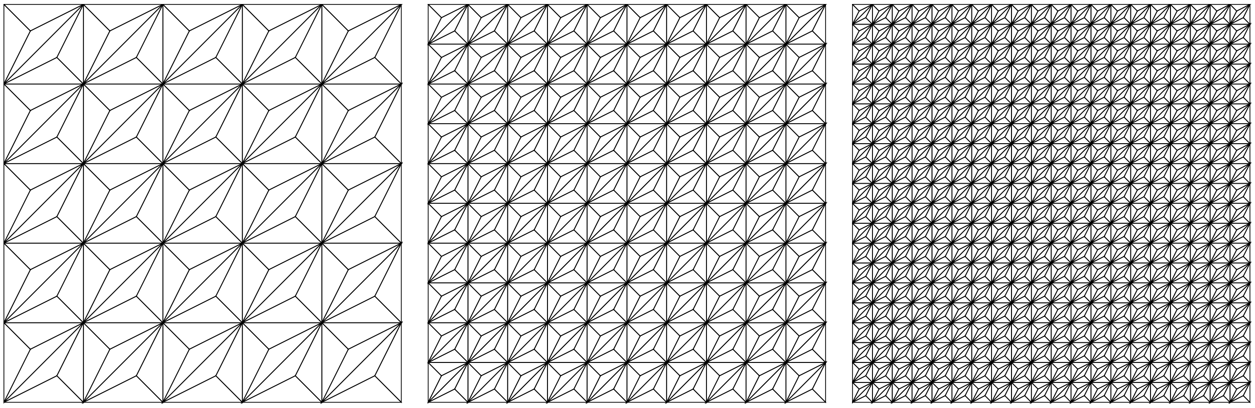
(a) (b) (c)

Figure 6.37. Structured triangular meshes for the manufactured problem. (a) 150 elements, (b) 600 elements, and (c) 2400 elements.

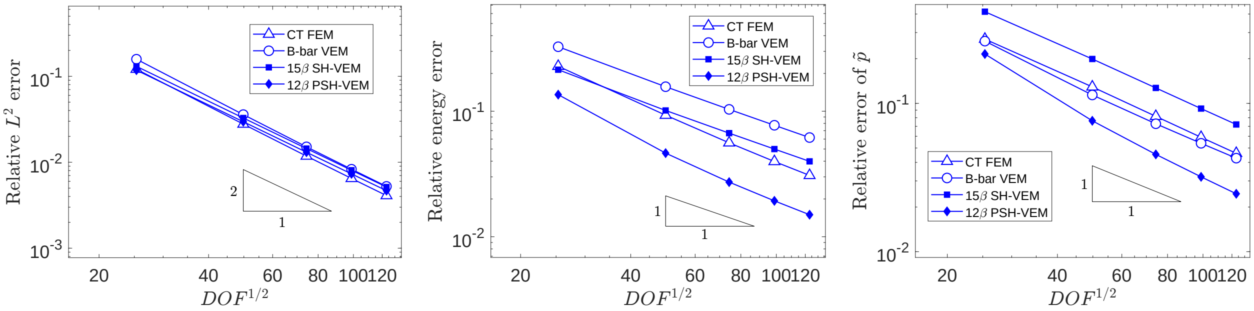

(a) (b) (c)

Figure 6.38. Comparison of CT FEM, B-bar VEM, SH-VEM, and PSH-VEM for the manufactured problem on structured meshes. (a) L^2 error of displacement, (b) energy error, and (c) L^2 error of hydrostatic stress.

Next, we use a mesh with convex and nonconvex elements with an example mesh shown in Figure 6.42a. The contour plots of the hydrostatic stress are given in Figure 6.42. The plots show that even for nonconvex elements, the three methods retain relatively smooth hydrostatic stress fields. In Figure 6.43, the contours of the trace of the strain field is presented. Similar to the unstructured case, the strain field of the three methods are nearly traceless.

6.3.10. Stabilized stress-hybrid methods. We also examined a stabilized formulation of 9β and 11β SH-VEM (both are rank deficient) using a 9-term and 11-term divergence-free basis, respectively. We found that the two stabilized stress-hybrid formulations did not show signs of

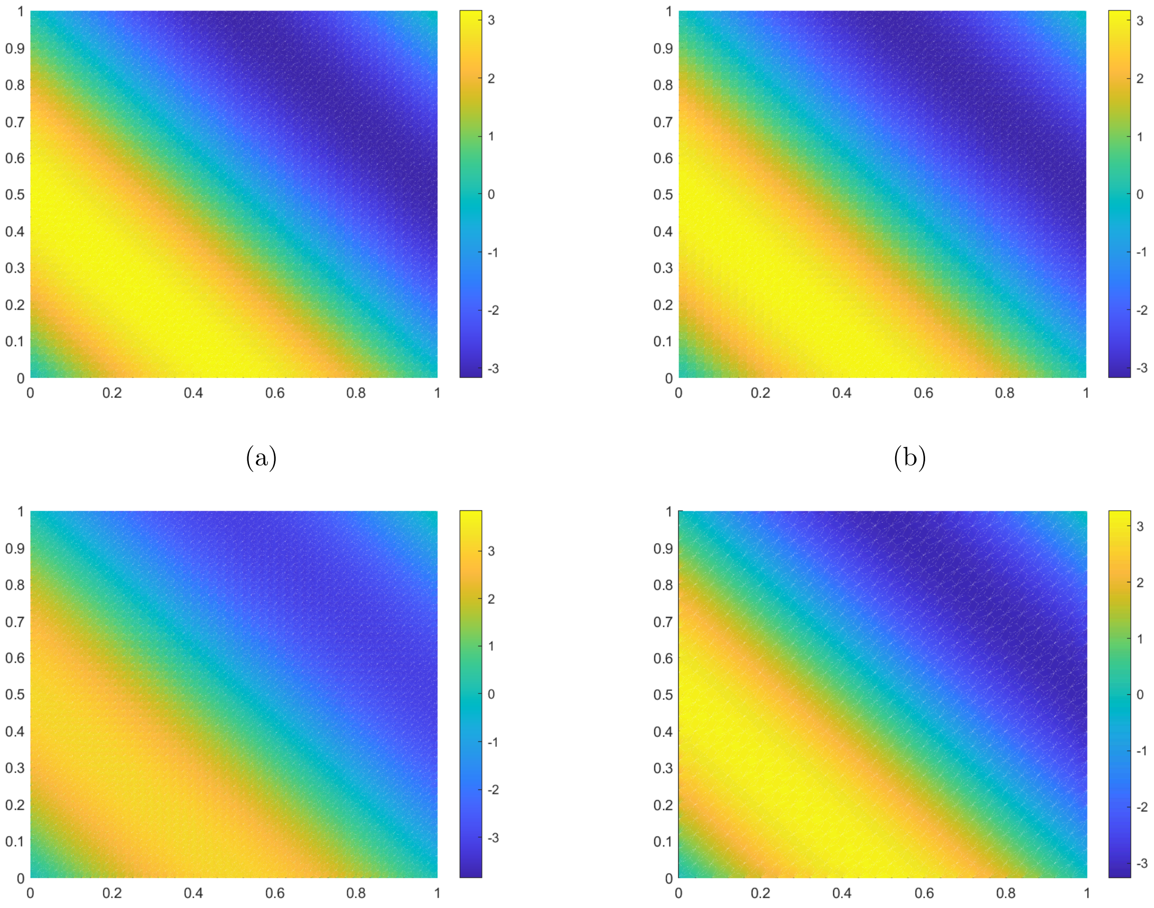

(a)

(b)

(c)

(d)

FIGURE 6.39. Contour plots of the hydrostatic stress on structured meshes for the manufactured problem. (a) CT FEM, (b) B-bar VEM, (c) SH-VEM, and (d) PSH-VEM.

volumetric locking, did not have spurious eigenvalues and attained higher accuracy than 15β SH-VEM. However, both stabilized methods were less accurate than the PSH method and they did not exhibit superconvergence in the hydrostatic stress. Further details can be found in Appendix B.

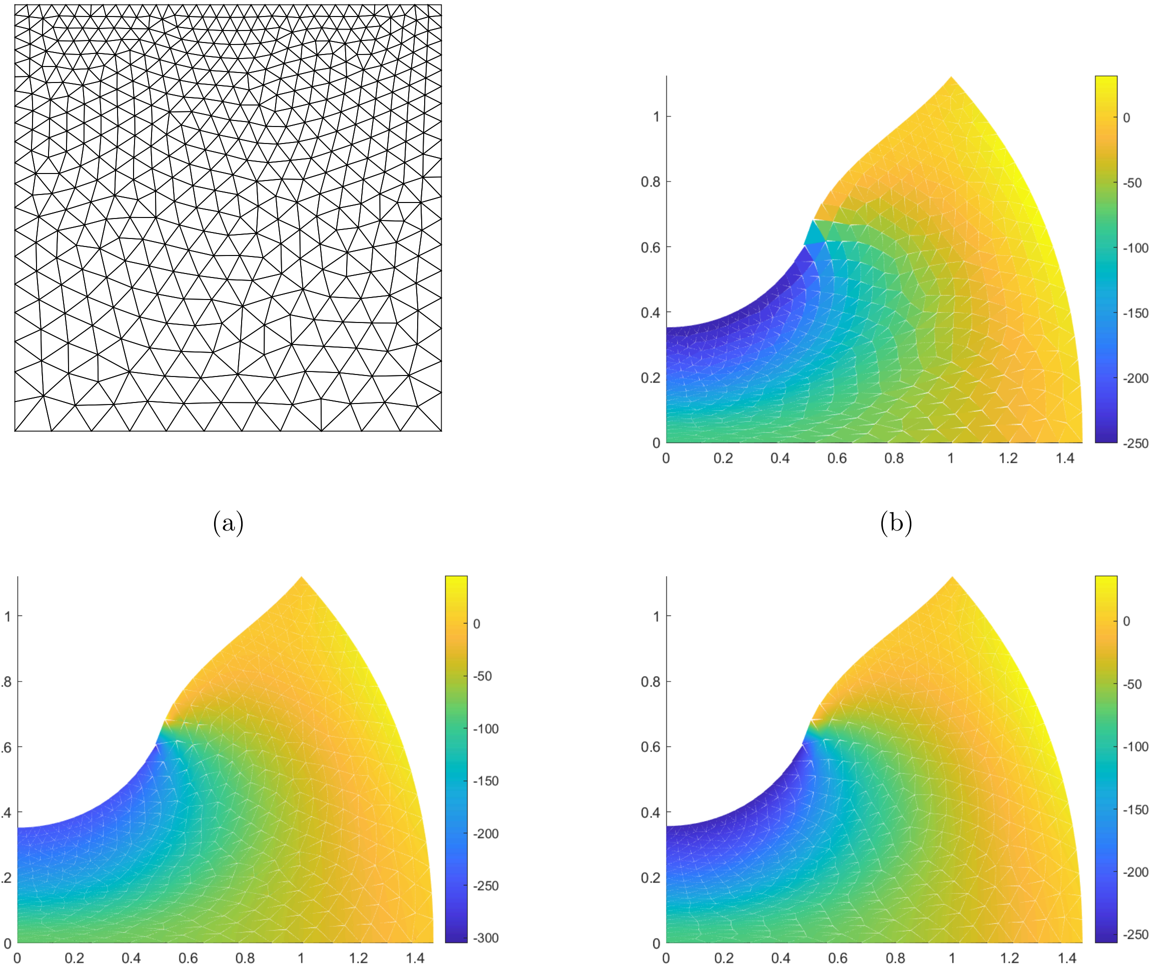

(a) (b)

(c) (d)

FIGURE 6.40. (a) Representative unstructured mesh for the punch problem. Contour plots of the hydrostatic stress for the punch problem plotted on the deformed configuration using unstructured meshes. (b) B-bar VEM, (c) SH-VEM, and (d) PSH-VEM.

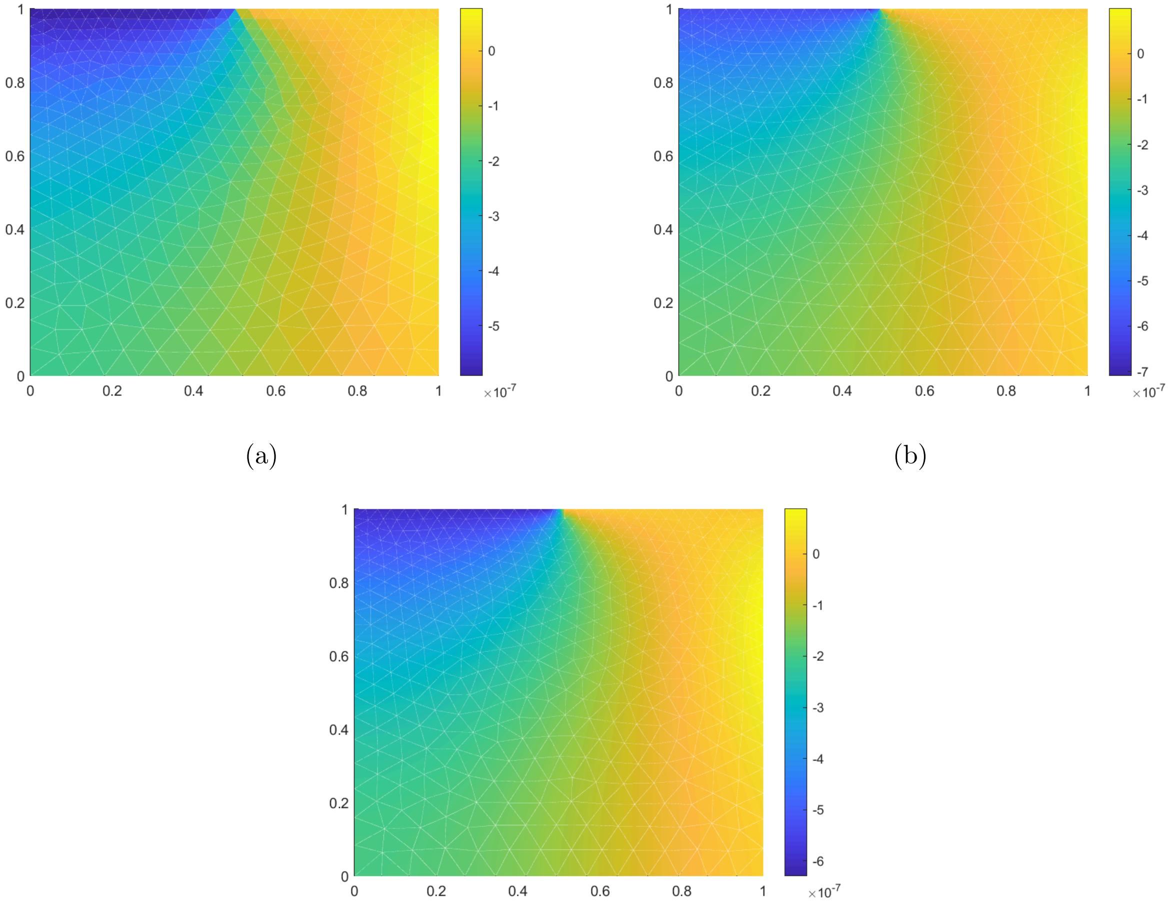

(a)

(b)

(c)

Figure 6.41. Contour plots of the trace of the strain field for the punch problem plotted on the undeformed configuration using structured meshes. (a) B-bar VEM, (b) SH-VEM, and (c) PSH-VEM.

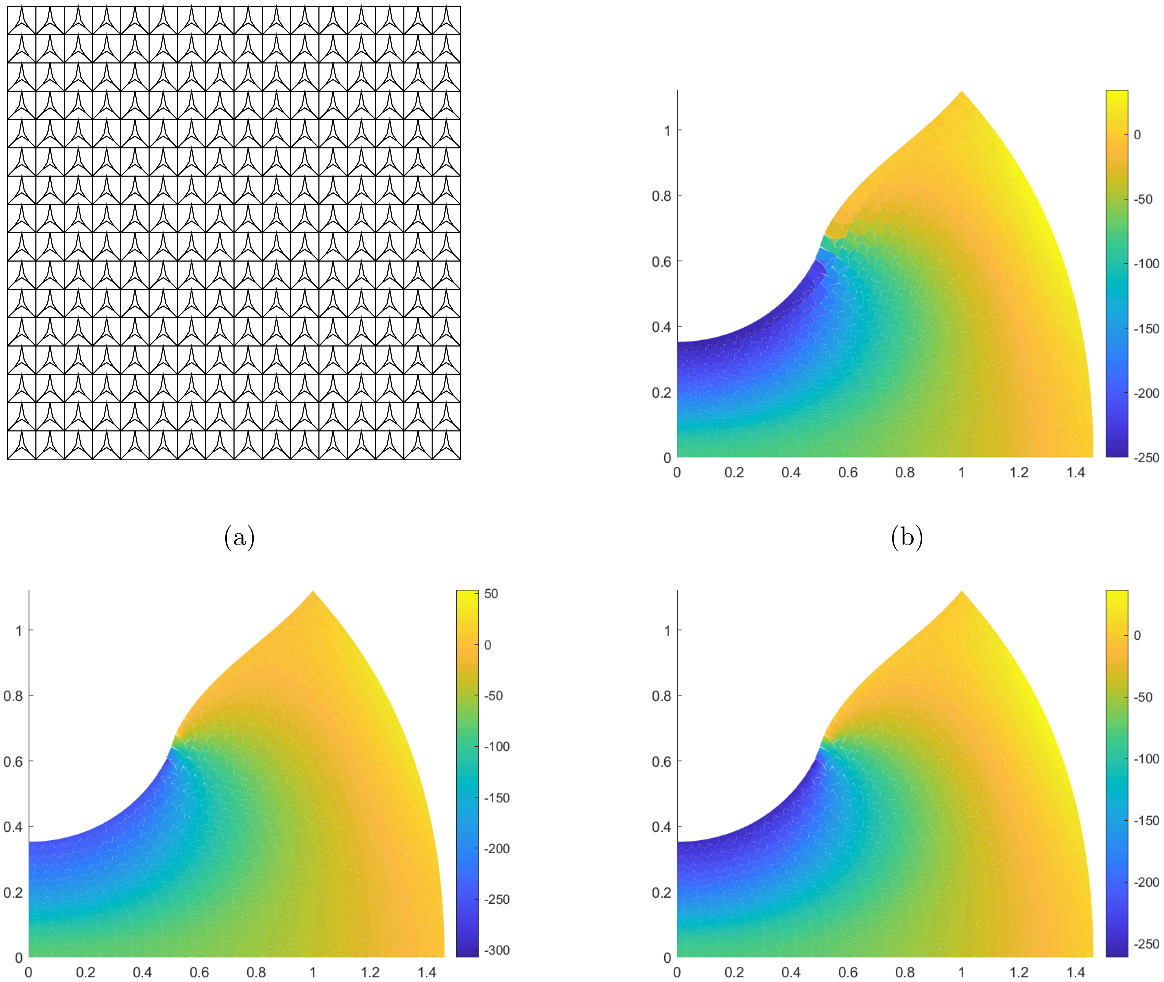

(a) (b)

(c) (d)

Figure 6.42. (a) Representative nonconvex mesh for the punch problem. Contour plots of the hydrostatic stress of PSH-VEM for the punch problem plotted on the deformed configuration using nonconvex meshes. (b) B-bar VEM, (c) SH-VEM, and (d) PSH-VEM.

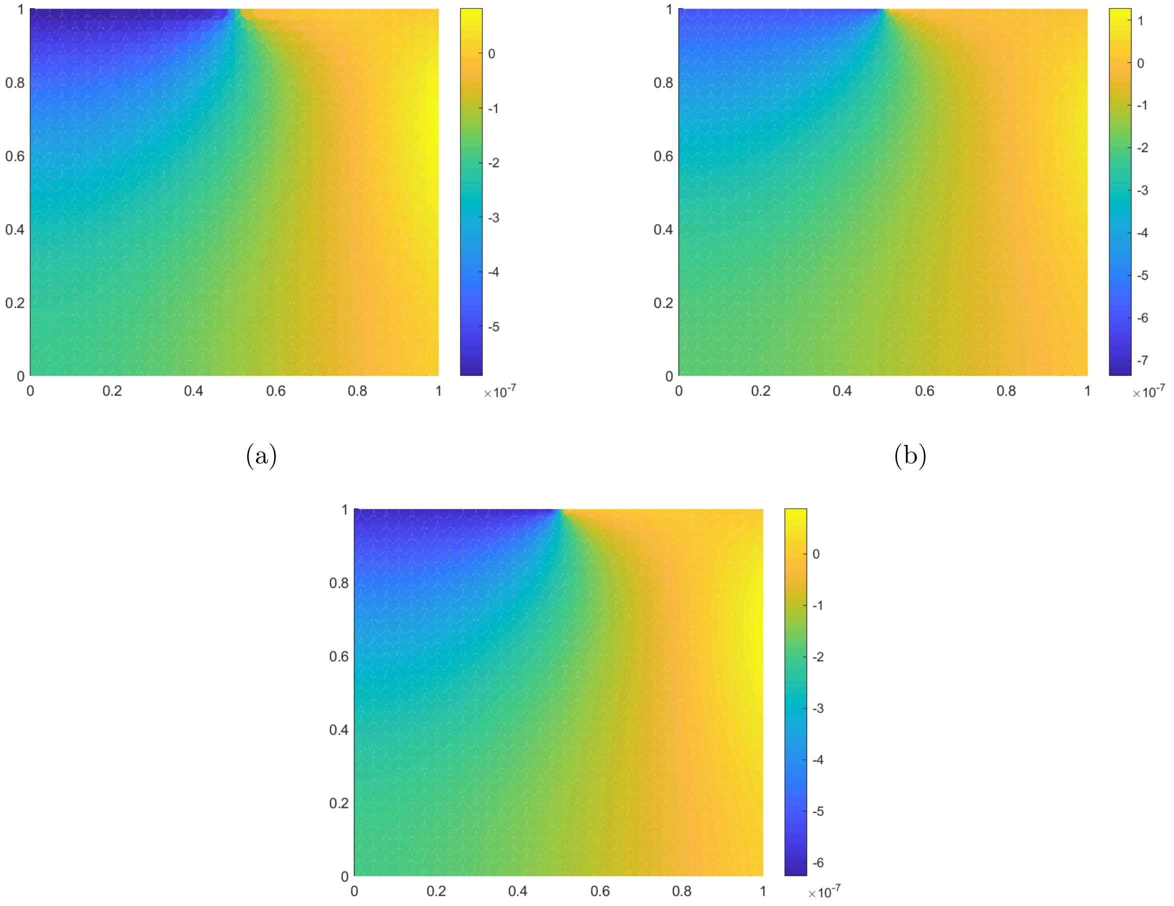

(a)

(b)

(c)

FIGURE 6.43. Contour plots of the trace of the strain field for the punch problem plotted on the undeformed configuration using nonconvex meshes. (a) B-bar VEM, (b) SH-VEM, and (c) PSH-VEM.

CHAPTER 7

Conclusions

In this thesis, we studied extensions of the Virtual Element Method (VEM) without a stabilization term to planar linear elasticity problems. In the standard VEM, a discrete space is constructed such that on an element, the space contains all polynomials up to degree k and also non-polynomial functions that satisfy a Poisson problem. On each element, function values along the boundary and internal integral moments are used as the degrees of freedom, which uniquely defines functions in the discrete space. The basis functions are chosen to satisfy a Lagrange property; however, these basis functions are not computed and are unknown (virtual). Since the basis functions do not need to be computed, it allows for the use of very general polygonal meshes when compared to the finite element method. Different projection operators are used to give polynomial approximations to the functions and their derivatives. Then the weak bilinear form of an elliptic problem is approximated by a polynomial term using the projection operator, which preserves consistency of solution (passes the patch test), and a stabilization term that preserves the coercivity. The stabilization term is not unique and depends on the underlying problem. However, for the Poisson problem, a simple choice of the dofi-dofi or a diagonal stabilization provides accurate results. It is shown that standard k-th order virtual element converges at the same theoretical rate as the corresponding finite element method.

We studied an extension of the stabilization-free virtual element method [19] to planar elasticity problems. To establish a stabilization-free method for solid continua, we constructed an enlarged virtual element space that included higher order polynomial approximations of the strain field. On each polygonal element we chose the degree ℓ of vector polynomials, and theoretically established that the discrete problem without a stabilization term was bounded and coercive. Error estimates of the displacement field in the L^2 norm and energy seminorm were derived. We set up the construction of the necessary projections and stiffness matrices, and then solved several problems from plane elasticity. For the patch test, we recovered the displacement and stress fields to near machine-precision. From an element-eigenvalue analysis, we numerically confirmed that the choice of ℓ was sufficient to ensure that the element stiffness matrix had no spurious zero-energy modes, and hence the element was stable. For problems such as cantilever beam under shear end load, infinite plate with a circular hole under uniaxial tension, and pressurized hollow cylinder under internal pressure, we found that the convergence rates of the stabilization-free VEM in the L^2 norm and energy seminorm were in agreement with the theoretical results.

For some problems, it is important to have higher accuracy to resolve nonlinear phenomena; therefore, we studied a higher order (serendipity) extension of the stabilization-free virtual element method [19, 37] for plane elasticity. To establish a high order stabilization-free method for solid continua, we constructed an enlarged virtual element space that included higher order polynomial approximations of the strain field. To eliminate additional degrees of freedom we incorporated the serendipity approach into the virtual element space [12]. On each polygonal element we chose the degree ℓ of vector polynomials such that the element stiffness is of correct rank. We set up the construction of the necessary projections and stiffness matrices, and then solved several problems from plane elasticity using a second- and third-order method. For the patch test, we recovered the displacement and stress fields to near machine-precision. From an element-eigenvalue analysis, we numerically examined a suitable choice of ℓ that was sufficient to ensure that the element stiffness matrix had no spurious zero-energy modes, and hence the element was stable. For a few manufactured problems and the cantilever beam problem under sinusoidal top load, we found that the convergence rates of the second- and third-order stabilization-free VEM in the L^2 norm and energy seminorm were in agreement with standard VEM theoretical results. However, consistent with expectations, we have verified that the serendipity virtual element method on affine edges has reduced convergence rates for domains with curved edges [16].

To treat nearly-incompressible materials in linear elasticity, we departed from the commonly used assumed-strain approaches in finite element methods that rely on the Hu–Washizu three-field variational principle [102, 103]. Instead, we revisited the assumed stress (or stress-hybrid) formulation that use the two-field Hellinger–Reissner variational principle [90]. In so doing, we proposed a stress-hybrid formulation [90] of the virtual element method on quadrilateral meshes for problems in plane linear elasticity. In this approach, the Hellinger–Reissner functional is used to define weak imposition of equilibrium equations and the strain-displacement relations to determine a suitable projection operator for the stress. On each quadrilateral element, we constructed a local coordinate system [43,44] and used a 5-term divergence-free symmetric tensor polynomial basis in the local coordinate system. The rotation matrix was then used to transform the stress ansatz to the global Cartesian coordinates so that element stiffness matrix computations could be conducted directly on the physical (distorted) element. On applying the divergence theorem on each element and using the divergence-free basis, we were able to compute the matrix representation of the stress projection solely from the displacements on the boundary. This resulted in a displacement-based method that was computable using the virtual element formulation. In Appendix A, we showed that the proposed approach was equivalent to a stress-hybrid virtual element formulation that follows the recipe of Cook [43] to transform the element stiffness matrix from local to global Cartesian coordinates. The SH-formulation was tested for stability, volumetric and shear locking, and convergence on several benchmark problems. From an element-eigenvalue analysis, we found that the proposed method was rotationally invariant and remained stable for a large class of convex and nonconvex elements without needing a stabilization term. For a manufactured test problem in the incompressible limit ($\nu \to 0.5$), we showed that the SH-VEM did not suffer from volumetric locking. From the bending of a thin beam and the bending in the Cook's membrane problem, we found that the method was not susceptible to shear locking. For a plate with a circular hole, the methods produced optimal convergence rates and smooth hydrostatic stress fields for both convex and nonconvex meshes. For the pressurized cylinder, optimal convergence rates in the L^2 norm and energy seminorm of the displacement field were realized, and both the B-bar VEM and the SH-VEM reproduced close to the exact hydrostatic stress on uniform meshes. However, it was observed that the hydrostatic stress field using the B-bar VEM and the SH-VEM on distorted *nonconvex meshes* produced larger errors, with the latter being more accurate. In the problem of a flat punch, the B-bar VEM and the SH-VEM produced relatively smooth hydrostatic stress fields that were comparable and the strain field was pointwise nearly traceless.

For complex geometries, it is difficult to automatically generate high-quality quadrilateral meshes. There are robust and well-established automatic meshers for triangular elements. However, triangular elements are known to suffer from shear locking for thin structures and also volumetric locking in the incompressible limit. We examine an extension of the stress-hybrid virtual element method [38] to first-order six-noded triangular virtual elements for linear elastic problems. This work is a first attempt to study two-dimensional virtual element formulations for incompressible elasticity on general triangular meshes (including Delaunay meshes). In this approach, we used the Hellinger–Reissner variational principle to construct a weak equilibrium and strain-displacement conditions. The weak strain-displacement condition is used along with the virtual element formulation to define a computable projection operator for the stress field. In the initial approach, we used a divergence-free polynomial tensor basis and by combining it with the divergence theorem, we were able to compute the stress projection with only the displacements along the boundary. When using a nondivergence-free basis, we relied on the modification of the virtual element space introduced in [20] and a secondary energy projection to recover the stress projection. However, we found that this requirement is rather restrictive and leads to elements being overly stiff. Therefore, we relaxed the condition by introducing a penalty term to weakly satisfy the element equilibrium condition and alleviate locking. The SH and PSH-formulations were then tested for stability using an eigenvalue analysis. For the divergence-free basis, a 15-term expansion was used to ensure no zero-energy modes appeared for highly distorted elements, while a complete bilinear 12-term expansion was used for the penalty element. For the thin cantilever beam and Cook's membrane problems we found both SH-VEM and PSH-VEM were not sensitive to shear locking. The PSH-VEM was able to reproduce nearly exact bending solutions even on coarse meshes. For the plate with a circular hole and pressurized cylinder the stress-hybrid method produced optimal convergence rates in the L^2 norm of the displacement, energy seminorm, and L^2 norm of the hydrostatic stress; while the penalty formulation produced superconvergent rates in energy seminorm and L^2 norm of the hydrostatic stress. The plate with a hole had relatively smooth hydrostatic stress fields, while for the pressurized cylinder it was observed that large errors concentrated around the interior boundary but the stress-hybrid methods were more accurate. In the manufactured problem, SH-VEM and PSH-VEM showed no signs of locking and had relatively smooth contours of hydrostatic stress. The PSH-VEM showed better accuracy for the manufactured problem; however, for our choice of penalty parameter, the PSH-VEM did not achieve superconvergent rates for the energy seminorm or L^2 norm of the hydrostatic stress. For the punch problem, both SH-VEM and PSH-VEM did not show instabilities in the hydrostatic stress field and produced nearly traceless strain fields. In Appendix B, we examined a stabilized version of the 9β SH-VEM and 11β SH-VEM. The 9β and 11β SH-VEM uses a 9-term and 11-term divergence-free basis, respectively. The stress-hybrid methods were then tested on additional benchmark problems. An eigenvalue analysis was used to test stability and volumetric locking of the two stress-hybrid methods. The thick cantilever beam problem showed that the stabilized methods with fewer basis functions were less stiff in bending. The plate with a hole problem showed that the stress-hybrid approaches converged optimally in all cases. The two stabilized methods attained better accuracy than 15β SH-VEM, with 9β SH-VEM having performance that is more comparable to the penalized approach. From these tests, we found that the two stabilized stress-hybrid formulations did not show signs of volumetric locking and did not have spurious eigenvalues.

In this work, we developed two different formulations of the stabilization-free virtual element method for solid continua. The first, strain-based, approach was shown to give comparable results to the standard VEM without needing to design a stabilization term. This approach has already been extended to three-dimensional problems and also to finite strain elasticity [119,120]; however, there are still questions about its computational efficiency and applicability to large-scale problems. The second approach, based on the hybrid-stress formulation, showed robust performance for thin beams and for nearly incompressible problems. The next step is to extend the stress-based approach to three dimensional elasticity. An ongoing effort is attempting to develop a ten-noded tetrahedral element that is stable, robust in the incompressible limit and is highly accurate for thin structures. A known problem with a stress-based approach is that it is more difficult to solve nonlinear problems since it involves inverting a nonlinear stress-strain law. However, by applying strategies developed in [1,65,66,67] it could be feasible to develop the SH-VEM for nonlinear problems. An alternative approach using the Hu–Washizu three field variational formulation [70,71], seems to strike a balance between the SF-VEM and SH-VEM. It uses a strain-based approach so it is easily applicable to nonlinear problems and shows promising performance for nearly incompressible problems. However, further investigations are needed to compare the differences in efficiency, accuracy and robustness of the stress and strain-based approaches.

APPENDIX A

A Stress-Hybrid Formulation Based on Cook's Approach

In this Appendix, we present an alternate formulation of the stress-hybrid virtual element method based on defining the element stiffness matrix on a rotated element as introduced by Cook [43]. Let E' be a rotated element, and following (5.17), define the corresponding matrices $\boldsymbol{H}'$ and $\boldsymbol{L}'$ by

$$\boldsymbol{H}' = \int_{E'} (\boldsymbol{P}')^T \boldsymbol{C}^{-1} \boldsymbol{P}' \, d\boldsymbol{x}', \quad \boldsymbol{L}' = \int_{\partial E'} (\boldsymbol{P}')^T \boldsymbol{N}^{\partial E'} \boldsymbol{\varphi}' \, ds', \tag{A.1a}$$

where $\boldsymbol{P}'$ is given in (5.11a) and $\boldsymbol{\varphi}'$ are the virtual element basis functions on E'. We then solve for the stress coefficients $\boldsymbol{\beta}'$ in terms of the rotated displacements using

$$\boldsymbol{\beta}' = (\boldsymbol{H}')^{-1} L' \boldsymbol{d}' := \boldsymbol{\Pi}'_\beta \boldsymbol{d}'. \tag{A.1b}$$

The element stiffness matrix on the rotated element E' is given as

$$\boldsymbol{K}'_{E'} = (\boldsymbol{\Pi}'_\beta)^T \left(\int_{E'} (\boldsymbol{P}')^T \boldsymbol{C}^{-1} \boldsymbol{P}' \, d\boldsymbol{x}' \right) \boldsymbol{\Pi}'_\beta = (\boldsymbol{\Pi}'_\beta)^T \boldsymbol{H}' \boldsymbol{\Pi}'_\beta, \tag{A.2}$$

and define the rotation matrix $\boldsymbol{R}$ as

$$\boldsymbol{R} = \begin{bmatrix} \boldsymbol{Q} & \mathbf{0} & \mathbf{0} & \mathbf{0} \\ \mathbf{0} & \boldsymbol{Q} & \mathbf{0} & \mathbf{0} \\ \mathbf{0} & \mathbf{0} & \boldsymbol{Q} & \mathbf{0} \\ \mathbf{0} & \mathbf{0} & \mathbf{0} & \boldsymbol{Q} \end{bmatrix}, \tag{A.3}$$

where $\boldsymbol{Q}$ is given in (5.10), and $\mathbf{0}$ is the 2×2 zero matrix. Then the element stiffness matrix in Cook's formulation on the original element E is recovered by:

$$\boldsymbol{K}_E^{\mathrm{C}} = \boldsymbol{R}^T \boldsymbol{K}'_{E'} \boldsymbol{R}. \tag{A.4}$$

Now, on applying (A.1b) and simplifying, we write the element stiffness matrix as

$$\boldsymbol{K}_E^{\mathrm{C}} = \boldsymbol{R}^T \big((\boldsymbol{H}')^{-1} \boldsymbol{L}' \big)^T \boldsymbol{H}' (\boldsymbol{H}')^{-1} \boldsymbol{L}' \boldsymbol{R} = (\boldsymbol{L}' \boldsymbol{R})^T (\boldsymbol{H}')^{-1} (\boldsymbol{L}' \boldsymbol{R}).$$

We now show that the SH-VEM using the basis $\boldsymbol{P}^*$ in (5.13) is identical to Cook's formulation, i.e., $\boldsymbol{K}_E^* = \boldsymbol{K}_E^C$.

Proof. On expanding the element stiffness matrix of the SH-VEM given in (5.20) and simplifying, we get

$$\boldsymbol{K}_E^* = \boldsymbol{\Pi}_\beta^T \boldsymbol{H}^* \boldsymbol{\Pi}_\beta = \big((\boldsymbol{H}^*)^{-1} \boldsymbol{L}^* \big)^T \boldsymbol{H}^* (\boldsymbol{H}^{-1} \boldsymbol{L}^*) = (\boldsymbol{L}^*)^T (\boldsymbol{H}^*)^{-1} \boldsymbol{L}^*.$$

We first examine the matrix $\boldsymbol{H}^*$. From (5.17a), we have

$$\boldsymbol{H}^* = \int_E (\boldsymbol{P}^*)^T \boldsymbol{C}^{-1} \boldsymbol{P}^* \, d\boldsymbol{x},$$

and after multiplying out the matrices and using an equivalent tensor representation, we write the components of $\boldsymbol{H}^*$ as

$$\boldsymbol{H}_{ij}^* = \int_E \boldsymbol{\mathcal{P}}_i^* : \mathbb{C}^{-1} : \boldsymbol{\mathcal{P}}_j^* \, d\boldsymbol{x},$$

where $\boldsymbol{\mathcal{P}}_{\boldsymbol{i}}^{\boldsymbol{*}}$ is the tensor representation of the i-th column of $\boldsymbol{P}^*$. Using (5.12), we rewrite this integral in terms of the rotated basis $\boldsymbol{\mathcal{P}}_i'$, that is

$$\boldsymbol{H}_{ij}^* = \int_{E'} \boldsymbol{Q}^T \boldsymbol{\mathcal{P}}_i' \boldsymbol{Q} : \mathbb{C}^{-1} : \boldsymbol{Q}^T \boldsymbol{\mathcal{P}}_j' \boldsymbol{Q} \, d\boldsymbol{x}'.$$

It can be shown that for an isotropic material modulli tensor $\mathbb{C}$, that

$$\boldsymbol{Q}^T \boldsymbol{\mathcal{P}}_i' \boldsymbol{Q} : \mathbb{C}^{-1} : \boldsymbol{Q}^T \boldsymbol{\mathcal{P}}_j' \boldsymbol{Q} = \boldsymbol{\mathcal{P}}_i' : \boldsymbol{Q}^T \boldsymbol{Q}^T \mathbb{C}^{-1} \boldsymbol{Q} \boldsymbol{Q} : \boldsymbol{\mathcal{P}}_j' = \boldsymbol{\mathcal{P}}_i' : \mathbb{C}^{-1} : \boldsymbol{\mathcal{P}}_j'.$$

Therefore, we now have for all $i, j = 1, 2, \ldots 5$:

$$\boldsymbol{H}_{ij}^* = \int_{E'} \boldsymbol{\mathcal{P}}_i' : \mathbb{C}^{-1} : \boldsymbol{\mathcal{P}}_j' \, d\boldsymbol{x}' = \boldsymbol{H}_{ij}'. \tag{A.6}$$

Next, we examine the matrix $\boldsymbol{L}^*$. From (5.17a), we have

$$\boldsymbol{L}^* = \int_{\partial E} (\boldsymbol{P}^*)^T \boldsymbol{N}^{\partial E} \boldsymbol{\varphi} \, ds,$$

After converting to an equivalent tensor representation, we write the components of $\boldsymbol{L}^*$ as:

$$\boldsymbol{L}^*_{ij} = \int_{\partial E} (\boldsymbol{\mathcal{P}}^*_{\boldsymbol{i}} \cdot \boldsymbol{n}) \cdot \boldsymbol{\varphi}_j \, ds.$$

Since $\boldsymbol{\varphi}_j$ and $\boldsymbol{\varphi}'_j$ are both piecewise affine functions on ∂E and $\partial E'$, respectively, it can be shown that the integration of $\boldsymbol{\varphi}_j$ along the boundary of an element E is equivalent to integrating $\boldsymbol{\varphi}'_j$ along the boundary of the rotated element E'. That is, for any vector field $\boldsymbol{f}$, we have

$$\int_{\partial E} \boldsymbol{f}(\boldsymbol{x}) \cdot \boldsymbol{\varphi}_j \, ds = \int_{\partial E'} \boldsymbol{f}(\boldsymbol{x}(\boldsymbol{x}')) \cdot \boldsymbol{\varphi}'_j \, ds'.$$

With this, we rewrite $\boldsymbol{L}^*_{ij}$ in the rotated coordinates as

$$\boldsymbol{L}^*_{ij} = \int_{\partial E} (\boldsymbol{\mathcal{P}}^*_{\boldsymbol{i}} \cdot \boldsymbol{n}) \cdot \boldsymbol{\varphi}_j \, ds = \int_{\partial E'} (\boldsymbol{Q}^T \boldsymbol{\mathcal{P}}'_i \boldsymbol{Q} \cdot \boldsymbol{Q}^T \boldsymbol{n}') \cdot \boldsymbol{\varphi}'_j \, ds' = \int_{\partial E'} (\boldsymbol{Q}^T \boldsymbol{\mathcal{P}}'_i \cdot \boldsymbol{n}') \cdot \boldsymbol{\varphi}'_j \, ds'.$$

If we take the basis functions in the standard order $\boldsymbol{\varphi}'_{2j-1} = (\phi'_j, 0)^T$ and $\boldsymbol{\varphi}'_{2j} = (0, \phi'_j)^T$, then we can simplify $\boldsymbol{L}^*_{ij}$ as:

$$\begin{aligned} \boldsymbol{L}^*_{i2j-1} &= c \int_{\partial E'} ((\boldsymbol{\mathcal{P}}'_i)_{11} \boldsymbol{n}'_1 + (\boldsymbol{\mathcal{P}}'_i)_{12} \boldsymbol{n}'_2) \phi'_j \, ds' - s \int_{\partial E'} ((\boldsymbol{\mathcal{P}}'_i)_{12} \boldsymbol{n}'_1 + (\boldsymbol{\mathcal{P}}'_i)_{22} \boldsymbol{n}'_2) \phi'_j \, ds' = c \boldsymbol{L}'_{i2j-1} - s \boldsymbol{L}'_{i2j} \\ \boldsymbol{L}^*_{i2j} &= s \int_{\partial E'} ((\boldsymbol{\mathcal{P}}'_i)_{11} \boldsymbol{n}'_1 + (\boldsymbol{\mathcal{P}}'_i)_{12} \boldsymbol{n}'_2) \phi'_j \, ds' + c \int_{\partial E'} ((\boldsymbol{\mathcal{P}}'_i)_{12} \boldsymbol{n}'_1 + (\boldsymbol{\mathcal{P}}'_i)_{22} \boldsymbol{n}'_2) \phi'_j \, ds' = s \boldsymbol{L}'_{i2j-1} + c \boldsymbol{L}'_{i2j}, \end{aligned}$$

where c and s given in (5.10). On multiplying out the matrix $\boldsymbol{L}'\boldsymbol{R}$, it can be shown that

$$\begin{aligned} (\boldsymbol{L}'\boldsymbol{R})_{i2j-1} &= c \boldsymbol{L}'_{i2j-1} - s \boldsymbol{L}'_{i2j} \\ (\boldsymbol{L}'\boldsymbol{R})_{i2j} &= s \boldsymbol{L}'_{i2j-1} + c \boldsymbol{L}'_{i2j}, \end{aligned}$$

and therefore for all $i = 1, 2, \dots 5$ and $j = 1, 2, \dots 4$, we have

$$\boldsymbol{L}^*_{i2j-1} = c \boldsymbol{L}'_{i2j-1} - s \boldsymbol{L}'_{i2j} = (\boldsymbol{L}'\boldsymbol{R})_{i2j-1} \tag{A.7a}$$

$$\boldsymbol{L}^*_{i2j} = s \boldsymbol{L}'_{i2j-1} + c \boldsymbol{L}'_{i2j} = (\boldsymbol{L}'\boldsymbol{R})_{i2j}. \tag{A.7b}$$

From (A.6) and (A.7), we obtain $\boldsymbol{H}^* = \boldsymbol{H}'$ and $\boldsymbol{L}^* = \boldsymbol{L}'\boldsymbol{R}$. On substituting these in (A.5) and using (A.4) leads us to the desired result:

$$\boldsymbol{K}^*_E = (\boldsymbol{L}^*)^T (\boldsymbol{H}^*)^{-1} \boldsymbol{L}^* = (\boldsymbol{L}'\boldsymbol{R})^T (\boldsymbol{H}')^{-1} (\boldsymbol{L}'\boldsymbol{R}) = \boldsymbol{K}^{\mathrm{C}}_E. \qquad \square$$

APPENDIX B

Stabilized Stress-Hybrid Methods

In the standard virtual element method, a stabilization term is necessary to ensure that the element stiffness matrix has correct rank. For completeness, we examine effects of a stabilization term on the two methods 9β SH-VEM and 11β SH-VEM, which were shown earlier to have zero-energy modes. The 9β SH-VEM is constructed from the first 9 terms of the basis given in (6.5), while the 11β SH-VEM uses the first 11 terms. For the stability term, we follow the construction given in [6]:

$$\boldsymbol{K}_S = \tau \left[\boldsymbol{I} - \boldsymbol{D}(\boldsymbol{D}^{\boldsymbol{T}}\boldsymbol{D})^{-1}\boldsymbol{D}^T \right], \tag{B.1a}$$

where τ is a scaling factor, $\boldsymbol{I}$ is the identity matrix and $\boldsymbol{D} \in \mathbb{R}^{12\times 6}$ is the matrix containing the degrees of freedom of the polynomials $\boldsymbol{m}_\alpha \in \widehat{\boldsymbol{M}}(E)$ given by

$$\boldsymbol{D} = \begin{bmatrix} \boldsymbol{m}_1(\boldsymbol{x}_1) & \boldsymbol{m}_2(\boldsymbol{x}_1) & \dots & \boldsymbol{m}_6(\boldsymbol{x}_1) \\ \boldsymbol{m}_1(\boldsymbol{x}_2) & \boldsymbol{m}_2(\boldsymbol{x}_2) & \dots & \boldsymbol{m}_6(\boldsymbol{x}_2) \\ \dots & \dots & \dots & \dots \\ \boldsymbol{m}_1(\boldsymbol{x}_6) & \boldsymbol{m}_2(\boldsymbol{x}_6) & \dots & \boldsymbol{m}_6(\boldsymbol{x}_6) \end{bmatrix}. \tag{B.1b}$$

It is common to choose the scaling factor to be proportional to the trace of the element stiffness matrix $\boldsymbol{K}_E$; however, this choice of scaling will lead to an overly stiff solution for nearly incompressible materials [85, 95]. For simplicity, we set $\tau = \frac{1}{2}$ in the following examples. The stabilized element stiffness matrix is then given by

$$\boldsymbol{K} = \boldsymbol{K}_E + \boldsymbol{K}_S. \tag{B.2}$$

B.0.1. Eigenvalue analysis. We first repeat the eigenvalue analysis presented in Section 6.3.1. Contour plots for the fourth smallest eigenvalue are presented in Figure B.1. The plots reveal that the stabilization term has eliminated the spurious eigenvalue for both 9β SH-VEM and 11β SH-VEM.

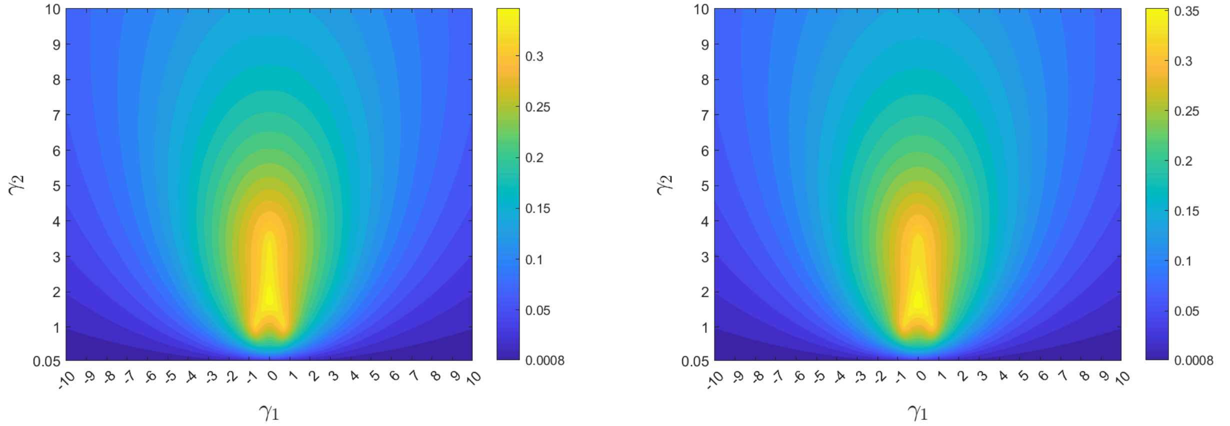

(a) (b)

FIGURE B.1. Contour plots of the fourth smallest eigenvalue of (a) stabilized 9β SH-VEM and (b) stabilized 11β SH-VEM.

Next, we repeat the eigenvalue analysis in Section 6.3.3 to test for locking in the near-incompressible limit. The five largest eigenvalues of the element stiffness matrix for 9β and 11β SH-VEM are given in Table B.1 for a regular six-noded triangular element and in Table B.2 for a nonconvex element. The tables show that both methods only have a single eigenvalue that tends toward infinity. This suggests that the two stabilized elements are not prone to volumetric locking.

Eigenvalue	9β SH-VEM	11β SH-VEM
1	7.8×10^{-1}	9.0×10^{-1}
2	1.2×10^{0}	1.3×10^{0}
3	1.3×10^{0}	1.5×10^{0}
4	4.6×10^{0}	4.6×10^{0}
5	4.2×10^{6}	4.2×10^{6}

TABLE B.1. Comparison of the five largest eigenvalues of the element stiffness matrix on a six-noded triangular element.

Eigenvalue	9β SH-VEM	11β SH-VEM
1	5.9×10^{-1}	7.9×10^{-1}
2	1.8×10^{0}	1.8×10^{0}
3	2.1×10^{0}	4.9×10^{0}
4	9.9×10^{0}	9.9×10^{0}
5	6.7×10^{6}	6.7×10^{6}

TABLE B.2. Comparison of the five largest eigenvalues of the element stiffness matrix on a six-noded nonconvex element.

B.0.2. Bending of a thick cantilever. We consider the bending of a cantilever beam under plane stress conditions with a shear end load as shown in [55, 56] for different triangular elements.

The material has a Young's modulus $E_Y = 30000$ psi and Poisson's ratio $\nu = 0.25$. The beam has a length of $L = 48$ inch, a height of $D = 12$ inch, and unit thickness. A shear load of $P = 40$ lbf is applied on the right boundary, while the left boundary is fixed. For this problem, we compare the tip displacement of the stress-hybrid methods: 15β SH-VEM, 12β PSH-VEM, 9β SH-VEM, 11β SH-VEM, and the 5β SH-VEM for quadrilaterals given in [38]. The mesh for the 5β SH-VEM consists of $N \times N$ ($N = 1, 2, 4, 8, 16$) structured quadrilateral elements with an aspect ratio of $4:1$, while the corresponding triangular mesh is constructed by splitting each quadrilateral element along a diagonal (see Figure B.2). In Table B.3, the normalized tip displacement for the different methods on each mesh is shown. The table shows that all the SH-VEM and PSH-VEM methods converge with mesh refinement, but the 15β SH-VEM, which uses higher order terms, is slightly stiffer. The other three methods on six-noded triangles have comparable performance to the 5β SH-VEM on quadrilaterals.

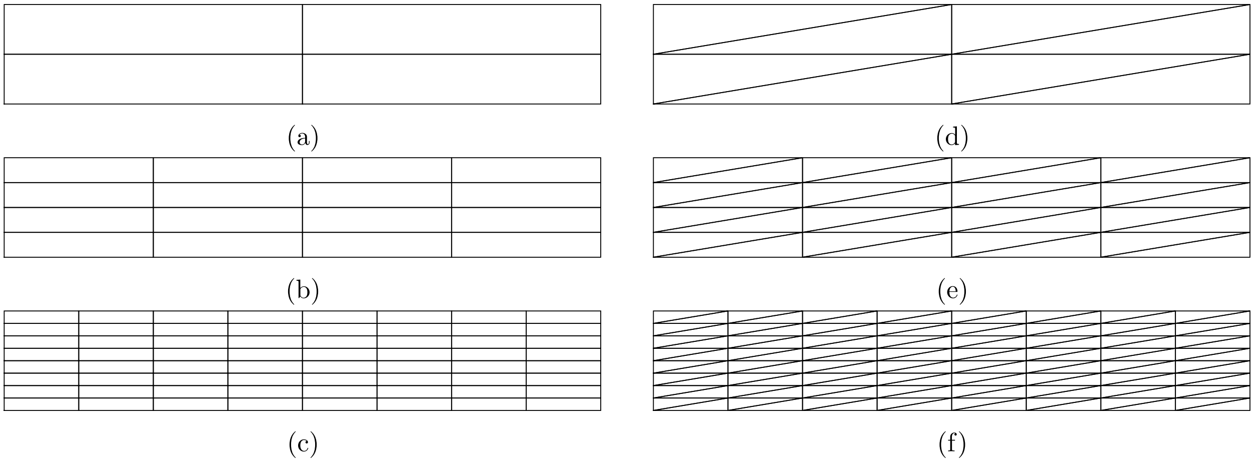

Figure B.2. Structured meshes for the thick cantilever beam problem. Meshes in (a)-(c) consists of quadrilaterals with an aspect ratio of $4:1$ and (d)-(f) consist of triangular meshes where each corresponding quadrilateral element is cut along the diagonal.

B.0.3. Plate with a circular hole. Finally, we revisit the plate with a circular hole problem that is presented in Section 5.4.5. For this problem, we compare the convergence of the stress-hybrid methods: 15β SH-VEM, 12β PSH-VEM, 9β SH-VEM, 11β SH-VEM, and the 5β SH-VEM, in the error norms given in (5.27). We first test this problem on structured quadrilateral and triangular meshes with the same number of global degrees of freedom; a few sample meshes are shown in Figure B.3. In Figure B.4, the convergence results are given for the stress-hybrid methods

	5β SH-VEM	15β SH-VEM	12β PSH-VEM	9β SH-VEM	11β SH-VEM
1×1	0.7637	0.4536	1.6185	0.4798	0.4778
2×2	0.9413	0.8236	1.0665	0.8668	0.8612
4×4	0.9856	0.9610	1.0133	0.9787	0.9770
8×8	0.9965	0.9917	1.0030	0.9971	0.9966
16×16	0.9992	0.9982	1.0007	0.9997	0.9996

TABLE B.3. Comparison of the normalized tip displacements for the cantilever beam problem on structured meshes. The meshes are constructed from $N \times N$ $(N = 1, 2, 4, 8, 16)$ quadrilaterals with aspect ratio of $4 : 1$.

and show that all the methods converge optimally in the displacement L^2 norm, energy seminorm and L^2 norm of the hydrostatic stress (the penalty approach attains superconvergence in energy and hydrostatic stress). The 5β SH-VEM has the smallest error in displacement, but the triangular SH-VEM have better accuracy in energy and hydrostatic stress, with the 12β PSH-VEM and 9β SH-VEM having the smallest errors.

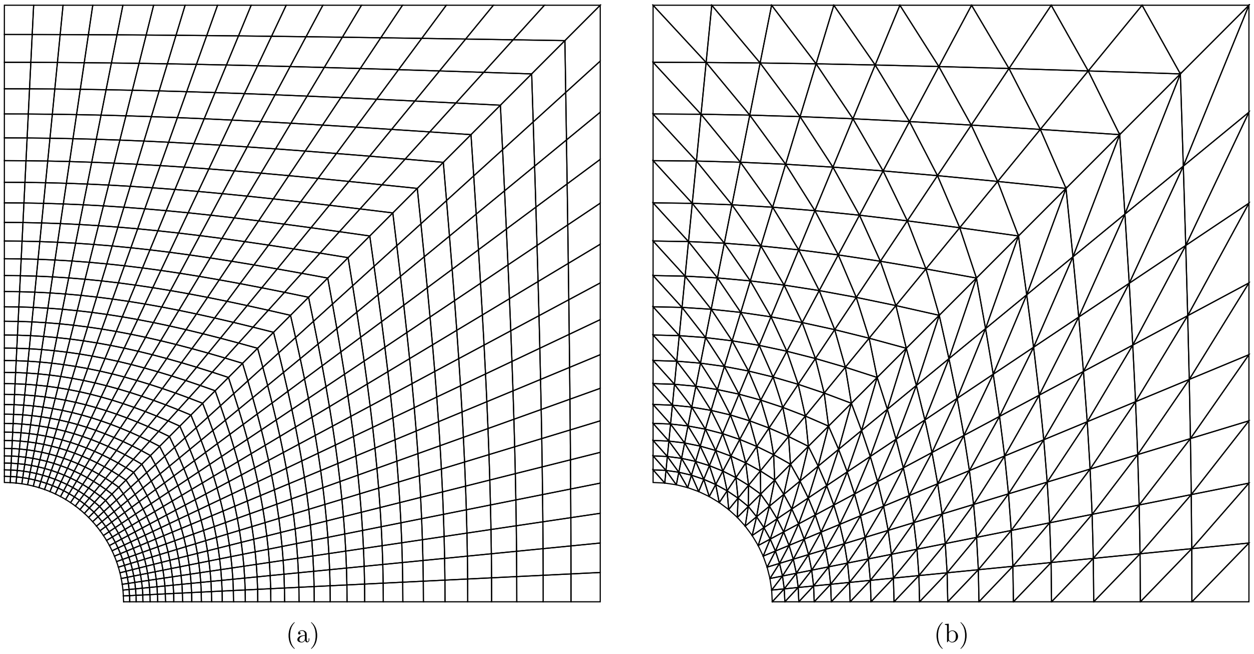
(a) (b)

FIGURE B.3. (a) A structured quadrilateral mesh and (b) a structured triangular mesh with the same number of degrees of freedom for the plate with a hole problem.

We now test the plate with a circular hole problem on unstructured meshes. The quadrilateral meshes for 5β SH-VEM are constructed by taking unstructured triangular meshes and splitting each triangle into three elements. Representative meshes with similar global degrees of freedom are shown in Figure B.5. In Figure B.6, we present the convergence rates of the five stress-hybrid

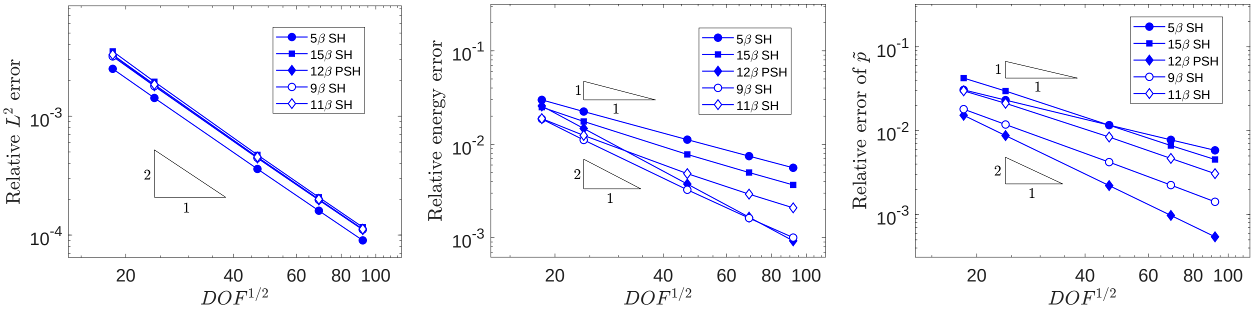

(a) (b) (c)

FIGURE B.4. Comparison of 5β SH-VEM, 15β SH-VEM, 12β PSH-VEM, 9β SH-VEM, and 11β SH-VEM for the plate with a hole problem on structured meshes (see Figure B.3). (a) L^2 error of displacement, (b) energy error, and (c) L^2 error of hydrostatic stress.

methods. Like the case of structured meshes, all five methods deliver optimal convergence rates on unstructured meshes, with 12β PSH-VEM followed by 9β SH-VEM delivering the lowest errors in the energy seminorm and L^2 norm of hydrostatic stress.

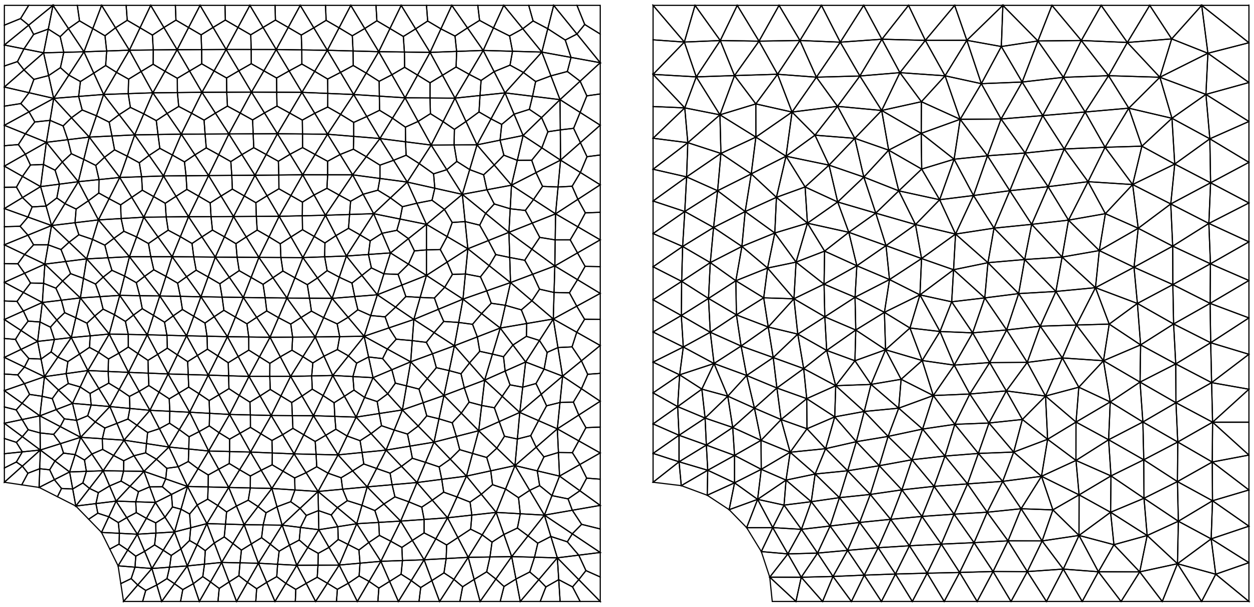

(a) (b)

FIGURE B.5. (a) An unstructured quadrilateral mesh and (b) an unstructured triangular mesh with a similar number of degrees of freedom for the plate with a hole problem.

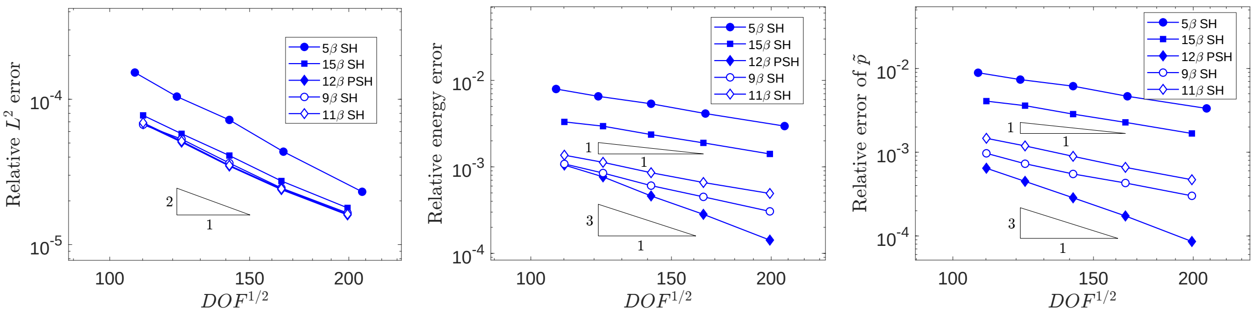

(a) (b) (c)

Figure B.6. Comparison of 5β SH-VEM, 15β SH-VEM, 12β PSH-VEM, 9β SH-VEM, and 11β SH-VEM for the plate with a hole problem on unstructured meshes (see Figure B.5). (a) L^2 error of displacement, (b) energy error, and (c) L^2 error of hydrostatic stress.

Bibliography

[1] M. Agrawal, A. Nandy, and C. S. Jog, *A hybrid finite element formulation for large-deformation contact mechanics*, Comput Methods Appl Mech Eng, 356 (2019), pp. 407–434.

[2] B. Ahmad, A. Alsaedi, F. Brezzi, L. D. Marini, and A. Russo, *Equivalent projectors for virtual element methods*, Comput Math Applications, 66 (2013), pp. 376–391.

[3] M. Ainsworth and C. Parker, *Unlocking the secrets of locking: Finite element analysis in planar linear elasticity*, Comput Methods Appl Mech Eng, 395 (2022), p. 115034.

[4] D. Arnold and G. Awanou, *The serendipity family of finite elements*, Foundations Comput Math, 11 (2011), pp. 337–344.

[5] E. Artioli, L. Beirão da Veiga, and F. Dassi, *Curvilinear virtual elements for 2D solid mechanics applications*, Comput Methods Appl Mech Eng, 359 (2020), p. 112667.

[6] E. Artioli, L. Beirão da Veiga, C. Lovadina, and E. Sacco, *Arbitrary order 2d virtual elements for polygonal meshes: part I, elastic problem*, Comput Mech, 60 (2017), pp. 355–377.

[7] E. Artioli, S. de Miranda, C. Lovadina, and L. Patruno, *A family of virtual element methods for plane elasticity problems based on the Hellinger–Reissner principle*, Comput Methods Appl Mech Eng, 340 (2018), pp. 978–999.

[8] E. Artioli, S. de Miranda, C. Lovadina, and L. Patruno, *A dual hybrid virtual element method for plane elasticity problems*, ESAIM: M2AN, 54 (2020), pp. 1725–1750.

[9] L. Beirão da Veiga, F. Brezzi, A. Cangiani, G. Manzini, L. D. Marini, and A. Russo, *Basic principles of virtual element methods*, Math Models Methods Appl Sci, 23 (2013), pp. 119–214.

[10] L. Beirão da Veiga, F. Brezzi, F. Dassi, L. Marini, and A. Russo, *Serendipity virtual elements for general elliptic equations in three dimensions*, Chinese Annals of Mathematics, Series B, 39 (2018), pp. 315–334.

[11] L. Beirão da Veiga, F. Brezzi, and D. Marini, *Virtual elements for linear elasticity problems*, SIAM J Numer Anal, 51 (2013), pp. 794–812.

[12] L. Beirão da Veiga, F. Brezzi, L. Marini, and A. Russo, *Serendipity nodal vem spaces*, Comput Fluids, 141 (2016), pp. 2–12.

[13] L. Beirão da Veiga, F. Brezzi, L. D. Marini, and A. Russo, *The hitchhiker's guide to the virtual element method*, Math Models Methods Appl Sci, 24 (2014), pp. 1541–1573.

[14] L. Beirão da Veiga, F. Brezzi, L. D. Marini, and A. Russo, *Virtual Element Method for general second-order elliptic problems on polygonal meshes*, Math Models Methods Appl Sci, 26 (2016), pp. 729–750.

[15] L. Beirão da Veiga, C. Lovadina, and A. Russo, *Stability analysis for the virtual element method*, Math Models Methods Appl Sci, 27 (2017), pp. 2557–2594.

[16] L. Beirão da Veiga, A. Russo, and G. Vacca, *The virtual element method with curved edges*, ESAIM: M2AN, 53 (2019), pp. 375–404.

[17] T. Belytschko and W. E. Bachrach, *Efficient implementation of quadrilaterals with high coarse-mesh accuracy*, Comput Methods Appl Mech Eng, 54 (1986), pp. 279–301.

[18] T. Belytschko and L. Bindeman, *Assumed strain stabilization of the 4-node quadrilateral with 1-point quadrature for nonlinear problems*, Comput Methods Appl Mech Eng, 88 (1991), pp. 311–340.

[19] S. Berrone, A. Borio, and F. Marcon, *Lowest order stabilization free virtual element method for the Poisson equation*. arXiv preprint: 2103.16896, 2021.

[20] ———, *Lowest order stabilization free virtual element method for the 2d Poisson equation*. arXiv preprint: 2103.16896, 2023.

[21] ———, *A stabilization-free virtual element method based on divergence-free projections*, Comput Methods Appl Mech Eng, 424 (2024), p. 116885.

[22] T. Blacker and T. Belytschko, *Superconvergent patch recovery with equilibrium and conjoint interpolant enhancements*, Int J Numer Methods Eng, 37 (1994), pp. 517–536.

[23] E. F. I. Boerner and P. Wriggers, *A macro-element for incompressible finite deformations based on a volume averaged deformation gradient*, Comput Mech, 42 (2008), pp. 407–416.

[24] C. Böhm, J. Korelc, B. Hudobivnik, A. Kraus, and P. Wriggers, *Mixed virtual element formulations for incompressible and inextensible problems*, Comput Mech, (2023).

[25] A. Borio, C. Lovadina, F. Marcon, and M. Visinoni, *A lowest order stabilization-free mixed virtual element method*, Comput Math Applications, 160 (2024), pp. 161–170.

[26] S. C. Brenner, Q. Guan, and L.-Y. Sung, *Some estimates for virtual element methods*, Comput Methods Appl Math, 17 (2017), pp. 553–574.

[27] S. C. Brenner and L. R. Scott, *The Mathematical Theory of Finite Element Methods*, Texts in Applied Mathematics, Springer, New York, third ed., 2008.

[28] F. Brezzi and M. Fortin, *Mixed and Hybrid Finite Element Methods*, Springer Series in Computational Mathematics, Springer, New York, first ed., 1991.

[29] G. Camacho and M. Ortiz, *Computational modelling of impact damage in brittle materials*, Int J Solids Struct, 33 (1996), pp. 2899–2938.

[30] A. Cangiani, G. Manzini, A. Russo, and N. Sukumar, *Hourglass stabilization and the virtual element method*, Int J Numer Methods Eng, 102 (2015), pp. 404–436.

[31] B. Cao, *Solutions of Navier equations and their representation structure*, Advances in Applied Mathematics, 43 (2009), pp. 331–374.

[32] Y. P. Cao, N. Hu, H. Fukunaga, J. Lu, and Z. H. Yao, *A highly accurate brick element based on a three-field variational principle for elasto-plastic analysis*, Finite Elem Anal Des, 39 (2003), pp. 1155–1171.

[33] Y. P. Cao, N. Hu, J. Lu, H. Fukunaga, and Z. H. Yao, *A 3d brick element based on Hu–Washizu variational principle for mesh distortion*, Int J Numer Methods Eng, 53 (2002), pp. 2529–2548.

[34] S. Cen, X.-R. Fu, and M.-J. Zhou, *8- and 12-node plane hybrid stress-function elements immune to severely distorted mesh containing elements with concave shapes*, Comput Methods Appl Mech Eng, 200 (2011), pp. 2321–2336.

[35] A. Chen, J. E. Bishop, and N. Sukumar, *Stress-hybrid virtual element method on six-noded triangular meshes for compressible and nearly-incompressible linear elasticity*, Comput Methods Appl Mech Eng, 426 (2024), p. 116971.

[36] A. Chen and N. Sukumar, *Stabilization-free serendipity virtual element method for plane elasticity*, Comput Methods Appl Mech Eng, 404 (2023), p. 115784.

[37] ———, *Stabilization-free virtual element method for plane elasticity*, Comput Math Applications, 138 (2023), pp. 88–105.

[38] ———, *Stress-hybrid virtual element method on quadrilateral meshes for compressible and nearly-incompressible linear elasticity*, Int J Numer Methods Eng, (2023). DOI: https://doi.org/10.1002/nme.7384.

[39] H. Chi, L. B. da Veiga, and G. Paulino, *Some basic formulations of the virtual element method (vem) for finite deformations*, Comput Methods Appl Mech Eng, 318 (2017), pp. 148–192.

[40] E. B. Chin, J. B. Lasserre, and N. Sukumar, *Numerical integration of homogeneous functions on convex and nonconvex polygons and polyhedra*, Comput Mech, 56 (2015), pp. 967–981.

[41] E. B. Chin and N. Sukumar, *Scaled boundary cubature scheme for numerical integration over planar regions with affine and curved boundaries*, Comput Methods Appl Mech Eng, 380 (2021), p. 113796.

[42] P. G. Ciarlet, *The Finite Element Method for Elliptic Problems*, Society for Industrial and Applied Mathematics, Philadelphia, second ed., 2002.

[43] R. D. Cook, *Improved two-dimensional finite element*, J Struct Div-ASCE, 100 (1974), pp. 1851–1863.

[44] R. D. Cook, *Avoidance of parasitic shear in plane element*, J Struct Div-ASCE, 101 (1975), pp. 1239–1253.

[45] R. D. Cook, *A plane hybrid element with rotational d.o.f. and adjustable stiffness*, Int J Numer Methods Eng, 24 (1987), pp. 1499–1508.

[46] R. D. Cook, *Some options for plane triangular elements with rotational degrees of freedom*, Finite Elem Anal Des, 6 (1990), pp. 245–249.

[47] M. Cremonesi, A. Lamperti, C. Lovadina, U. Perego, and A. Russo, *Analysis of a stabilization-free quadrilateral virtual element for 2d linear elasticity in the Hu-Washizu formulation*, Comput Math Applications, 155 (2024), pp. 142–149.

[48] E. Cáceres, G. N. Gatica, and F. A. Sequeira, *A mixed virtual element method for a pseudostress-based formulation of linear elasticity*, Appl Numer Math, 135 (2019), pp. 423–442.

[49] L. B. da Veiga, A. Chernov, L. Mascotto, and A. Russo, *Exponential convergence of the hp virtual element method in presence of corner singularities*, Numer Math, 138 (2018), pp. 581–613.

[50] K. T. Danielson, *Fifteen node tetrahedral elements for explicit methods in nonlinear solid dynamics*, Comput Methods Appl Mech Eng, 272 (2014), pp. 160–180.

[51] F. Dassi, C. Lovadina, and M. Visinoni, *Hybridization of the virtual element method for linear elasticity problems*, Math Models Methods Appl Sci, 31 (2021), pp. 2979–3008.

[52] F. Dassi and L. Mascotto, *Exploring high-order three dimensional virtual elements: Bases and stabilizations*, Comput Math Applications, 75 (2018), pp. 3379–3401.

[53] M. L. De Bellis, P. Wriggers, and B. Hudobivnik, *Serendipity virtual element formulation for nonlinear elasticity*, Computers and Structures, 223 (2019), p. 106094.

[54] A. M. D'Altri, S. de Miranda, L. Patruno, and E. Sacco, *An enhanced VEM formulation for plane elasticity*, Comput Methods Appl Mech Eng, 376 (2021), p. 113663.

[55] J. Eom, J. Ko, and B. Chai Lee, *A macro plane triangle element from the individual element test*, Finite Elem Anal Des, 45 (2009), pp. 422–430.

[56] C. A. Felippa, *A study of optimal membrane triangles with drilling freedoms*, Comput Methods Appl Mech Eng, 192 (2003), pp. 2125–2168.

[57] J. W. Foulk III, J. T. Ostien, B. Talamini, M. R. Tupek, N. K. Crane, A. Mota, and M. G. Veilleux, *Extending a 10-node composite tetrahedral finite element for solid mechanics*, Int J Numer Methods Eng, 122 (2021), pp. 3845–3875.

[58] A. L. Gain, C. Talischi, and G. H. Paulino, *On the virtual element method for three-dimensional linear elasticity problems on arbitrary polyhedral meshes*, Comput Methods Appl Mech Eng, 282 (2014), pp. 132–160.

[59] S. Ghosh and R. Mallett, *Voronoi cell finite elements*, Comput Struct, 50 (1994), pp. 33–46.

[60] Y. Guo, M. Ortiz, T. Belytschko, and E. A. Repetto, *Triangular composite finite elements*, Int J Numer Methods Eng, 47 (2000), pp. 287–316.

[61] K. Hormann and N. Sukumar, eds., *Generalized Barycentric Coordinates in Computer Graphics and Computational Mechanics*, Taylor & Francis, CRC Press, Boca Raton, 2017.

[62] J. Jirousek and A. Venkatesh, *Generation of optimal assumed stress expansions for hybrid-stress elements*, Comput Struct, 32 (1989), pp. 1413–1417.

[63] C. S. Jog, *A 27-node hybrid brick and a 21-node hybrid wedge element for structural analysis*, Finite Elem Anal Des, 41 (2005), pp. 1209–1232.

[64] ———, *Improved hybrid elements for structural analysis*, Mech Mater, 5 (2010), pp. 507–528.

[65] C. S. Jog and R. Bayadi, *Stress and strain-driven algorithmic formulations for finite strain viscoplasticity for hybrid and standard finite elements*, Int J Numer Methods Eng, 2009 (2009), pp. 773–816.

[66] C. S. Jog and G. S. J. Gautam, *A monolithic hybrid finite element strategy for nonlinear thermoelasticity*, Int J Numer Methods Eng, 112 (2017), pp. 26–57.

[67] C. S. Jog and P. P. Kelkar, *Non-linear analysis of structures using high performance hybrid elements*, Int J Numer Methods Eng, 68 (2006), pp. 473–501.

[68] C. Kadapa, *Novel quadratic Bézier triangular and tetrahedral elements using existing mesh generators: Applications to linear nearly incompressible elastostatics and implicit and explicit elastodynamics*, Int J Numer Methods Eng, 117 (2019), pp. 543–573.

[69] A. Karimipour and E. Noroozinejad Farsangi, *Airy stress function for proposed thermoelastic triangular elements*, J Eng Math, 138 (2023), p. 11.

[70] A. Lamperti, M. Cremonesi, U. Perego, A. Russo, and C. Lovadina, *A Hu–Washizu variational approach to self-stabilized virtual elements: 2d linear elastostatics*, Comput Mech, (2023).

[71] ———, *A Hu-Washizu variational approach to self-stabilized quadrilateral virtual elements: 2d linear elastodynamics*, Comput Mech, (2024).

[72] L. Leonetti and M. Aristodemo, *A composite mixed finite element model for plane structural problems*, Finite Elem Anal Des, 94 (2015), pp. 33–46.

[73] T. Li, X. Ma, J. Xili, and W. Chen, *Higher-order hybrid stress triangular Mindlin plate element*, Comput Mech, 58 (2016), pp. 911–928.

[74] C. S. Long, S. Geyer, and A. A. Groenwold, *A numerical study of the effect of penalty parameters for membrane elements with independent rotation fields and penalized equilibrium*, Finite Elem Anal Des, 42 (2006), pp. 757–765.

[75] X. Ma and W. Chen, *Refined 18-dof triangular hybrid stress element for couple stress theory*, Finite Elem Anal Des, 75 (2013), pp. 8–18.

[76] R. H. MacNeal and R. L. Harder, *A proposed standard set of problems to test finite element accuracy*, Finite Elem Anal Des, 1 (1985), pp. 3–20.

[77] D. S. Malkus and T. J. Hughes, *Mixed finite element methods — reduced and selective integration techniques: A unification of concepts*, Comput Methods Appl Mech Eng, 15 (1978), pp. 63–81.

[78] L. Mascotto, *Ill-conditioning in the virtual element method: Stabilizations and bases*, Numer Meth Part D E, 34 (2018), pp. 1258–1281.

[79] J. Meng, X. Wang, L. Bu, and L. Mei, *A lowest-order free-stabilization virtual element method for the laplacian eigenvalue problem*, J Comput Appl Math, 410 (2022), p. 114013.

[80] M. Mengolini, M. F. Benedetto, and A. M. Aragón, *An engineering perspective to the virtual element method and its interplay with the standard finite element method*, Comput Methods Appl Mech Eng, 350 (2019), pp. 995–1023.

[81] E. A. S. Neto, F. M. A. Pires, and D. R. J. Owen, *F-bar-based linear triangles and tetrahedra for finite strain analysis of nearly incompressible solids. part i: formulation and benchmarking*, Int J Numer Methods Eng, 62 (2005), pp. 353–383.

[82] V. M. Nguyen-Thanh, X. Zhuang, H. Nguyen-Xuan, T. Rabczuk, and P. Wriggers, *A virtual element method for 2d linear elastic fracture analysis*, Comput Methods Appl Mech Eng, 340 (2018), pp. 366–395.

[83] H. Nguyen-Xuan, K. N. Chau, and K. N. Chau, *Polytopal composite finite elements*, Comput Methods Appl Mech Eng, 355 (2019), pp. 405–437.

[84] A. Ortiz-Bernardin, R. Silva-Valenzuela, S. Salinas-Fernández, N. Hitschfeld-Kahler, S. Luza, and B. Rebolledo, *A node-based uniform strain virtual element method for compressible and nearly incompressible elasticity*, Int J Numer Methods Eng, 124 (2023), pp. 1818–1855.

[85] K. Park, H. Chi, and G. Paulino, *B-bar virtual element method for nearly incompressible and compressible materials*, Meccanica, 56 (2020), pp. 1423–1439.

[86] K. Park, H. Chi, and G. H. Paulino, *On nonconvex meshes for elastodynamics using virtual element methods with explicit time integration*, Comput Methods Appl Mech Eng, 356 (2019), pp. 669–684.

[87] K. Park, H. Chi, and G. H. Paulino, *Numerical recipes for elastodynamic virtual element methods with explicit time integration*, Int J Numer Methods Eng, 121 (2020), pp. 1–31.

[88] P.-O. Persson and G. Strang, *A simple mesh generator in MATLAB*, SIAM Rev, 46 (2004), pp. 329–345.

[89] T. H. H. Pian, *Derivation of element stiffness matrices by assumed stress distributions*, AIAA Journal, 2 (1964), pp. 1333–1336.

[90] T. H. H. Pian and K. Sumihara, *Rational approach for assumed stress finite elements*, Int J Numer Methods Eng, 20 (1984), pp. 1685–1695.

[91] T. H. H. Pian and P. Tong, *Relations between incompatible displacement model and hybrid stress model*, Int J Numer Methods Eng, 22 (1986), pp. 173–181.

[92] T. H. H. Pian and C.-C. Wu, *A rational approach for choosing stress terms for hybrid finite element formulations*, Int J Numer Methods Eng, 26 (1988), pp. 2331–2343.

[93] R. Piltner and R. L. Taylor, *A quadrilateral mixed finite element with two enhanced strain modes*, Int J Numer Methods Eng, 38 (1995), pp. 1783–1808.

[94] ———, *A systematic construction of b-bar functions for linear and non-linear mixed-enhanced finite elements for plane elasticity problems*, Int J Numer Methods Eng, 44 (1999), pp. 615–639.

[95] B. D. Reddy and D. van Huyssteen, *A virtual element method for transversely isotropic elasticity*, Comput Mech, 64 (2019), pp. 971–988.

[96] M. Rezaiee-Pajand and A. Karimipour, *Three stress-based triangular elements*, Eng Comput, 36 (2020), pp. 1325–1345.

[97] A. Russo and N. Sukumar, *Quantitative study of the stabilization parameter in the virtual element method*, 2023.

[98] M. H. Sadd, *Elasticity Theory, Applications, and Numerics*, Academic Press, Burlington, Massachusetts, first ed., 2005.

[99] G. Scovazzi, B. Carnes, X. Zeng, and S. Rossi, *A simple, stable, and accurate linear tetrahedral finite element for transient, nearly, and fully incompressible solid dynamics: a dynamic variational multiscale approach*, Int J Numer Methods Eng, 106 (2016), pp. 799–839.

[100] T. Shilt, P. J. O'Hara, R. Deshmukh, and J. J. McNamara, *Solution of nearly incompressible field problems using a generalized finite element approach*, Comput Methods Appl Mech Eng, 368 (2020), p. 113165.

[101] J. Simo, F. Armero, and R. Taylor, *Improved versions of assumed enhanced strain tri-linear elements for 3d finite deformation problems*, Comput Methods Appl Mech Eng, 110 (1993), pp. 359–386.

[102] J. C. Simo and T. J. R. Hughes, *On the variational foundations of assumed strain methods*, J Appl Mech, 53 (1986), pp. 51–54.

[103] J. C. Simo and M. S. Rifai, *A class of mixed assumed strain methods and the method of incompatible modes*, Int J Numer Methods Eng, 29 (1990), pp. 1595–1638.

[104] R. L. Spilker, *Improved hybrid-stress axisymmetric elements including behaviour for nearly incompressible materials*, Int J Numer Methods Eng, 17 (1981), pp. 483–501.

[105] R. L. Spilker, S. M. Maskeri, and E. Kania, *Plane isoparametric hybrid-stress elements: Invariance and optimal sampling*, Int J Numer Methods Eng, 17 (1981), pp. 1469–1496.

[106] K. Y. Sze, *On immunizing five-beta hybrid-stress element models from 'trapezoidal locking' in practical analyses*, Int J Numer Methods Eng, 47 (2000), pp. 907–920.

[107] C. Talischi, G. H. Paulino, A. Pereira, and I. F. Menezes, *Polymesher: a general-purpose mesh generator for polygonal elements written in Matlab*, Struct Multidiscipl Optim, 45 (2012), pp. 309–328.

[108] P. Thoutireddy, J. F. Molinari, E. A. Repetto, and M. Ortiz, *Tetrahedral composite finite elements*, Int J Numer Methods Eng, 53 (2002), pp. 1337–1351.

[109] S. P. Timoshenko and J. N. Goodier, *Theory of Elasticity*, McGraw-Hill, New York, third ed., 1970.

[110] D. van Huyssteen and B. Reddy, *The incorporation of mesh quality in the stabilization of virtual element methods for nonlinear elasticity*, Comput Methods Appl Mech Eng, 392 (2022), p. 114720.

[111] C. Wang, X. Zhang, and P. Hu, *Assumed stress quasi-conforming triangular element for couple stress theory*, Acta Mech Solida Sin, 30 (2017), pp. 335–344.

[112] N.-E. Wiberg and F. Abdulwahab, *Patch recovery based on superconvergent derivatives and equilibrium*, Int J Numer Methods Eng, 36 (1993), pp. 2703–2724.

[113] E. L. Wilson, R. L. Taylor, W. P. Doherty, and J. Ghaboussi, *Incompatible displacement models*, in Numerical and Computer Methods in Structural Mechanics, S. J. Fenves, N. Perrone, A. R. Robinson, and W. C. Schnobrich, eds., Elsevier, 1973, pp. 43–57.

[114] P. Wriggers, B. D. Reddy, W. Rust, and B. Hudobivnik, *Efficient virtual element formulations for compressible and incompressible finite deformations*, Comput Mech, 60 (2017), pp. 253–268.

[115] P. Wriggers, W. T. Rust, and B. D. Reddy, *A virtual element method for contact*, Comput Mech, 58 (2016), pp. 1039–1050.

[116] C.-C. Wu and Y. Cheung, *On optimization approaches of hybrid stress elements*, Finite Elem Anal Des, 21 (1995), pp. 111–128.

[117] C.-C. Wu and Y. K. Cheung, *Penalty-equilibrating approach and an innovative formulation of 4-noded hybrid stress elements*, Commun Numer Meth En, 12 (1996), pp. 707–717.

[118] Q. Xiao, B. Karihaloo, and F. Williams, *Application of penalty-equilibrium hybrid stress element method to crack problems*, Eng Fract Mech, 63 (1999), pp. 1–22.

[119] B.-B. Xu, F. Peng, and P. Wriggers, *Stabilization-free virtual element method for finite strain applications*, Comput Methods Appl Mech Eng, 417 (2023), p. 116555.

[120] B.-B. Xu and P. Wriggers, *3d stabilization-free virtual element method for linear elastic analysis*, Comput Methods Appl Mech Eng, 421 (2024), p. 116826.

[121] O. C. Zienkiewicz, *Displacement and equilibrium models in the finite element method by B. Fraeijs de Veubeke, chapter 9, pages 145–197 of Stress Analysis, edited by O. C. Zienkiewicz and G. S. Holister, published by John Wiley & Sons, 1965*, Int J Numer Methods Eng, 52 (2001), pp. 287–342.